Thèse n° 10135

Fast ion transport phenomena in turbulent toroidal plasmas

Présentée le 10 septembre 2020

à la Faculté des sciences de base
SPC - Physique des Plasmas de Base
Programme doctoral en physique

pour l'obtention du grade de Docteur ès Sciences

par

Fabian MANKE

Acceptée sur proposition du jury

Prof. F. Courbin, président du jury
Prof. I. Furno, directeur de thèse
Prof. Å. Fredriksen, rapporteuse
Prof. F. Zonca, rapporteur
Prof. A. Fasoli, rapporteur

École
polytechnique
fédérale
de Lausanne

2020

"Moving fast is not the same as going somewhere."
— Robert Anthony

To the ones who will continue this work

Abstract

In the field of plasma physics, suprathermal ions are encountered e.g. in astrophysical jets, the solar wind, as well as fusion plasmas, where they originate from neutral beam injection or fusion reactions. One aspect of shared interest with astrophysical settings is their transport by different forms of plasma turbulence that may generally exhibit non-diffusive character. Therefore, fast ion cross-field transport by electrostatic turbulence is investigated on the TORoidal Plasma EXperiment (TORPEX), in the simple magnetized torus geometry. Lithium ions in the 30-70 eV range are injected toroidally into hydrogen plasmas, with electron temperatures of typically below 5 eV. Previous studies identified sub- to superdiffusive regimes of transport, depending on the fast ion energy and related gyro- and drift-averaging effects.

The first part of this thesis investigates the phenomenon of local intermittency, as quantified by the skewness of fast ion time-series. A comprehensive data-set of fast ion time-series is presented to establish observations of intermittency across all non-diffusive transport regimes. Through the development of an experiment-based particle tracing algorithm, the physical picture of a small, but meandering fast ion beam is clarified and the generation of local intermittency demonstrated through synthetic time-series. Furthermore, an analytical model is presented to predict the skewness of such time-series solely based on their time-average value and two basic beam parameters. Its application to the experimental data shows very good agreement between the predicted and the measured skewness. These combined findings demonstrate conclusively how intermittency is generated across all transport regimes in our system, or by any type of meandering beam.

The second part of this thesis advances the statistical description of non-diffusive fast ion transport through Fractional Diffusion Equations (FDEs). To improve upon physical shortcomings of models that assign distributions with infinite variance to the random jumps of particles, we utilize tempered Lévy distributions, that exponentially truncate jumps beyond a chosen scale. The FDE and propagator of Truncated Asymmetrical Fractional Lévy Motion (TAFLM) are derived by judiciously adapting earlier path-integral methods. Being generally non-Gaussian at early times, the propagators converge arbitrarily slowly to Gaussians in the long-time limit, while preserving their overall non-diffusive behaviour. Very good agreement with fluid-tracer results from the Global Braginskii Solver is found in the most strongly spread, quasi-diffusive regime. Here, the finite domain size of the turbulent plasma structures can now take effect through the truncation scale. Further use of these statistical methods can be discussed across the wider field of bounded, non-diffusive transport.

Abstract

Key words: *Plasma physics, statistics, turbulence, blobs, fast ions, anomalous transport, superdiffusion, subdiffusion, intermittency, particle beam, Lévy distributions, fractional diffusion, truncation effects, tempered stable random process*

Résumé

A travers le domaine de la physique des plasmas, les ions supra-thermiques sont trouvés par exemple dans les jets astrophysiques, le vent solaire, et bien-sûr dans les plasmas de fusion, où ils proviennent de l'injection des faisceaux de particules neutres ou des réactions de fusion. Un aspect d'interêt commun pour ces domaines, est leur transport par des différentes formes de turbulence de plasma, qui peut s'effectuer, en général, d'une manière non-diffusive. Donc, le transport de tels ions rapides par la turbulence électrostatique à travers des champs magnétiques est étudié sur une EXpérience de Plamsa TORoidale (TORPEX), dans une configuration magnétique hélicale et ouverte. Des ions de lithium d'une énergie de 30 à 70 eV sont injectés toroidalement dans un plasma d'hydrogène, dont la température des électrons vaut typiquement moins de 5 eV. Auparavant, des régimes de transports sous- à supra-diffusifs furent identifiés, ainsi que leur dépendence de l'énergie des ions rapides qui est liée à des effets de moyennement par les gyrations et les dérives des ions dans le champ.

La première partie de cette thèse traite le phénomène d'intermittence locale, qui se quantifie par l'asymétrie statistique des séries chronologiques des ions rapides. Une base de données exhaustive est présentée pour établir des observations d'intermittence à travers tout les régimes de transport non-diffusif. Par le développement d'un algorithme numérique pour trouver les trajectoires des ions à partir de données experimentales sur la turbulence, nous clarifions la nature physique de notre système comme un faisceau concentré, mais perpétuellement en mouvement transversal. La génération d'intermittence dans ce système est démontrée par des séries chronologiques numériques. Ensuite, un modèle analytique est présenté qui permet de prédire l'intermittence de telles séries chronologiques directement à partir de leurs valeurs moyennes, et deux paramètres de base du faisceau. Son application à la base de données experimentale montre un bon accord entre les prédictions et l'intermittence mesurée. L'ensemble de ces résultats démontre de façon concluante comment de l'intermittence est générée à travers tous les régimes de transport dans notre système, ainsi que par des faisceaux en mouvement transversal en général.

La deuxième partie de cette thèse présente des avancées sur la description statistique du transport non-diffusif des ions rapides par des Equations de Diffusion Fractionnaires (FDEs). Pour surmonter certains défauts physiques de tels traitements qui modélisent les sauts aléatoires des particules par des distributions avec une variance infinie, nous exploitons des distributions de Lévy tempérées, qui tronquent la probabilité des sauts de façon exponentielle sur une échelle de longueur donnée. La FDE et le propagateur du modèle de Truncated Asymmetrical Fractional Lévy Motion sont donc dérivés en adaptant judicieusement des méthodes d'intégrale de chemin vues auparavant. Généralement non-Gaussien au début, les propagateurs convergent lentement à la forme Gaussienne plus tard, mais en gardant le même caractère non-diffusif. Une correspondance excellente avec des distributions numériques des ions rapides, sur la base du code fluide Global Braginskii Solver, est trouvée dans le régime quasi-diffusif et long-terme, où les ions se sont répandus le plus. La taille finie du domaine des structures de plasma turbulentes peut maintenant prendre effet par la longueur de troncature. Davantage d'applications de ces méthodes statistiques pourraient se présenter à travers le domaine général de transport non-diffusif spatialement délimité.

Mots clefs : *Physique des plasmas, statistique, turbulence, blobs, ions rapides, transport anormal, supra-diffusion, sous-diffusion, intermittence, faisceau de particlues, distributions de Lévy, diffusion fractionnaire, effets de troncature, processus aléatoire stable tempéré*

Zusammenfassung

Im Gebiet der Plasmaphysik werden suprathermische Ionen sowohl in astrophysikalischen Jets und im Sonnenwind behandelt, als auch in Fusionsplasmen, wo sie durch Neutralteilcheninjektion oder Fusionsreaktionen entstehen. Ein Aspekt von gleichsam geteiltem Interesse ist ihr Transport durch verschiedene Formen von Plasmaturbulenz, welcher im allgemeinen nicht-diffusive Chrakteristika haben kann. Daher wird die Streuung von solch ‘schnellen’ Ionen durch elektrostatische Turbulenz im TORoidalen Plasma EXperiment (TORPEX) untersucht, senkrecht zu dessen helikalen Magnetfeldlinien. Lithiumionen im Energiebereich von 30 bis 70 eV werden toroidal in Wasserstoffplasmen injiziert, welche typische Elektronentemperaturen von weniger als 5 eV aufweisen. Vorausgegangene Untersuchungen identifizierten sub- bis superdiffusive Transportformen, abhängig von der Injektionsenergie, welche die durchschnittlichen Auswirkungen turbulenter elektrischer Felder während der magnetischen Kreis- und Driftbewegung der Ionen bestimmt.

Der erste Teil dieser These untersucht das Phänomen lokaler Intermittenz, welche durch die statistische Schiefe von Zeitreihenmessungen der lokalen Dichte schneller Ionen quantifiziert wird. Ein umfassender experimenteller Datensatz wird präsentiert, der die Beobachtung solcher Intermittenz in jedweder nicht-diffusiver Transportform der schnellen Ionen hinterlegt. Ein Algorithmus zur Simulation ihrer Teilchenbahnen mithilfe experimenteller Messungen des Hintergrundplasmas wurde entwickelt, und verdeutlicht die Erscheinungsform eines kleinen, konzentrierten Teilchenstrahls von schnellen Ionen, der durch die Plasmaturbulenz quer bewegt und abgelenkt wird. Die Entstehung lokaler Intermittenz wird durch die resultierenden Spitzen in künstlichen Zeitreihenmessungen veranschaulicht. Desweiteren wird ein analytisches Modell präsentiert, welches erlaubt die statistische Schiefe der Zeitreihen vorherzusagen, lediglich aufgrund ihrer Mittelwerte, sowie zwei grundlegender Parameter des Teilchenstrahls. Angewandt auf die experimentellen Zeitreihenmessungen wird eine sehr gute Übereinstimmung zwischen der vorhergesagten und gemessenen Schiefe sichtbar. Die Gesamtheit dieser Erkenntnisse demonstriert auf schlüssige Weise, wie lokale Intermittenz in unserem System in allen nicht-diffusiven Transportformen entsteht, gleichwie auch bei jeder ähnlichen Art von beweglichem Teilchenstrahl.

Der zweite Teil dieser These verbessert die statistische Beschreibung des globalen Transports der schnellen Ionen durch Fraktionale Diffusionsgleichungen. Um die physikalischen Unzulänglichkeiten von Modellen zu überwinden, die Wahrscheinlichkeitsverteilungen mit unendlicher Varianz für die zufälligen Schritte der Teilchen ansetzen, benutzen wir temperierte Lévy-Verteilungen, welche die Wahrscheinlichkeit von Schritten über einer gewissen

Abschnittslänge exponentiell unterdrücken. Die Diffusionsgleichung und Greensche Funktion des Modells der Truncated Asymmetrical Fractional Lévy Motion (TAFLM) wird durch die sorgfältige Anpassung früherer Methoden basierend auf Pfadintegralen hergeleitet. Obwohl sie anfangs eine im allgemeinen nicht-Gaußsche Form hat, konvergiert die Greensche Funktion beliebig langsam zu einer Normalverteilung üeber längere Zeiträume, wobei ihre Streuung ihren nicht-diffusiven Charakter beibehält. Sehr gute Übereinstimmung mit der Entwicklung von simulierten Teichenverteilungen, erstellt mithilfe des Global Braginskii Solvers, besteht während der asymmetrischen, quasi-diffusiven Transportform, in welcher die schnellen Ionen am weitesten gestreut werden. Hier kann nun die typische Weite des Wirkungsbereiches der verantwortlichen Plasmaturbulenz durch die gesetzte Abschnittslänge des TAFLM Modells beschrieben werden. Weitere Anwendungen dieses Modells im allgemeinen Rahmen von Studien zu räumlich begrenztem, nicht-diffusivem Transport können diskutiert werden.

Stichwörter: *Plasmaphysik, Statistik, Turbulenz, Blobs, Schnelle Ionen, Anomaler Transport, Superdiffusion, Subdiffusion, Intermittenz, Teilchenstrahl, Lévy-Verteilungen, Fraktionale Diffusion, Begrenzte Zufallsschritte, Temperierte stabile Zufallsprozesse*

Contents

Abstract (English/Français/Deutsch) **i**

1 Introduction **1**
- 1.1 Approaches to sustainable energy 1
- 1.2 Fusion energy 2
  - 1.2.1 Basic concepts 2
  - 1.2.2 Inertial Confinement Fusion 5
  - 1.2.3 Magnetic Confinement Fusion 5
- 1.3 Turbulence and fast ions 9
- 1.4 Motivation and outline for this thesis 11

2 Experiments on TORPEX **13**
- 2.1 The TORPEX device and turbulence 13
- 2.2 Langmuir probe measurements 17
- 2.3 Other plasma diagnostics 22
- 2.4 Fast ion experimental set-up 24
  - 2.4.1 Fast ion injection 24
  - 2.4.2 Fast ion detection 26
  - 2.4.3 Recent additions 27
- 2.5 Previous fast ion studies 34
  - 2.5.1 Basic fast ion dynamics 34
  - 2.5.2 Measuring time-average cross-field transport 35
  - 2.5.3 GBS fluid-tracer simulations 35
  - 2.5.4 Non-diffusive transport regimes 38
  - 2.5.5 Fractional diffusion models 39
  - 2.5.6 Time-resolved measurements and intermittency 39

3 Time intermittency studies **41**
- 3.1 Quantifying intermittency 41
- 3.2 Statistics of measured time-series 45
- 3.3 Conditional Sampling 48
- 3.4 Motivations for further analysis 54

4 Experiment-based particle tracing **57**

4.1 Particle tracing 57
4.2 Incorporating HEXTIP measurements 59
4.3 Time-average cross-field transport 63
4.3.1 Comparison to experiments and GBS 63
4.4 Average vs. single bunch profiles 66
4.5 Synthetic time-series 71
4.6 Conclusions and outlook 73

5 Analytical modeling 75
5.1 The meandering fast ion beam 75
5.2 Intermittency in subdiffusion 77
5.3 Intermittency in super- to quasi-diffusion 80
5.4 Comparison to two-valued time-series 83
5.5 Conclusions 85

6 Statistical modeling of non-diffusive transport 87
6.1 Review of diffusion models 87
6.1.1 Einstein's random walk model 88
6.1.2 Langevin's approach 89
6.1.3 The Gaussian limit 91
6.2 Non-diffusive transport 93
6.2.1 Lévy stable distributions 94
6.2.2 Continuous Time Random Walks 96
6.2.3 Generalized Langevin Equations 99
6.3 Tempered stable distributions 104
6.3.1 A truncated CTRW 105
6.4 Truncated Asymmetrical Fractional Lévy Motion 107

7 Truncated Lévy motion in fast ion transport 115
7.1 Treating numerical fast ion distributions 115
7.2 TAFLM analysis of the moments of fast ion distributions 117
7.3 Fitting the TAFLM propagator 119
7.3.1 Subdiffusive regime 120
7.3.2 Superdiffusive regime 122
7.3.3 Quasi-diffusive regime 124
7.4 Conclusions 126

8 Outlook and conclusions 129
8.1 Other avenues of investigation 129
8.1.1 Multiple time-series 129
8.1.2 Onset of transport 130
8.1.3 Complex field-line configurations 131
8.2 Intermittency studies 135

8.3 Truncation effects 136

A Fitting methods **139**
A.1 Chi-squared fitting 139
A.2 Bootstrap error estimates 140
A.3 Acceptable fits of the TAFLM propagator 141

B The Boris algorithm **145**

C Fractional derivatives **147**

Acronyms **151**

Repeatedly used symbols **153**

Figure attributions **155**

Bibliography **159**

Acknowledgements **177**

Curriculum Vitae **179**

1 Introduction

To give context to this work, we firstly outline how the growing global demand for energy is approached by current technologies and introduce Magnetic Confinement Fusion (MCF) as a sustainable long-term concept. Due to the extreme temperatures required for fusion reactions, the reactants are present in the form of a plasma. The occurrence of both turbulence as well as energetic ions are central to many settings across plasma physics, ranging from fusion devices to astrophysics. We thus motivate the experimental, numerical and analytical studies of this thesis, that aims at describing general transport phenomena of fast ions in plasma turbulence on the TORoidal Plasma EXperiment (TORPEX).

1.1 Approaches to sustainable energy

One of the most pressing challenges of our time is to satisfy humanity's ever growing demand for energy [1, 2]. With limits on many fossil resources seeming imminent in our life-time[3], and the first irreversible effects of climate change becoming a reality [4, 5, 6], it is more crucial than ever that this demand be satisfied through sustainable, emission-free energy production. Unfortunately, global political initiatives culminating in the Paris Climate Agreement are mostly falling short in both their goals [7, 8] and application [9]. Substantial investments are required towards the implementation of renewable energies such as wind and solar power [1, 10, 2]. In fact, they are already becoming an appreciable portion of e.g. the German and European energy market [2], despite various subsidy programs not yielding long-term economic success [11]. Regardless, many projections on the requirements for the future energy market identify these renewable energies as a cornerstone [1, 2, 12].

Therefore, it is imperative to address certain limitations intrinsic to these methods of energy production. For reasons of climate and geography, many countries have difficulties implementing solar or wind power on a self-sustaining scale, as both require a certain minimum of available area and high-load periods with favourable conditions to be viable [13]. While solar power is additionally restricted to day-time hours, the high-load periods for wind power are more irregular. This 'intermittency' in energy production must be compensated by optimizing the relative contributions of wind- and solar power, as well as provisions for power redistribution, storage or back-up to satisfy a likewise variable base-line demand, unless excessive over-capacities in solar and wind power are to be developed [10, 14, 15]. Although e.g. a fully coordinated European grid would be highly beneficial, it is far from implemented and the most important contributions in terms of power compensation would come from outlying countries with relatively independent weather conditions, such as Spain, that would in turn stand to profit the least [10, 15]. While highly desirable from an environmental standpoint, hydrogen-based storage systems are under development, but face clear technical and economical challenges, hindering large scale deployment [16].

Hydro-electricity is an emission-free renewable energy to compensate intermittent energy production as both storage and back-up, but most countries can only derive a modest percentage of their energy from it, since the extent of potentially exploitable river-sections or coast-line remains limited [17, 13, 1]. The globally growing number of droughts [4] is an additional constraint on how much water could be dedicated to energy production [17].

France, for instance, supplies the largest portion of their base-load from nuclear fission power-plants [14, 2] instead. The proposed ‘generation IV’ power-plants are to improve on most aspects of safety, maintenance and cost, while waste-management in particular is to be improved through closed fuel cycles e.g. in fast neutron reactor types, which also reduce the amount of required fuel through breeding reactions [18, 19]. However, this latter aspect may result in conflicts with certain nuclear non-proliferation agreements, and exemplifies how nuclear fission programs are bound to face national and international security concerns [19]. Further public and political reluctance was rekindled with long-term impacts by the Fukushima Dai-ichi incident [12, 2]. However, even renewable energies on their own can come with potential drawbacks before an uncertain political or even security-related background, as they render different locales vulnerable to energy dependencies [20]. This thesis is not going to help change any of this. However, fusion energy just might, and we will be discussing applications of the presented work related to this domain.

1.2 Fusion energy

1.2.1 Basic concepts

In nature, nuclear fusion is the energy source of stars such as our sun, and therefore the original fuel of most surface-based processes on our planet [21, 22], including life. In young proto-stars, hydrogen is compressed and heated under its own gravity eventually forming a plasma [23]. Once the present protons are energetic enough to tunnel through their repulsive Coulomb potential during collisions, fusion reactions are initiated and liberate nuclear binding energy [23] (see Fig 1.1). As nucleo-synthesis progresses towards heavier isotopes and elements, stars develop complex fusion reaction cycles and evolve in a dynamic equilibrium of outward heat transport and gravity [23].

Experimentally, the fusion of deuterium ions was discovered in beam-target experiments by Oliphant, Harteck and Rutherford [24] even 4 years before the documentation of neutron-induced uranium fission through Hahn, Meitner and Frisch in 1938 [25]. However, since light-element fusion does not allow for the same kind of avalanche-like process [21], it took longer to utilize the much greater energetic potential offered by fusion reactions such as [26]

$$\mathrm{D}+\mathrm{D} \longrightarrow \begin{cases}\mathrm{T}+\mathrm{p} & (4\,\mathrm{MeV}) \\ {}^{3}\mathrm{He}+\mathrm{n} & (3.3\,\mathrm{MeV})\end{cases} \tag{1.1}$$

$$\mathrm{D}+\mathrm{T} \longrightarrow {}^{4}\mathrm{He}+\mathrm{n} \quad (17.6\,\mathrm{MeV}) \tag{1.2}$$

$$\mathrm{D}+{}^{3}\mathrm{He} \longrightarrow {}^{4}\mathrm{He}+\mathrm{p} \quad (18.3\,\mathrm{MeV}) \tag{1.3}$$

$$\mathrm{T}+\mathrm{T} \longrightarrow {}^{4}\mathrm{He}+2\,\mathrm{n} \quad (11.3\,\mathrm{MeV}) \quad . \tag{1.4}$$

Their reaction probabilities (cross-sections, see Fig. 1.2) still require very high temperatures, although they are not diminished by any electro-weak processes, such as β-decay in solar proton fusion [23, 27]. The first man-made fusion device was the 'Trinity' hydrogen bomb in 1951, which surpassed the achievable yield of early fission warheads by multiple orders of magnitude [28], also due to the higher difference in nuclear binding energy per reactive nucleon. The fission process however was still needed to compress and heat the hydrogen isotope fuel sufficiently [28]. Due to the greater reaction cross-section at the same energies, a D-T mixture has since been chosen as fuel for most fusion applications [21, 27].

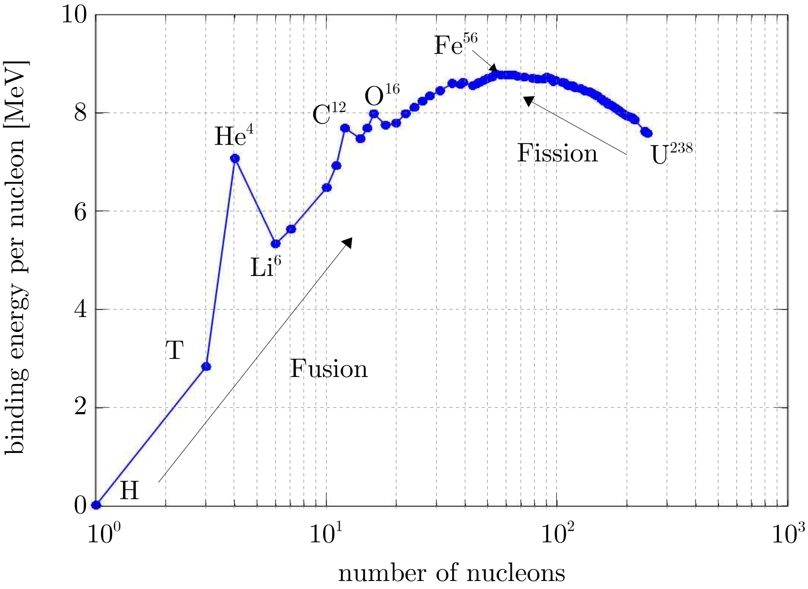

Figure 1.1 – Nuclear binding energy (per nucleon) for a given number of nucleons in an atomic nucleus. Fusion reactions of light elements (e.g. hydrogen) or fission reactions of heavy elements (e.g. uranium) can liberate the difference in binding energy between products and reactants. Data retrieved from [29], see attributions.

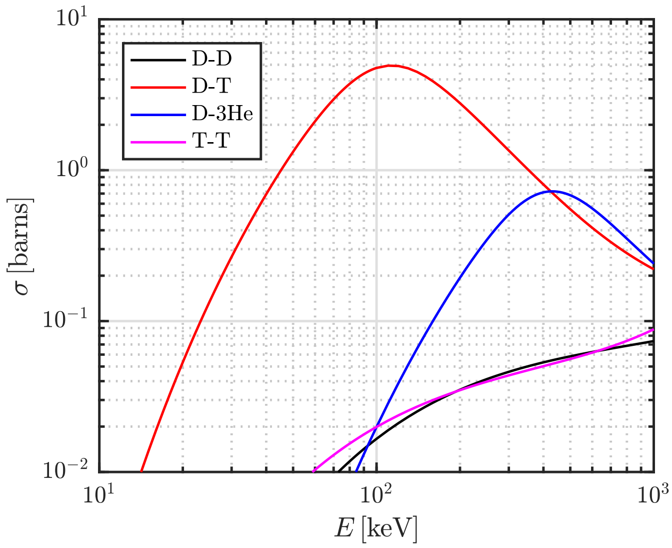

Figure 1.2 – Cross-sections σ for the given fusion reactions, in which the first given reactant is incident as a beam with energy E onto the second reactant as stationary target. Note the much larger cross-sections of the D-T-reaction (red). This tendency still holds in a fusion plasma, where the full velocity distributions for both reactants need to be considered [21, 22]. Calculated from [26].

The extreme required temperatures became however only one part of the challenge for the simultaneously initiated pursuit of stable, controlled fusion energy [30, 22]. Since the reactants must remain in the form of a plasma, its particles and energy need to be confined over a sufficient amount of time to self-initiate enough fusion reactions to achieve a stable net-energy gain [30, 21]. Intuitively, this requires that the losses through outward transport and Bremsstrahlung from the fusion plasma be offset by the confined heating power from the fusion-born α-particles and externally supplied heating power[21]. Such a power-balance leads to the given temperature T and density n of a fusion plasma placing a minimum constraint on its confinement time τ_E and vice-versa. The minimum value of their 'triple-product' for a D-T plasma is found near $T \approx 15\,\mathrm{keV}$ and further constrained by the fact that the ratio of fusion power to heating power (the 'Q-factor') be greater than 1 to gain energy [21]. Similarly presented by Lawson in 1957 [31], the achievement of such a 'break-even' in fusion is thus characterized by

$$n T \tau_E \geq \frac{Q}{Q+5} 8.3\,\mathrm{atm\,s} = f_\alpha 8.3\,\mathrm{atm\,s}, \tag{1.5}$$

where f_α denotes the fraction between α-heating to total heating power. Once α-heating contributes at least as much as the external heating power, i.e. $f_\alpha = 0.5 \iff Q = 5$, the fusion plasma is designated as 'burning' and if no external heating power is required, $f_\alpha = 1 \iff Q = \infty$, the point of full 'ignition' is reached [21].

1.2.2 Inertial Confinement Fusion

Inertial Confinement Fusion (ICF) attempts ignition by imploding only a millimeter-sized capsule of frozen DT-fuel directly or indirectly using high-power lasers [21, 27] as illustrated in Fig. 1.3(a). The extreme increase in density and temperature involved are traded-off against only less than a nano-second of confinement time, during which the fuel remains compressed under its own inertia [27]. Due to the scalable similarities with hydrogen bombs, much research into this US-based approach remained largely classified until the 90ies [30]. Since then, a more international effort has been put forth [27] while the National Ignition Facility (NIF) was implemented [32, 33] at Lawrence Livermore National Lab. Despite an achieved break-even between absorbed and emitted power within the capsule [34], the point of ignition has not been achieved [35], e.g. due to multi-scale hydrodynamic instabilities [see Fig. 1.3(b)] forming at the ablation front and preventing sufficient hot-spot heating and 'burn-through' of the D-T fuel [36, 27, 37]. Improvements in laser pulse shapes [38], implosion capsule and hohlraum design [39, 40], diagnostic modeling [41, 42] and possibly pre-magnetization [43, 44] can aid to increase performance, but have so far been insufficient. While this intrinsically pulsed approach to controlled fusion would have the advantage of not requiring any steady-state control, it would likely require more than one successfully ignited implosions per second [27]. This aim seems still further from realistic as, for instance, the required 1.8 MJ flash-bulb pumped lasers have shown recovery times of at least over 5 hours and opto-electrical efficiencies of $\lesssim 1\%$ [45]. Recent improvements in efficiency and repetition rate through pumping diodes have been realized only on much smaller energy scales [46].

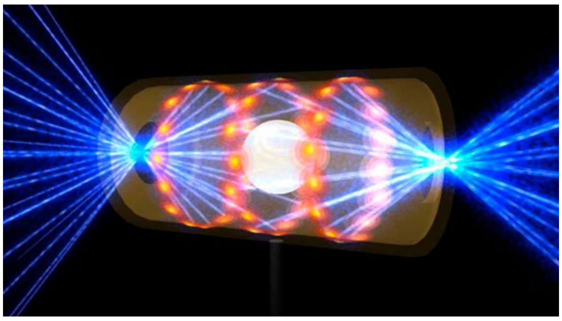

(a) Artists impression of the 'indirect drive' set-up as used on the NIF. The laser-beams illuminate the inner wall of a hollow metal cylinder, the 'hohlraum', from which intense X-rays are re-emitted that ablate the outer layer of the fuel capsule within, driving the implosion. Source: LLNL , see attributions.

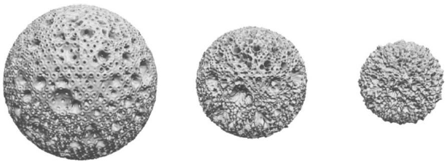

(b) Evolution of seeded multi-mode instabilities during a 'high-foot'-pulse implosion illustrated with constant density contours simulated with the CHIMERA 3D code. Reprinted from [41] with permission from AIP. See attributions.

Figure 1.3 – Illustrations for the Inertial Confinement Fusion concept.

1.2.3 Magnetic Confinement Fusion

The concept of Magnetic Confinement Fusion (MCF) is instead based on the fact that the charged particles in a fusion plasma interact with magnetic fields through the Lorentz-force, which constrains them onto helical trajectories around magnetic field lines [22, 21]. Based on initial concepts by Tamm and Sacharov in 1951, Russian teams thus pursued devices featuring a ring-shaped magnetic geometry of closed field-lines to pursue the stable confinement of a low-density plasma [47]. Later dubbed "toroidal chamber and magnetic coil", abbreviated in Russian to 'to-ka-mak', this arrangement was the first step towards the most thoroughly developed fusion energy concept today [47, 30, 21] (see Fig. 1.4).

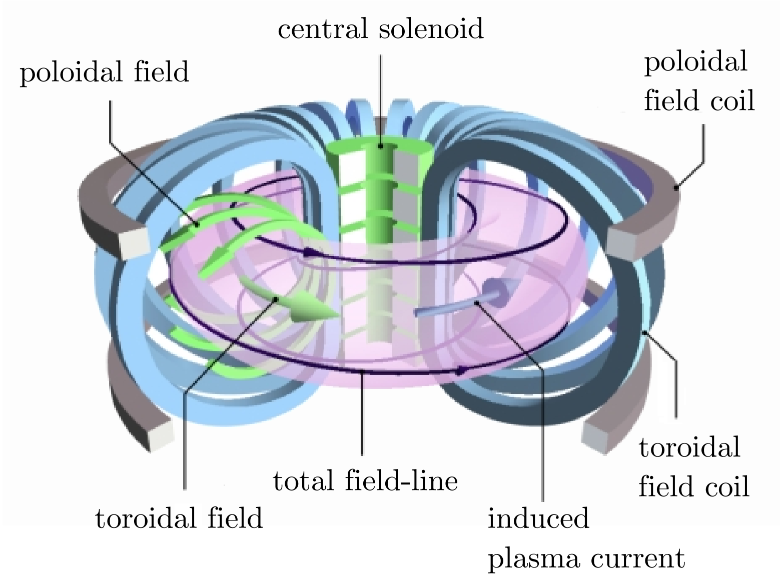

Figure 1.4 – Principal coils and magnetic field configuration of a tokamak. The central solenoid drives the inductive plasma current and its 'flux swing' thus limits the operation time, unless other methods of non-inductive current drive are used [21]. Source: Hindawi open access, see attributions.

In addition to the toroidal magnetic field, a poloidal field is introduced by driving a toroidal current through the plasma, as well as respective field coils. This prevents vertical charge separation due to particle drifts, which would destabilize the plasma quickly [21]. Other waves and instabilities stem from perturbations of the magnetic field due to interactions with the plasma as well as the present currents [48]. This has led to a concerted effort to optimize the magnetic geometry of the tokamak further through theory, simulations and experiments [49]. Since 1992, the Tokamak à Configuration Variable (TCV) [50] at the Swiss Plasma Center (formerly Centre de Recherche en Physique de Plasma, CRPP) equipped with 16 independently adjustable poloidal field coils is central to this effort (see Fig. 1.5).

Plasma heating is firstly achieved as the current driven in the plasma incurs resistance [21], which unfortunately diminishes with rising temperatures [51]. Beyond this point, microwave heating techniques successfully exploit a complex set of resonances in the motion of the plasma particles around the present magnetic field-lines, and can also drive currents non-inductively [49]. When used in a localized and well-timed manner, microwave-injection

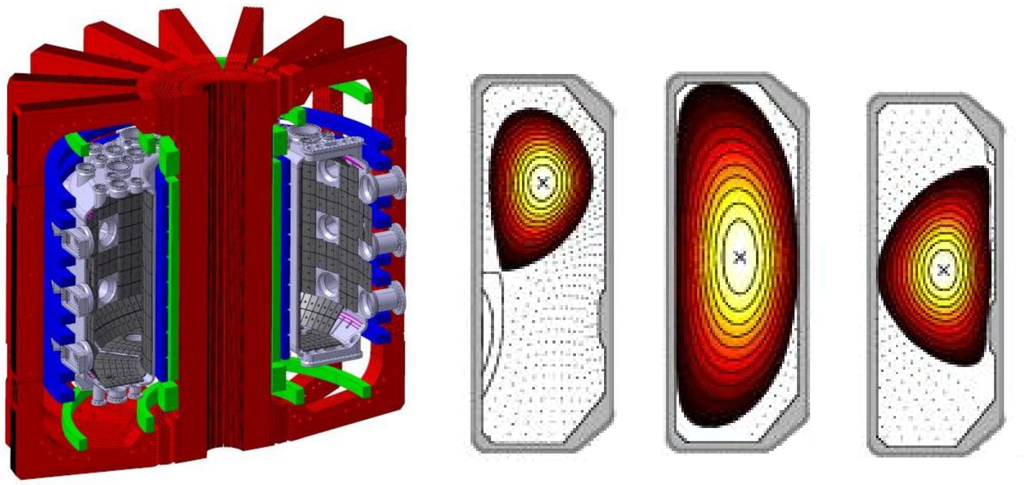

(a) Technical drawing of the TCV tokamak vacuum vessel (light gray) with carbon tiles (dark gray), and equipped with 14 toroidal field coils (red), 16 poloidal shaping coils (blue) and the solenoid coils (green).

(b) Classical single-null, diverted

(c) Maximum elongation, limited

(d) Minimum triangularity, limited

Figure 1.5 – TCV schematic and small selection of available plasma shapes. Source: SPC, see attributions.

can also prevent or stabilize certain resistive magnetic perturbations, so-called neoclassical tearing modes [52]. In addition, Neutral Beam Injection (NBI) is used in most larger MCF devices for directly transferring energy and momentum into the plasma core, as well as driving current [49]. Further research, especially at TCV [53], is for instance addressing problems of real-time control, disruption physics and the optimization of the ‘divertor’ concept [49, 54]. By purposefully opening the outer field-lines of the tokamak plasma [see Fig. 1.5(b)], particles and energy are to be guided onto particularly heat- and radiation-resistant plates. In ’limited’ plasma configurations [see Fig. 1.5(c,d)], the closed field-lines directly intersect the material boundary, which offers less control over both heat and impurity transport. In both cases, the region of open-field lines beyond the closed plasma core is denoted as Scrape-Off-Layer (SOL). To render the divertor power-fluxes of prospectively more than $10\,\mathrm{MW\,m^{-2}}$ managable, the concept of ‘detachment’ is currently being optimized, whereby the plasma and power-flux to the divertor-target are reduced through a localized increase in neutral gas and impurity density and the resulting increase in omnidirectional radiative power-losses [54, 55, 56]. The most powerful operational tokamak to date is the Joint European Torus (JET), based in the UK, which in 1997 temporarily achieved $Q = 0.62$ during its most successful D-T campaign [57, 58].

A different magnetic confinement concept was proposed by Spitzer already in 1951 [59]. "Stellarators" employ coil geometries that directly introduce a rotational transform in the field-lines to cancel magnetic particle drifts, and thus reduces classical transport while also

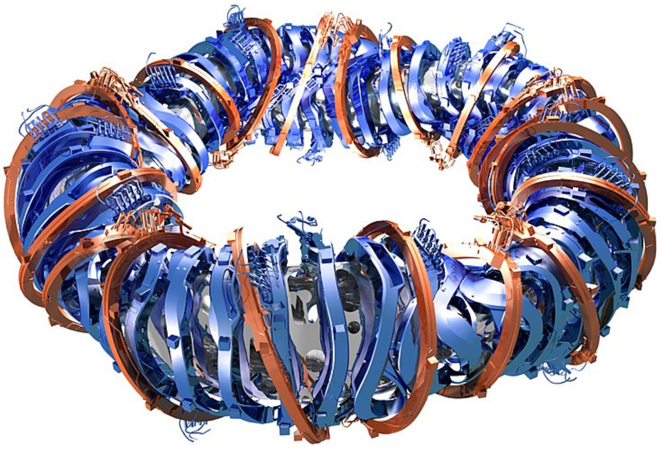

Figure 1.6 – Vacuum-vessel (gray) with planar (red) and non-planar (3D) magnetic coils (blue) of the Wendelstein 7-X stellarator, featuring magnetic field-lines with a 5-fold rotational transform. Source: IOP open access, see attributions.

eliminating the need to drive a large plasma current [22, 21]. Nonetheless, the confinement times of early devices such as the "model C" did not nearly match those of competing tokamaks [47]. However, the concept has received renewed attention since the late 1980ies [30, 22], as the current-driven instabilities in large scale tokamaks became evident, which are avoided in stellarators [21]. After optimizing non-planar coil configurations to further control the neo-classical transport of different plasma components, the most advanced stellarator today is the Wendelstein 7-X [60], based in Germany. While it is currently reaching all the goals that motivated its design, it remains a much more demanding machine to construct and maintain compared to tokamaks of a similar scale, due to the loss of axis-symmetry. Uncertainties also remain with regards to scalability [61] and burning plasma operation.

Therefore, the first fusion reactor aimed at achieving a significant and stable power-gain will be the ITER tokamak [62] with construction underway in southern France [63]. The current ‘European Research Roadmap to the Realisation of Fusion Energy’ [64] from the EUROfusion consortium plans the start of operation by the end of 2025, and D-T experiments at $Q = 10$ in the 2030ies. Based on these findings and pending input from the stellarator community, the design of the first demonstration power plant (DEMO) [65, 66] is to be finalized in parallel. With operation to begin around 2050, fusion energy is to be available for the international energy market in the 2nd half of this century [64].

Only $\gtrsim 100\,\mathrm{kg}$ of reactants are needed to drive a GW-scale power-plant over a year [67]. As tritium has a radioactive half-life of only 12.3 years, it is not found in nature, but is to be bred directly at the power-plant [67] or in fission facilities [68] from lithium-6. Lithium is currently mined at reasonable cost, but is also extractable from virtually inexhaustible reserves in sea-water [69]. Deuterium likewise occurs naturally with $\approx 30\,\mathrm{g}$ per tonne of sea-water, so that the primary resources for D-T fusion could potentially meet the global demand for millions

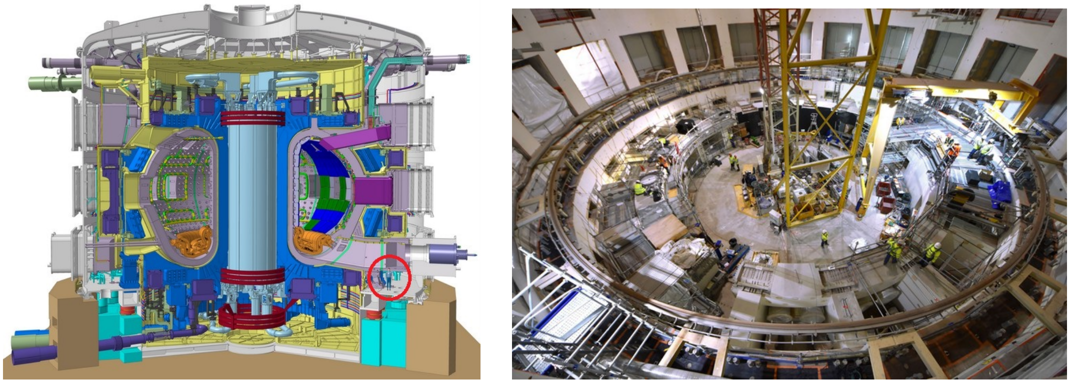

(a) Technical drawing of the ITER tokamak including surrounding cryostat chamber, with a standard-person for scale (red circle).

(b) Photo of the 'pit' into which the ITER cryostat is to be placed, taken in September 2019.

Figure 1.7 – Illustrations of the ITER tokamak project. Source: ITER Organization, see attributions.

of years [61]. The helium produced in fusion reactions is chemically inert, and a valuable resource in itself e.g. for superconductors. Other neutron-activated materials in the reactor would require regular decomissioning, but with much lower radio-toxicity compared to fission reactors, while some alternatives could even permit recycling within a century [61]. This and the complete absence of greenhouse-gas emissions during operation make nuclear fusion the kind of abundant, sustainable and 'green' energy source humankind requires. The small quantities and long-term availability of reactants also make the operation of fusion-based power-plants feasible in most locations around the globe, pending construction logistics and cost [30]. Clearly, fusion energy is also not bound to the same kind of intermittency as solar or wind power, but represents an on-demand source of energy [30, 21]. Since fusion therefore has the potential to offset all the discussed limitations of renewable energies, its most likely commercial use will be to complement them whenever required to ensure a constant, safe and sustainable baseline production of energy [30, 61].

1.3 Turbulence and fast ions

One of the main challenges in MCF is the spontaneous development of waves that can grow into instabilities through the different energy sources available within the plasma and are often accompanied by the development of turbulence in the non-linear regime [21]. Where present, the formation of irregular flows, eddies and structures associated with turbulence leads to non-local 'anomalous' transport of particles and energy [21], which often dominates over predictions based on particle orbits in neo-classical theory [70]. For instance, in the core of MCF devices, temperature and density gradients lead to instabilities at the ion and electron cyclotron scale, causing micro-turbulence and fluctuations in density, temperature and plasma potential, while in some conditions even magnetic perturbations could play an appreciable role [[71, 72] and references therein]. The steep gradients near the plasma edge of tokamaks also drive mainly electrostatic turbulence and the associated filamentary transport accounts for the majority of heat and particle losses across the SOL [72, 73, 74, 75]. Overcoming this limitation is the main motivation for operation in H-mode [76], i.e. a high confinement regime in which extremely steep gradients near the edge can form in conjunction with shear flows that mitigate turbulence [77, 78, 79]. Advanced tokamak scenarios aim to similarly create additional internal transport barriers using specialized magnetic configurations and localized heating [71].

Another important feature of fusion plasmas is the presence of ions with far greater speeds than the thermal average in the plasma. These suprathermal, or 'fast', ions occur as fusion reaction products or through the use of NBI in fusion plasmas [49]. Their confinement in particular is essential to the success of any future fusion device, as they need to transfer their energy to the rest of the plasma through collisions to effectively achieve and maintain a self-heating or 'burning' fusion plasma [80, 81, 82]. In the closed field-lines of tokamaks, they are known to interact with and drive a variety of alfvénic and tearing modes [83, 80, 81]. The effects of micro-turbulence on fast ions have likewise been investigated [84, 85].

In space and astrophysical plasmas, both turbulence as well as fast ions are likewise present, albeit on very different scales. Specifically, magneto-hydrodynamic types of turbulence are more ubiquitous here [86], ranging from interstellar turbulence [87, 88] to the solar wind [89] in interplanetary space. In the interstellar medium, cosmic ray protons are found from jets of massive stellar objects, or super-nova-like events, and indeed interact with magnetic turbulent structures if their gyro-radii are of smaller scales [90, 91]. In the solar wind, fast ions are found in the form of Solar Energetic Particles (SEPs) stemming from magnetic reconnection events and related turbulent dynamics [92]. They are subject to interactions with the solar and interplanetary magnetic fields and the turbulent features arising within them [93, 94, 95, 96].

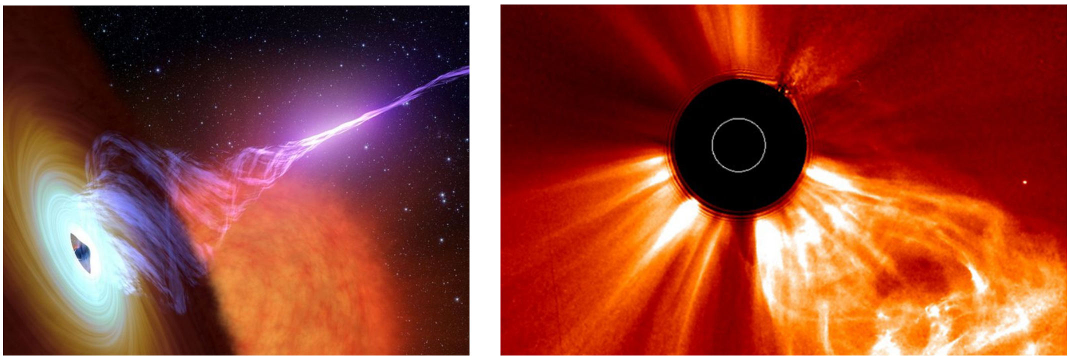

(a) Astrophysical jets above the accretion discs of black holes produce ultra-high energy particles.

(b) Solar Energetic Particles are produced during regular solar activity, but particularly accompany solar storms.

Figure 1.8 – Examples for the occurrence of suprathermal ions in astrophysical settings. Source: NASA, see attributions.

In general, the interaction of fast ions with turbulence can be subject to a variety of non-local features and memory-like effects, that render transport processes very complex to describe. For an efficient macroscopic description it can thus become necessary to abandon the usual paradigm that all transport be a combination of diffusion and advection, but has non-gaussian and non-diffusive characteristics instead. Furthermore, the direct observation of fast ions in many of the mentioned settings is limited to single-point measurements, like Fast Ion Loss Detectors (FILD) in MCF devices [82], or satellites in the magnetosphere [97].

1.4 Motivation and outline for this thesis

The fundamental investigation of suprathermal ion transport by plasma turbulence has therefore become central to the research on the TORoidal Plasma EXperiment (TORPEX) [98, 99, 100]. This basic plasma device allows the controlled generation of turbulence with very well-characterized features in a helical geometry of open magnetic field-lines [101]. We inject and study the broadening of a toroidally propagating beam of suprathermal Li-6 ions through the present electrostatic turbulence [102, 99]. Already previous studies identified this process as generally non-diffusive [103], also by leveraging fluid-tracer simulations [104, 105] based on the Global Braginskii Solver (GBS) code [106]. Locally measured time-series of the fast ion current undergoing superdiffusion were found to feature significant time intermittency, as quantified by their skewness [107]. To effectively reflect the non-local and non-markovian features determining the time-average cross-field transport, the model of Asymmetrical Fractional Lévy Motion (AFLM) was developed [108].

In this thesis, we present significant advances in the description of all these different fast ion transport phenomena. Certain avenues of research, like links between the intermittency in local fast ion time-series and the globally present transport regime, are drawn to a preliminary conclusion [109, 110, 111]. Others, like the use of Fractional Diffusion Equations (FDEs) are continued and generalized to account for physical bounds in fast ion transport [112]. Yet other avenues are opened, like investigations with a newly commissioned multi-point fast ion detector [113], or the description of turbulent fast ion transport in more complex magnetic geometries.

Throughout, we place strong emphasis on the judicious and utility-driven development and application of statistical methods to infer and describe general features of the present system. Often, they will appear to take priority over the treatment of the underlying physical processes, that in many aspects have already been quantified successfully in earlier works [104, 107]. We ask the reader to bear with us in these sections, as it is precisely the versatility of these methods and models that has the potential to contribute to the more meaningful interpretation of transport phenomena in a variety of related systems or even other fields of science.

This thesis is organized as follows: Chapter 2 introduces the TORPEX experiment and gives an overview over the different studies carried out here in parallel. New additions to the hardware are presented and the experimental set-up and methods for fast ion studies are described in detail. Chapter 3 exhaustively presents measurements to characterize the prevalence of local fast ion time-series intermittency across different global transport regimes ranging from sub- to super- and quasi-diffusion. To motivate different aspects of the later analysis, chapter 4 shows relevant findings from a numerical fast ion tracing algorithm, that was developed to utilize Langmuir probe measurements in TORPEX to provide the relevant 3D fields. After comparison to expectations from experiments and GBS fluid-code simulations, the focus is on the qualitative comparison between the fast ion beam profile at a given instant and the time-average profile. After thus motivating the physical picture of a meandering instantaneous fast ion beam, chapter 5 presents an analytical model to predict the skewness of local time-series from their time-average value. By successfully applying this model to the data presented in chapter 3, we conclusively demonstrate how intermittency is generated across all observed non-diffusive transport regimes. Further considerations on simple two-valued time-series complement the analysis as a potential model for extremely narrow meandering beams. In Chapter 6, we proceed towards the second central subject of this thesis, Fractional Diffusion Equations (FDEs) [114, 115, 116]. We give a review of the differences to local and markovian processes, and how non-diffusive features are implemented in Continuous Time Random Walks (CTRWs) [117, 116] and Generalized Langevin Equations (GLEs) [118, 119]. The focus is then placed on truncation effects achieved by exponentially tempering the heavy tailed Lévy-distributions of particle step-sizes [120, 114]. Finally, we combine the truncated description of step-sizes from a CTRW with a non-markovian GLE and derive the propagator and FDE of Truncated Asymmetrical Fractional Levy Motion (TAFLM) using path-integrals for the first time to our knowledge. The propagator features many advantageous properties compared to un-truncated descriptions, such as exponentially tempered tails and analytical and finite moments at all orders, while maintaining a non-diffusive spreading at all times. As expected, the analytical expressions for its variance, skewness and kurtosis reflect non-Gaussian features at short times, but eventually recover Gaussianity due to the Central Limit Theorem. Consequently, we apply the TAFLM description to numerically obtained fast ion distributions in chapter 7 and illustrate its general advantages and limitations in describing non-diffusive systems. Chapter 8 briefly summarizes further avenues of fast ion research on TORPEX that have been embarked upon, including the use of an X-point magnetic geometry, before reviewing the central findings of the thesis and highlighting the most important conclusions.

2 Experiments on TORPEX

In this chapter, we give an overview of the plasma production and dynamics on the TORoidal Plasma EXperiment (TORPEX), and the main diagnostics used in their characterization. Since they are essential to the results presented in the upcoming chapters, particular emphasis is given to Langmuir Probes (LPs) and the HEXagonal Turbulence Imaging Probe Upgrade (HEXTIP-U). Thereafter, the equipment and measurement techniques directly dedicated to fast ions are introduced. The key elements of previous studies are reviewed, as well as recent additions to the experimental set-up, before presenting measurements on the intermittency of fast ion transport in the next chapter.

2.1 The TORPEX device and turbulence

All experiments presented in this thesis have been carried out on the TORPEX basic plasma device (see Fig. 2.1) [121, 99, 100], which has been in operation at the Swiss Plasma Center (formerly Centre de Recherche en Physique de Plasma) at the École Polytechnique Fédérale de Lausanne since 2003 [98]. The project was originally aimed at the reliable reproduction and characterization of different plasmas in helical magnetic field-lines, i.e. in the Simple Magnetized Torus (SMT) geometry [101], through its uniquely flexible and comprehensive diagnostic access [122, 121]. The most important parameters of the machine and the SMT plasmas relevant to the following chapters are summarized in table 2.1.

Hydrogen plasmas can be created through the injection of microwaves in the Electron Cyclotron (EC) frequency range [48]. As the toroidal magnetic field strength features its characteristic $1/R$-dependence, it serves to set the location of the plasma source via the radial position of the EC-resonance layer on the High-Field-Side (HFS) [124]. With increasing plasma density, a significant amount of plasma is also produced at the less localized Upper-Hybrid (UH) resonance [124], as both O-mode and X-mode polarizations are present due to wall reflections of the injected waves. At a microwave-power of 150 W, we can achieve an ionization of $< 1\%$ of the neutral gas. This set-up can be maintained for more than 20 minutes using a 1 kW magnetron that injects microwaves continuously from the bottom of the vessel. For

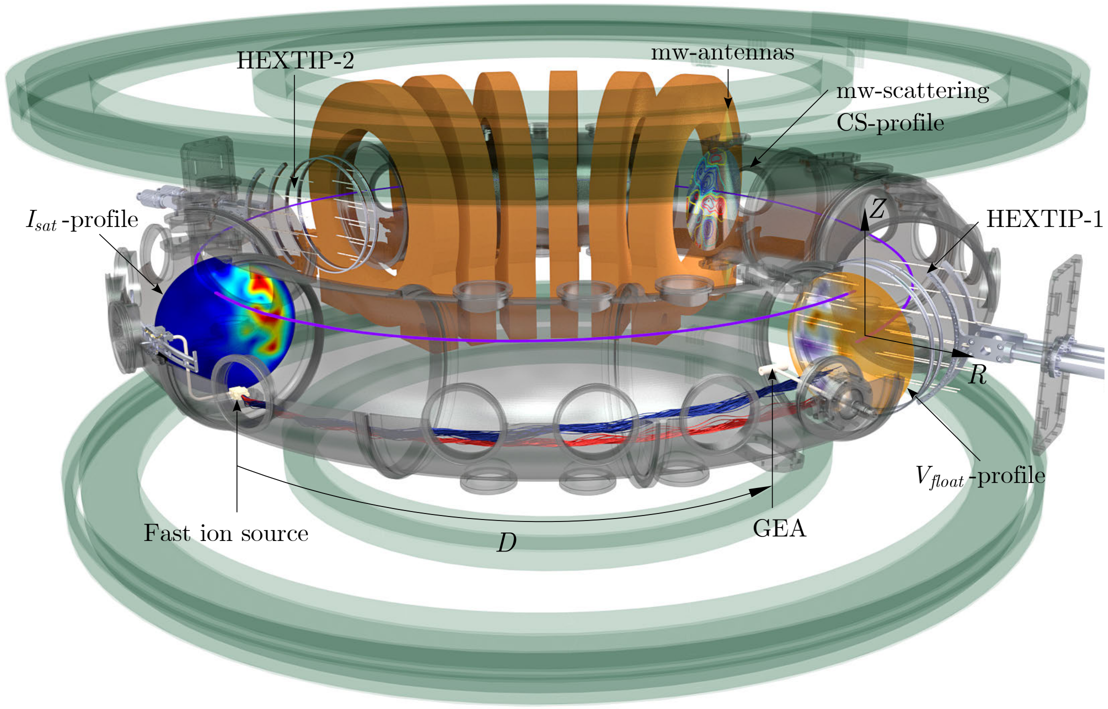

Figure 2.1 – The TORPEX device and fast ion set-up in the SMT configuration. The combination of toroidal field coils (beige) and vertical field coils (green) produces the helical magnetic field as indicated by the purple field-line. The Langmuir probe arrays HEXTIP-1 and -2 are used to characterize the plasma profile at 250 kHz through ion saturation current (left) and floating potential (right) measurements (Figs. 2.5,2.9, Sec. 2.2). Fast ions with energies E of 30 eV (red) to 75 eV (blue) are injected from a modulated, toroidally movable source and propagate over a toroidal distance D to the poloidally movable Gridded Energy Analyzer (GEA), performing locked-in or time-resolved measurements (see Secs. 2.4,2.5 and Ch. 3). Independently, the scattering of micro-waves by plasma structures has been studied using separate microwave antennas outlined in the back to produce Conditionally Sampled profiles of the scattering process ([123], Sec. 2.3).

usually less than 800 ms, a larger magnetron can alternatively inject up to 50 kW of pulsed power from the Low-Field-Side (LFS), whereby the higher densities lead to strongly dominant absorption at the UH-layer [125]. The generated SMT plasma is continuously subject to rapid parallel transport along the magnetic field-lines, such that all structures within the plasma are relatively well field-aligned [101]. With the given pitch angle, a field-line takes $N \approx 2.4$ toroidal turns from the bottom to the top of the vessel, so that one often finds similar plasma densities at a vertical separation of $\Delta Z \approx 16\,\mathrm{cm}$ in the same poloidal cross-section [101, 126].

Driven by the radial pressure gradient, this results in the formation of an ideal interchange mode with a vertical wave number of $k_z \approx \frac{2\pi}{\Delta Z} \approx 35\,\mathrm{rad\,m^{-1}}$ [127, 128]. At a frequency of $f_{int} \approx 10\,\mathrm{kHz}$, the interchange mode propagates upwards with a phase velocity of $\approx 1.6\,\mathrm{km\,s^{-1}}$, resulting in vertical losses of plasma [129]. As intrinsic to interchange modes, charge separation occurs and leads to potential gradients within its plasma density structures, due to the curvature and gradient drifts in this magnetic geometry [22]. Since they reinforce the density perturbations via E×B-drifts to highly non-linear regimes, this allows turbulence to develop [122, 126, 121]. TORPEX plasmas generally have $\beta < 10^{-4}$, so that magnetic perturbations are negligible and the observed modes and turbulence remain electrostatic [130, 121]. Within the turbulence excited through the ideal interchange mode, the intermittent formation of coherent, dipolar plasma filaments, so-called 'blobs', is observed [121, 131]. They detach from the mode, especially in the presence of a steepened local density gradient [132], and continue to propagate outward under their E×B-drifts [131, 133]. Generally, a wide range of sizes and speeds of blobs is produced in different gases [134], but structures in an interchange-dominated hydrogen plasma with a FWHM of $d_{blob} > 3\,\mathrm{cm}$ typically propagate with a velocity of $\sim 1\,\mathrm{km\,s^{-1}}$ and thus reach the LFS region within less than $100\,\mu s$ while decaying. For an increased $N \gtrsim 7$, field-parallel dynamics become important and a resistive interchange regime has been identified through simulations [128]. Collisionalities in TORPEX appear too high to accommodate the steep pressure gradients required for a drift-interchange dominated scenario suspected earlier [130]. While most structures observed at these higher N appear thus sheath-disconnected with $k_{||} \neq 0$, blobs show nonetheless the described dominant interchange character during their generation, as reflected in the $\frac{\pi}{2}$ phase between their density and potential fluctuations [129]. Throughout this thesis, we will focus on SMT plasmas in the ideal interchange regime.

Electrostatic turbulence and blobs are a ubiquitous feature within the source-free open magnetic field lines in the Scrape-Off-Layer (SOL) of tokamaks, where they are the main contributor to the 'anomalous' transport of heat and particles in the plasma edge [72, 73, 74]. It is due to this relevance, that they have been studied fundamentally in TORPEX as outlined above. In particular, the Global Braginskii Solver (GBS) fluid code [128, 106] became central to this effort and has been extensively validated against experiments [137, 138], as have other turbulence simulations since [75].

In 2013, an internal toroidal conductor was added into TORPEX [139]. This copper 'wire' with a diameter of 2 cm can carry up to 1 kA of current to generate a poloidal field within the vessel. Even though the most delicate pieces of the current feed-through into the vessel are water-cooled, such currents can be maintained only over a few seconds without the risk of melting parts of the assembly. The wire is fixed at $R = 0$ and can be moved to different vertical positions by raising or lowering the feed-through as well as 3 stainless steel filaments from which it is suspended. By carefully choosing this position and the currents in the wire and the vertical field-coils, we can now access a variety of more complex magnetic field-line configurations such as a quasi-circular geometry, different single X-points, a double X-point and even a snowflake configuration [139]. Studies of the plasma dynamics in quasi-circular field-lines [140] and blob propagation in an X-point geometry [141] which were carried out in the frame of Fabio Avino's thesis [135] are only relevant for the final outlook of this one. When TORPEX is operated in the SMT configuration, the wire is suspended at $Z = 17.5\,\mathrm{cm}$, where it acts as a merely locally important plasma sink, such as the TORPEX vessel.

Table 2.1 – TORPEX key parameters for the SMT plasmas used for the fast ion measurement campaigns in this thesis. The given values are to be understood as bounds and approximations due to the intrinsic variability of plasma conditions. The given collision frequencies and mean free paths are calculated from the basic plasma parameters as shown in [22], while the estimates for the Coulomb logarithms are taken from [26]. Similar results are given e.g. in [135, 136].

TORPEX device	
Major / minor radius	$R_0 = 1\,\mathrm{m} \quad a = 0.2\,\mathrm{m}$
Toroidal field coils	28
Toroidal field current	$I_{B\Phi} = 367\,\mathrm{A}$
Toroidal magnetic field at $R = 0$	$B_\Phi = 74\,\mathrm{mT}$
Vertical field coils	6
Vertical field current	$I_{Bz} = 95\,\mathrm{A}$
Vertical magnetic field	$B_z \approx 2\,\mathrm{mT}$
Pitch angle and connection length	$\theta \approx 1.5^\circ \quad \Rightarrow \quad L \approx 15\,\mathrm{m}$
MW heating power	$P_{mw} = 150\,\mathrm{W}$
EC-resonance position	$R_{EC} \approx -14\,\mathrm{cm}$
H2 pressure	$p_{H2} \approx 6 \times 10^{-5}\,\mathrm{mbar}$
HEXTIP grid constant	$d_{HT} = 3.5\,\mathrm{cm}$
HEXTIP acquisition rate	$f_{HT} = 250\,\mathrm{kHz}$
Main plasma parameters	
e^- / ion temperature	$T_e \approx 4\,\mathrm{eV} \quad \gg \quad T_i < 1\,\mathrm{eV}$
e^- / ion density	$n_e = n_i \approx 10^{16}\,\mathrm{m}^{-3}$
e^- / ion thermal velocity	$v_{th,e} \approx 840\,\mathrm{km\,s}^{-1} \quad \gg \quad v_{th,i} < 9.8\,\mathrm{km\,s}^{-1}$
e^- / ion Larmor frequency	$\Omega_e \approx 13\,\mathrm{GHz} \quad \gg \quad \Omega_i \approx 7.1\,\mathrm{MHz}$
e^- / ion Larmor radii	$\rho_{L,e} \approx 0.1\,\mathrm{mm} \quad \ll \quad \rho_{L,i} < 2\,\mathrm{mm}$
e^- Debye length	$\lambda_D \approx 0.15\,\mathrm{mm}$
Plasma frequency	$\omega_e \approx 5.6\,\mathrm{GHz}$
e^- / ion collision frequency [22]	$\nu_{ee} \approx 71\,\mathrm{kHz} \quad > \quad \nu_{ii} \approx 10\mathrm{kHz}$
e^- / ion mean free path	$\lambda_{ee}^{mfp} \approx 11.8\,\mathrm{m} \quad > \quad \lambda_{ii}^{mfp} \approx 0.9\,\mathrm{m}$
Radial pressure gradient scale	$L_p = \frac{p}{\partial_R p} \approx 4\,\mathrm{cm}$
Neutral density	$n_n \approx 1.5 \times 10^{18}\,\mathrm{m}^{-3}$
Ionization fraction	$f_i < 1\%$
e^- / ion-neutral collision frequency	$\nu_{en} \approx 250\,\mathrm{kHz} \quad \gg \quad \nu_{in} \approx 15\mathrm{kHz}$
e^- / ion-neutral mean free path	$\lambda_{en}^{mfp} \approx 3.3\,\mathrm{m} \quad > \quad \lambda_{in}^{mfp} \approx 0.7\,\mathrm{m}$
Interchange mode and blobs	
Mode vertical wave number	$k_z \approx 35\,\mathrm{rad\,m}^{-1}$
Mode parallel wave number	$k_{\|} \approx 0$
Mode frequency	$f_{int} \approx 10\,\mathrm{kHz}$
Blob frequency near $R = 0$	$f_{blob} \sim 1\mathrm{kHz}$
Blob FWHM near $R = 0$	$d_{blob} \approx 3 - 7\,\mathrm{cm}$
Blob velocity (radial)	$v_{blob} \sim 1\,\mathrm{km\,s}^{-1}$

We now give an overview of the most important diagnostics and analysis methods employed to characterize TORPEX plasmas.

2.2 Langmuir probe measurements

Langmuir Probes (LPs) are electrodes that are exposed directly to the plasma. Since the first descriptions of their working principles by Irving Langmuir in the early 1920ies [142], their versatility and practical simplicity have been utilized across the field and their physics thus subject of ongoing research, as well as many more standard texts [143, 144, 145]. Only a conceptual summary is given here, focusing on the probe types and measurement techniques employed to obtain the plasma density, temperature and potential on TORPEX.

Depending on the specific purpose and location, the plasma facing probe tip of an LP can take various shapes, but is generally kept small, such that its presence does not perturb the ambient plasma more than necessary. This perturbation occurs through a plasma 'sheath' that forms around the probe tip, as it would on any surface. The lighter, and thus generally faster electrons are adsorbed more readily onto the surface than the ions, such that the quasi-neutrality of the plasma is broken within this layer of multiple Debye-lengths thickness. The negative charge on the surface results in a potential drop that leads to the effective repulsion of further electrons and acceleration of ions towards the sheath. The thus affected pre-sheath region and the sheath therefore find an equilibrium, that is largely determined by the local temperature difference between ions and electrons. In settings with $T_e \gg T_i$ as in TORPEX, this simplifies to an electron temperature T_e dependence for both the pre-sheath size and the local potential drop ΔV. Furthermore, this equilibrium leads to the Bohm-criterion, requiring the ions to enter the sheath above their sound speed $c_s = \sqrt{\frac{k_B T_e}{m_i}}$. If the LP is left floating, no net current is drawn from the plasma, i.e. leading to 'ambipolar' flows. With a known T_e, this requirement can be used to infer the the local plasma potential V_p from measurements of this (negative) floating potential V_f,

$$V_p = V_f + \Delta V = V_f + \underbrace{\ln\sqrt{2\pi\frac{m_i}{m_e}}}_{\approx 3\,\text{for}\, m_i = m_p} T_e \quad \text{for} \quad T_i \ll T_e \tag{2.1}$$

If a more negative bias is applied to the probe, the potential drop is enhanced and the sheath region expands as discussed further below. While ions are drawn towards the probe, electrons are being repelled rapidly as the bias reaches values comparable to $\frac{-2k_B T_e}{e}$, i.e. enough to repel electrons across the wider range of their thermal speeds. Beyond the point where electrons are effectively repelled, the obtainable ion current density saturates with decreasing bias towards a value j_{sat}, which is constrained by the local number of ions that are available. While still subject to the marginal Bohm-criterion, the total ion saturation current I_{sat} on a probe can therefore be used to infer the plasma (ion) density n_i through

$$I_{sat} = A_{eff}\,\underbrace{q\frac{n_i}{2}c_s}_{j_{sat}} = A_{eff}\,q\frac{n_i}{2}\sqrt{\frac{k_B T_e}{m_i}} \quad , \tag{2.2}$$

if the effective probe surface A_{eff}, and local T_e are a known. When applying a bias between V_f and V_p, the probe begins to draw more electron current. From the roll-over into this steep slope of the I-V characteristic of the LP in this range of bias (see Fig. 2.2), one can in fact deduce T_e (and thus V_p), by fitting it to the established analytical formula

$$I(V) \;=\; A_{eff}\,j_{sat}\left[1-\exp\left(\frac{V-V_f}{k_B T_e e^{-1}}\right)\right] \quad , \tag{2.3}$$

as predicted from a basic 1D model of a non-magnetized sheath with Maxwellian electrons and cold ions, valid up to $V \lesssim V_p$ [144]. When $V \ll V_p$ for non-planar LPs, one furthermore needs to account for the ‘sheath expansion’ enhancing A_{eff}, e.g by additionally fitting the slope of the I_{sat} branch in the I-V curve, or by using the Child-Langmuir law to deduce an expression for $A_{eff} = A_{eff}(V - V_p)$ [146]. For $V > V_p$, ions are fully repelled and large, often fluctuating, electron currents are drawn from the plasma. The consistent analytical description of currents in this electron saturation region is still open [145]. In practice, the much larger currents drawn [see Fig. 2.2(a)] can pose a heating risk to the integrity of the cabling and electronics of the probe. Therefore, consistently strongly positive bias is usually avoided in LPs.

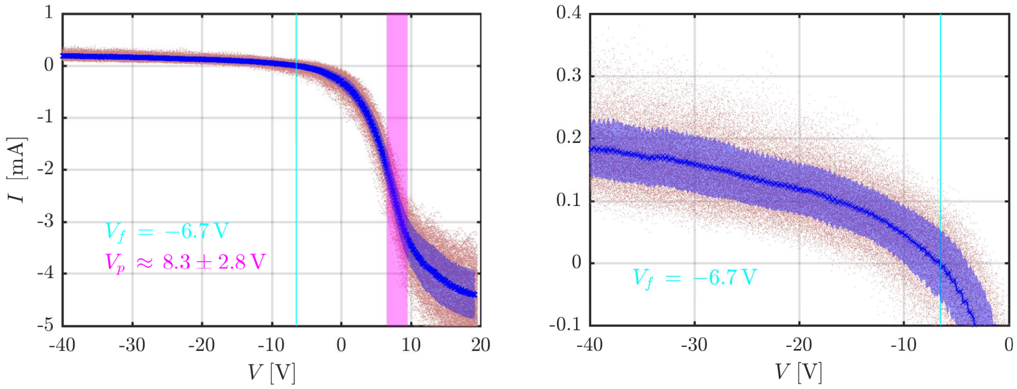

(a) Full range of bias voltage sweep.

(b) Zoom of the I_{sat} branch.

Figure 2.2 – Example of an I-V characteristic obtained from $\approx 2.5 \times 10^5$ samples during a 330 Hz sweep on a probe of the SLP diagnostic. The red dots represent the calibrated measurements, while the dark blue crossed line and surrounding shaded area show the mean and standard deviation from Gaussian weighted moving average smoothing. The current variations are due to fluctuations in the plasma, as well as pick-up noise and possibly probe contamination. Also shown are the floating potential (cyan) at $I = 0$ and the range of suspected plasma potentials (magenta), depending on the estimated $T_e \approx 4.8 \pm 0.5\,\mathrm{eV}$. In the I_{sat} branch for $V < V_f$, note the steadily increasing current with decreasing bias due to sheath expansion in (b).

Various types of LPs and LP arrays have been commissioned for TORPEX (see Fig. 2.3). The Slow Langmuir Probe (SLP) array features eight aligned LP tips and can be moved radially across the plasma and rotated to adjust resolution in the vertical direction [101, 121, 147]. The 2-dimensional Single Sided Langmuir Probe (2DSSLP) array provides 8 probes separated by 1.5 cm, and is mounted on a ball-joint probe arm to scan across the plasma cross-section [140]. Since their probe tips are covered on all but one flat side, they are not affected by sheath expansion and one can even compare asymmetries in the plasma conditions in the toroidal direction. Coupled to the appropriate amplifiers and acquisition circuits [148], all these probes can be fed a periodic bias voltage sweep at frequencies of commonly $\approx 330\,\mathrm{Hz}$. The acquired full I-V characteristics, as shown in Fig. 2.2, are digitized at a frequency of 250 kHz. While all plasma parameters can be inferred from these sweeps as described above, the respective quantities by definition represent time-averages. Since arbitrarily rapid sweeps are often unfeasible and ultimately limited by the acquisition frequency, measurements with floating probes or under constant bias (typically $\approx -40\,\mathrm{V}$) are used to acquire V_f or I_{sat} time-series describing the local evolution of the plasma.

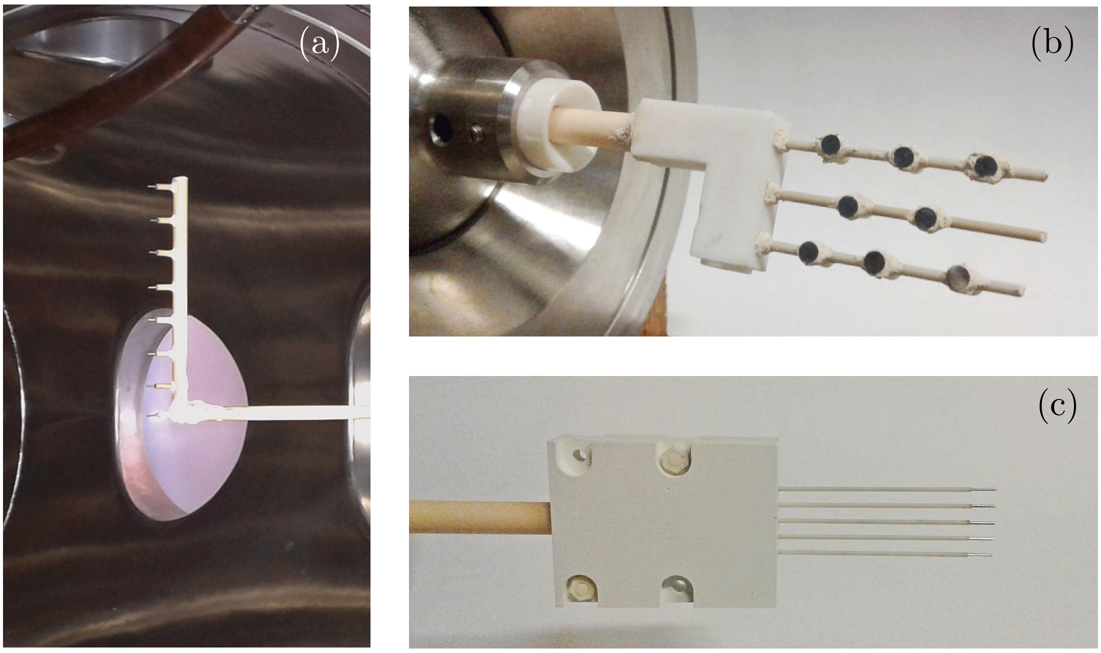

Figure 2.3 – Selection of movable Langmuir probes currently available on TORPEX: (a) The Slow Langmuir Probe (SLP), (b) the 2-Dimensional Single Sided Langmuir Probe (2DSSLP) and (c) the Five tip tRIPLE probe (FRIPLE).

The most comprehensive 2D studies of plasma structures in TORPEX were undertaken with the HEXagonal Turbulence Imaging Probe (HEXTIP). Commissioned in 2005, HEXTIP was a single, fixed array of 86 cylindrical LPs covering most of the poloidal cross-section with a grid-constant of 3.5 cm [122]. Twelve subgroups of probes can either be used independently either in V_f, I_{sat} or swept mode. The probe signals are filtered and amplified by respectively suitable circuitry and digitized likewise at a sampling frequency of 250 kHz. In 2015, we

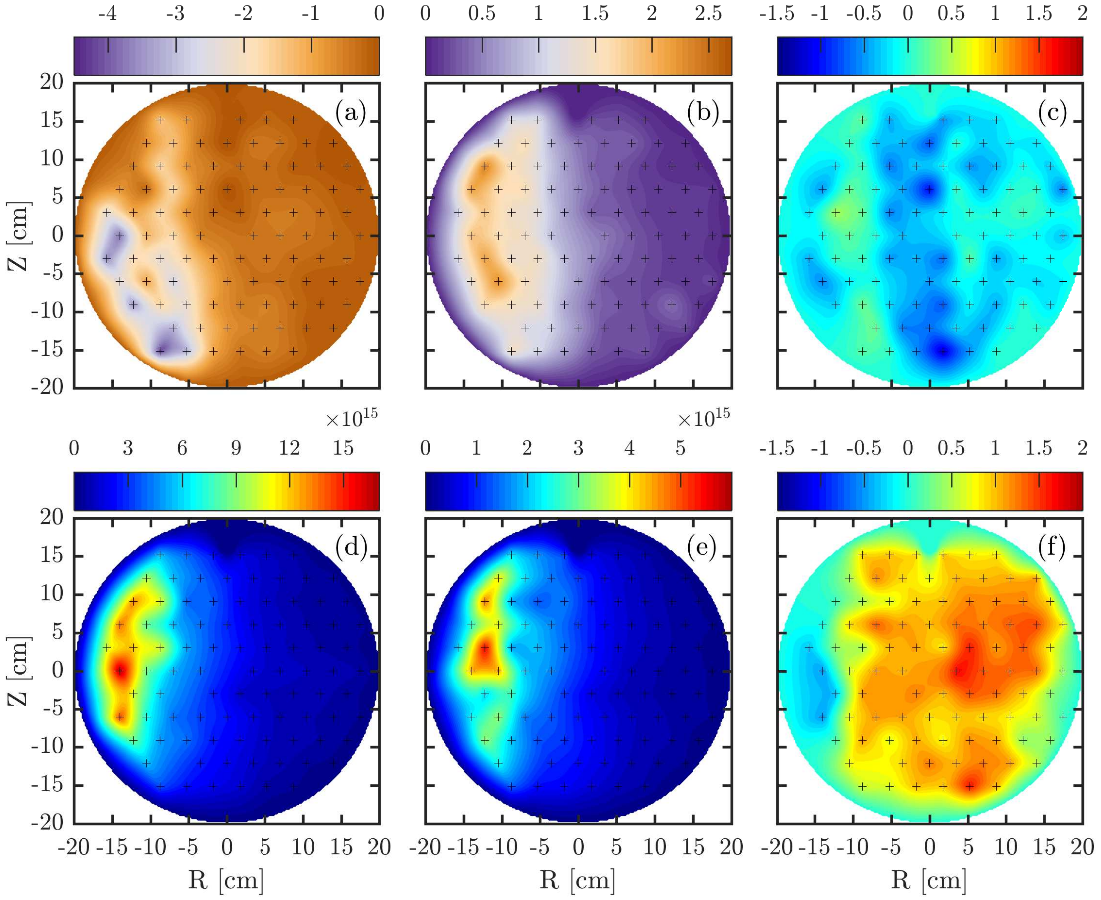

Figure 2.4 – Profiles interpolated from the basic statistics of time-series measurements of V_f on HEXTIP-1 (a-c) and plasma density (from I_{sat}) on HEXTIP-2 (d-f). Crosses indicate the positions of active probe tips. The time-average (mean) is shown in (a,d) and the standard deviation in (b,e), both in units of V and m^{-3} respectively. Note the localization of the strongest fluctuations in the mode region near $R \approx -12$ cm in (e). The transition to the blob-region is identified by their intermittent density peaks leading to positive skewness in (f), beginning near $R \approx -10$ cm. However, both detached blob- and elongated mode-structures can be present intermittently, with blobs gradually dominating towards the centre and HFS (see Fig. 2.5).

commissioned the Upgraded version of the diagnostic, HEXTIP-U, as detailed in Ref. [149]. It consists now of two poloidal LP arrays, HEXTIP-1 and HEXTIP-2 (see Fig. 2.1), at opposite toroidal locations with 95 probes each. The probes near the centre and the LFS are mounted on a pair of movable arms to facilitate operation with the internal toroidal conductor. This two-fold set-up has allowed direct and time-resolved 3D measurements regarding the field-alignment of all structures within the plasma [149]. Many blobs appear to remain in fact connected to the mode along one portion of the field-line, while they already appear detached on another. In keeping with the above definitions, we will therefore prefer the more general term ‘plasma structures’ when describing different effects on the propagation of fast ions.

Furthermore, we can now acquire time-resolved measurements of V_f and I_{sat} over the full poloidal cross-section simultaneously, by dedicating one HEXTIP array to each (see profiles in Figs. 2.1).

To approximate plasma density values from the I_{sat} data using Eq. 2.2, we assume $T_e \approx 5\,\mathrm{eV}$ from swept measurements in the mode region, and $A_{eff} = 13\,\mathrm{mm}^2$ near a bias of $V \approx -40\,\mathrm{V}$. Profiles interpolated from the mean of the resulting density and V_f time-series in the SMT are shown in Fig. 2.4(a,d) respectively and are in good agreement with scans from swept probes. The profiles of their standard deviations in (b,e) indicate the location of the interchange mode on the HFS, while the intermittent character of blob propagation in the centre and LFS is commonly quantified by the positive skewness of the density time-series as in (c) [126, 150, 151]. The skewness is defined as the 3rd standardized central moment of the time-series [152] and will be given detailed treatment in the context of fast ion transport in Ch. 3. Note the differences to Fig. 2.5 and Fig. 2.9, showing instantaneous ‘snapshots’ of the plasma density and floating potential for comparison. To further assess the statistical average behaviour of plasma structures, the technique of Conditional Sampling (CS, see Sec. 3.3) has long been known through investigations e.g. in unmagnetized, beam-generated ion acoustic turbulence [153, 154], as well as studies of coherent structures in toroidal magnetized plasmas [155, 156]. Therefore, it has since also been utilized on TORPEX across many different plasma scenarios [133, 131, 147]. Both of these methods are therefore also adapted to analyze the propagation of fast ions within these turbulent plasmas (see Ch. 3, Ref. [107]). A wide range of other techniques was also applied to study the statistical properties of different plasma structures, ranging from simple correlation studies over Fourier methods to 2D gradient analysis and structure tracking [126, 121, 129]. However, they are not as pertinent to what follows.

To finally characterize the local evolution of T_e, time-resolved measurements can be taken with a triple Langmuir probe. The Five tip tRIPLE probe (FRIPLE) is the most advanced such probe in TORPEX and can also provide direct measurements of the plasma potential and vertical electric field across the 1.6 cm covered by its tips [157]. Therefore it has been used to study the validity of the ‘isothermal assumption’, whereby T_e of plasma structures is on average approximated by a known constant. Already conditionally sampled sweeps with SLP in hydrogen showed $T_e \approx 2.4 \pm 0.3\,\mathrm{eV}$ across typical blobs [133, 147]. This indicates a possible systematic over-estimate of density measurements with HEXTIP of up to ≈ 30% for similar structures on the HFS. Averages based on time-resolved measurements with FRIPLE generally confirmed the results of swept LPs but found significant T_e fluctuations in the mode region. However, these appear to only introduce an error of $< 15\,\%$ in instantaneous density estimates here, and averages are well recovered. However, they can be more significant for the estimate of the sheath potential drop and V_p here [157]. While this still plays a role in the blob-dominated region, the fluctuations in the directly measured floating and plasma potential appear much more similar here and radial particle flux measurements are dominated by fluctuations in V_f [157]. Moreover, the deduction of E×B-flow patterns based on V_f-profiles had already been demonstrated as a feasible approximation during blob-propagation studies [129]. While their

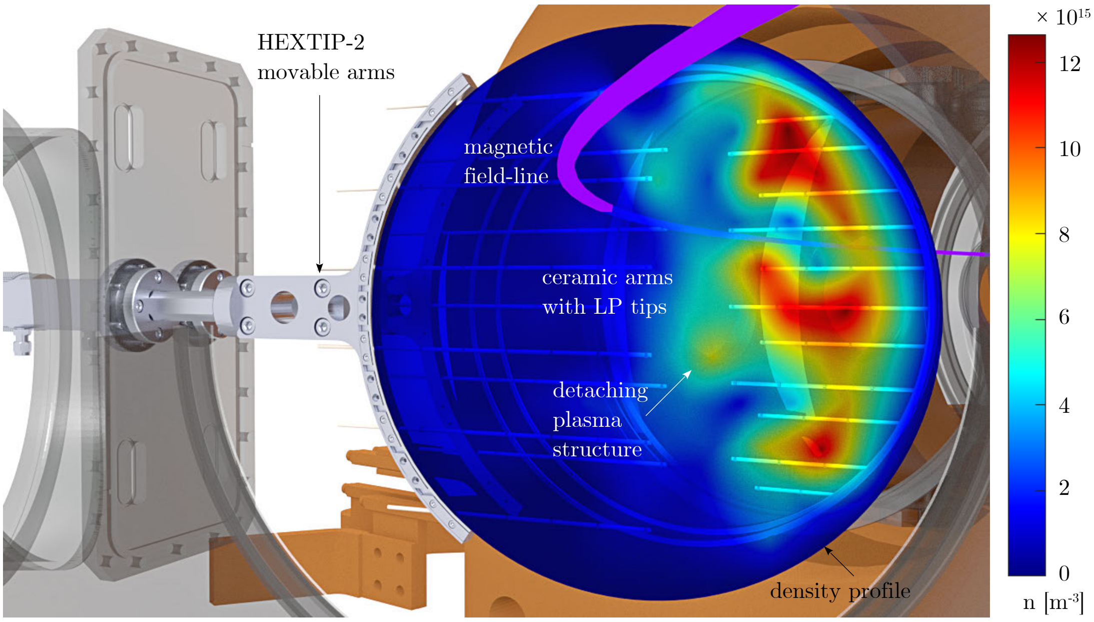

Figure 2.5 – Instantaneous plasma density profile ('snapshot'), interpolated from one set of I_{sat} measurements on HEXTIP-2, as digitized every 4 μs. Note the mode structures connected to the plasma source region on the HFS, and one slowly detaching blob-like structure. Probes on the LFS ceramic arms can be radially displaced by up to 7 cm from outside the vessel.

accuracy can thus be expected to deteriorate towards the mode region and the HFS, we will estimate turbulent electric fields based on the gradients of V_f-measurements in upcoming chapters. Fast ions mostly remain in the centre of the cross-section, so that this method is in particular applied when analyzing their cross-field motion.

2.3 Other plasma diagnostics

A number of other diagnostics have been employed on TORPEX to complement LPs and pursue further investigations outside the frame work of this thesis. For instance, a Photron Ultima APX-RS fast framing camera can be used in conjunction with a Hamamatsu C10880-03 image intensifier unit to observe visible light emissions at acquisition frequencies of up to 100 kHz. A detailed description of early studies until 2008 can be found in Ref. [158]. This set-up can capture mid- to high-resolution images, depending on the chosen acquisition rate, while representing a fully non-perturbative method of measurement. Although observations tangential to the toroidal direction successfully imaged blob-like plasma structures in a wide field of view, their statistical properties do not directly correspond to LP observations, as the recorded light emissivities are intrinsically line-integrated measurements. For observations at an angle perpendicular to the toroidal direction (along Z), the field of view was restricted to part of the mode-region of the plasma. However, the PDF of the amplitudes of emissivity fluctuations and their power spectral density were in strong overall agreement with the corresponding statistics of plasma density fluctuations simultaneously recorded on HEXTIP. To address the line-integration problem in the tangential view, a tomographic inversion technique was employed and allowed a spatial resolution of 2 cm in the poloidal plane [159]. Both, the time-averaged plasma emissivity profiles and the location, extent and frequency of the interchange mode agreed well with electrostatic measurements. Further analysis using Conditional Sampling and Fourier-techniques corroborated these observations, as well as the expected presence of small-scale structures beyond the resolution of HEXTIP [159, 99].

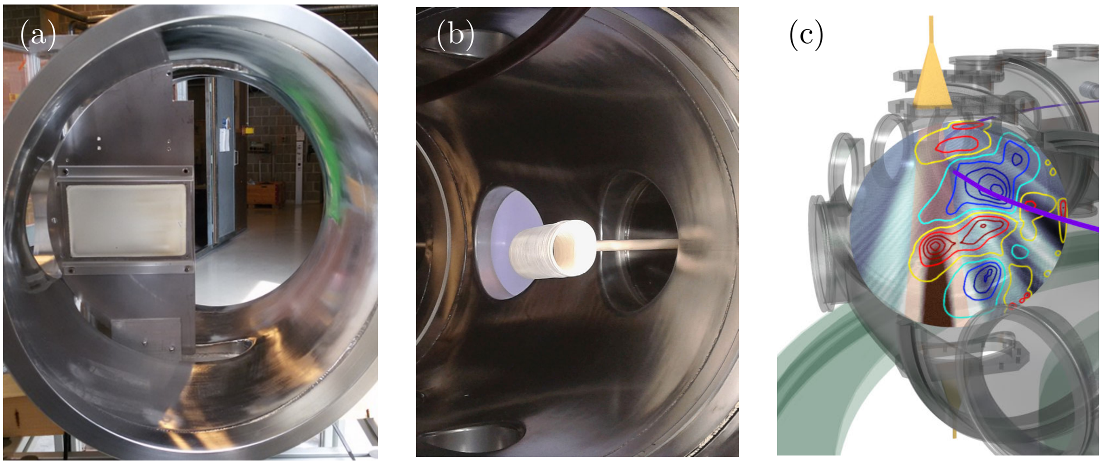

Figure 2.6 – (a) Cathodoluminescent screen installed on a limiter inside a TORPEX sector. (b) Solenoid for locally enhancing the axial magnetic field towards EC-resonance to produce seeded blobs. (c) Rendering of a TORPEX sector with horn antennas for the injection and detection of mm-range microwaves. The profile shows conditionally sampled contours for positive (red) and negative (blue) density fluctuations based on I_{sat} measurements on HEXTIP, and the corresponding simulated microwave intensity on a gray-scale. Note the shadows behind density peaks and adjacent high intensity due to wave scattering.

Since 2017, we have explored an alternative method to specifically study smaller scales in a single poloidal plane through the installation of a cathodoluminescent ZnO-Zn screen onto a limiter. With optical filters for most of the direct emissions from the plasma, the fast camera recorded mm-resolution traces of plasma density fluctuations exciting a range of ~ 500 nm-wavelength emissions from the screen. Preliminary studies were performed on SMT hydrogen plasmas as well as on argon plasma blobs seeded with an in-vessel coil (Fig. 2.6(a,b), [160]). They reveal the presence of decaying plasma structures down to millimeter scales. Their trajectory-averaged speed and size seem to mostly follow expectations from previously established scaling-laws. Further studies will focus on the fragmentation process of the seeded blobs and the identification of secondary instabilities.

From 2014 to 2017, the fundamental mechanisms of microwave-scattering by plasma structures has been investigated on TORPEX [123], in the frame of a Eurofusion Enabling Research project ‘Physics of radiofrequency wave scattering by turbulent structures’. Microwaves are injected at 29.7 GHz by a horn antenna through an elongated top-side flange, and detected by another identical antenna through the opposite bottom flange. To reduce the ubiquitous presence of ambient microwave noise from the magnetron, a custom insulated microwave detection circuit was implemented [161]. It was demonstrated that plasma structures scatter the injected microwaves in a clear pattern that is consistent with the change in plasma frequency and refractive index induced by their density fluctuations. Full-wave simulations in COMSOL were devised from first principles and show excellent agreement with measurements. This holds especially when they were applied to plasma density profiles, that are obtained by averaging over many detected instances of each particular type of plasma structure (CS plasma profiles, see Fig. 2.1, background). For the details of these highly fruitful investigations and their successful continuation on TCV [162], we refer to the thesis of Oulfa Chellaï [163].

2.4 Fast ion experimental set-up

The fundamental interactions of suprathermal ions with plasma turbulence have been investigated on TORPEX since 2006 [102]. The key parameters of the current experimental set-up in the SMT geometry are summarized in table 2.2. We firstly introduce its different principal components in the following, as similarly described in previous works [164, 136], before presenting new additions to the equipment.

2.4.1 Fast ion injection

With plasma temperatures of typically less than 5 eV, suprathermal ions can be injected via thermionic emission from an $^6\mathrm{Li}^+$ ion source [99], with the full source assembly illustrated in Fig. 2.7(a). Thermionic emission requires a source temperature of over 1000 °C, which is achieved by driving 2.2 A of current through a heating filament within the source. At 9-9.5 V, this results in $P_{heat} \approx 24\,\mathrm{W}$ of heating power [136]. When heating a source for the first time, this power needs to be built up slowly by augmenting the voltage by 0.5 V every 20-30 minutes to allow an appropriate time for the source to de-gas in the vacuum. The source is mounted within a two-grid assembly of molybdenum and tungsten, chosen to withstand the immediate temperatures around the source. The source itself is positively biased, as well as its surrounding molybdenum casing, while a negative bias is applied to the first, ‘internal’ grid in front of the source. A full illustration of the biasing schemes of the ion source as well as the detector is given in Fig. 2.8. The perpendicular electric fields resulting from the total voltage drop between source and grid serve to extract the fast ions and accelerate them into a beam-like current. The second, ‘external’ grid is grounded to shield the internal parts of the assembly from the plasma. Therefore, ions decelerate in this region and the fast ion injection energy E is effectively set by the source bias alone. Furthermore, the external grid is used to measure part of the injected current, to provide a base-line for the expected fast ion current densities during measurements (see below). With a computed grid opacity of $\approx$ 25%, the current on the external grid represents at most one third of the actually injected current in

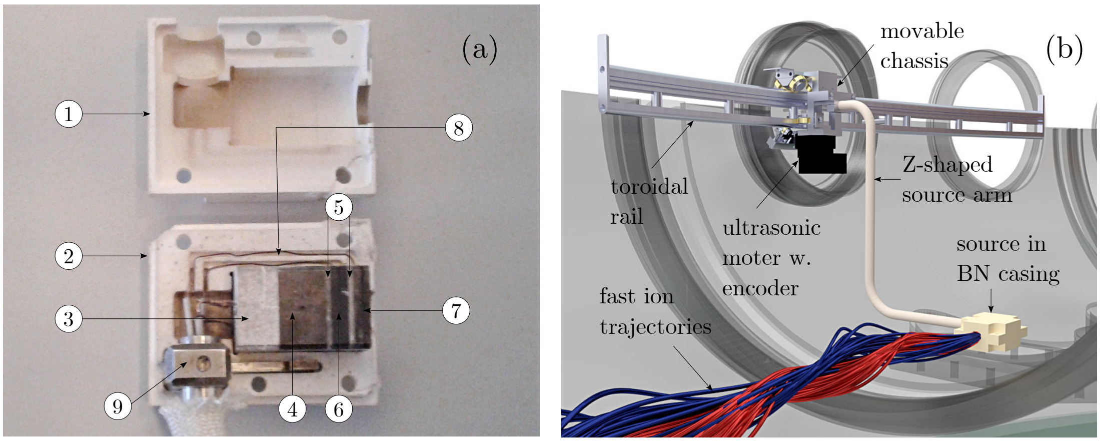
(a)
①
②
③
④
⑤
⑥
⑦
⑧
⑨
(b)
movable chassis
toroidal rail
Z-shaped source arm
ultrasonic moter w. encoder
source in BN casing
fast ion trajectories

Figure 2.7 – (a) Photo of the ion source grid assembly and its casing. The numbered parts are: (1) Casing top (Boron Nitride), (2) Casing base (BN), (3) Source mount (BN) with heating wires clamped to the source, (4) Biased source housing (Mo), (5) Grid spacers (BN), (6) Internal grid (W) clamped in holder (Mo), (7) External grid with holder, (8) Canals with grid wiring, (9) Fixture for source arm, setting the injection angle θ. (b) Labeled rendering of the ion source movable system. Fast ion trajectories from simulations (see Ch. 4) are illustrated again in red and blue for 30 eV and 70 eV ions respectively. The wiring is shown separately in Fig. 2.10.

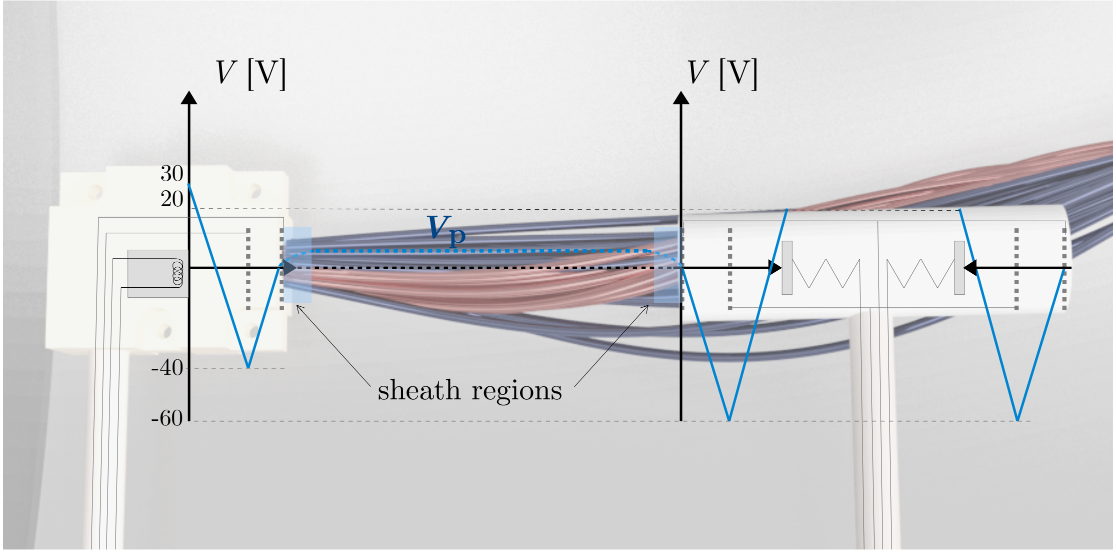
V [V]
V [V]
30
20
-40
-60
V_p
sheath regions

Figure 2.8 – Schematic illustration of the voltages and biases the fast ions experience from their thermionic emission from the Li^6-doped source, up until they reach the collector electrode inside the front-side Gridded Energy Analyzer (see below). A second back-side detector features the same biasing to produce a reference signal of pure noise from the plasma. Note that a sheath potential drop of a few volts is experienced by the fast ions both when exiting as well as entering the external grids of the source assembly and detector respectively.

the absence of a plasma. During the incremental heating, this current is acquired with a multi-meter to verify the quality of each source. The same method was still used to monitor source quality between different TORPEX discharges for much of the presented data. However, residual current fluctuations during certain discharges became quite apparent when an ion source began to be ‘depleted’, i.e. when its current response to a given bias weakens due to use. Hence, a separate circuit was designed to directly acquire the external grid current in each shot during phases without plasma (see Sec. 2.4.3). The source and grid assembly is encased in boron-nitride (BN). This material is both vacuum-compatible and heat-resistant while it insulates most conducting parts of the assembly from the plasma. The two-component casing is held together by 4 ceramic screws, which are additionally secured with liquid ceramics. As shown in Fig. 2.7(b), the casing is mounted on a Z-shaped arm, insulated with fiber glass mesh, that fixes the source position in the poloidal plane at $[R = -1\,\text{cm},\ Z = -14.5\,\text{cm}]$. There, the source is fixed such that the fast ion beam is injected at an angle of $6.5 \pm 1.5°$ with respect to the horizontal direction. While the injection energy largely determines the fast ion velocity parallel to the magnetic field $v_{||}$, this angle sets their perpendicular velocity $v_{\perp}$ and therefore their Larmor radii ρ_L. The source arm is mounted in turn on a movable chassis, that can be advanced along a toroidal rail with an ultrasonic motor over a distance of 48 cm. At both ends of the rail, two breaker switches engage on the chassis, preventing the motor from advancing any further. From the chassis, the various cable contacts for the motor, its encoder, the end-of-rail sensors and the source itself are guided through a custom flange connector to the outside of the vessel and their respective power-supplies. Recent improvements to the wiring and hardware inside the vessel are detailed in Sec. 2.4.3.

2.4.2 Fast ion detection

Once the fast ions have propagated through the plasma over the chosen toroidal distance D, we employ two back-to-back Gridded Energy Analyzers (GEAs) to detect them [102]. Also referred to as retarding field analyzers, these detectors consist of a series of two tungsten grids and a copper collector, that follow a similar biasing scheme to the fast ion source assembly. The first, external grid is grounded to shield most of the bulk plasma. Since the density of the injected fast ion current is less than 0.001% that of the bulk plasma, additional filtering is necessary. The second, internal grid is biased to $V_{int} = -60\,\text{V}$ to specifically reject even the high-energy tail of plasma electrons. The collector is biased to $V_{col} \geq +15\,V$ to repel any residual high-energy bulk ions. Nonetheless, significant noise remains in the fast ion signal. For instance, secondary electrons that are emitted through collisions onto the internal grid can cause significant stray signals. Moreover, the intricate wiring, filter and amplification circuitry is bound to pick up a minimum of electrical noise (see Sec. 2.4.3). Therefore a second GEA is mounted on the back-side of the first. Since its signal should consist of the same noise from the plasma, pick-up and cross-talk, the backside-signal is subtracted the front-side signal during the last stage of the signal amplification. While this is found to result in a significant noise reduction on average, some residual noise remains in the final GEA signal, which is digitized at a frequency of 250 kHz. In order to establish statistical differences between the fast ion signal and the residual noise, the fast ion source is modulated into alternating ‘on-phases’ and ‘off-phases’ at a frequency of 23 Hz, which become apparent on the source current signal

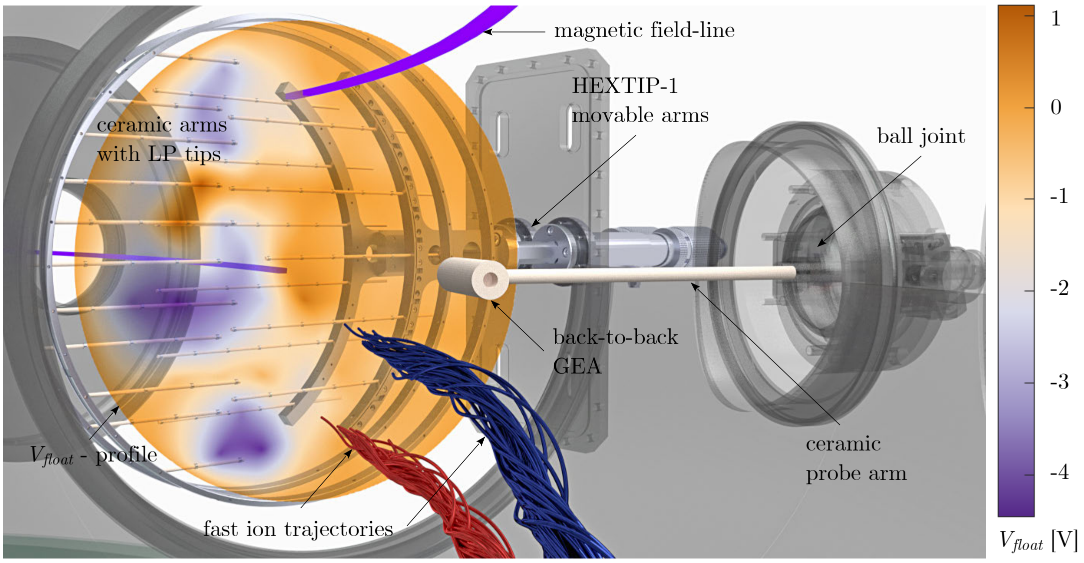

Figure 2.9 – Rendering of the back-to-back Gridded Energy Analyzer, mounted on a retractable ceramic arm through a flange with a ball joint. This allows the detection of fast ions across most of the poloidal cross section. An instantaneous floating potential profile, interpolated from one set of V_f measurements on HEXTIP-1, is shown in the background. The trajectories of the 30 eV (red) and 70 ev (blue) fast ions were integrated using the tracing method in Ch. 4 based on V_f data from the same shot and time-period as the profile shown.

(see Fig. 2.12(b)) and the GEA signal (see Ch. 3). All measurements of the GEA are presented as current densities, as the calibrated measured current is divided by the detector aperture.

2.4.3 Recent additions

In the following, we turn towards improvements and additions that were made to the fast ion experimental equipment in the course of the presented thesis work. Their development was chiefly motivated by the challenges and questions raised when acquiring the results presented in Ch. 3. Since the systems described in the later subsections have thus only become available more recently, they are to firstly contribute to the ongoing investigations outlined in Ch. 8.

Improved ion source equipment

From the very beginning of our experimental campaign, one of the main challenges was the installation of the fast ion source and its arm, without the ability to remove the corresponding sector from TORPEX. With the internal toroidal conductor, removing the adjacent movable sector is now also substantially more demanding as the conductor needs to be lowered to the centre of the vessel beforehand, and even then the sector can only be displaced by less than 17 cm radially. Furthermore, the choice of sector was limited through the installation of the

Table 2.2 – Parameters of the fast ion injection and detection system, as well as their trajectories. Vertical drifts are comprised of pitch-angle, curvature and a negligible gradient component (see [136]). The average Larmor radii and speeds for ions on 'realistic trajectories' account for the given (Gaussian) uncertainties in the injection angle and energy. Their values are thus drawn from particle distributions from the Monte-Carlo simulations in Ch. 4.

Injection			
Injection energy	$E = 30 - 70 \pm 2\,\mathrm{eV}$		
Injection angle	$\theta = +6.5 \pm 1.5°$ (w.r.t. horizontal)		
Injection position (poloidal)	$R = -0.5\,\mathrm{cm}$, $Z = -14.5\,\mathrm{cm}$		
Filament heating power	$P_{heat} \lesssim 25\,\mathrm{W}$		
Total filament bias	$70 - 140\,\mathrm{V}$		
Total injected current	$I_{in} \approx 10 - 15\,\mu\mathrm{A}$		
Source life-time under bias	$5 - 12\,\mathrm{h}$		
Measurement			
Source-detector distance	$D = 126 - 171\,\mathrm{cm}$ (toroidal)		
Detector aperture	$A = \frac{\pi}{4} \times (8\,\mathrm{mm})^2 = 50\,\mathrm{mm}^2$		
Internal grid bias	$V_{int} = -60\,\mathrm{V}$		
Collector bias	$V_{col} = +15 - 20\,\mathrm{V}$		
Peak and total measured current	$I_p \approx 1.5\,\mu\mathrm{A} \lesssim I = 2.2 - 5.0\,\mu\mathrm{A}$		
Total amplifier gain	$56 \times 10^3 \times [20 - 200]$		
Ideal trajectories		**30 eV**	**70 eV**
Larmor frequency	$\Omega_f =$	1.2 MHz	
Velocity parallel to B	$v_{\parallel} =$	$38\,\mathrm{km\,s^{-1}}$	$58\,\mathrm{km\,s^{-1}}$
Velocity perpendicular to B	$v_{\perp} =$	$3.3\,\mathrm{km\,s^{-1}}$	$5\,\mathrm{km\,s^{-1}}$
Larmor radius	$\rho_f =$	2.8 mm	4.2 mm
Propagation time over $D = 171\,\mathrm{cm}$	$\tau_{tof} \approx$	$55\,\mu\mathrm{s}$	$36\,\mu\mathrm{s}$
Vertical drift speed	$v_z \approx$	$0.8\,\mathrm{km\,s^{-1}}$	$1.8\,\mathrm{km\,s^{-1}}$
Vertical displacement ($D = 171\,\mathrm{cm}$)	$\Delta_f \approx$	4.5 cm	6.8 cm
ion collision frequency [22, 26]	$\nu_{fi} \lesssim$	42 Hz	20 Hz
ion mean free path	$\lambda_{fi}^{mfp} \gtrsim$	0.9 km	3.1 km
neutral collision frequency	$\nu_{fn} \sim$	23 kHz	35 kHz
neutral mean free path	$\lambda_{fn}^{mfp} \sim$	1.7 m	
Realistic trajectories		**30 eV**	**70 eV**
Av. velocity parallel to B	$v_{\parallel} \approx$	$30\,\mathrm{km\,s^{-1}}$	$46\,\mathrm{km\,s^{-1}}$
Av. velocity perpendicular to B	$v_{\perp} \approx$	$6\,\mathrm{km\,s^{-1}}$	$9\,\mathrm{km\,s^{-1}}$
Av. Larmor radius	$\rho_L \approx$	4.9 mm	7.5 mm
Av. vertical drift speed	$v_z \approx$	$0.8\,\mathrm{km\,s^{-1}}$	$1.8\,\mathrm{km\,s^{-1}}$
Av. vertical displacement ($D = 171\,\mathrm{cm}$)	$\Delta_f \approx$	4.5 cm	6.8 cm

second HEXTIP array, and ultimately determined by the maximum achievable source-detector distance without having the fast ion beam cross this probe array. While the mechanical installation and alignment of the source arm became simply more challenging, the delicate individual electric connections from the source arm to the chassis proved too fragile to handle.

Two copper wires with a diameter of ≈ 0.25 mm apply the bias for the internal and external source grids, while wires with a diameter of ≈ 0.6 mm carry the heating current and bias of the fast ion source. The latter ones would intermittently loose contact during the heating procedure, which would often result in uncontrollable, perpetually oscillating heating currents. Furthermore, the given number of individual exposed connectors posed a risk for mechanical faults (see Fig. 2.10(a)).

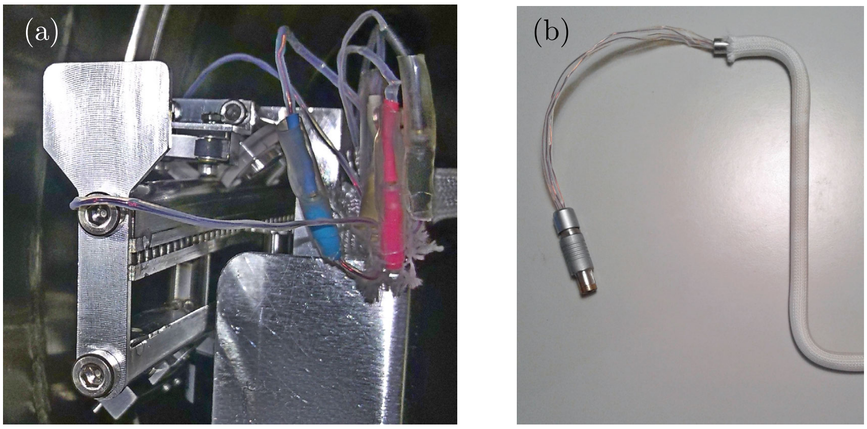

Figure 2.10 – (a) Photo of the old individual connections between the source arm and the chassis. One cable wrapped itself around the end of the rail, immobilizing the chassis. (b) Photo of the improved wiring with 4-pin Fischer connector.

Therefore, the electrical wiring of the source arm was entirely replaced. All four contacts to the source assembly remained copper wiring, insulated by heat-shrink made of teflon (PTFE, PolyTetraFluoroEthylene). Close to the source, the teflon transitions as before to ceramic tubing to withstand the source temperatures during operation. The individual electrical contacts from the source arm to the chassis were however replaced by one single 4-pin Fischer connector (see Fig. 2.10(b)). The current oscillations during the source heating were significantly reduced, along with the risk of cables wrapping around the ends of the rail. Additionally, the exposed copper wiring near the source grids was bent into a slightly wave-like form. When one of the grids would snap from its wire due to wear over time, the remaining contact can now be straightened and reconnected to the grid, instead of requiring a full replacement.

Additional source arms

The detailed investigation of time-resolved fast ion measurements during the early ballistic transport phase has become another research interest on TORPEX. The onset of measurable correlations with HEXTIP data or entropy transfer to the fast ions could be used to quantify the transition into the interaction phase more precisely. Such measurements require the ion source to be positioned only centimetres away from the GEA. Given the minimum distance between the corresponding flanges on TORPEX, and the fixed length of the toroidal rail of the fast ion chassis, this positioning required the development of a new, extended source arm as shown in Fig. 2.11(a).

This extended source arm advances the position of the fast ion source by 25 cm in the toroidal direction and fixes it at [$R = -1$ cm, $Z = -3.5$ cm] in the poloidal plane. These coordinates can easily be reached by the movable system of the GEA, whose radial motor is not powerful enough to operate reliably were the GEA to be inclined by more than $-17°$ w.r.t. the horizontal. At the same time, the source arm accounts for the significant curvature of the toroidal coordinate over this length, so that the injection angle of the fast ions remains purely vertical. Another attachment was added onto the opposite end of the source arm, so that its orientation w.r.t. the chassis is fixed even under the weight of the arm and source. Since the toroidal torque of this assembly is also significant, and the movable chassis is not designed to cope with it, a precise counter-weight was added along the negative toroidal direction. The only remaining inevitable torque on the chassis is thus counter-clockwise around the rail, due to the combined weight of all these components. While the motor of the chassis should in principle be largely unaffected by this change, the chassis itself was not designed robustly enough to maintain the required precision in its alignment with the rail. After extensive testing and a full replacement of all movable parts including the motor, it has become clear that certain elements of the chassis structure and the rail itself will need to be adapted to allow a reliable operation without risk to the delicate piezo-electric elements of the ultrasonic motor. While the principal design changes have been agreed upon, such as a more symmetric distribution of the alignment springs, the implementation and testing of the new chassis will be beyond the time frame of this thesis.

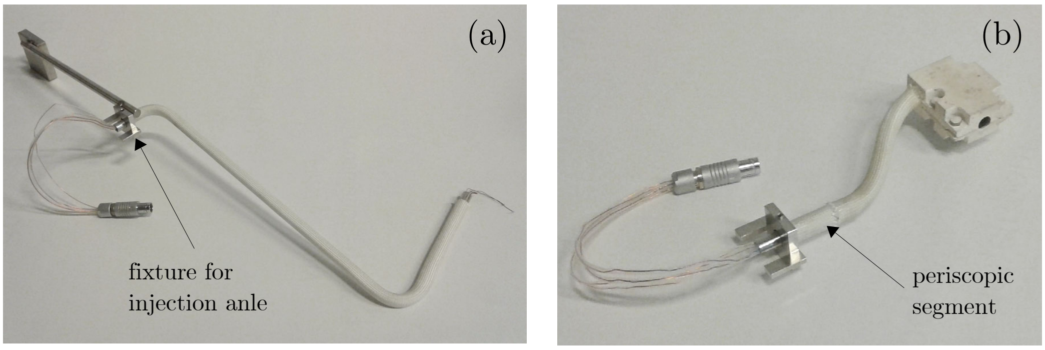

Figure 2.11 – (a) Photo of the extended source arm for investigations of the ballistic transport phase. Note its curvature in the toroidal direction and the counter-weight at the back. (b) Photo of the source arm for flexible injection positions around $R = Z = 0$, including a periscopic segment. Both arms are equipped with a custom fixture to place and install them more consistently and securely on the chassis.

A third source arm shown in Fig. 2.11(b) was commissioned for the investigation of fast ion propagation in a magnetic geometry featuring an X-point. Due to the interplay of the vertical magnetic and electrostatic drifts, the number of fast ions crossing the X-point is expected to change significantly depending on their injection position in its vicinity (see Sec. 8.1.3).

Therefore, the source arm for this investigation allows for a flexible injection position near the centre of the poloidal cross-section. The vertical source position can be set over the interval of $Z = [-2, 6]$ cm by rotating the arm, while the simultaneous change in the toroidal location of the source should only affect the injection angle of the fast ions negligibly. By adjusting the periscopic segment close to the chassis, the horizontal source position can be set between $R = [-1, 1]$ cm. This degree of flexibility allows to compensate offsets in the measured position of the X-point and conduct comparative studies for injection positions above and below this location.

Injection current acquisition

Many of the statistics from time-resolved fast ion measurements in the following chapters will be shown to depend on the total fast ion current. The total detectable current is found by integrating the fast ion mean profiles, and appears a useful proxy in most scenarios. However, the actually injected current can vary and fluctuate between different discharges and measurement positions, especially as the ion source begins to be depleted. While these changes were formerly tracked on a multi-meter connected between the external grid and the ground, this practice appeared insufficient to account for injection current fluctuations during a given discharge (see Ch. 3). Therefore a dedicated circuit has been implemented (see Fig. 2.12), so that a time-resolved current signal from the external grid of the source assembly can be acquired during each such ‘shot’. These currents of 10s of μA are converted into a voltage signal by a trans-impedance amplifier, which is then filtered and further amplified in a second stage. Due to the highly sensitive nature of the measurement, both are equipped with decoupling capacitors. The gain of the first amplifier is fixed at $\times 10^3$, while the second can be chosen as $\times 10^3$ or $\times 10^4$. The 1st order low-pass filter can thus be set to a cut-off frequency of between 1.67 Hz, and 167 Hz. However, since we usually employ the 23 Hz source modulation, the latter cut-off is set, as well as a total gain of $\times 10^6$, by using the 10 nF capacitor and the 100 kΩ resistor. With this gain, we arrive at a sensitivity of 1 V per 1 μA of external grid current. With an opacity of $\approx 25\%$, the fast ion current actually injected into the plasma should be $\approx 3\times$ larger. When a plasma is present, the electron current drawn on the external grid is approximately 3 orders of magnitude larger, so that the circuit quickly saturates and becomes unstable. Therefore, a brief acquisition period without plasma is added at the end the discharge, and allows for the acquisition of a clear fast ion current signal, as illustrated in Fig. 2.12(b). Although the chosen cut-off frequency is significantly above the source modulation, a residual capacitive effect is apparent before the acquired current reaches a stable value in each on-phase.

It should be noted that there remains a factor of $\approx 3-4$ disagreement between the corresponding injected currents and the integrated current of the mean-profiles in the following chapter. A reduction of $\approx 40\,\%$ is certainly due to the $\approx 20-25\%$ opacity of the external and internal grid of the GEA respectively. Furthermore, some current is likely lost directly at injection as the source casing aperture is slightly smaller than the source grids. Further losses can be caused by irregularities and sheath effects at the plasma interfaces or due to the Larmor motion of

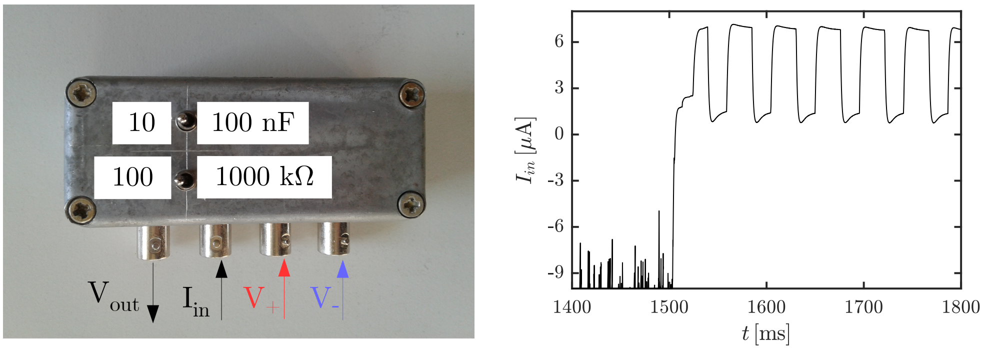

(a) Photo of the circuit box, with labeled connectors and switches to choose resistors and capacitors as outlines in (c).

(b) Acquired time-series $I_{in}(t)$. The plasma production is stopped at 1.5 s, so that the circuit no longer saturates from e^{-} currents.

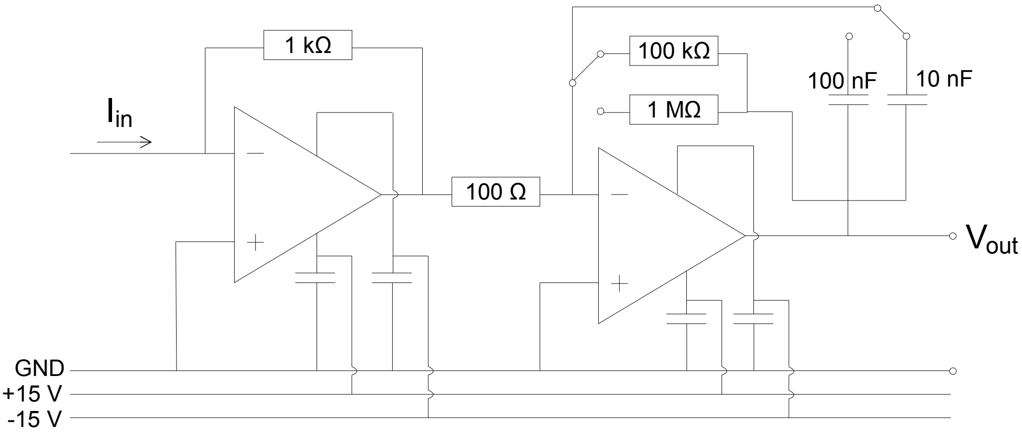

(c) Circuit diagram. The decoupling capacitors are to buffer potential noise from the power supply and have capacitances of 100 nF each. While future iterations could employ a fixed filter on the first amplifier or even 2nd order filtering, the signal can likely still saturate during plasma operation.

Figure 2.12 – Illustrations of the acquisition circuit for the current on the external source grid.

the ions leading to a modified effective detector area. Lastly, some minor attenuation of the beam might be due to neutral collisions, which will be discussed in Sec. 2.5. For $D = 171$ cm, the current estimate results in $\approx 20\%$ losses, while a possible error of 50% in λ_{fn}^{mfp} would yield up to $\approx 60\,\%$ losses. Nonetheless, measurements indicate that both the measured injected and total detected current are approximately proportional to one another. Therefore, either can be used when assessing relative differences in statistics between different fast ion profiles. However, only a consistent measure of the injected current can account for shot-to-shot variations.

Multi-channel fast ion detector

As described above, the back-to-back GEA system is restricted to single point measurements. Many analysis methods, such as Fourier analysis, or correlation studies rely on at least two simultaneous measurements, so that the concept of a multi-channel detection system has long been under discussion at TORPEX. Finally, this concept has taken shape in the form of a 5-fold Gridded Energy Analyzer, short 'multi-GEA' (see Fig. 2.13), that we have designed, implemented and commissioned in the frame of the TP4 internships and 'travail de spécialisation' of the master student Lyes Kadi.

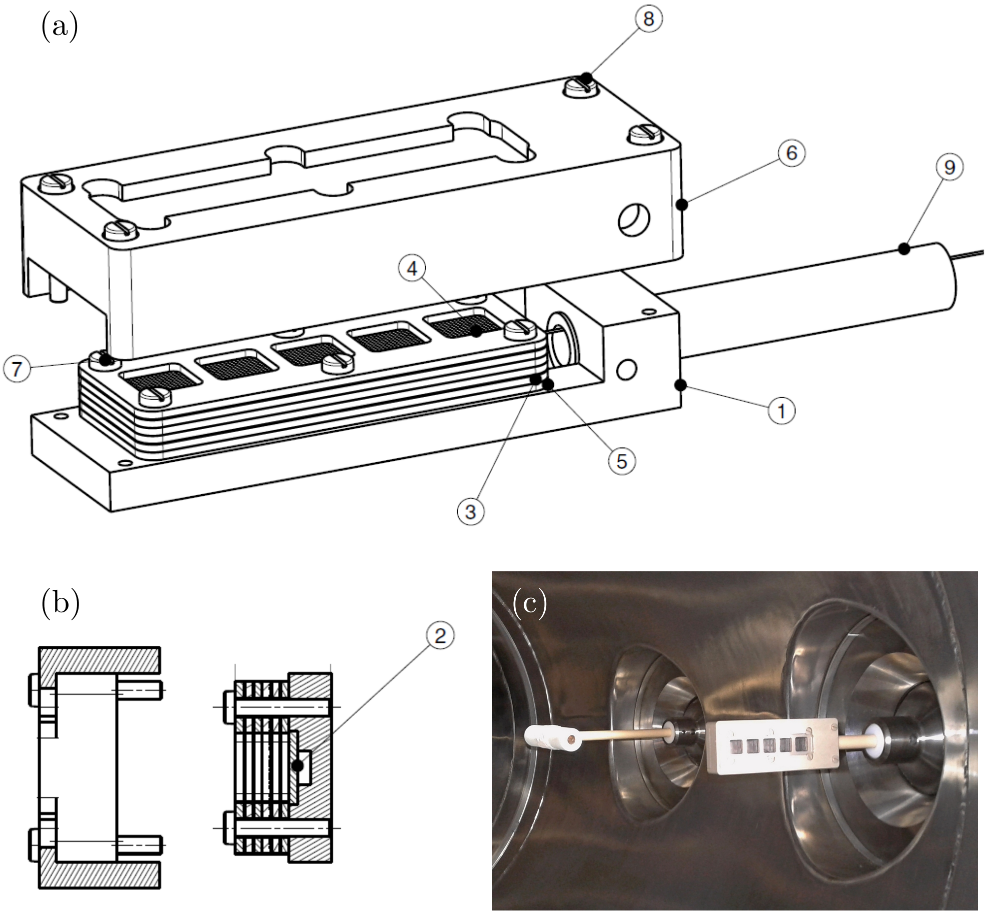

Figure 2.13 – (a) Isometric view and (b) side-view cross-section of the multi-GEA assembly. The numbered parts are: (1) Casing base (PEEK), (2) Collectors (steel) with wiring gap, (3) Grid-holders (steel), (4) Grid (external, tungsten), (5) Grid spacer (PEEK), (6) Casing shell (PEEK), (7) Grid screws (PEEK), (8) Casing screws (steel), (9) Probe arm (ceramic), secured with steel screw. In (c), we show a photo of the installed multi-GEA inside TORPEX, next to the single-point, back-to-back GEA. Both are retracted to the LFS.

Various considerations influenced its design. The horizontal orientation is meant to facilitate two-point studies related to the radial fast ion transport in the SMT to complement most previous and current investigations. Five separate collector were implemented, to simultaneously study correlations at different separations and ensure a certain redundancy should any one detector fail. The size of each collector was chosen as large as the existing GEA, so that the same lower limit on detectable currents should apply. A quadratic shape was preferred however, such as to not waste any space in the detector cross-section. The device size was in turn restricted to not exceed the dimensions of existing diagnostics, that are known to perturb the plasma for a significant portion of the torus behind them. Other dimensions, such as its thickness were set by practical constraints for the available materials and the efforts in mounting the GEA on a ceramic probe arm. The casing and spacer-elements are machined in PEEK (PolyEther Ether Ketone), which is both vacuum-compatible and heat-resistant enough for operation in TORPEX. All collectors share the same tungsten grids, which are secured by stainless steel frames in front of the 5 separate stainless steel collectors. The detector casing as well as the steel-frames are secured with PEEK-screws, so that each grid and collector is fully insulated from one another. All wiring is executed in standard insulated copper, that has proven sufficiently compatible with the TOPEX vacuum in the past. The 1 mm separation between all exposed conducting elements was chosen as similar to the spacings in the ion source. Detailed estimates show that the risk of electrical breakdown within the vacuum-regime of TORPEX is negligible at the given magnitudes of bias voltages of less than 100 V. The first findings from the detector tests and preliminary results from fast ion measurements, as well as the path towards upcoming studies are outlined as an outlook in Sec. 8.1.1.

2.5 Previous fast ion studies

The principal behaviour and non-diffsuive spreading of fast ions in the SMT geometry of TORPEX have been the subject of extensive experimental investigations in the frame of the doctoral theses of G. Plyushchev [164] and A. Bovet [136], as well as the numerical work of K. Gustafson [104]. Here, we aim to recall the most crucial results to give more specific context and motivations for the investigations pursued in the following chapters.

2.5.1 Basic fast ion dynamics

After injection along the toroidal direction, the studied $^6\mathrm{Li}^+$ ions are found to generally drift vertically upwards, as expected from the magnetic pitch angle, curvature and gradient drifts, although the contribution of the latter is almost negligible [104]. Their mean free path for collisions on thermal ions of $\lambda_{fi}^{mfp} > 900\,\mathrm{m}$, indicates fast ion transport in the experiments presented is effectively collision-less, pending collisions with neutral particles. Lacking more precise cross-section data for this specific interaction, a classical hard-sphere estimate yields $\lambda_{fn}^{mfp} \approx 8\,\mathrm{m}$ [136], if one also neglects the contribution of H_2 molecules. Cross-sections of similar non-resonant collisions are available for example for T^+ on H_2 [165]. This result in an estimate of $\sim 6\,\mathrm{m}$, but since $^6\mathrm{Li}^+$ features an occupied s-shell, lower values might be found. Measurements of the fast ion beam without plasma generation do not show significant broadening, indicating that neutral collisions do not strongly affect the spatial distribution of fast ions. Furthermore, due to the lower mass of the neutrals, elastic collisions may only lead to $\lesssim 25\%$ momentum loss for central impacts. The broadening of e.g. their perpendicular velocity distribution, due to variations in injection energy and angle (see Tab. 2.2, 'Realistic trajectories', and Ch. 4), most likely exceeds such collisional effects from the start. Therefore it has been assumed that, on average, the dominant source of broadening of the propagating fast ion beam are the turbulent E×B-drifts due to potential fluctuations associated with the various electrostatic plasma structures [104, 107, 103].

Owing to the field aligned nature of the ideal interchange-driven turbulence with $k_{||} \approx 0$, the strongest electric fields and associated drifts develop in the poloidal plane. The propagation of turbulent structures occurs on similar time-scales as the interchange mode of $f_{int} \approx 10\,\mathrm{kHz}$, so that their local variations are on similar or slower time-scales compared to the fast ion gyro frequency of $\frac{\Omega_f}{2\pi} = 190\,\mathrm{kHz}$. Polarization drifts associated with the local time-variations in the turbulent electric fields are consequently small compared to E×B-dynamics, and only lead to small average increases of the fast ion energy in some cases [104].

2.5.2 Measuring time-average cross-field transport

During the most comprehensive experimental studies [103], the broadening of the injected fast ion beam was investigated by acquiring the time-averaged poloidal profile at various toroidal locations at injection energies of either 30 eV or 70 eV. To improve the signal to noise ratio, lock-in amplification was used with a source modulation frequency of 1073 kHz [166]. The typical acquisition frequencies were reduced to 500 Hz and the shot duration extended to $\lesssim 10\,\mathrm{min}$, during which the movable GEA scanned multiple locations in the poloidal plane. The time average poloidal fast ion profile, 'mean profile' in the following, was interpolated from these measurements. To better quantify the broadening of the mean profile, the horizontal width of the fast ion beam was calculated at each toroidal location through an average of the variances of horizontal slices of the profile, each weighed by the proportion of the total fast ion current it contained [166]. The obtained data is shown by the squares in Fig. 2.14, and compared to numerical results based on GBS fluid-tracer simulations (bands) discussed below. The total detected fast ion current I is defined by numerically integrating the mean profile. The horizontal width was preferred to the vertical, as no magnetic drifts should occur in this direction, so that only the effects of the turbulent electric fields should manifest. While initially subject to Larmor oscillations, the fast ion beam width was observed to increase much more strongly for lower fast ion injection energies [103].

2.5.3 GBS fluid-tracer simulations

To assess the broadening of the fast ion beam in terms of transport, consistent knowledge of the fast ion propagation time is required. While there exists an approximate mapping to the propagation distance, i.e. the source-detector distance D, the small variations in the injection

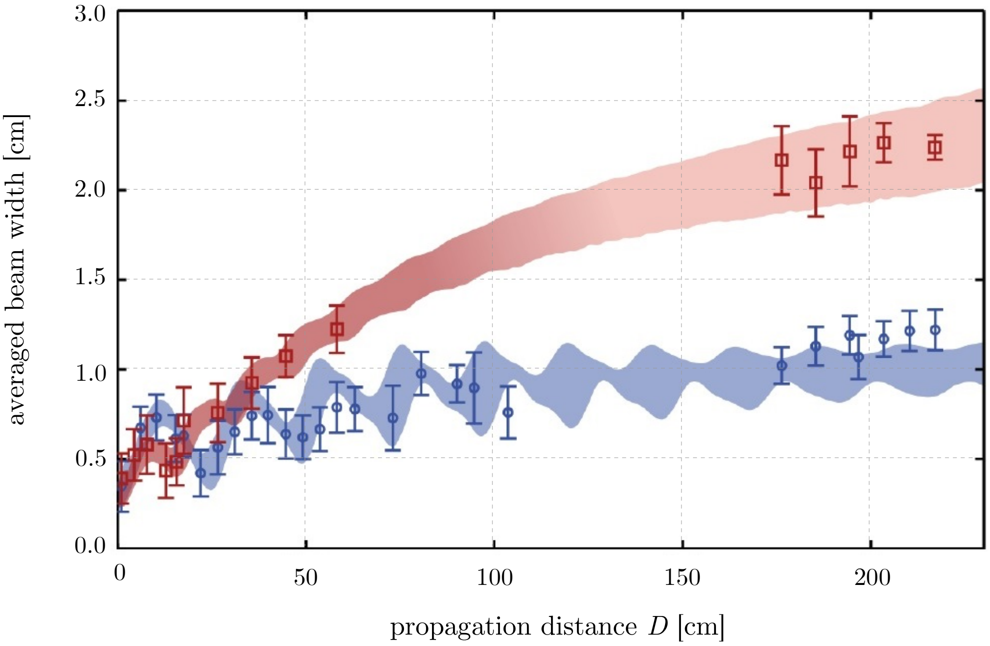

Figure 2.14 – Comparison of the experimental fast ion beam width (squares) with expectations based on GBS simulations (bands) for $E = 30\,\text{eV}$ (red) and $E = 70\,\text{eV}$ (blue). Most experimental data agrees well with GBS simulations (bands, see Fig. 2.15), within expected measurement errors. Reproduced and adapted with permission from [103], see attributions.

energy E and injection angle θ do lead to time-of-flight dispersion especially at larger D [103]. Furthermore, the measured fast ion beam width is bound to reflect uncertainties e.g. in the injected current and GEA position across different measurements in the mean profile.

Basic methodology

Therefore, numerical fast ion simulations [104, 105] were undertaken using the Global Braginskii Solver (GBS) fluid code [167, 128, 106]. The locally more than 100× lower density of the fast ions compared to the bulk density justifies the treatment of fast ions as tracer particles. The employed 2D version of GBS solves the drift-reduced Braginskii equations describing the evolution of the line-integrated plasma potential, density and electron temperature in SMT geometry (including curvature effects) [104, 137], without separating equilibrium and fluctuation scales. In the radial direction R, Dirichlet boundary conditions are used for density, temperature and vorticity [136], while the boundary conditions in the vertical direction are periodic [137]. On an initial background of random noise, constant density and temperature sources are modeled in accordance with the EC and UH resonance layer positions in TORPEX [137]. These build up gradients such that turbulent radial transport develops and grows until the total wall losses balance the sources and a quasi-steady state is reached [137, 104]. Numerically, derivatives w.r.t. time are approximated by an RK-4 scheme, and spatial derivatives by 2nd order central differences [168]. The time-step is normalized [137] to $\frac{R_0}{c_s} \approx 50\,\mu\text{s}$ and spatial coordinates to $\sim \frac{c_s}{\Omega_i} \approx 2.8\,\mathrm{mm}$ in TORPEX SMT plasmas.

Assumptions and feasibility

While the assumptions of $T_i \ll T_e$ and $\beta \ll 1$ are clearly justified here, other conditions for the application of this fluid model required further attention, especially regarding particle collisions (see Tab. 2.1). As the plasma is strongly magnetized, the characteristic scale of steps between collisions perpendicular to the magnetic field is of the order of the Larmor radii, and thus indeed much smaller than the described turbulent structures. However, parallel step-sizes are characterized by the thermal mean free paths, and only ion-ion mean-free-paths are significantly smaller than the field-line connection length. Regarding collision frequencies, electrons collide with each other (or with ions) at a frequency above that of the interchange mode, whereas ion-ion collisions occur merely on the same time-scale. Therefore, thermal equilibration within the turbulent structures, as assumed by a fluid treatment, is not fully obvious to justify. Furthermore, the vast majority of the particles in TORPEX are neutral atoms and molecules, with which both ions and electrons collide much more frequently and well within the scales of the device, possibly contributing to thermal equilibration. Nonetheless, the simulated modes and turbulent features in the 2D and 3D versions of GBS were found in good structural agreement with measurements, e.g. from HEXTIP and FRIPLE, throughout a wide range of validation studies in the quasi-steady regime[137, 128, 138].

Fast ion tracer simulations

Consequently, the described 2D version of GBS was also used in conjunction with fast ion studies, with certain adjustments to the crucial plasma potential fluctuations. For instance, the potential fluctuation level was rescaled by a weighing function, such that their impact on fast ion transport could be investigated more systematically, or to achieve better agreement with measured electric field profiles. For instance, near the fast ion injection position, the fluctuations in the plasma potential measured by FRIPLE appeared on average weaker than those in simulations, so the latter were scaled by ×0.75 during simulations pertaining to the direct comparisons with experimental fast ion profiles [166, 136]. Therein, the trajectories of bunches of 40 such tracer particles were simultaneously integrated over propagation times far in excess of those observed experimentally [103]. To allow a comparison to the experiment, their injection speed, orientation and position were assigned randomly according to Gaussian distributions appropriately representing the ion source [104, 166]. To obtain a statistically meaningful simulation of the time-average fast ion transport, 4000 such bunches were traced at regularly timed intervals. This provides a statistically significant sample of different plasma structures from GBS [136]. The simulated horizontal fast ion beam variance as a function of propagation time $\sigma_R^2(t)$ was found to converge within 0.01% to results using up to 6000 bunches of 100 tracers [136]. To compare the simulations to experimental results, the poloidal profile of the fast ion beam as a function of fast ion propagation distance was extracted using a synthetic diagnostic [166]. The horizontal width of these time-averaged profiles was then calculated as a weighted average of multiple horizontal slices [169, 166]. As shown in Fig. 2.14, excellent agreement with experimental measurements was established [103].

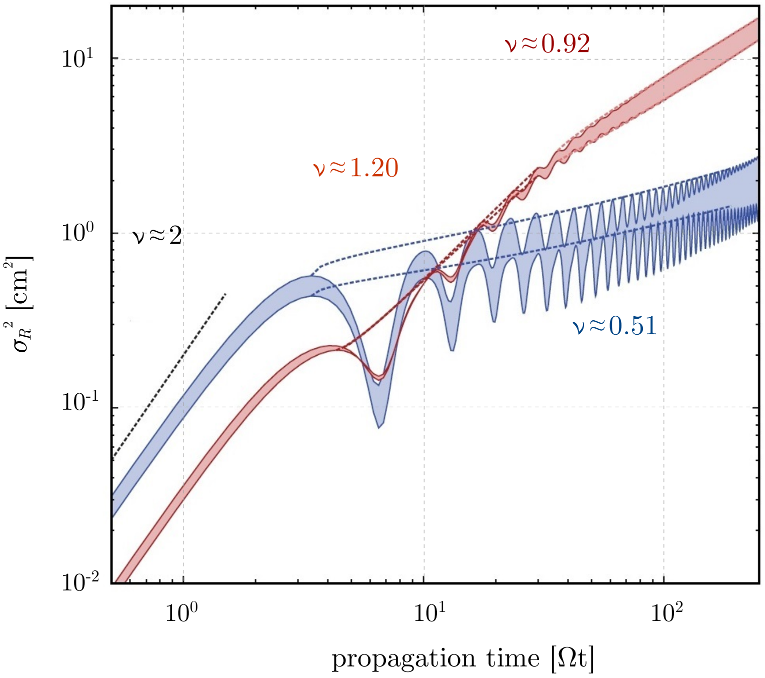

Figure 2.15 – Radial variance of the simulated fast ion trajectories as function of propagation time, for the same settings and energies as in Fig. 2.14. The transport exponents for the different non-diffusive regimes are indicated where they were fitted to the slope. Reproduced and adapted with permission from [103], in attributions.

2.5.4 Non-diffusive transport regimes

Larmor-oscillations notwithstanding, the numerically obtained horizontal variance of the beam $\sigma_R^2(t)$ were found to often grow non-linearly in time, i.e. $\sigma_R^2 \propto t^\nu$ with $\nu \neq 1$ in various studies [104, 166, 103]. This confirmed the fast ion transport in the TORPEX SMT configuration as generally non-diffusive, with a 'transport exponent' ν, as illustrated in Fig. 2.15 [103]. Initially, the injected fast ions require a certain time before interaction with the plasma becomes measurable, so that transport features a ballistic phase ($\nu \approx 2$), approximately lasting for their first half gyro-period [104]. During the following 'interaction phase' fast ions with an injection energy of $E = 30\,\text{eV}$ are transported superdiffusively ($\nu > 1$), while ions of $E = 70\,\text{eV}$ undergo subdiffusion ($\nu < 1$) [104, 103]. This reduction for higher ion energies was conclusively attributed to stronger gyro- and drift-averaging over the present plasma structures and their potential fluctuations, due to their larger Larmor-radii and stronger vertical drifts. After 4-5 gyro-periods, the superdiffusive fast ions have spread over a horizontal distance comparable to the plasma density and temperature gradient scales and smoothly transition into quasi-diffusion ($\nu \approx 1$) [103]. Furthermore, their radial distribution is significantly skewed during this ‘asymmetric’ transport phase [104, 103]. Higher energy ions continue to experience subdiffusion at all times considered [103].

2.5.5 Fractional diffusion models

Albeit initialized as Gaussians, the radial fast ion distributions in simulations quickly attain strongly non-gaussian shapes [108]. Since the present transport is heavily determined by gyro-averaging and drift-effects in a turbulent environment, it clearly presents certain non-local and non-markovian features [170, 108]. When attempting a mathematical description in terms of a random walk, this corresponds to the potential presence of heavy-tailed step-size and waiting-time distributions, so that the propagator of this transport is indeed no longer subject to the classical Central Limit Theorem (CLT) [118, 114]. The specific framework for such descriptions are usually either Continuous Time Random Walks (CTRWs) [117, 116, 114] or Generalized Langevin Equations (GLEs) [118, 119]. To interpret TORPEX fast ion data, one successful approach was the development of Asymmetrical Fractional Lévy Motion (AFLM). This model was able to successfully recover many of the non-gaussian features of the radial fast ion distribution in the super- to quasi-diffusive case [108]. However, the heavy tails of the propagator represented a strong over-estimate far from the bulk of the distributions. Furthermore, certain moments of the AFLM-based distributions intrinsically diverge, which cannot be fully reconciled with the finite width and moments of the physical fast ion distributions. These limitations are thus to be addressed and circumvented through the formalism presented in Sec. 6.4. It should be noted that an earlier description in terms of a CTRW-based Lévy-Walk also fruitfully recovered different non-diffusive transport regimes, while bounding step-sizes by a certain waiting-time through a power-law [170]. However, this coupling between their distributions prevents the derivation of analytical forms of their propagator and diffusion equations in all but exceptional cases [136]. Furthermore, no asymmetrical features could be recovered and the correlations between the step-sizes and waiting times inferred in simulations were not well described by the fitted power-laws at all scales [170, 136].

2.5.6 Time-resolved measurements and intermittency

With the principal fast ion transport regimes established [103], a first set of time-resolved measurements were taken [107] without lock-in amplification at $D = 40\,\mathrm{cm}$, similar to those described in Sec. 2.4. The intermittency of the acquired time-series was quantified by their skewness during the ion-source on-phases, compared to the off-phases. Intermittency levels distinctly above the background values were only found for fast ions undergoing superdiffusion and local time intermittency therefore suspected as a possible hallmark of this transport regime [107]. It is clear that any such link between the global nature of non-diffusive transport and local features of time-resolved measurements would be highly valuable in any setting with limited diagnostic access. Given the extreme conditions in a fusion plasma and the intrinsic limitations in measuring fast ions in space, there is no shortage of such situations across the field of plasma physics. Conditional Sampling of the fast ion mean-profiles was used to quantify their average response to plasma structures detected on HEXTIP and superdiffusive ions showed the expected stronger deviations from their mean position. These deviations were found in good qualitative agreement with the dipole-like nature of these structures and the resulting localized E×B-drifts [107], although no direct conditional measurement of the plasma potential was included.

The detailed investigation of the prevalence and generation of local time intermittency during the non-diffusive transport of the fast ion is the first central subject of this thesis. It is addressed through an extensive and comprehensive set of measurements across all fast ion transport regimes on TORPEX in Ch. 3. Numerical particle tracing as performed on GBS results is combined with experimental measurements of floating potential fluctuations in Ch. 4 to semi-quantitatively illustrate important aspects of the instantaneous and time-average response of fast ions to plasma structures. In Ch. 5, the insights from these preceding chapters are then leveraged to motivate an analytical model, that can predict the local skewness of a fast ion time-series solely based on its mean-value.

3 Time intermittency studies

The first central subject of this thesis is the study of local time-intermittency during the non-diffusive spreading of the fast ion beam through its interaction with plasma turbulence. As outlined in chapter 1, preliminary studies associated intermittency exclusively with the superdiffusive transport regime. Since such a direct link between a local observation and the globally present transport regime would be highly intriguing, more detailed studies have been undertaken and presented in Refs. [110],[111], from which we will draw extensively in what follows and Ch. 5. Beginning from a clearer picture on how we quantify intermittent behavior using the skewness of GEA time-series, a comprehensive set of measurements is presented that leads us to observe intermittency with varying prevalence across all present non-diffusive fast ion transport-regimes. Using conditional sampling in conjunction with HEXTIP-1 and HEXTIP-2, we then verify how the generation of intermittency in different parts of the time-average fast ion beam is related to the movement of positive and negative plasma density and potential fluctuations. Further analysis is shown to require at least qualitative knowledge on the instantaneous dynamics of the full fast ion beam, motivating the numerical investigations in Ch. 4.

3.1 Quantifying intermittency

Naturally, the first question to address is how one should meaningfully quantify any local time-intermittency in our system. Already the term ‘intermittency’ itself is often used rather loosely in the literature to denote a variety of irregularly occurring behaviors in complex systems. A more clearly defined application to time-series is found in the context of chaos, where intermittency describes the seemingly spontaneous and unpredictable emergence of bursts of chaotic, irregular behaviour during an otherwise well-predictable process [171]. As such, it is often treated based on its description in the field of fluid-dynamics and turbulence [86], where the term ‘intermittency’ is commonly used to describe the irregular formation of coherent structures in a turbulent environment. Furthermore, the term distinguishes these structures from other, regular and periodic patterns, as e.g. the waves and modes that may drive the turbulence. If one observes a large enough region of the turbulent fluid, the appearance of irregularly spaced coherent ‘patches’ has thus been described as ‘intermittent’ [86]. When performing a continuous single point measurement, e.g. of the fluid vorticity, such patches can lead to the local observation of irregular and ‘intermittent’ bursts and patterns if a macroscopic flow is present in the fluid. However, distinctly different spatial patterns can give rise to locally very similar observations. For instance, if the flow pattern is not well-known at all times, one cannot always distinguish between locally forming and decaying structures or irregularly spaced, stable patches that are advected by a turbulent flow. These spatial details are rarely fully known in settings with a limited number of measurement points such as ours. We therefore use the term *‘time-intermittent’* to solely describe the irregular local observation of bursts, or ‘peaks’ in the acquired fast ion current density time-series as shown in Fig. 3.1. It is implied, that the occurrence of these peaks is distinct from any Gaussian random noise (see insets), and does not follow a regular mode-like pattern. To further clarify, the term is not used to describe the rare attainment of any particular peak value compared to others. Given the ubiquitous presence of noise in our measurements, we rather intend it to describe the irregular observation of a variety of possible peak-values distinctly above the local mean and standard deviation of the time-series. Assumptions on any underlying spatial distributions will be developed step-by step using different analysis methods. In chapter 5, we finally incorporate the essential aspects of these assumptions into an analytical model to predict the local time-intermittency of the fast ion transport based on the local time-average fast ion current density.

Having defined our use of the term ‘time-intermittency’, it remains to quantify its observation. For this, accounting for the present noise in the fast ion time-series is essential at every step. Therefore, we generally describe the value of the locally measured GEA on-phase signal as a random variable $\mathcal{S}$ that represents the sum of the random variables for the actual local fast ion current density $\mathcal{J}$ and the local noise $\mathcal{N}$, i.e. we have $\mathcal{S} = \mathcal{J} + \mathcal{N}$. For simplicity, we assume $\mathcal{J}$ and $\mathcal{N}$ to be independent random variables and verify this assumption where appropriate. While the statistical properties of the distribution of $\mathcal{S}$ are measurable during the on-phases of the GEA signal, the properties of the noise $\mathcal{N}$ are available during the off-phases. By combining this information in a statistically meaningful way, one can draw conclusions on the statistics of our query $\mathcal{J}$.

In particular, the higher order central standardized moments of a time-series, such as its skewness γ and kurtosis κ, have proven useful in quantifying time-intermittency across different settings [86, 172], including SMT plasmas [126, 150, 173] and previous work on fast ions [107] on TORPEX. For a time-series $S_i = S(t_i)$, drawn at N regular time-intervals t_i from the random variable $\mathcal{S}$, they are respectively defined as

$$\gamma_{\mathcal{S}} = \frac{\sum_i^N (S_i - \mu_{\mathcal{S}})^3}{\left[\sum_i^N (S_i - \mu_{\mathcal{S}})^2\right]^{\frac{3}{2}}} = \frac{\mu_{\mathcal{S}3}}{\sigma_{\mathcal{S}}^3} \tag{3.1}$$

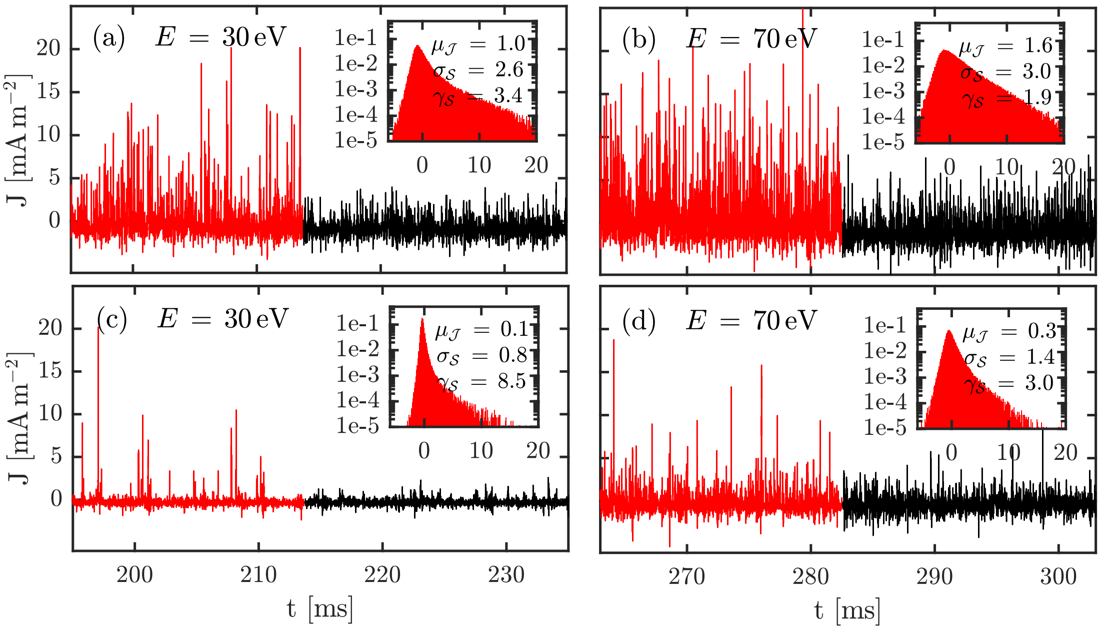

Figure 3.1 – Samples from fast ion time-series for $E = \{30, 70\}\,\mathrm{eV}$ acquired at $D = 171\,\mathrm{cm}$, with on-phases shown in red, off-phases in black. The inset PDFs belong to the on-phase and are annotated with the local fast ion signal mean $[\mu_{\mathcal{J}}] = \mathrm{mA\,m^{-2}}$, the on-phase standard deviation $[\sigma_{\mathcal{S}}] = \mathrm{mA\,m^{-2}}$ and the (dimensionless) on-phase skewness $\gamma_{\mathcal{S}}$. In (a,c), we show time-series with the highest $\mu_{\mathcal{J}}$ for the given E and D, while (b,d) correspond to the highest $\gamma_{\mathcal{S}}$. While all distributions feature heavy tails, note the higher skewness in time-series with more distinct outliers w.r.t. the lower local mean. Their acquisition locations in the poloidal plane are indicated in Figs. 3.2,3.4(c,f).

and

$$\kappa_{\mathcal{S}} = \frac{\sum_i^N (S_i - \mu_{\mathcal{S}})^4}{\left[\sum_i^N (S_i - \mu_{\mathcal{S}})^2\right]^2} = \frac{\mu_{\mathcal{S}4}}{\sigma_{\mathcal{S}}^4} \quad . \tag{3.2}$$

As the sums representing the higher order central moments $\mu_{\mathcal{S}3,4}$ in the numerators are most strongly incremented by the contributions furthest from the mean $\mu_{\mathcal{S}}$, they naturally indicate the presence of peaks and outliers [86, 174]. The appropriate normalization w.r.t. the standard deviation $\sigma_{\mathcal{S}} = \mu_{\mathcal{S}2}^{1/2}$ of the time-series ensures that the values of these statistics are sensibly scaled towards the average fluctuation level, that would be expected to characterize an underlying Gaussian process. Deviations from the resulting Gaussian reference values can therefore indicate any disproportionate presence of peaks, and thus time-intermittency, as described above. When calculating the skewness, any such statistical deviations that are symmetric about the mean of the time-series cancel of course. However, peaks due to the fast ion current density must be strongly positive by definition, so that this concern is mitigated. While we have nonetheless investigated both the skewness and kurtosis in the quantification and analysis of time-intermittency, we thus often focus on the skewness as the more practical statistical quantity. The presence of high kurtosis across the fast ion time-series was generally found to follow very similar trends.

Since the cumulants of independent random variables are additive [152], it is possible to decompose any moment-based statistics into contributions from the fast ions current $\mathcal{J}$ and the noise $\mathcal{N}$. For the on-phase mean and variance, one straightforwardly finds [107]

$$\mu_{\mathcal{S}} = \mu_{\mathcal{J}} + \mu_{\mathcal{N}} \qquad , \qquad \sigma^2_{\mathcal{S}} = \sigma^2_{\mathcal{J}} + \sigma^2_{\mathcal{N}} \quad . \tag{3.3}$$

Using this and the preceding definitions, the on-phase skewness becomes

$$\gamma_{\mathcal{S}} = \frac{\mu_{\mathcal{S}3}}{\sigma^3_{\mathcal{S}}} = \frac{\mu_{\mathcal{J}3} + \mu_{\mathcal{N}3}}{\left(\sigma^2_{\mathcal{J}} + \sigma^2_{\mathcal{N}}\right)^{\frac{3}{2}}} = \frac{\sigma^3_{\mathcal{J}}\gamma_{\mathcal{J}} + \sigma^3_{\mathcal{N}}\gamma_{\mathcal{N}}}{\left(\sigma^2_{\mathcal{J}} + \sigma^2_{\mathcal{N}}\right)^{\frac{3}{2}}} \tag{3.4}$$

and the kurtosis

$$\kappa_{\mathcal{S}} = \frac{\mu_{\mathcal{S}4}}{\sigma^4_{\mathcal{S}}} = \frac{\mu_{\mathcal{J}4} - 3\sigma^4_{\mathcal{J}} + \mu_{\mathcal{N}4} - 3\sigma^4_{\mathcal{N}}}{\left(\sigma^2_{\mathcal{J}} + \sigma^2_{\mathcal{N}}\right)^2} + 3 = \frac{\sigma^4_{\mathcal{J}}(\kappa_{\mathcal{J}} - 3) + \sigma^4_{\mathcal{N}}(\kappa_{\mathcal{N}} - 3)}{\left(\sigma^2_{\mathcal{J}} + \sigma^2_{\mathcal{N}}\right)^2} + 3 \quad . \tag{3.5}$$

Wishing to quantify the properties of the fast ion signal component $\mathcal{J}$, we rearrange for its mean and variance (for comleteness)

$$\mu_{\mathcal{J}} = \mu_{\mathcal{S}} - \mu_{\mathcal{N}} \qquad , \qquad \sigma^2_{\mathcal{J}} = \sigma^2_{\mathcal{S}} - \sigma^2_{\mathcal{N}} \quad . \tag{3.6}$$

as well as for the skewness

$$\gamma_{\mathcal{J}} = \frac{\sigma^3_{\mathcal{S}}\gamma_{\mathcal{S}} - \sigma^3_{\mathcal{N}}\gamma_{\mathcal{N}}}{\left(\sigma^2_{\mathcal{S}} - \sigma^2_{\mathcal{N}}\right)^{\frac{3}{2}}} \tag{3.7}$$

and for the kurtosis

$$\kappa_{\mathcal{J}} = \frac{\sigma^4_{\mathcal{S}}(\kappa_{\mathcal{S}} - 3) - \sigma^4_{\mathcal{N}}(\kappa_{\mathcal{N}} - 3)}{\left(\sigma^2_{\mathcal{S}} - \sigma^2_{\mathcal{N}}\right)^2} + 3 \quad . \tag{3.8}$$

All quantities on the RHS of Eqs. 3.6-3.8 are available through measurements in either the on- or off-phases of the fast ion source modulation. While $\gamma_{\mathcal{J}}$ and $\kappa_{\mathcal{J}}$ represent statistics that meaningfully quantify time-intermittency from the fast ion signal component, these quantities feature a major practical drawback as they diverge in regions with a low fast ion signal, where $\sigma_{\mathcal{S}}$ and $\sigma_{\mathcal{N}}$ take on similar values. However, it is precisely at the low density edge of the time-average fast ion beam where the most distinctively time-intermittent behaviour is expected [107]. Therefore, the above quantities are not employed to describe and compare the locations and dynamics of the strongest time-intermittency in the time-resolved fast ion profiles or CS fast ion profiles in the upcoming sections. Instead, we use the on-phase skewness $\gamma_{\mathcal{S}}$. In contrast to previous studies [107], we do not subtract the local background noise skewness $\gamma_{\mathcal{N}}$, as the difference of these quantities is no longer a skewness itself (see Eq. 3.7). Instead, we focus on the prevalence of $\gamma_{\mathcal{S}}$ above the maximal observed background value of $\gamma_{\mathcal{N}} \approx 2$. The injected fast ion current has been sufficiently increased to allow distinctive enough time-series measurements for this comparison. Nonetheless, we will make use of all the above considerations repeatedly in chapter 4, when comparing simulated fast ion statistics to our measurements, and in chapter 5, when predicting measurements based on an analytical model.

3.2 Statistics of measured time-series

The primary method to assess the prevalence of local time-intermittency across the various fast ion transport regimes are time-resolved fast ion profiles, constructed from the statistics of time-series measurements taken across the poloidal plane at one specific source-detector distance $126\,\mathrm{cm} \leq D \leq 171\,\mathrm{cm}$, and at a constant injection energy of $E = \{30, 50, 70\}\,\mathrm{eV}$. According to earlier studies [103] (see Sec. 2.5), fast ion with $E = 70\,\mathrm{eV}$ undergo subdiffusive transport here, whereas those injected with $E = 30\mathrm{eV}$ are completing a smooth transition from a super- to a quasi-diffusive regime, with strongly asymmetric radial transport. Fast ions with $E = 50\,\mathrm{eV}$ are assumed to represent an intermediate, and therefore subdiffusive case. To verify the time-average fast ion drifts and transport, the mean-profiles shown in Figs. 3.2,3.3,3.4(a-c) are based on an interpolation from locally determined values of $\mu_{\mathcal{J}}$, accounting for the offsets due to noise and the acquisition system. The width and location of these profiles is in reasonably good agreement with expectations from previous studies with lock-in detection [103].

A small increase in most measured widths by ≈ 15% is likely due to slight systematic variations in the injection angle θ. While the corresponding transport exponents would therefore likely differ to some degree from earlier finds, their precise values are of little consequence to the analysis of time-intermittency in the following. However, since we intend to quantify and localize its prevalence via interpolated skewness profiles based on $\gamma_{\mathcal{S}}$ [see Figs.3.2-3.4(d-f)], the importance of the local noise $\mathcal{N}$ compared to the fast ion signal $\mathcal{J}$ (see Eq. 3.4) becomes crucial. This holds in particular for comparisons between different profiles, since the total detected fast ion current I varied significantly between them. This was inevitable due to differences in the overall quality of the ion sources, as well as their gradual depletion during each campaign. Despite best efforts to compensate for these issues by continually adapting the source bias via the internal grid, the total detected currents found by numerically integrating each mean-profile vary between $I \approx 2.2 - 5\,\mu\mathrm{A}$, as detailed in the captions of Figs.3.2-3.4, with an average of $I_{av} = 2.85\,\mu\mathrm{A}$.

To account for these variations between profiles, we normalize the moments of the fast ion component $\mathcal{J}$ in the measured $\mu_{\mathcal{J}}$ and $\gamma_{\mathcal{S}}$ by the factor $c = \frac{I_{av}}{I}$ for each profile, i.e. we let

$$\mu_{\mathcal{J}} \mapsto c\mu_{\mathcal{J}} \qquad , \qquad \gamma_{\mathcal{S}} \mapsto \frac{c^3\sigma_{\mathcal{S}}^3\gamma_{\mathcal{S}} + (1-c^3)\sigma_{\mathcal{N}}^3\gamma_{\mathcal{N}}}{(c^2\sigma_{\mathcal{S}}^2 + (1-c^2)\sigma_{\mathcal{N}}^2)^{3/2}} \quad , \tag{3.9}$$

before interpolating the shown profiles. Note that in the limit of $c \to \infty$, one retrieves $\gamma_{\mathcal{S}} \mapsto \gamma_{\mathcal{J}}$ (see Eq. 3.7), as the impact of the noise contribution becomes negligible. The noise contribution to $\gamma_{\mathcal{S}}$ that avoids the divergence in the region of $\sigma_{\mathcal{S}}^2 \to \sigma_{\mathcal{N}}^2$ is thus given a more experimentally consistent weight relative to the fast ion contribution to the measurements. Remaining variations in the detectable current between the discharges within some profiles were found non-negligible, particularly in Fig. 3.3(c,f). Therefore later analysis was performed predominantly on the data taken at $E = 30\,\text{eV}$ and $E = 70\,\text{eV}$. Here, fluctuations were mostly held within a margin of ∼ 15%, indicated by the external source grid currents between shots. The applied source bias was hence kept more stable. Nonetheless, these findings motivated the development of the injection current acquisition circuit (Sec. 2.4.3), which confirmed this estimate of the fluctuations.

From the skewness profiles shown in Figs.3.2-3.4(d-f), it is clear that there are instances of $\gamma_{\mathcal{S}}$ distinctly above the maximum background value of $\gamma_{\mathcal{N}} \approx 2.2$ across all fast ion energies and propagation distances. The highest values of $\gamma_{\mathcal{S}}$ still appear on the edge of the mean-profile towards the LFS. Towards the HFS, the noise contribution increases with the average intensity of local plasma density fluctuations (see Fig. 2.4(d,e)) and lowers $\gamma_{\mathcal{S}}$. As before [107], the highest values of skewness are neither observed near the peak of the mean-profile, since the increased $\mu_{\mathcal{J}}$ diminishes the contribution of the outlying peaks in the 3rd central moment (see Eq. 3.1, Fig. 3.1(a,c)). The maxima of $\gamma_{\mathcal{S}}$ across all profiles are summarized in Fig. 3.5.

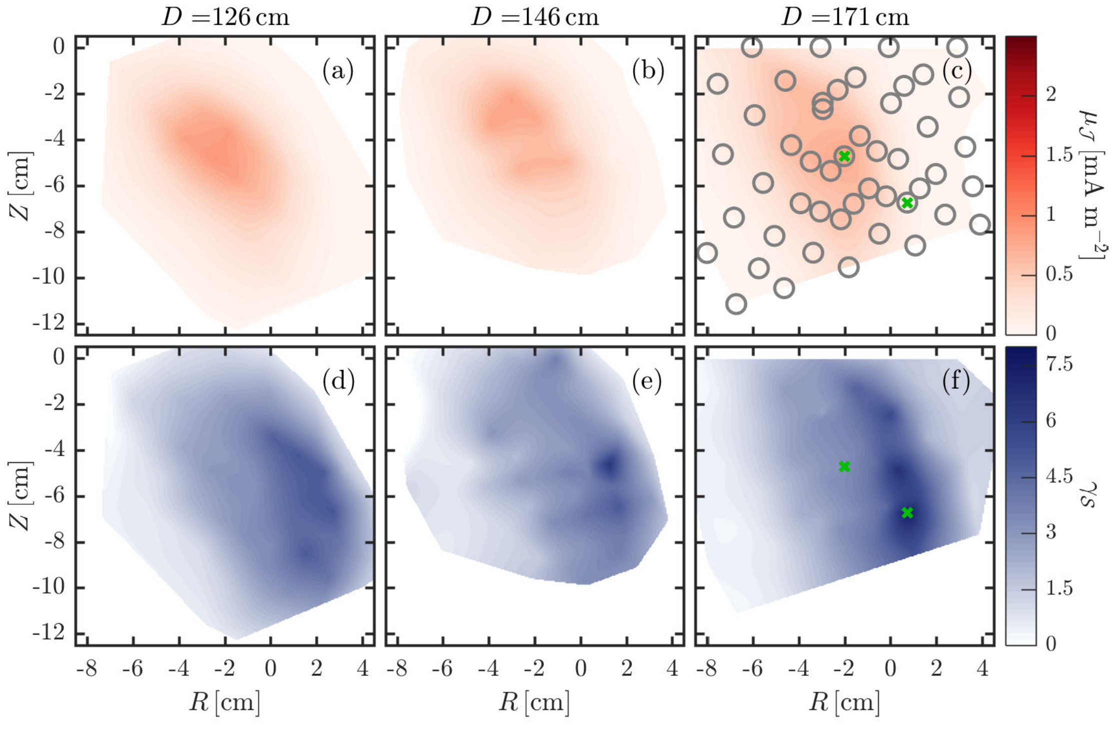

Figure 3.2 – Profiles of the fast ion signal mean $\mu_{\mathcal{J}}$ (a-c) and on-phase skewness $\gamma_{\mathcal{S}}$ (d-f) for an injection energy of **E = 30 eV** at increasing source-detector distances D. With a total detected fast ion currents of $I \approx \{2.3, 2.4, 3.3\}\,\mu\text{A}$ (a-c), all profiles have been normalized according to Eq. 3.9. The circles in (c) show the different GEA positions where measurements were taken, while their size approximately indicates the detector aperture with 8 mm diameter. Note the wider spread and lower vertical position of the mean profiles compared to higher energies in Figs. 3.3, 3.4. Furthermore, the highest instance of normalized $\gamma_{\mathcal{S}} \approx 7.7$ is found in (f). The green crosses in (d,f) show the positions where the time-series for Fig. 3.1(a,c) were taken.

Note how they follow more consistent trends after normalization (see circles vs. crosses), especially in the 70 eV case. The maximum γ_S appear higher in the super- to quasidiffusive case of $E = 30\,\mathrm{eV}$, and generally constant or increasing with longer propagation distances D. While the precise values of these maxima do depend on the specifically chosen value of c, these general trends appear rather consistent across a range of at least ±20% (see error-bars). The reasons for this behavior will become more apparent when investigating the generation of time-series in Ch. 4 and when motivating the analytical model for the prediction of γ_S in Ch. 5.

However, the presented measurements already allow the conclusion that time-intermittency in our context is not an intrinsic feature of any particular non-diffusive transport regime, but occurs to varying degrees across all of them. This key result presented in [110, 111] thus signifies a departure from the expectations of earlier studies [107], ultimately prompting the more detailed numerical and analytical studies on the generation of intermittency in this

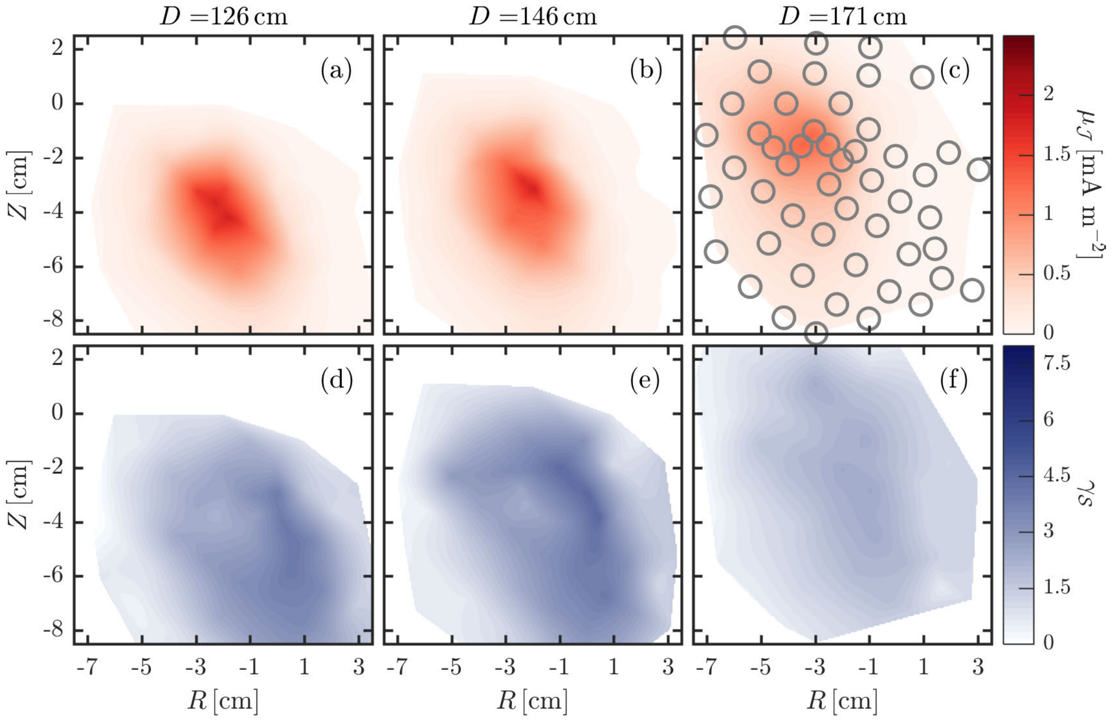

Figure 3.3 – Normalized profiles of the fast ion signal mean $\mu_{\mathcal{J}}$ (a-c) and on-phase skewness γ_S (d-f) for an injection energy of $\mathbf{E = 50\,eV}$ at source-detector distances D and with total detected fast ion currents of $I \approx \{2.2, 2.2, 2.7\}\,\mu\mathrm{A}$ (a-c). The circles in (c) show again the different GEA measurement positions and aperture size. The spread and vertical positions in (a-c) lie between the two extremes in Figs. 3.2,3.4. The skewness values in (f) appear diminished compared to lower D, which can be due to more unstable injection currents between and during the discharges in this profile, which occurred as the ion-source began to deplete. The source bias was adjusted in an attempt to compensate, and the total detected current thus increased on average nonetheless.

system, as presented in Ch. 4 and Ch. 5 respectively. To firstly characterize the occurrence of the intermittent peaks within fast ion time-series in relation to the propagation of different plasma structures on a purely experimental basis, we now extend their analysis through conditional sampling methods [107].

3.3 Conditional Sampling

The technique of Conditional Sampling (CS) [153, 156] has long been used on TORPEX [131, 133, 99] to establish a statistical relation from observations on one *reference* time-series measurement, usually from an LP, to concurrent observations on time-series data from other diagnostics, which have included other LPs, the fast framing camera, or the GEA. To do so, one firstly defines *events* of interest via the reference time-series. For instance, we detect the local propagation of a plasma structure such as a blob, by imposing an absolute threshold on the measured plasma density fluctuation $\delta n(t) = n(t) - \langle n \rangle_t$, where $\langle \rangle_t$ denotes the local time average [see Fig. 3.6(a)].

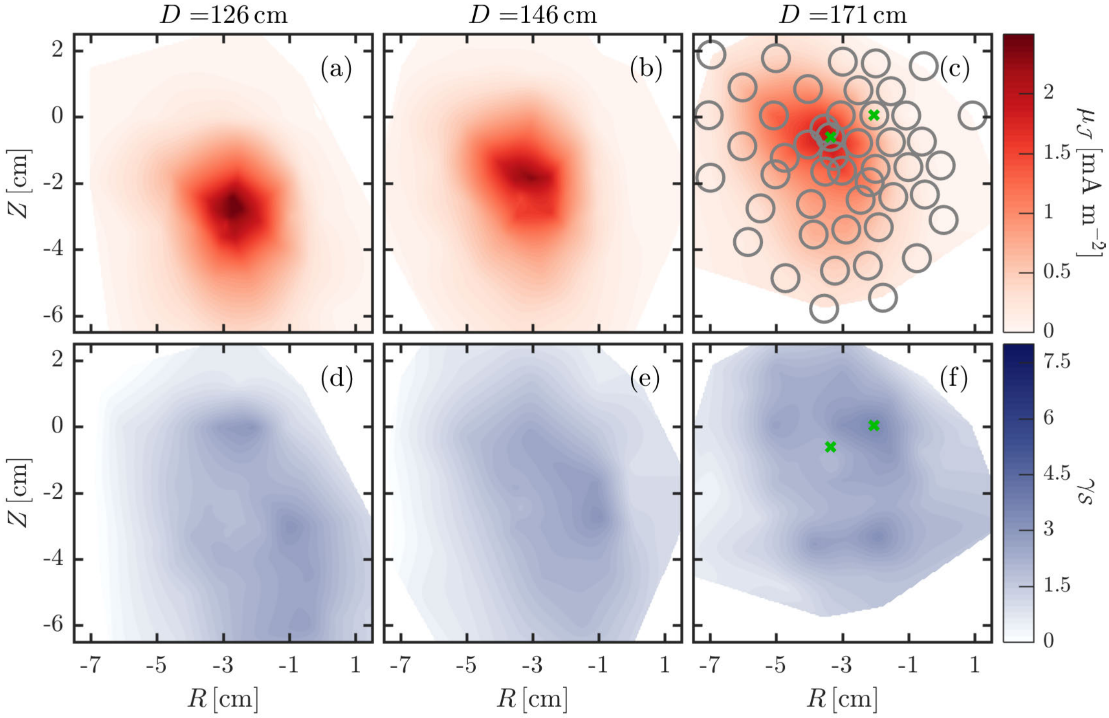

Figure 3.4 – Normalized profiles of the fast ion signal mean $\mu_{\mathcal{J}}$ (a-c) and on-phase skewness $\gamma_{\mathcal{S}}$ (d-f) for an injection energy of **E = 70 eV** at the source-detector distances D. The total detected fast ion currents are $I \approx \{5.0, 3.0, 2.4\}\,\mu$A. Note the diminished spreading and higher vertical positions in (a-c) compared to Figs. 3.2,3.3. The normalized $\gamma_{\mathcal{S}}$ are consistently lower than for lower E, but there are still instances above the maximum measured background value of $\gamma_{\mathcal{N}} \approx 2.2$. The green crosses in (d,f) show the positions where the time-series for Fig. 3.1(b,d) were taken.

The precise time-index of each event is defined as the first peak-value within each interval exceeding the defined threshold [see Fig. 3.6(b)]. A consistent time window of $\tau = \pm 120\,\mu$s at a $4\,\mu$s time-step is selected around the event ($\tau = 0$), defining each conditional sample (shaded green). These time-windows defined by the reference are then also selected on all other concurrently measured time-series [e.g. the GEA in Fig. 3.6(c)]. By averaging the values of a time-series within all the selected time-windows separately for each time-step in τ, one obtains the Conditionally Averaged Sampling (CAS) result for this time-series. Collectively, these CAS results can thus characterize the average dynamics of our system around the times when the imposed condition on the reference is met. For example, by interpolating profiles for each τ from the CAS results of $\delta n(t)$ data from HEXTIP, one observes the propagation of a CAS plasma structure around the selected reference probe (c.f. 'CAS blobs' [131]), as illustrated for $\tau = 0$ in Fig. 3.9(a).

Consequently, we wish to characterize the average dynamics of the fast ion beam in response to CS plasma density structures using the GEA time-series [107, 136]. This however requires two more adaptations of the sampling method. Firstly, only one fast ion time-series was taken

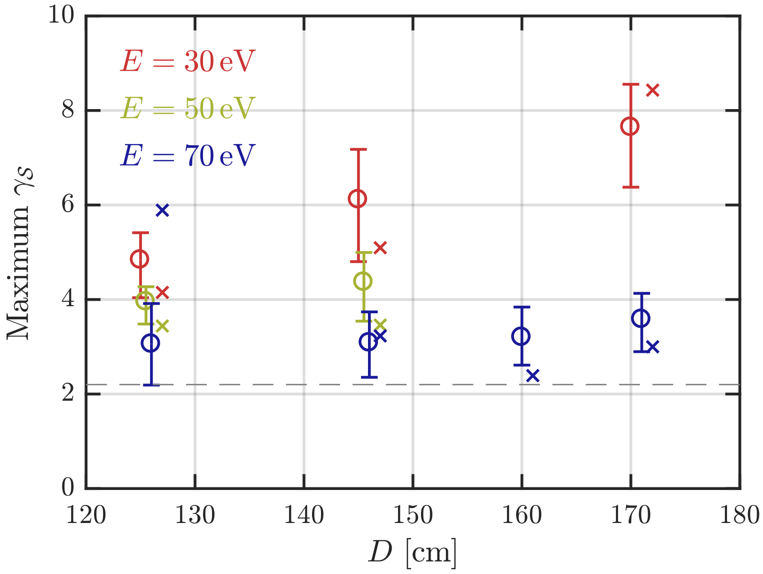

Figure 3.5 – The circles show the maxium values of γ_S for the profiles shown in Figs. 3.2-3.4, except 3.3(f) due to current fluctuations. An additional profile for $E = 70\,$eV at $D = 160\,$cm was included as well. For reference, crosses show the corresponding values before normalization. The top of each error-bar corresponds to a 20% increase in the normalization factor c, the bottom to the same decrease. If they were produced by a different choice of I_{av}, the errors shown would thus be systematic. However, this likewise serves to illustrate the influence of random errors through fluctuations in the injected current I, that for the shown profiles are usually estimated as smaller. Any offsets in D from $D = \{126, 146, 171\}\,$cm have been added merely for better visibility. The dashed line indicates the highest measured background skewness $\gamma_{\mathcal{N}}$.

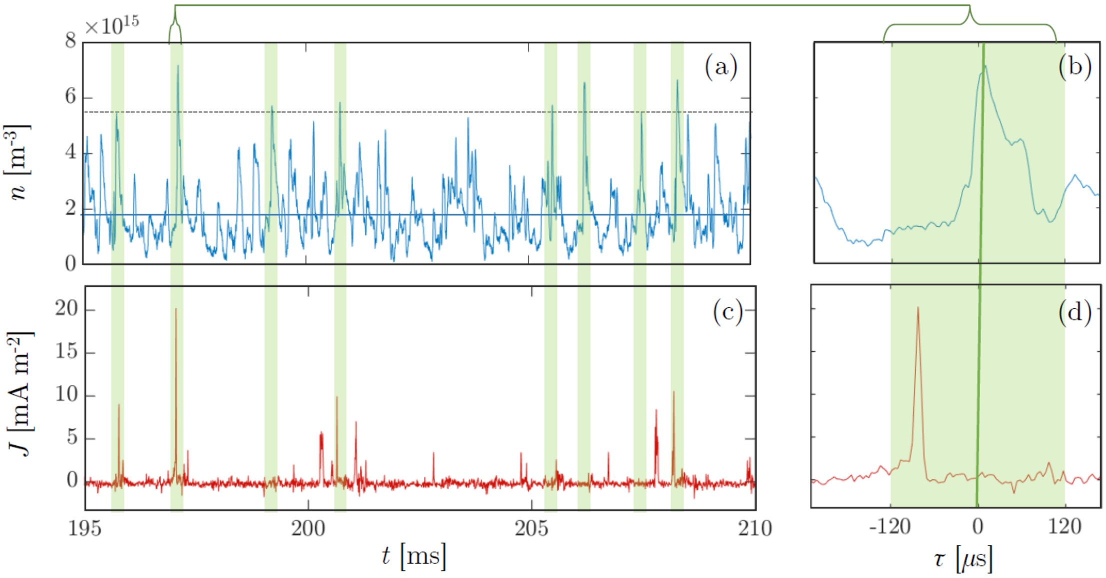

Figure 3.6 – Illustration of the conditional sampling process. The plasma density time-series from HEXTIP-1 (a), is taken as reference and events defined by an absolute threshold (dashed black) above the mean (blue), which is commonly removed during sampling. The time-windows of conditional samples are shaded green on the reference as well as the concurrently sampled GEA-signal (c). As shown in (b), the samples are centered with $\tau = 0$ on their first reference signal peak. To obtain the conditional average, the samples from each time-series are averaged at each value of τ at 4 μs time-resolution. Note that not all peaks in (a) correspond to a signal peak in (c), indicating statistical variations between the events defined in (a) as well as in the response of the fast ion beam. The fact that the peak of the fast ion signal can precede the plasma density peak, as in (b,d), is mostly due to the GEA being positioned ≈ 3 cm below and outward from the reference in this shot. The conditional average dynamics relevant to these examples are illustrated in Fig. 3.7(a-c).

during each discharge. Therefore, we have to include all the discharges pertaining to a given fast ion profile, and obtain one conditional average each. Based on the GEA measurement position of each discharge, profiles are then obtained across all measurement positions for each τ. The reference probe on HEXTIP and the chosen density threshold thus need to be kept consistent throughout all shots in the profile, and the high reproducibility of TORPEX plasmas becomes indispensable. Secondly, one needs to treat the on- and off-phases within the fast ion signal appropriately. As for the mean profile of $\mu_{\mathcal{J}}$, we average the conditional samples of each type of phase separately and subtract the off-phase conditional average from the on-phase conditional average before interpolating the fast ion CS-profiles, as shown in Figs. 3.7,3.8. This subtraction does not only remove constant signal offsets, but also reduces any systematic noise signatures that specifically occur (on average) due to the passage of a structure across the GEA, e.g. through secondary electron emission from its internal grid (see Sec. 2.4).

In Fig. 3.7, we show the response of the fast ion CS-profile to the propagation of positive

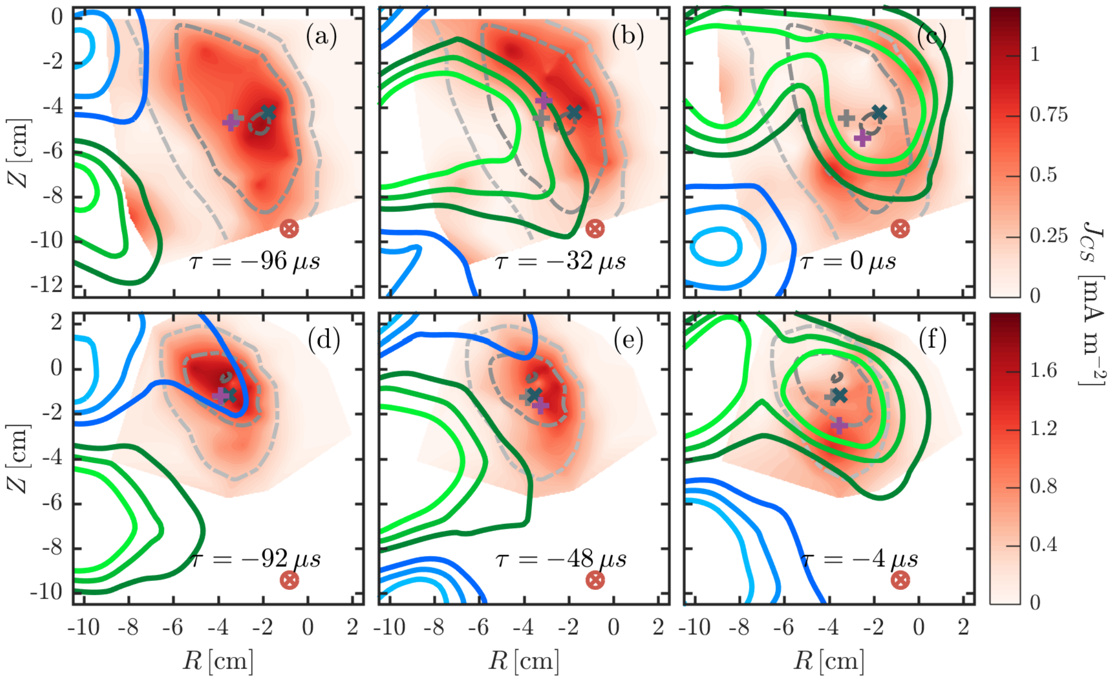

Figure 3.7 – Fast ion CS-profiles (red scale) for $E = 30\,\text{eV}$(a-c) and $E = 70\,\text{eV}$ (d-f) at $D = 171\,\text{cm}$ during the propagation of a positive CS plasma density structure. Positive (green) and negative (blue) plasma density contours are shown at $\delta n = \pm\{0.6, 1.2, 1.8\} \times 10^{15}\,\text{m}^{-3}$. The gray dashed outlines show the fast ion mean profile at its 10%, 50%, and 90% contour. The gray cross shows the centre-of-mass for the mean profile, the purple cross for the CS-profile. The chosen HEXTIP reference probe is marked by the green x.

density fluctuations detected with $\delta n > 3.5 \times 10^{15}\,\text{m}^{-3}$ on a HEXTIP reference probe (green cross), based on the treatment of time-series data as detailed in Fig. 3.6. The contours of δn (green, blue) represent conditional average samples of plasma structures. Given the position of the fast ion beam and the reference probe, they do not represent 'CAS-blobs', but also average over contributions from particularly elongated mode structures (see Secs. 2.1,2.2). These structures feature typical auto-correlation times of $\tau_{ac} \lesssim 50\,\mu\text{s}$ [107], which is close to the half-period of the mode with $f_{int}^{-1} \sim 100\,\mu\text{s}$. For $\tau \ll \tau_{ac}$ in the Fig. 3.7(a,d), the plasma conditions are less constrained by the applied sampling and therefore the fast ion profiles resemble their time-average (gray contours). Once the CS plasma structure approaches at $\tau \approx -\tau_{ac}$ (b,e), the fast ion profiles are displaced outward to the LFS. Finally, the fast ions appear to stream down and back around the structure when it passes the reference probe at $\tau \approx 0$ in (c,f). The displacements of their centre-of-mass (purple cross) from its time-average position becomes maximal, before slowly returning to the mean position for $\tau > 0$. Generally, these displacements are more distinct for $E = 30\,\text{eV}$ than for $E = 70\,\text{eV}$, with peak values of $\approx 2\,\text{cm}$ and $\approx 1.2\,\text{cm}$ respectively. As seen in previous studies at $D \approx 40\,\text{cm}$ [107], the effects of gyro- and drift-averaging over the turbulent structures are reflected more strongly in the subdiffusive 70 eV case. However, due to the $\approx 4\times$ longer time-of-flight of the fast ions, their overall displacements are larger as they interacted with the plasma structures for longer. The fast ions giving rise to the profile at $\tau = 0$ can thus be affected by the field-aligned plasma structures along their whole trajectory after their emission at the source (marked red) at $\tau \approx -55\,\mu$s and $\tau \approx -36\,\mu$s, depending on the associated potential fluctuations.

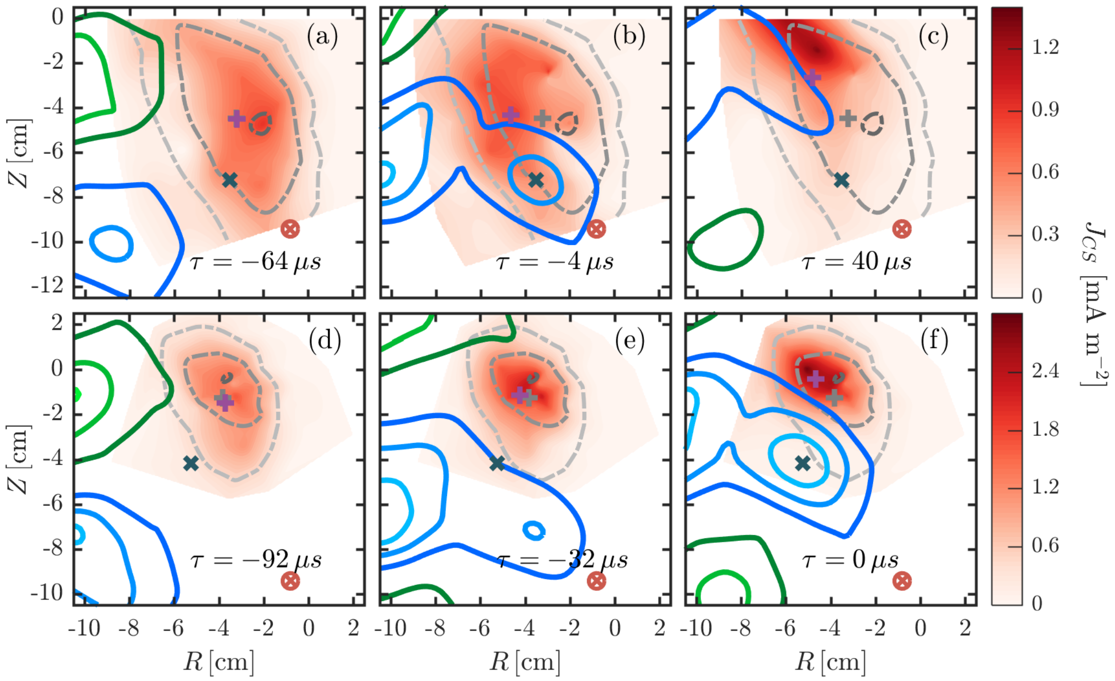

Figure 3.8 – Fast ion CS-profiles (red scale) for $E = 30\,$eV(a-c) and $E = 70\,$eV (d-f) at $D = 171\,$cm during the propagation of a negative CS plasma density structure. Positive (green) and negative (blue) plasma density contours are shown again at $\delta n = \pm\{0.6, 1.2, 1.8\} \times 10^{15}\,\mathrm{m}^{-3}$, and all other elements have the same significance as in Fig. 3.7. Note that the HEXTIP reference probes (green x) are chosen below the mean-profiles in this case.

Qualitatively, the displacement pattern described above is in good agreement with the clockwise E×B-flows around the negative side of a dipole near the bottom of the density fluctuation, as expected from an ideal interchange mode and the blobs detaching from it [131, 129, 107]. This is illustrated in Fig. 3.9(a), for the same conditionally sampled plasma density contours as in Fig. 3.7(c). To further verify this behavior, a complementary CS analysis on the passage of negative density fluctuations illustrated in Fig. 3.8 was performed by selecting $\delta n < -1.8 \times 10^{15}\,\mathrm{m}^{-3}$ on the plasma density time-series of a HEXTIP probe again for both $E = 30\,$eV and $E = 70\,$eV at $D = 171\,$cm. The fast ion CS-profiles still resemble their time-average for $\tau \ll \tau_{ac}$(a,d), it is displaced inwards to the HFS in (b,e) and then upward in (c,f) as the negative density fluctuation propagates through the region of the time-average fast ion beam. This pattern would be consistent with the anti-clockwise E×B-flows on the right of an expected positive potential fluctuation towards the middle and bottom of the negative density fluctuation [see Fig. 3.9(a)]. The time-indices τ in (b,c,d,f) were chosen to illustrate the strongest horizontal and overall displacements of the centres of mass, which are again

≈ 2× stronger in the 30 eV case. The offset in the values of τ compared to the 70 eV case can in part be attributed to their difference in time-of-flight and the position of the two different references probes, now between the source and the mean-profile. For the fast ions to be affected by the inward drift as in (b,d), the fluctuation needs to propagate past the region of the source, so that fast ions are displaced during a significant portion of their trajectory before being detected ≈ 56 μs and 36 μs later. Hence, the effect should appear earlier for the 70 eV case, and so should the following upward displacement by the same argument. Furthermore, due to the lower position of the reference probes compared to Fig. 3.7, we find the fast ions affected at larger values of τ, when the suspected potential fluctuation is fully crossing through the region of the time-average fast ion profile. Furthermore, most quantitative features of these profiles, such as the precise direction and magnitude of the centre-of-mass displacement, are affected by statistical uncertainties, especially in the edge shapes of the fast ion CS profiles [see already Fig. 3.7,3.8(a,d)]. Thus there is also uncertainty in which τ illustrates these features best. Nonetheless, the qualitative observations of the effect of different plasma structures are in good agreement with the expected E×B dynamics.

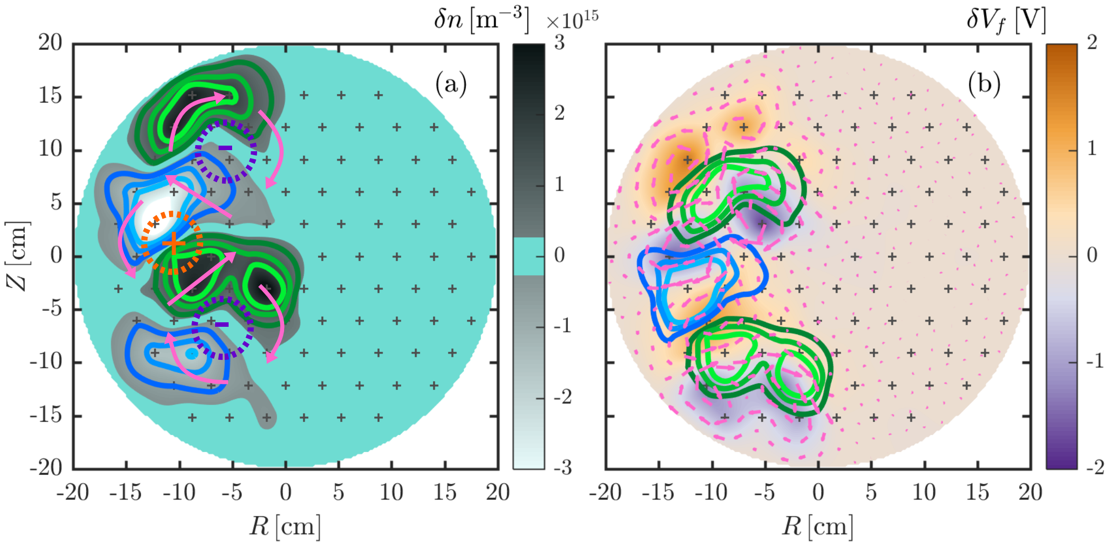

Figure 3.9 – (a) Full CS plasma density profile from HEXTIP-1, corresponding to Fig. 3.7(c), with the potential structures (dashed) and associated E×B drifts (magenta) as qualitatively estimated from the observations of the fast ion CS profiles. (b) Corresponding full CS floating potential profile, based on concurrent measurements with HEXTIP-2, with superimposed CS density contours projected along magnetic field lines. Note that both density and potential fluctuations are similar at vertical separations of ≈ 16 cm due to the field alignment of plasma structures in the ideal interchange regime of the SMT.

To obtain a more concrete description of the conditionally averaged E×B-drifts experienced by the fast ions in Fig. 3.7, we used the array HEXTIP-2 to obtain floating potential time-series concurrent to density time-series on HEXTIP-1 used above. In Fig. 3.9(b), the CS profile of floating potential fluctuations $\delta V_f(t) = V_f(t) - \langle V_f \rangle_t$ corresponding to the CS density profile in (a) is shown. The density contours super-imposed on (b) are projected along the SMT field-lines to account for the toroidal separation of both arrays. The arrows show the direction and relative magnitude of E×B-drifts induced by the potential gradients. They are expected to constitute a valid approximation at least towards the centre of the TORPEX cross-section (see Sec. 2.2). These drifts indeed follow the expectations from the motion of the fast ions indicated in (a), and feature the $\frac{\pi}{2}$ phase w.r.t. the density fluctuations characteristic for an ideal interchange mode. Since the CS was performed with positive density fluctuations as reference, the drifts around the negative ones are less distinct, and the negative potential fluctuations in the wake of more elongated or detaching plasma structures are offset towards the LFS. Note that the potential fluctuations around positive density structures appear more detached from the interchange-mode than the density contours.

Lastly, we wish to outline how the indicated reference probes on HEXTIP were chosen. As a first criterion, their distance from the time-average fast ion profile is constrained by the spatially limited correlations in this turbulent environment, as observed on HEXTIP [149], making the probe nearest to the peak of the fast ion profile (as in Fig. 3.7) the intuitive choice. However, the extended time-period spent by the fast ions in the plasma, and the vertical distance over which they propagate may also be needed to take into account by choosing a lower probe. Since the subject of interest was the generation of the most intermittent time-series [marked in Figs. 3.2,3.4(f)], a reversed CS analysis was performed by choosing their on-phases as a reference with a $2\sigma_S$ threshold for fast ion peaks, and sampling the concurrent HEXTIP measurements during the same time-windows. These conditionally sampled plasma density profiles showed the most significant density fluctuations propagating near the chosen probes. Conversely, CS with other reference probes on HEXTIP led to similar, but often less consistent results than those shown above, especially when increasing the distance from the fast ion beam region.

3.4 Motivations for further analysis

Although CS-profiles can give very illustrative insights on the physical effects leading to the movement of the fast ion beam. The dipolar potential structures associated with positive and negative plasma density fluctuations have been found to displace the fast ions towards the locations of the most intermittent measurements, respectively in the lower LFS and upper HFS portion of the time-average fast ion profiles. However, the fast ion CS-profiles represent by definitions average statistics, from which individual events can differ strongly especially if significant noise is present in the analyzed time-series. One key indication that this difference is important in our case is the fact that the detected peaks in the fast ion time-series (see Fig. 3.1) attain distinctly higher values than found anywhere in the CS-profiles. This would suggest that the profiles of the fast ion beam at a given moment, henceforth the *instantaneous profile*, can be much more narrow and concentrated than the time-average mean profile. This picture of a meandering instantaneous fast ion beam, that gives rise to larger time-average profiles through its motion, is the very basis for the analytical model that was devised to predict the skewness of the locally generated time-series as detailed in Refs. [109],[110],[110]. Before presenting these results in Ch. 5, it is thus instructive to review the investigations attempting to further characterize the instantaneous profiles of the beam in the next chapter. Since such profiles cannot be obtained from single point measurements, we turn mostly towards numerical studies, which are nonetheless guided by experimental measurements of the SMT plasma conditions in TORPEX.

4 Experiment-based particle tracing

In this chapter we aim to characterize the fast ion beam and its profiles at a given time, the *instantanoeus beam*, in relation to its conditional and total time-averages shown in the preceding chapter. With multi-point measurements of fast ions becoming available only now (see Sec. 2.4.3), the following investigations had to be pursued using numerical simulations. A particle tracer using floating potential measurements from HEXTIP has been implemented and is used to shed light on the qualitative dynamics of the instantaneous beam. Predictions on the time-average profile are used for matching experimental measurements and previous results based on GBS. While certain quantitative limitations are found mainly due to the finite resolution of HEXTIP, statistical features such as the skewness of synthetic time-series are in good agreement with expectations. The obtained results aid us in establishing a more concrete picture of the meandering instantaneous fast ion beam, which will be helpful for developing the analytical model in the following chapter.

4.1 Particle tracing

The explicit Boris-algorithm [175], as detailed in appendix B, is one of the most well established ways to numerically integrate the trajectories of charged particles in response to the Lorentz force, with the equations of motion

$$\begin{aligned} d_t\vec{r} &= \vec{v} \\ d_t\vec{v} &= \frac{q}{m}\left(\vec{E}(\vec{r},t)+\vec{v}\times\vec{B}(\vec{r},t)\right) \quad . \end{aligned} \tag{4.1}$$

To advance the particle positions $\vec{r_i}$ and velocities $\vec{v_i}$ from one time-frame τ_i to the next $\tau_{i+1} = \tau_i + \Delta\tau$, half of the contribution from the electric field is added before, the other half after the contribution from the magnetic field is treated. Due to its excellent long-term numerical stability e.g. in terms of energy conservation, even at time steps that are only a few times smaller than the particle gyro-orbit, different variants of this algorithm have been used in a wide range of Particle In Cell (PIC) [176] simulations as well as full-orbit codes for fast ion studies [177, 178]. Only recent studies have clarified that these favourable features are indeed linked to volume conservation in phase-space [179]. Albeit different methods have been chosen for tracing fast ions based on GBS results [104], comparisons with the Boris-algorithm were still employed to validate initial tests. Therefore the Boris-algorithm has also been used as the basis for the particle tracer implemented in the frame of this thesis. For numerical simplicity, an implementation in a Cartesian coordinate system (x, y, z) was chosen into which all inputs to the tracer were transformed from the practically more convenient rotated local coordinates (x_1, y_1, z_1) as shown in Fig. 4.2.

These required inputs are the initial velocity and position of a particle, as well as the magnetic field $\vec{B}_i(\vec{r_i}, \tau_i)$ and electric fields $\vec{E}_i(\vec{r_i}, \tau_i)$ that it experiences at a given time-frame and position. To firstly sample the time-average fast ion beam, we integrate the trajectories of particle bunches of $N_p \geq 400$ tracers each, injected at intervals $\Delta t \leq 50\,\mu$s over a duration of ≥ 200 ms, similar to studies with GBS for later comparison. The initial conditions for the particle position, injection energy and the vertical and horizontal injection angles are drawn randomly, mostly from Gaussian distributions. The specific initial conditions for different studies are given in their respective sections below.

Just as for GBS, we assume toroidally symmetric magnetic fields that do not vary in time. They are computed using routines established for a variety of magnetic geometries during the thesis work of Fabio Avino [135], that only require inputs for the currents to the toroidal and vertical field coils of TORPEX, as well as the internal toroidal conductor if used. In practice, the toroidal field features a ‘ripple’ depending on the distance to the closest field-coil, but these variations [see Fig. 4.1(a-b)] amount to < 10% for $x_1 < 1.1$ m and are thus neglected for computational efficiency. In the SMT, we use the ‘vertical ideal’ configuration for the poloidal field as illustrated in Fig. 4.1(c). The full field $\vec{B}_i(\vec{r_i}, \tau_i) = \vec{B}_i(x_{1,i}, y_{1,i})$ is computed at $\Delta x_1 = \Delta y_1 = 1$ mm spatial resolution across the poloidal cross section.

The flexibility in the choice of magnetic field is one intrinsic advantage over GBS, that also motivated the complementary development of this tracing algorithm. Changing to a magnetic geometry different from the slab or SMT, and especially to X-points, has been a major analytical and numerical undertaking for GBS spanning the past and current thesis works of Paola Paruta [168] and Carrie Beadle [180]. The capacity to feed any available magnetic geometry on TORPEX into the present tracing algorithm is however already implemented from the start, pending the availability of inputs for the continually evolving turbulent electric fields on TORPEX. We will attempt to extract statistically useful approximations of these fields from the gradients of interpolated time-resolved V_f measurements from HEXTIP (see Fig. 2.9), in contrast to GBS, where the plasma potential can be evolved continuously down to sub-mm and sub-μs scales. The principal trade-off is therefore between the small-scale accuracy of the FORTRAN90-based GBS and the flexibility and simplicity of the experiment-based tracer implemented in MATLAB.

In the next sections, we discuss how the evolving electric fields in this tracing algorithm are computed, and address the impacts of the limited resolution and probe arrangement of

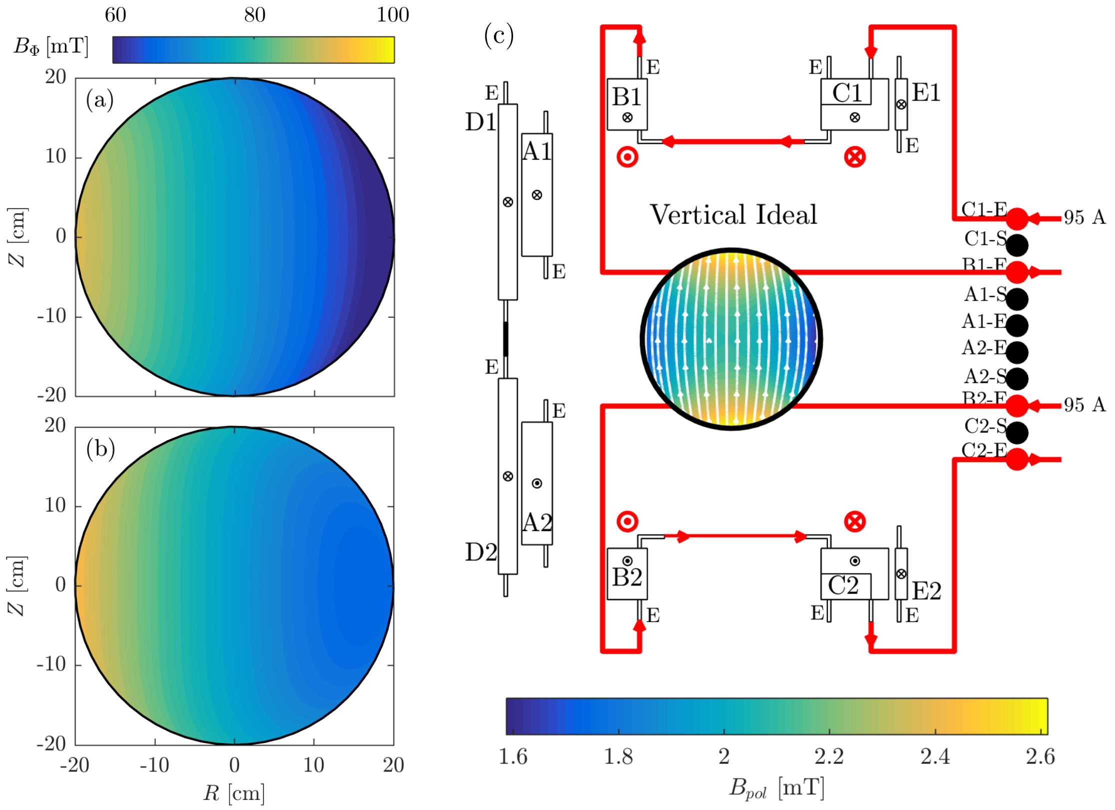

Figure 4.1 – The toroidal magnetic field strength B_Φ in our settings is shown across the poloidal cross section for a toroidal location between adjacent field coils in (a), and in the plane of a field-coil in (b). The variations towards the LFS, commonly known as field 'ripple', are of limited consequence to the fast ions propagating and are therefore neglected here. In (c) direction and field-strength of the poloidal magnetic field B_{pol} is shown, along with the present vertical field coils and their currents. No currents are fed to the supplementary E-coils or the central solenoid A-coils. While the variations in both field components are small near the centre of the cross-section, they do affect the local magnetic pitch angle. All related quantities are thus often indicated as approximate.

HEXTIP on the type of conclusions one can draw to complement or prepare more demanding studies with GBS in the future.

4.2 Incorporating HEXTIP measurements

As outlined in Sec. 2.2, previous studies on CAS-blobs and with FRIPLE have shown that at least statistically, the gradients of V_f can provide a consistent basis for the computation of electric fields. Thus we utilize time-resolved V_f measurements across the poloidal plane from at least one array of HEXTIP, available at intervals of $4\,\mu$s during a shot of ≈ 1 s duration. Since the trajectories of the fast ions are integrated over their full orbits of $\approx 5.3\,\mu$s duration, the V_f time-series samples required for the integration of each injected bunch of tracers are interpolated onto a time-resolution of typically $\Delta\tau = 0.1\,\mu$s during propagation. Some studies with a higher time-resolution of $\Delta\tau = 0.05\,\mu$s were performed as well, but only negligible differences in the statistics of the fast ion trajectories could be discerned.

Within the area covered by the probes of HEXTIP, a 2D floating potential profile of 1 mm resolution is produced using natural neighbour interpolation for each τ_i during the propagation of each injected bunch, as shown near HEXTIP in Fig. 4.2. With a typical time-of-flight $\approx \{56, 36\}\,\mu$s for tracers with $E = 30$ eV and $E = 70$ eV, respectively, over $D \approx 171$ cm, this corresponds to $N_\tau \approx \{560, 360\}$ interpolations for each of the ≈ 4000 injected bunches. Fully recalculated interpolations in MATLAB at each instant would augment run-times by ~ 90 h. However, the geometry of the interpolations remains constant over all instances. Therefore, the specific indices and weights for the natural neighbours of all query-points are pre-calculated from the appropriate voronoi tessellations with the HEXTIP probe positions, and stored as constant arrays. Thus, each interpolation can be reduced to a simple vector operation and sum, shortening the allocated run-time by factor of ×20. Furthermore, should the propagation times of consecutively injected bunches overlap, only the interpolations for new τ_i are re-calculated.

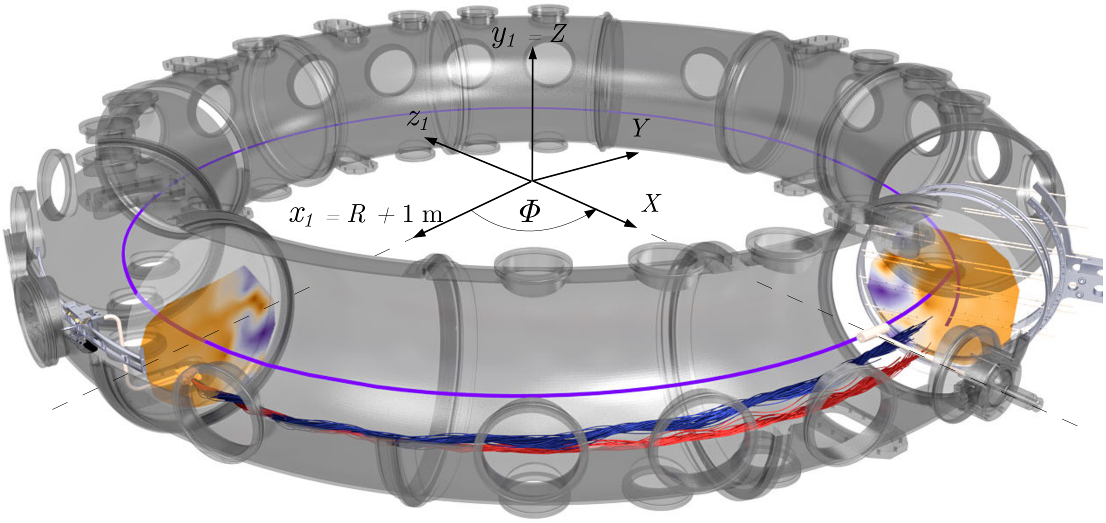

Figure 4.2 – Illustration of the projection of V_f profiles interpolated on HEXTIP (right) along magnetic field lines (purple) to a different toroidal location (left), here near the fast ion source. The profiles appear accordingly similar where the field-line intersects them. Note furthermore, that due to the increase in magnetic pitch angle towards the LFS, the projected profile appears lowered further there. Again, fast ion trajectories are shown in red for $E = 30$ eV and in blue for $E = 70$ eV and have been obtained with the presented tracer. The static Cartesian coordinate system (X, Y, Z) used by the Boris-algorithm is indicated in the centre, along with the rotated coordinate system (x_1, y_1, z_1) used to project V_f and calculate the electric fields. Both are right-handed, with a counter-clockwise rotation angle Φ. We choose $\Phi = 0$ on the X-axis to lie in the detector plane.

As detailed in Sec. 2.1, field-aligned electrostatic turbulence is observed in the settings investigated here. But albeit field-aligned, the interpolated potential profiles on the poloidal plane of HEXTIP are not simultaneously representative of the plasma along the full trajectory of the tracer particles. To obtain a better approximation at another toroidal location, field-lines are traced from the local poloidal plane (resolved at likewise 1 mm) onto the HEXTIP plane, and the floating potential value of each field-line calculated by 2D linear interpolation on the HEXTIP V_f profile, as illustrated near the fast ion source in Fig. 4.2. The limited statistical impact of neglecting fluctuations in plasma temperature on the ultimately derived E×B flows has been discussed in Sec. 2.2. Of course, such a field-line calculation at each τ_i is again far too computationally demanding. Therefore, the indices and weights for the interpolation of the V_f of each field-line are again pre-calculated and stored as constant arrays, so that they are executable with the same efficiency as the natural neighbour interpolations described above. However, these indices and weights depend on the specific toroidal location of interest, so that a larger array is required if the toroidal direction is to be well-resolved.

The appropriate toroidal location during the propagation of a bunch of tracers is determined by the elapsed time-of-flight τ_i, i.e. by approximating all toroidal locations by a local mean for the purpose of the local potential calculation. The necessary field-line projection is thus carried out once at each τ_i for each bunch, requiring up to N_τ sets of interpolation indices and weights to be readily stored for different field-lines. The Boris-algorithm iterates on the exact position and velocity for each tracer, showing that mainly due to an initial spread of injection energies and angles, the toroidal velocities of the tracers is approximately Gaussian distributed. However, even at the final τ_i, when the toroidal mean position of the particle distribution is crossing the detector plane, ≈ 95% of the tracers' toroidal positions are still found within ±20 cm of their mean location. Given a magnetic pitch angle of $\theta \approx 1.5°$, we find up to ≈ 2.5 mm vertical offsets in the field-line position for the 1σ majority of the tracers. It furthermore reduces approximately linearly towards zero for lower τ_i. Therefore, this offset in projecting the V_f profile for different tracers is deemed statistically acceptable for the majority of the integrated trajectories.

The local profiles of the electric field in the x_1 and y_1 direction are calculated for each τ_i through a 4th order central difference gradients on the interpolated and projected V_f profiles, as illustrated in Fig. 4.3. While no artifacts due to the 1 mm resolutions or projections are apparent, it is clear that the strongest values and gradients, e.g. of the vertical electric field in (b), are centred on the projected probe locations of HEXTIP. The peaks of density and potential measurements tending to be centred on the probe locations is a well-known limitation of this diagnostic, so that such artifacts in the profiles are expected. Smaller structures especially can appear to jump between probes or completely fail to be resolved [160]. While it is still deemed the dominant source of uncertainty and statistical errors in the tracing algorithm, a few factors mitigate ensuing issues.

Firstly, the CS-analysis in the preceding chapter strongly indicates that larger, well-resolved plasma structures are responsible for the dominant motion of the fast ion beam, especially towards the locations where the strongest intermittency is measured. Since we are ultimately

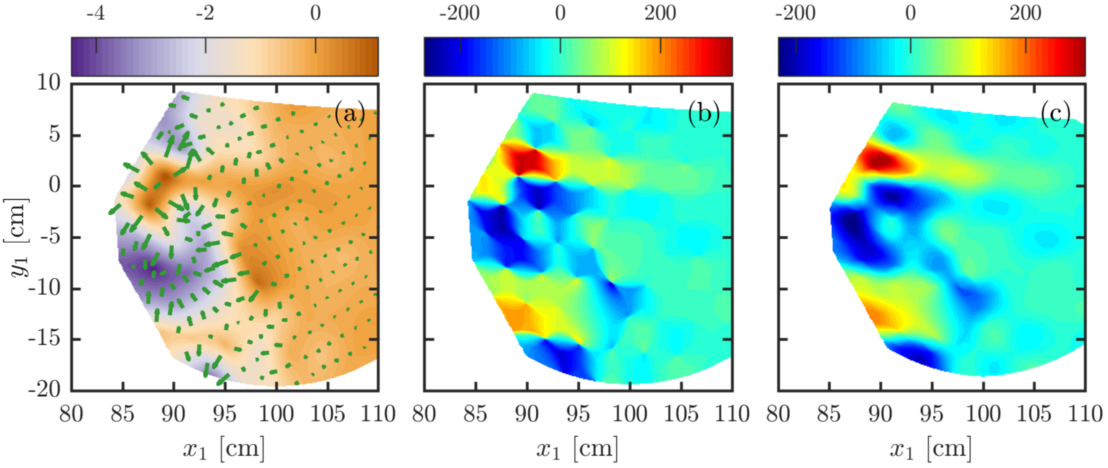

Figure 4.3 – (a) Interpolated and field-line projected instantaneous V_f profile (in V), as shown on the left in Fig. 4.2. The green arrows indicate the locally calculated electric fields, perpendicular to the contours. In (b) the vertical electric field component (in $\mathrm{V\,m^{-1}}$) is shown, with clearly dominant variations near the peaks of the potential profile at the projected probe locations of HEXTIP. Such deviations are alleviated in (c), showing the gyro-averaged vertical electric field, for an assumed gyro-radius of 7 mm.

most interested in this specific behavior and the generation of the observed time-series peaks, unresolved smaller structures may not be crucial for the assessment. The underlying reason is that, secondly, the trajectories of fast ions average over small structures, and thus also over any local deviations in the electric fields. The gyro-averaged electric fields shown in Fig. 4.3(c) show indeed a clear reduction of the artifacts seen in (b). Moreover, due to their vertical drifts, fast ions at later τ_i have propagated at varying distances of HEXTIP probe locations, so that related over- and under-estimates of the local fields can again average to some degree over their trajectory. As established before [104, 103], both gyro- and drift-averaging effects should be more important, and in this case thus more beneficial, to the treatment of tracers with higher injection energies.

It should be mentioned that since there is no uniquely defined approach to finding gradients on irregular grids, other methods for the calculation of the electric fields have been tried. Although e.g. Shepard's method [181] results in electric fields that feature much less distinctive peaks near the probe-positions, they effectively reduce the resolution of HEXTIP even further as each gradient point is based on a weighted average of the V_f values of multiple surrounding probes. This obfuscates the shape and propagation of all but the very largest structures and the calculated fields are clearly no longer perpendicular to the interpolated floating potential contours.

4.3 Time-average cross-field transport

In studies with GBS, the amplitude of simulated plasma potential fluctuations was weighted by a function along the major radius R (here x_1) [104, 136], and the amplitude of the extracted vertical electric fields in some cases [136] scaled again by a constant to match experimental measurements with FRIPLE. While such a scaling of the fields extracted from HEXTIP of the order of ×2 appears again necessary compared to FRIPLE, the present irregularities near the HEXTIP probe positions hinder a more detailed comparison. Furthermore, different scaling factors appear appropriate towards the HFS and LFS, i.e. towards the interchange mode or further across the blob-dominated region respectively. Thus, the situation would have to be re-examined if one were to change the fast ion injection position e.g. to investigate statistical variations between these different environments.

Since the focus of this numerical investigation will be the behaviour of the fast ion beam at a given instant, we therefore instead use the time-average fast ion beam to determine the most appropriate scaling factor E_f in our specific settings. The evolution of the horizontal variance of the time-average beam as a function of propagation time is matched to the results from GBS (see Sec. 2.5) for both the 30 eV case and the 70 eV case individually. For the fitting of their transport exponents, the corresponding variance is defined based on the displacements of the tracer particles, so that the results are not offset by the spatial distribution of the initial particle positions. While one could choose a point-like injection, previous studies used Gaussian distributions to more accurately model the aperture size of the fast ion source [136]. However, we select larger uniform distributions with a width of 1.2 cm along x_1 and 14 cm along y_1, centered in the middle of the poloidal cross-section, to further average any dependence of the results on the initial distance from HEXTIP probe positions.

The remaining initial conditions correspond to those of the most pertinent cases in GBS [103, 136]. The injection energy is normally distributed with a mean of $E = \{30, 70\}$ eV and a standard deviation of 5% of these values. Two injection angles are set, with $\delta_1 = -0.1$ rad corresponding to the average vertical angle with the toroidal direction $-z_1$, and $\delta_2 = \pm 0.1$ rad taken as the average horizontal angle to the same axis. The second angle is defined as positive for injection towards the HFS. Since we should have $\delta_2 \approx 0$ in the experimental setting, the average is set to a positive or negative value primarily to assess the impact of systematic variations during particle injection on our results. Again, both angles are normally distributed with a standard deviation of 0.08 rad, to represent uncertainties and the impact of stray fields during injection. This results in a significant initial spread in parallel velocity $v_{||}$ and also Larmor radii ρ_L, as shown for both ion energies in Fig. 4.4. Based on the mean values of these distributions, the 'realistic' fast ion parameters in Tab. 2.2 were calculated.

4.3.1 Comparison to experiments and GBS

To obtain the time-average fast ion distribution for each τ_i, bunches of $N_p = 400$ particles are injected at 50 μs intervals over a duration of 200 ms. At each τ_i, their displacements (x_1, y_1)

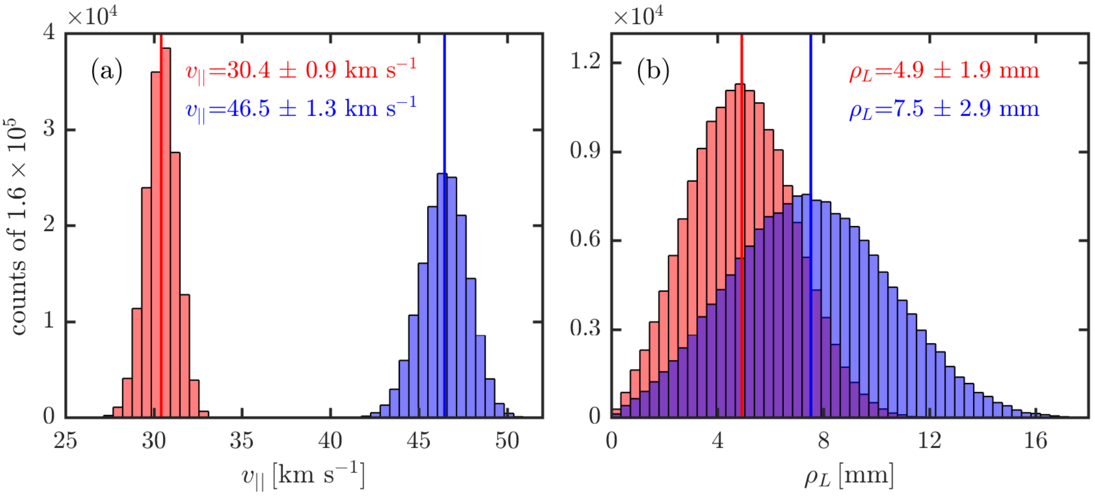

Figure 4.4 – In (a) the initial distributions of velocities $v_{||}$ parallel to $\vec{B}$ is shown for $N_p = 1.6 \times 10^5$ tracers with the injection angles $|\delta_1| = |\delta_2| = 0.1 \pm 0.08$ rad. Red indicates an injection energy of $E = 30 \pm 1.5$ eV, blue the case of $E = 70 \pm 3.5$ eV. With velocities perpendicular to $\vec{B}$ of thus typically ≈ 10% of $v_{||}$, the resulting distributions of Larmor-radii are shown in (b). The lines indicate the mean-values of the ditributions, as given together with their standard deviation as uncertainty.

are calculated from the Cartesian (X, Y, Z) coordinates in the Boris-algorithm and binned at 1 mm resolution. Only a negligible number of tracers ever propagates beyond the limits of the projected interpolation region of the floating potential, and is declared lost. Figure 4.5 shows the variance of the binned fast ion beam along x_1, i.e. the cross-field direction R in our case. For both the 30 eV case in (a) and the 70 eV case in (b), the results appear in good qualitative agreement with those from GBS, as retrieved from Fig. 2.15 [103] and shown in a darker shade here.

However, there is a difference in gyro-frequency between both sets of results, that is likely related to slight differences in the prescribed magnetic fields and the field chosen to calculate the average gyro-frequency Ω. Furthermore, if ions were to propagate into systematically different radial positions they would experience a different average magnetic field strength along their trajectories. Therefore, the agreement between both sets of results is not readily quantified e.g. by the R^2 or the χ^2 between the curves (see App. A). Instead, we choose to take the differences between the values of the closest local maxima into account, mostly since the calculation of the shown transport exponents is based on these points. These differences are then divided by their appropriate statistical errors, before taking the squared sum. The requisite error estimates include both, the upper and lower bound on the GBS results, as well as the ≈ 15 % uncertainty on the current results, estimated e.g. by changing δ_2. Since we wish to later investigate the instantaneous beam during the latest shown propagation times, corresponding to most tracers reaching $D \approx 171$ cm, the fit of the last maximum is prioritized. In the 30 eV case, the shown result is a compromise between the best final and

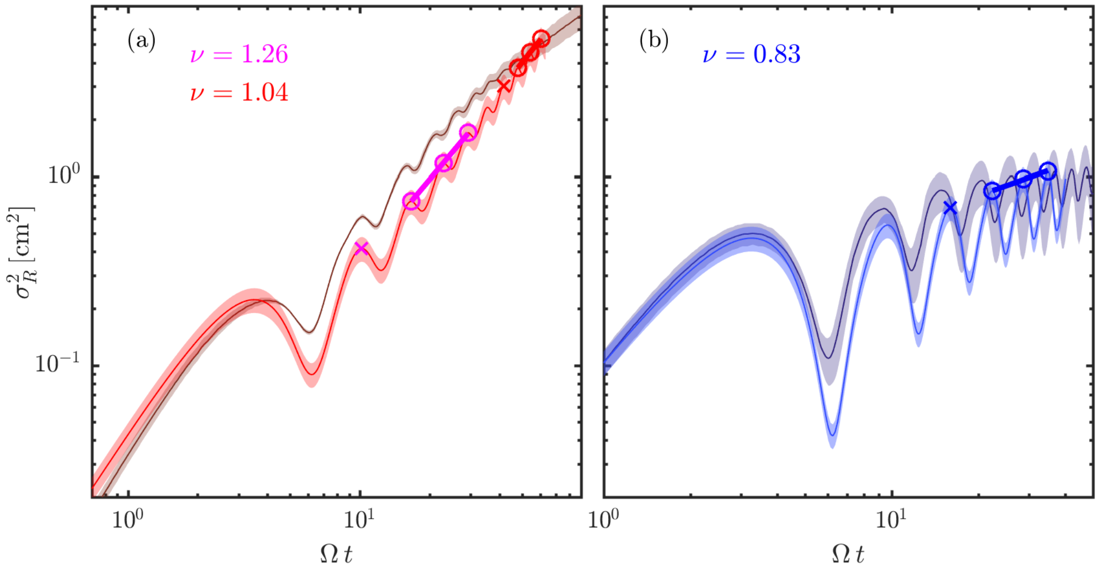

Figure 4.5 – Evolution of the variance of the horizontal displacement of the tracers as a function of propagation time, averaged over all injected bunches for $E = 30\,\mathrm{eV}$ in (a) and $E = 70\,\mathrm{eV}$ in (b). The graphs shown correspond to the best match with the previous results (darker shaded) based on GBS, as specified in the text. The points used for extracting the displayed transport exponents from the fitting the displayed slopes (bold), are shown in magenta, red and blue for the super-, quasi- and subdiffusive transport regimes respectively.

overall agreements, and achieved for $\delta_1 = \delta_2 = -0.1\,\mathrm{rad}$ and $E_f \approx 2.3$. In the 70 eV case, both the best overall and final fit are found simultaneously for $\delta_2 = +0.1\,\mathrm{rad} = -\delta_1$ and $E_f \approx 1.6$.

The difference between the values for E_f between both energies are likely related to the different degrees of gyro- and drift averaging especially over structures of smaller scales. The transport induced by these unresolved features is likely to play a role especially during early τ_i, prompting stronger deviations between different trajectories even before the fast ions propagate over the scale of larger structures. Lacking these small scale contributions, the parameter E_f is to compensate their role by enhancing the fields of the resolved structures by a different degree for both ion energies. Since small scale structures are found to play a lesser role in the 70 eV case, it is reasonable to assume that this leads to a lower appropriate value of E_f. Later during transport, once the beams have spread across few cm, we however find an over-estimate of the continued radial spreading.

Nonetheless, the principal non-diffusive transport regimes of the fast ions are well recovered by fitting the slope of the maxima in Fig. 4.5. As before, the variance and propagation times fitted (circles) in each transport phase were reduced by the values at the first maximum of said phase (crosses), treated as the respective initial condition. The details for all such fits are discussed in Ref. [136] and generalized more formally in Ch. 7. It is however important to note that any specific values of fitted transport exponents should be treated as local averages in propagation time. Should we choose, for instance, to include the second maximum into the fit in (b), the transport exponent would drop to $\nu \approx 0.6$. Including the first maximum into the superdiffusive fit would increase the transport exponent to $\nu \approx 1.5$. While the principal transport regimes thus remain through most of the indicated fits, their particular transport exponents should be regarded rather as transient at most scales, in both the current and the previous results from GBS [103, 136].

4.4 Average vs. single bunch profiles

To assess the behaviour of a fast ion beam, we now use normally distributed initial positions in x_1 and y_1, with standard deviations of 1.2 mm, centered at $x_1 = 0$ and $y_1 = -10$ cm. While this does change e.g. the evolution of σ_R^2 compared to Fig. 4.5, deviations approximately lie within the indicated uncertainties and the principal transport regimes are mostly unaffected. Figure 4.6 shows examples of the binned positions of the tracers of all injected bunches, at the indicated propagation times. They correspond to the end of ballistic transport in (a,d), early super- and subdiffusive transport in (b) and (e) respectively, and the time when most tracers are crossing the detector plane at $D \approx 171$ cm in (c,f).

Neglecting at first the described toroidal time-of-flight dispersion of the tracers, these profiles $J(x_1, y_1, \tau_i)$ can serve as an approximation of the time-average fast ion profiles $\mu_{\mathcal{J}}(R, Z)$ as shown in Sec. 3.2. For comparison, they are therefore likewise normalized such that they show the local density of a supposed $I_{av} = 2.85\,\mu$A of injected fast ion current. Furthermore, the raw data is convolved with a circular box kernel with 8 mm diameter to account for the finite resolution of the GEA detector. Note the good qualitative agreement of the shape and densities between Figs. 3.2,3.4(c) and Fig. 4.6(c,f) respectively, owing to the choice of initial conditions and E_f. Only the vertical position y_1 was chosen ≈ 5 cm higher in the tracer, further from the boundary of the interpolation region of V_f.

To finally investigate how much smaller the instantaneous fast ion beam is compared to the time-average, we firstly compare the size of single bunches $j(x_1, y_1, \tau_i)$ of injected tracers to the presented average over all bunches $J(x_1, y_1, \tau_i)$. To ensure a significant sample size, the number of injected particles was augmented to $N_p = 160,000$ for every bunch, still injected at time intervals of $50\,\mu$s over a duration of 200 ms. Due to the optimized handling of vector-operations in MATLAB, this increases the run-time of the tracer algorithm only from ≈ 10 h to ≈ 50 h. The variances of the particle positions of every injected bunch σ_j^2 is calculated along x_1 and y_1 at each τ_i and stored.

Figure 4.7(a,b) shows the $\sigma_j(\tau)$ for both ion energies along both directions, averaged over all bunches. The τ when most tracers arrive at the detector distance $D = 171$ cm are given in cyan for $E = 70$ eV and magenta for $E = 30$ eV. The dashed lines show intervals in τ that correspond to up to ≈ 15 cm of spread among the tracers along D at these times. Conversely, most tracers crossing the detector plane at any given instant should thus be contained within these indicated intervals of propagation time τ. Certain fundamental differences in the behaviour of $j(x_1, y_1)$ become clear between both energies. Especially the horizontal width in (a) is still

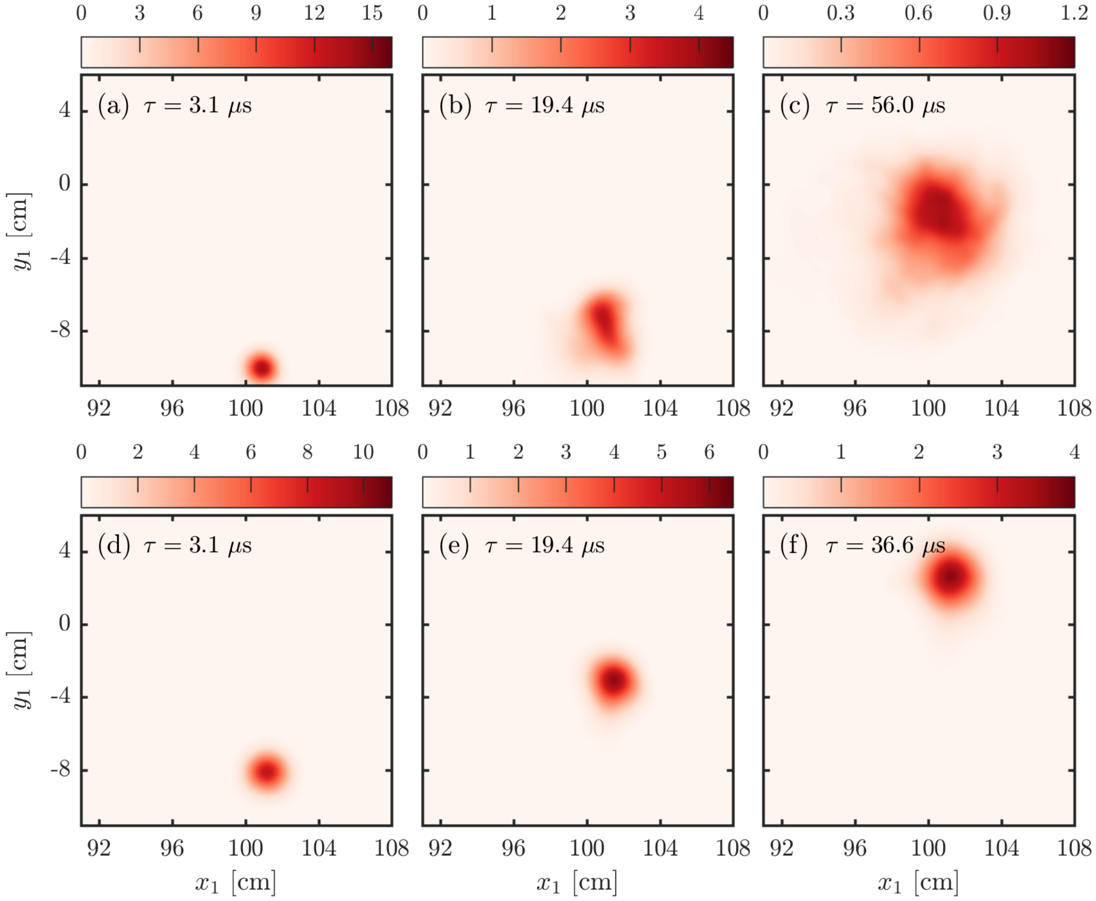

Figure 4.6 – Profiles $J(x_1, y_1, \tau_i)$ in mA m^{-2}, based on binning all injected tracer bunches for $E = 30$ eV (a-c) and $E = 70$ eV (d-f) at the given propagation times τ, as proxies for time-averaged fast ion profiles in Ch. 3, pending deviations from time-of-flight dispersion of the tracers.

dominated by the gyro-phase of the fast ions in the 70 eV case, whereas the bunches for the 30 eV case are often more strongly affected by the turbulent electric fields. The shape of $j(x_1, y_1)$ at a given τ can thus vary, depending on which gyro-phase it belongs to. Tracers that arrive simultaneously at the given detector location can represent an average over many possible gyro-phases, and thus yield yet different profiles (see Fig. 4.9). Near detection, the average widths of the bunches are however similar between both energies however. Nonetheless, 70 eV bunches spread more quickly in the vertical direction due to their overall higher magnetic drift velocities (see Tab. 2.2). Therefore it is predominantly 30 eV ions for which we still find some contribution with $\sigma_j < 4$ mm, that can result in the most dominant observed peak current densities. This is further explored in the context of skewness measurements in the following section and Sec. 5.4.

In Fig. 4.7(c,d), we show the ratios between σ_j in the x_1 and y_1 directions and the respective standard deviation of the $J(x_1, y_1, \tau_i)$, denoted $\sigma_J(\tau)$. The bands are again defined by the 1σ

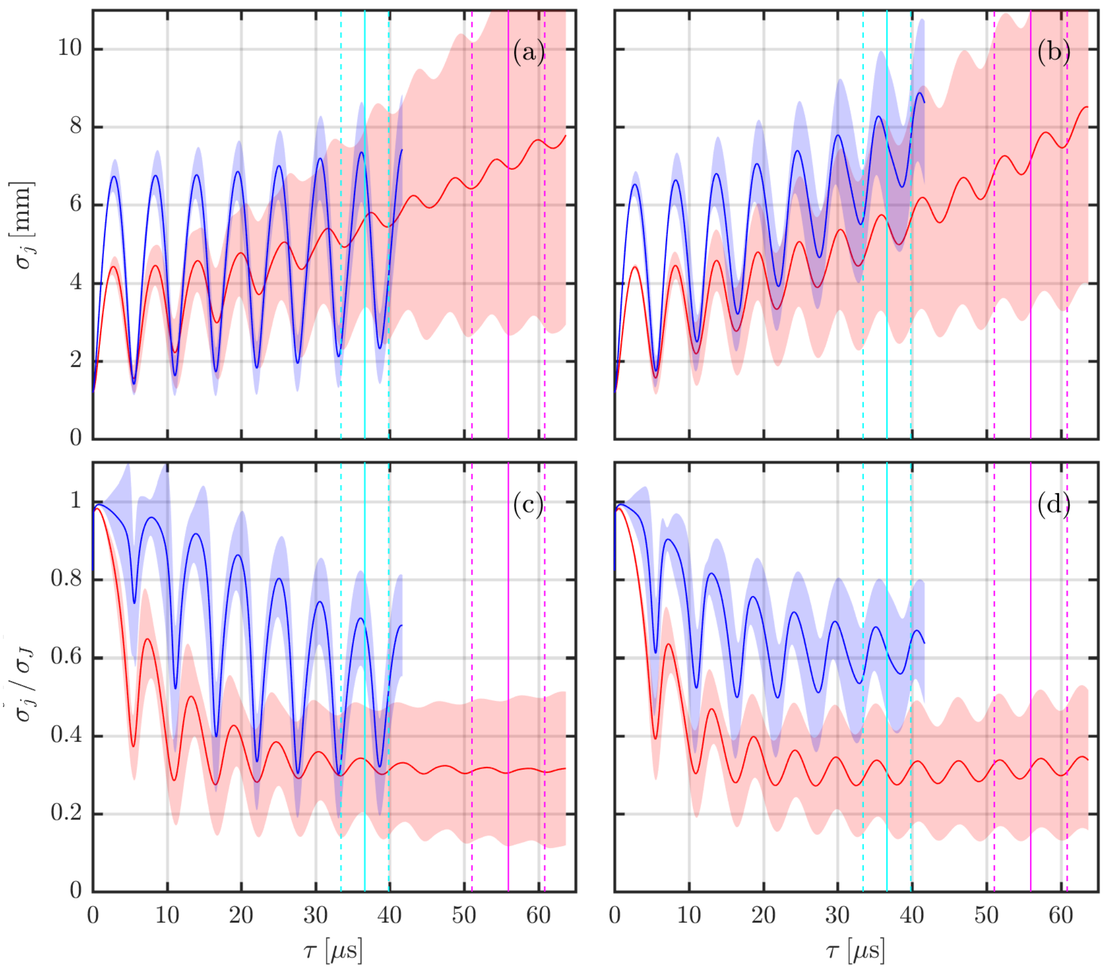

Figure 4.7 – The average width (standard deviation) σ_j of the single bunch profiles $j(x_1, y_1)$ is shown along x_1 and y_1 in (a) and (b) respectively. The results for the 30 eV case are shown in red, the 70 eV case in blue. The bands indicate the 1σ width of the generally non-Gaussian distributions of σ_j for each τ. In (c) and (d) the ratio of σ_j with the standard deviation σ_J of the average bunch profiles (see Fig. 4.6) is shown, again along x_1 and y_1 respectively. The intervals of τ relevant to the detector plane at $D = 171$ cm are shown in cyan and magenta as described in the text.

interval of the distributions of $\sigma_j(\tau)$. The single bunches $j(x_1, y_1, \tau_i)$ near detection appear on average ≈ ×3 and ≈ ×1.7 smaller than their total average $J(x_1, y_1, \tau_i)$ in the 30 eV and the 70 eV case, respectively. This again points toward a more strongly meandering ion beam for lower ion energies, which will be described by an analytical model in Sec. 5.3.

To better illustrate the shapes and locations of $j(x_1, y_1, \tau_i)$, the positions of the tracers at their final τ_i are binned for 300 such bunches. Figures 4.8,4.9(a) allow direct comparisons with the total averages for $E = \{30, 70\}$ eV, respectively, as shown in Fig. 4.6(c,f) for a few selected examples. The binned $j(x_1, y_1)$ are scaled to show densities for $I_{av} = 2.85\,\mu$A of total fast ion current, and convolved with the kernel representing the GEA aperture. Note that the peak

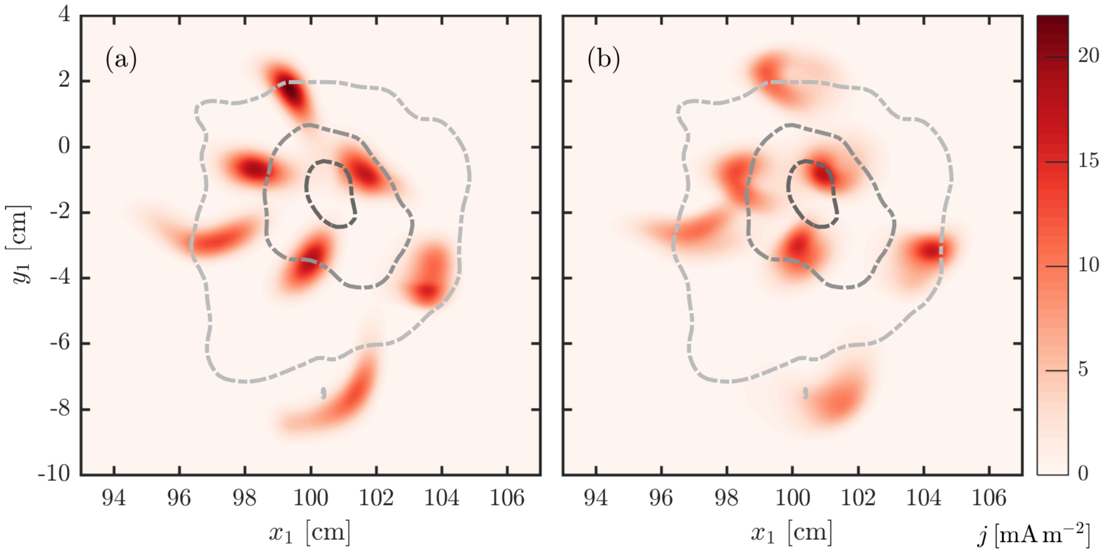

Figure 4.8 – Profiles of 7 examples of single bunches $j(x_1, y_1)$ for $E = 30\,\text{eV}$, binned at a single $\tau_i = 56\,\mu\text{s}$ in (a) or binned with the synthetic diagnostic at the corresponding $D = 171\,\text{cm}$ in (b), across all relevant τ. The gray contours show the average bunch profile from Fig. 4.6(c), at its 10%, 50% and 90% contours.

observed values on the color-scales (j_p) are in generally good agreement with the time-series peaks in Ch. 3, pending differences in the total current.

Again, all bunch profiles are clearly consistent with the expected picture of a smaller, more concentrated instantaneous fast ion beam that forms the time-average profiles at the detector location through its meandering motion while generating the observed intermittent peaks in the detected signal, as expected from Fig. 4.7. The shapes of individual profiles vary greatly, from circular to streak-like, especially for $E = 30\,\text{eV}$. Nonetheless, many of the most peaked examples approximate unimodal and only slightly elliptical shapes.

The profiles in Figs. 4.8,4.9(b) are computed using a synthetic diagnostic plane at $D = 171\,\text{cm}$. The positions of the tracers are not binned at one given τ_i, but as they each cross this toroidal position, before being convolved with the GEA aperture kernel. If each $j(x_1, y_1, \tau_i)$ remained constant as its tracers cross the detector plane, there would be no discernible difference to the profiles in (a). However, in the 30 eV case, the synthetic diagnostic profiles appear on average less peaked and more spread out, as the bunch is continuously being deflected and sometimes deformed in response to the turbulent electric fields. This effect is expected to be weaker in the 70 eV case, due to slower and more localized responses to the turbulent fields as found in Sec. 3.3. Conversely, we indeed find the synthetic diagnostic profiles in (b) to be on average more peaked than their counterparts in (a). This is likely due to the gyro-phase effects as seen in Fig. 4.7(a,b), that dominate the widths of these profiles. Focusing on the stronger horizontal variations in (a), one would expect the average width over the interval τ relevant to the synthetic diagnostic (marked in cyan) to be only ≈ 70% of the width at the central τ_i

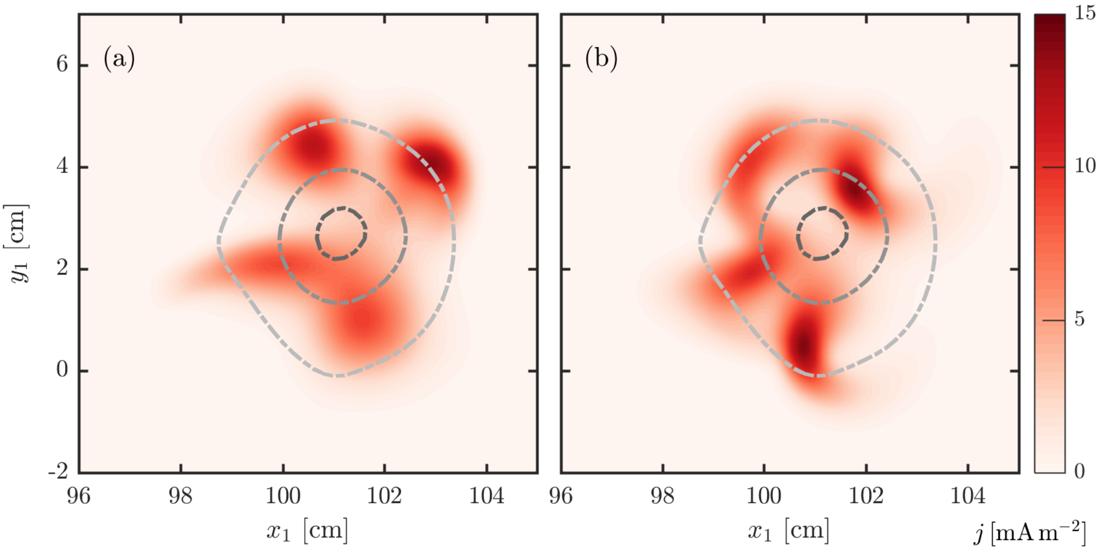

Figure 4.9 – Profiles of 4 examples of single bunches $j(x_1, y_1)$ for $E = 70\,\text{eV}$, binned at a single $\tau_i = 36.6\,\mu\text{s}$ in (a) or binned with the synthetic diagnostic at the corresponding $D = 171\,\text{cm}$ in (b). The gray contours show the average bunch profile from Fig. 4.6(f), at its 10%, 50% and 90% contours.

used for binning the profiles in Fig. 4.9(a). Reciprocally, the ≈ 40% increase in the observed densities in (b) concurs with these expectations.

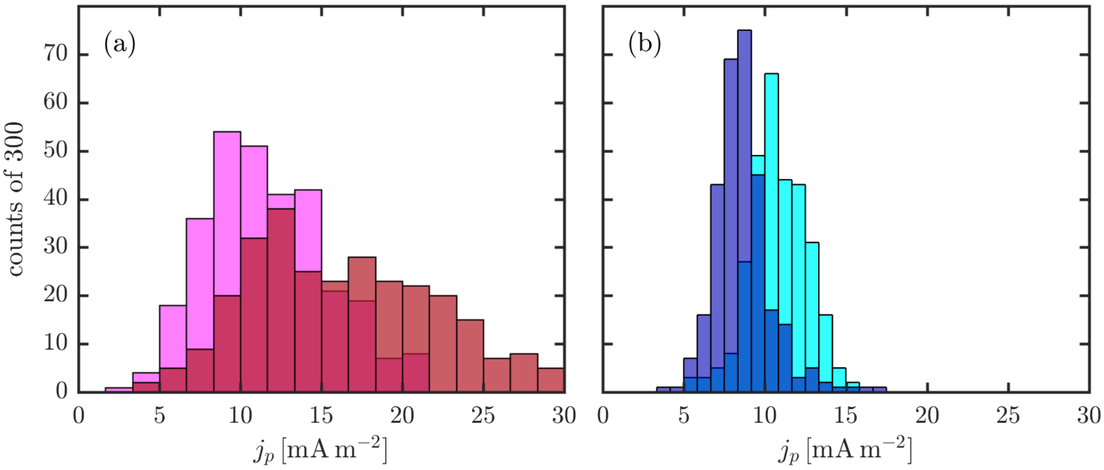

Figure 4.10 – Histograms of the peak detected values j_p of the profiles $j(x_1, y_1)$, for $E = 30\,\text{eV}$ and $E = 70\,\text{eV}$ in (a) and (b), respectively. Results for the profiles binned at a single τ_i in Fig. 4.8,4.9(a) are shown in the darker red and blue respectively, while those for binning with the synthetic diagnostic are shown in magenta and cyan.

To succinctly assess the statistical differences between the profiles binned at a single τ_i and those binned with the synthetic diagnostic at $D = 171\,\text{cm}$, Fig. 4.10 shows the histograms of the peak values of $j(x_1, y_1)$, designated j_p, for all 300 recorded profiles in the 30 eV case and the 70 eV case in (a) and (b), respectively. They clearly reflect the different behaviors between the two energies as described above, while the given range of values in the 30 eV case fit the approximate magnitudes of the peaks observed in Fig. 3.1(a,c), pending differences in total fast ion current. The values in the 70 eV case appear at least ≈ 30% too low even then, possibly due to a reduced effective detector area for the larger Larmor radii of these ions, or a systematic numerical over-estimate of their spreading. Indeed, a truly continuous tracer injection would probably impart more tracers in a gyro-phase with a more concentrated beam into the profiles in Fig. 4.9(b), raising the average detected j_p.

4.5 Synthetic time-series

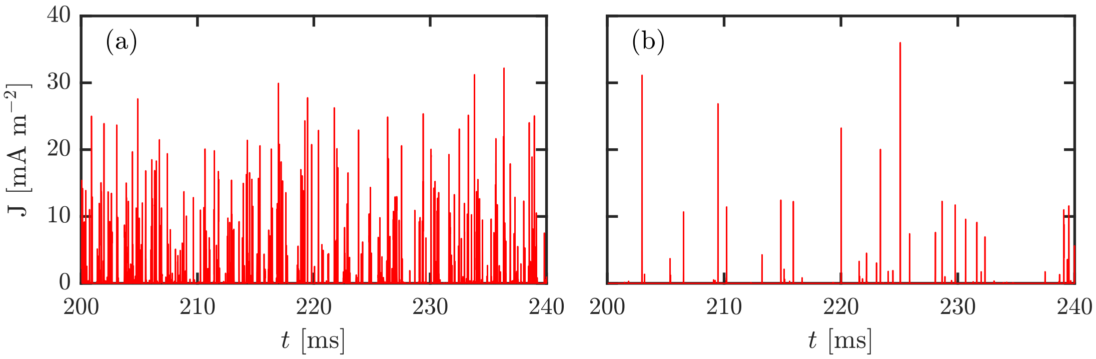

Figure 4.11 – Examples of synthetic fast ion time series, obtained as described in the text. In (a), we show the time series with the highest time-average, and in (b) the highest skewness, after including the noise contribution. The respective maxima of $\mu_{\mathcal{J}} = 0.79\,\mathrm{mA\,m^{-2}}$ and $\gamma_S = 8.9$ can be read in Fig. 4.12, where their positions are indicated by green crosses.

This leads us to the key point of generating synthetic time-series to analyze their statistics in comparison to those found in the preceding chapter. In any case, their treatment demands significant computational time, as one needs to inject tracer bunches at the very least every $4\,\mu$s, given by the original time-resolution of the acquisition systems of HEXTIP and other LPs. Currently, this requires ≈ 48 h of run-time for every 16 ms of synthetic time-series. In the simplest case, we treat each bunch of tracers as arriving simultaneously at the diagnostic at one given τ_i, similarly to the profiles $j(x_1, y_1)$ shown in Fig. 4.8,4.9(a). However, we do not bin their locations in this case, but calculate their distance from a given set of detector locations, simply due to memory constraints. For each tracer within $\frac{d}{2} = 4\,$mm of such a location, the corresponding value of the time-series at this instant is augmented by one. The time-series are in the end re-scaled to the given total current $I_{av} = 2.85\,\mu$A corresponding to the full number of tracers $N_p = 1.6 \times 10^5$. Examples generated with $E = 30\,$eV are shown in Fig. 4.11. The synthetic mean-profile generated from such a set-up for is shown in Fig. 4.12(a), similar to the profile in Fig. 4.6(c). However, an injection position at $y_1 = -14.5\,$cm was chosen here, in concordance with the experimental set-up. Similarly, the average injection angle was set to $\delta_2 = 0$ along the horizontal and $\delta_1 = +0.1\,$rad along the vertical. The electric field scaling factor

$E_f = 2.4$ yielded a slightly wider profile, but with overall similar statistics compared to the above, as partly published in [109].

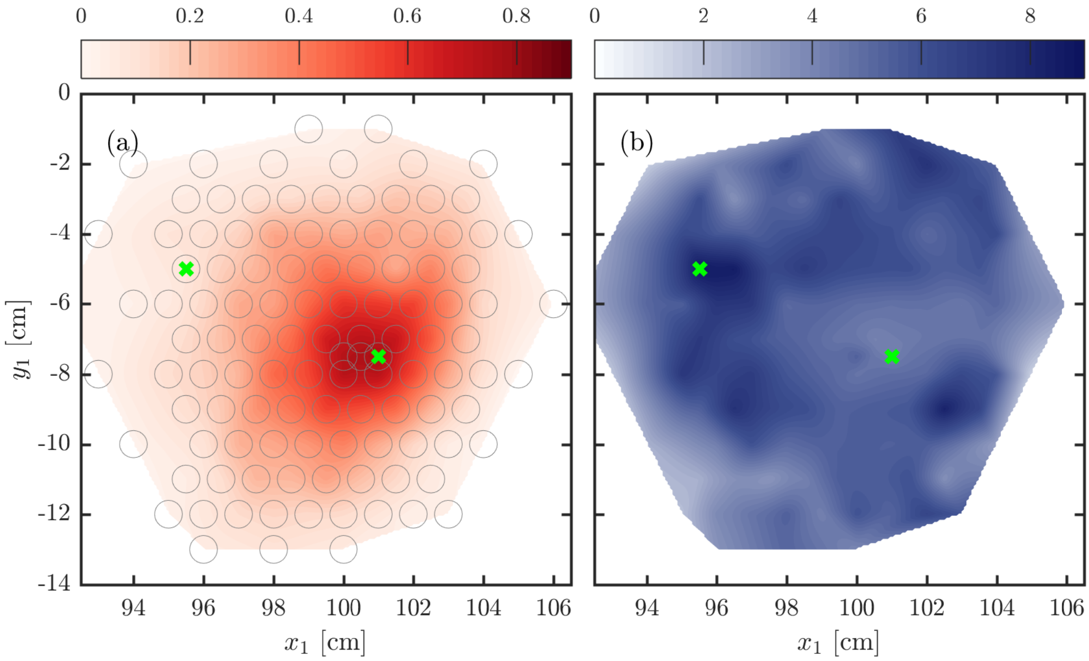

Figure 4.12 – In (a), the mean-profile interpolated from the time-average of 46 ms long synthetic time-series is shown. The 116 detector locations and the relevant aperture size are shown by the gray circles. In (b) the values of their skewness $\gamma_{\mathcal{S}}$ are interpolated, with average noise contributions added as specified in the text. Both profiles would likely become smoother for longer durations of the time-series, but already feature a distinct resemblance to their experimental counterparts in Fig. 3.2(c,f), pending increased noise towards the HFS. The green crosses indicate the positions where the time-series shown in Fig. 4.11 were generated.

To generate the on-phase skewness ($\gamma_{\mathcal{S}}$) profile in Fig. 4.12(b), from the skewness of the time-series ($\gamma_{\mathcal{J}}$), the noise contribution is added according to Eq. 3.4. We choose $\sigma_N = 1\,\mathrm{mA\,m^{-2}}$ and $\gamma_{\mathcal{N}} = 1.3$ as typical values near the injection position along x_1. While the specific values for $\gamma_{\mathcal{S}}$ vary for different choices, we find good qualitative agreement with expectations from Sec. 3.2 and previous work, as the highest values of $\gamma_{\mathcal{S}}$ lie around the maximum of the synthetic mean-profile in (a). Furthermore, the maximum $\gamma_{\mathcal{S}} \approx 8.9$ is similar to the maximum found in Figs. 3.2(f) and 3.5 of $\gamma_{\mathcal{S}} \approx 7.9$, especially given the potential uncertainties of the injected current. However, especially since the noise contribution should diminish towards the LFS, the skewness maxima there are likely over-estimating the experimental results. Given the higher accessible values of j_p for this kind of profile as shown red in Fig. 4.10(a), compared to the time-series e.g. in Fig. 3.1(a,c), this is not entirely unexpected. However, the application of a planar synthetic diagnostic, resulting in a range of j_p shown in magenta may not necessarily yield better results in all cases. Since the integration time and time-resolution of the GEA is typically smaller than the up to $\approx 10\mu$s passage time of the bunch through the diagnostic plane, the observed spreading of the obtained profiles $j(x_1, y_1)$ and the diminished values of j_p in Fig.

4.10(a) are at least partially artificial. Furthermore, the application of this synthetic diagnostic for every bunch would increase the run-time of the tracer even further. However, especially in the 70 eV case, its necessity becomes evident as any j_p-distributions and thus the time-series skewness obtained as shown here would strongly depend on the specific gyro-phase of the tracer bunches at the final τ_i.

If we wish to appropriately account for the residual effects due to the simplified tracer detection conditions, one would be required to generate the synthetic time-series while injecting bunches at much shorter intervals than the given GEA time-resolution, ideally quasi-continuously at intervals near the integration time-step $\Delta\tau = 0.1\mu$s. Furthermore, the synthetic diagnostic would have to keep track of the absolute time-base at every τ_i for every bunch, so that multiple bunches contribute to the number of detected tracers at a given step in the time-series. Clearly, this would require a strong increase in computational resources, although e.g. the time needed for interpolations of the floating potential would be limited due to overlap between bunches, and the treatment of different time-series intervals can be run in parallel. For a better idea of scale, it should be pointed out that while keeping $N_p = 1.6 \times 10^5$ for good 2D resolution, with bunches injected at intervals of 0.1μs, we would effectively integrate one tracer trajectory for approximately every 4 actual ^{6}Li ions in TORPEX, assuming a total current of $1\,\mu$A.

With such substantial efforts required, one needs to weigh them against the potential improvements in the quality of the generated data. Especially given the assumptions, approximations and interpolations needed for obtaining the turbulent electric fields for the tracer, a better agreement with experiments than obtained here would seem in any case ostensibly difficult to justify quantitatively.

4.6 Conclusions and outlook

In this chapter, we have described the application of a full-orbit Monte-Carlo fast ion tracer, based on the Boris-algorithm. The strongest uncertainties in the statistics of the integrated fast ion trajectories are probably due to the interpolations employed to approximate the time-resolved turbulent electric fields from floating-potential measurements with HEXTIP. After scaling the fields and adopting similar initial conditions, good agreement between the non-diffusive spreading of the time-average fast ion beam, as an average over all bunches, was found in comparison to GBS and thus also to experimental measurements in current and previous studies [103, 136]. We then bin single bunches of tracers in the poloidal plane either at given propagation times or at a fixed detector distance. This clearly establishes the physical picture of an instantaneous fast ion beam, that generates larger time-average profiles through its meandering motion across the poloidal plane, which also leading to intermittent time-series. Certain key parameters of the meandering instantaneous beam have been estimated, such as its potential shapes, its width σ_j compared to that of the total average σ_J, and the distributions of detected current density peaks j_p. They will all be relevant for the application of an analytical model of the time-series skewness in the following chapter. It now also appears more clear, how the total and conditional averaged profiles in preceding sections are constructed, and we have the capacity to better formulate expectations for the envisaged use of multiple simultaneous detectors, as outlined in Sec. 2.4.3. The generated synthetic time-series yield similar for the mean- and skewness profiles compared to experiments in Sec. 3.2. Therefore, the presented tracer appears to be a qualitatively, and to a limited degree also quantitatively, useful tool for the statistical characterization of fast ion motion in the turbulent plasmas of TORPEX.

Instead of pursuing ever better time-resolutions and quantitative predictions, it seems more worthwhile to focus on some of the intrinsic advantages of this tracer for upcoming studies. For instance, it is straightforward to inject tracers only at time-indices retrieved by conditionally sampling any HEXTIP signal, or even the GEA. Using the floating potential data for these specific times, one can directly construct conditionally averaged synthetic profiles for comparison with experiments. Furthermore, one could directly observe how far the distributions of the bunches during these times deviate from the distributions observed without any condition.

Furthermore, changing the ion-species or the magnetic geometry inside TORPEX is a basic feature of this tracer, pending the availability of HEXTIP data. Initial tests for the characterization of the propagation of Li^+ ions in the vicinity of an X-point or of Ca^+ ions in the SMT have already begun. Of course, as detailed in the preceding sections, the parameters of the tracer, and especially the electric field scaling, will have to be adapted e.g. by comparisons of time-average measurements in experiments.

If more quantitatively accurate statistical simulations are required in a well-specified case, it would appear instructive to return to GBS, especially if small-scale structures are expected to play a distinctive role in the spreading of the fast ions. With single [168] and even double-null [180] configurations now available, the extensive benchmarking of GBS results against upcoming experiments on TORPEX will likely prove the most reliable basis for estimating local transport exponents, although an estimate on some general transport regimes could possibly be obtained from the tracer as shown here. The generation of synthetic time-series based on GBS results should be possible in the same way as outlined above, but would likely also face intrinsic challenges in terms of computational effort.

5 Analytical modeling

Based on the findings in the preceding chapters, we now introduce an analytical model for the prediction of intermittency in the local time-series generated by a meandering particle beam. This formalism originally presented in Ref. [109], allows to predict the skewness of such a time-series based on its time-average (mean) value. Only up to two basic parameters of the system need to be known, and are treated as free fit parameters here to illustrate the consistency between the predicted and measured skewness $\gamma_{\mathcal{S}}$ during the GEA on-phases for the profiles taken at $E = \{30, 70\}$ eV. Good agreement is found across all present non-diffusive transport regimes. Fluctuations in the injected fast ion current are confirmed as the most likely dominant source of remaining uncertainties. In the last section, we consider a simplified model of a highly concentrated meandering beam, resulting in time-series with only two values, alternating as the beam enters and leaves the detector area. Comparing the simplified form of the skewness $\gamma_{\mathcal{S},\mathcal{B}}$ in such a case with measurements of $\gamma_{\mathcal{S}}$ shows better agreement in the 30 eV case due to the on average smaller instantaneous beam profiles there (see Ch. 4). In our specific case, this can thus be seen as an indirect relative indicator for a time-series to belong to the super- to quasi-diffusive set of measurements. Most of the concepts and results of this chapter have been similarly published in Refs. [110] and [111].

5.1 The meandering fast ion beam

The basic elements of the analytical model describing the meandering beam profile are illustrated in Fig. 5.1. Since we wish to treat the observed distributions of particles across the poloidal plane at one given toroidal location based on the measurements in Ch. 3, we return to the coordinates $\mathbf{R} = (R, Z)$ for convenience. At a given detector location $\mathbf{R}_0$, the local time-average current density $J(\mathbf{R}_0)$ is given by the convolution of the current density profile at a given instant $j(\mathbf{R})$ with a PDF $f(\mathbf{R})$, which describes probability of finding $j(\mathbf{R})$ centred at any given position at any time. In this sense, $f(\mathbf{R} - \mathbf{R}_0)$ acts as the propagator of $j(\mathbf{R})$ towards $\mathbf{R}_0$ and is referred to as the 'displacement PDF' reflecting the statistics of the meandering motion

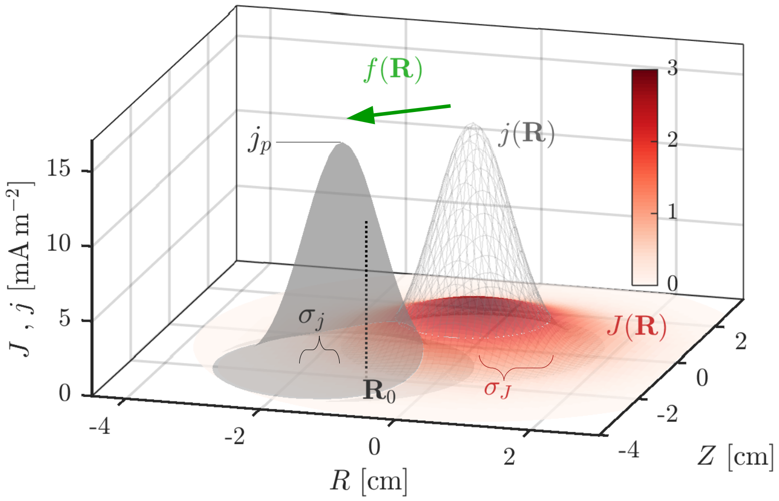

Figure 5.1 – Illustration of the key quantities and parameters used in the analytical model of the meandering fast ion beam, as described in the text.

of the fast ion beam. Through the symmetry of convolutions [182], we can likewise write

$$J(\mathbf{R}_0) = \int j(\mathbf{R} - \mathbf{R}_0)\, f(\mathbf{R})\, dR\, dZ \quad . \tag{5.1}$$

For simplicity, all distributions are assumed to be well-bounded and feature constant, and rotationally symmetric, unimodal shapes. Compared to Ref. [109], we have furthermore made the implicit assumption that the response function of the GEA detector at $\mathbf{R}_0$ is uniform across its aperture, by defining $J(\mathbf{R})$ and $j(\mathbf{R})$ as the corresponding current densities, consistent with the preceding chapters. Based on certain basic parameters of these distributions, like their standard deviations σ_J and σ_j or the peak value of the instantaneous profile j_p, we aim to describe the skewness of time-series measurements at any given measurement location. This is accomplished by finding expressions for the requisite moments of these measurements, that at an order q are defined by generalizing Eq. 5.1 to

$$J_q(\mathbf{R}_0) = \int j(\mathbf{R} - \mathbf{R}_0)^q\, f(\mathbf{R})\, dR\, dZ \quad , \tag{5.2}$$

where we identify $J_1(\mathbf{R}) = J(\mathbf{R}) = \mu_{\mathcal{J}}(\mathbf{R})$ as seen in Ch. 3. Specifically, we require the second and third order *central* moments $J_{C,2}$ and $J_{C,3}$ given in general by [182]

$$J_{C,2} = J_2 - J^2 \quad , \quad J_{C,3} = J_3 - 3JJ_2 + 2J^3 \quad , \tag{5.3}$$

to express the fast ion signal skewness $\gamma_{\mathcal{J}}$ as defined by [182]

$$\gamma_{\mathcal{J}} = \frac{J_{C,3}}{J_{C,2}^{3/2}} = \frac{J_3 - 3JJ_2 + 2J^3}{\left(J_2 - J^2\right)^{3/2}} \quad . \tag{5.4}$$

For practicality, we obtain an expression for the on-phase skewness $\gamma_{\mathcal{S}}$ again by adding the contribution of the local noise as measured during off-phases of the ion source, according to Eq. 3.4

$$\gamma_{\mathcal{S}} = \frac{J_3 - 3JJ_2 + 2J^3 + \sigma_{\mathcal{N}}^3\gamma_{\mathcal{N}}}{\left(J_2 - J^2 + \sigma_{\mathcal{N}}^2\right)^{3/2}} \quad . \tag{5.5}$$

Thus, the prediction of the intermittency of the observed time-series as quantified in Ch. 3 is contingent on finding useful expressions for J_q.

5.2 Intermittency in subdiffusion

As the simplest scenario, we can attempt to approximate the distributions of $j(\mathbf{R})$, $f(\mathbf{R})$ and thus by extension $J(\mathbf{R})$ as Gaussians with zero mean i.e.

$$j(\mathbf{R}) = \frac{I}{2\pi\sigma_j^2} e^{-\frac{(R^2+Z^2)}{2\sigma_j^2}} = j_p e^{-\frac{(R^2+Z^2)}{2\sigma_j^2}} \tag{5.6}$$

$$f(\mathbf{R}) = \frac{1}{2\pi\sigma_f^2} e^{-\frac{(R^2+Z^2)}{2\sigma_f^2}} \tag{5.7}$$

$$\Rightarrow J(\mathbf{R}) = \frac{I}{2\pi\sigma_J^2} e^{-\frac{(R^2+Z^2)}{2\sigma_J^2}} \quad , \tag{5.8}$$

where I again represents the total fast ion current and we have $\sigma_J^2 = \sigma_j^2 + \sigma_f^2$ by definition. In this case, the integral in Eq. 5.2 can be solved analytically to yield

$$\begin{aligned} J_q(\mathbf{R}) &= q^{-1} s_q \rho^{(2-2s_q)} j_p^{(q-s_q)} J(\mathbf{R})^{s_q} \\ \text{with} \quad s_q &= \left[1 - \rho^2\left(1 - q^{-1}\right)\right]^{-1} \quad , \end{aligned} \tag{5.9}$$

where we have defined the width ratio of the instantaneous to the time-average profile $\rho = \frac{\sigma_j}{\sigma_J} < 1$. With this parameter as well as $j_p = \frac{I}{2\pi\sigma_j^2}$ we can therefore write the moments of any locally observed time-series in terms of the local value of the time-average profile $J(\mathbf{R}) = \mu_{\mathcal{J}}(\mathbf{R})$ and thus predict its skewness using Eq. 5.5. While we could take estimates for both parameters e.g. from the results of Ch. 4, we firstly assess whether this method can at all yield a consistent result for the prediction of the skewness purely within a given set of experimental data. Therefore, we treat both ρ and j_p as free parameters in a least-χ^2-fit (see App. A) of the predicted $\gamma_{\mathcal{S}}$ against its experimentally measured values.

The expected errors ϵ of the predicted skewness are calculated similarly to those for the peak measured on-phase skewness shown in Fig. 3.5, i.e. by assuming up to 15% uncertainty in the injected fast ion current and applying Eq. 3.9 to find the resulting difference in $\gamma_{\mathcal{S}}$.To avoid over-weighing data-points with low values of $\gamma_{\mathcal{S}}$ and $J(\mathbf{R})$, a minimum bound for this error was enforced based on intrinsic statistical variations of the measured skewness quantified through *bootstrapping*, analogous to the discussed method for Ch.7 in App. A.

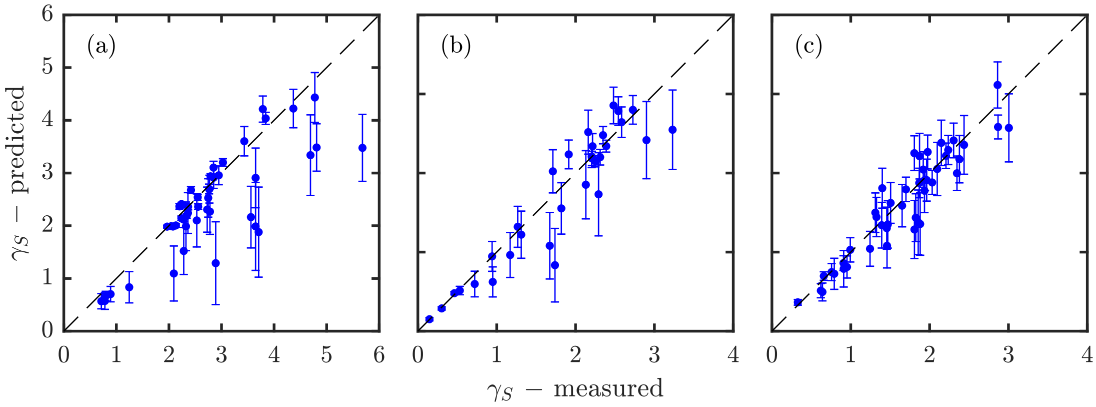

Figure 5.2 – Predicted vs. measured on-phase skewness γ_S for 70 eV ions at $D = \{126, 146, 171\}$ cm (a-c) as shown in the profiles in Fig. 3.4(d-f). The predictions are based on a minimum-χ^2-fit of the analytical model assuming Gaussian distributions.

The results of this fit for the subdiffusive regime are shown in Fig. 5.2 and there appears generally strong agreement between predictions and measurements with minimal *reduced* χ^2 (see App. A) of $\chi_r^2 = \{5.4, 1.1, 0.9\}$ for (a-c). It appears remarkable that it is indeed the strongest outliers from the fit, especially in (a), that feature the largest potential errors. Furthermore, these errors place the bounds of these values often very close to the diagonal. This indicates that the fluctuations of the injected current that these error-estimates are based upon are indeed a consistent qualitative and quantitative explanation for the dominant deviations of some predictions.

The peak current density for the best fits with $j_p = \{37.4, 26.1, 19.0\}\,\mathrm{mA\,m^{-2}}$. When scaling these towards $I_{av} = 2.85\,\mu$A from the given total currents of $I = \{5.0, 3.0, 2.4\}\,\mu$A we find $j_p = \{21.2, 25.0, 22.9\}\,\mathrm{mA\,m^{-2}}$. These values appear similar to the highest time-series peaks e.g. in Fig. 3.1(b,d), which belong to the data-set in (c), but still include noise. The histograms from the tracing algorithm in Fig. 4.10 also correspond to the case in (c), but indicate systematically lower values. This can be due to a combination of effects such as a different width of the instantaneous profile σ_j, possibly due to gyro-motion effects, or an over-estimate of the effective detector area. Yet, the fitted width-ratio parameters $\rho = \{0.67, 0.68, 0.65\}$ appear realistic e.g. compared to the range of numerical estimates in Fig. 4.7, which do not include aperture effects. Choosing an effective detector diameter of $d = 4-6$ mm instead of 8 mm brings the tails of j_p-histograms up to $j_p \approx 20\,\mathrm{mA\,m^{-2}}$, suggesting a significant, albeit not exclusive, contribution to the observed differences. Comparing to Fig. 4.9(b) for instance, one can also see that the instantaneous fast ion beam $j(\mathbf{R})$ can often deviate from the assumed Gaussian shape. Nonetheless, results with similarly good agreement were firstly presented in Ref. [110], where a least-R^2-fit was performed simultaneously on the predicted expressions for $J_{C,2}$ and $J_{C,3}$. While the importance of injection current fluctuations for outliers in the fits was stipulated, it was not demonstrated as consistently as through the above error analysis. For comparison, Fig. 5.3 shows the predictions of $J_{C,2}$ and $J_{C,3}$ (blue) compared to the

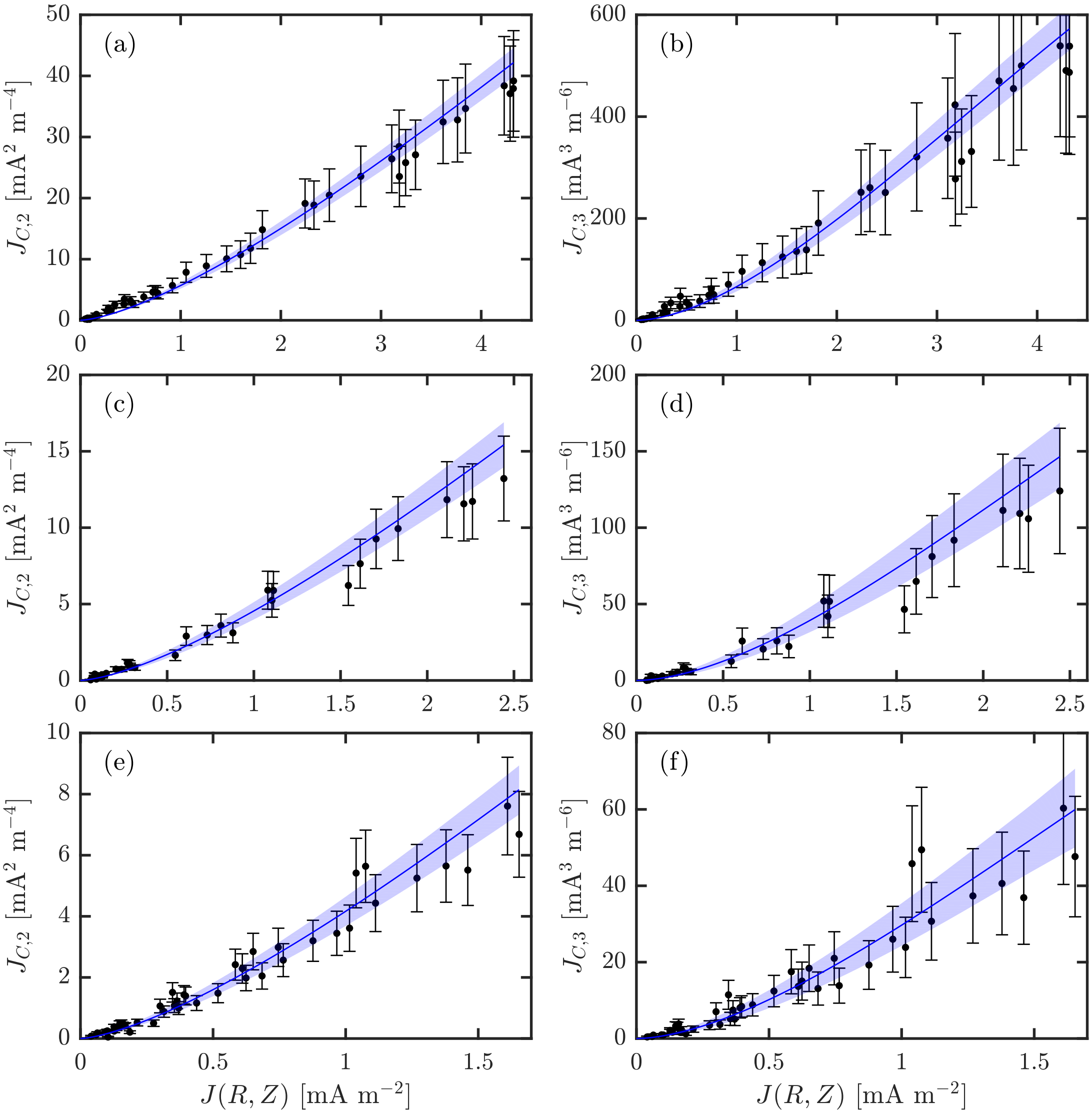

Figure 5.3 – The second and third central moment $J_{C,2}$ and $J_{C,3}$ of the fast ion signal shown for the subdiffusive $E = 70\,\mathrm{eV}$ case for the profiles at $D = \{126, 146, 171\}$ cm from top to bottom. The black dots represent experimental values and the blue lines predictions based on the results from Fig. 5.2. The calculation of both, including their indicated errors and the 95% confidence bands, are detailed in the text.

values computed from measurements (dots), as done in Eq. 3.6 and the numerator of Eq. 3.7 respectively. The results shown here are not fitted, but computed directly using the parameters from the fits of the on-phase skewness. The bands identify predictions based on the 95% confidence region of the fit parameters as detailed in App. A. The error-bars on the data are based on the impact of an estimated 10% variation in the injected fast ion current. Since the noise contributions have been removed from the experimental data, this leads directly to relative errors of up to 21% and 33% respectively. Since a current fluctuation would affect both moments proportionately, the errors in γ_S are smaller and the errors in γ_J should fully cancel by definition. This is another reason for which the fitting of the skewness was preferred given the present method of error-estimation.

Although the experimental obtained profiles in Fig. 3.4 as well as numerically generated instantaneous profiles in Fig. 4.9(b) clearly show non-Gaussian features, it is thus shown that the assumptions made here still produce fairly accurate predictions of time-intermittency in the subdiffusive transport regime.

5.3 Intermittency in super- to quasi-diffusion

For the larger super- to quasi-diffusive profiles obtained with $E = 30\,\mathrm{eV}$, fits of similar quality can be obtained using the Gaussian model, but the fitted parameters ρ over-estimate the expected range of values from Fig. 4.7 by a factor of $\approx \times 2$. The time-average profiles (see Fig. 3.2) show even more strongly non-Gaussian features and the highest values of skewness are obtained in their heavy tail regions, so that the assumptions of purely Gaussian distributions in the model can clearly no longer be valid. Therefore, a different approach for finding the moments J_q is needed. We now perform a 2nd order Taylor expansion in R and Z of the displacement PDF $f(\mathbf{R})$ in Eq. 5.2 about $\mathbf{R}_0$, i.e. letting

$$\begin{aligned} J_q(\mathbf{R}_0) &= \iint j(\mathbf{R}-\mathbf{R}_0)^q f(\mathbf{R})\, dR\, dZ \\ &\approx \iint j(\mathbf{R}-\mathbf{R}_0)^q \big[f(\mathbf{R}_0) + (R-R_0)\partial_R f\big|_{\mathbf{R}_0} + (Z-Z_0)\partial_Z f\big|_{\mathbf{R}_0} \\ &\quad + \frac{1}{2}(R-R_0)^2 \partial_R^2 f\big|_{\mathbf{R}_0} + \frac{1}{2}(Z-Z_0)^2 \partial_Z^2 f\big|_{\mathbf{R}_0} \\ &\quad + (R-R_0)(Z-Z_0)\partial_Z \partial_R f\big|_{\mathbf{R}_0} \big]\, dR\, dZ \quad . \end{aligned} \tag{5.10}$$

All odd orders can be dropped for any symmetric (even) form of $j(\mathbf{R})$. Specifically, we will continue to approximate $j(\mathbf{R})$ as a symmetric Gaussian as in Eq. 5.6. This straightforwardly results in the properties

$$\iint j(\mathbf{R})^q\, dR\, dZ = \iint j_p^q \exp\left[\frac{-q(R^2+Z^2)}{2\sigma_j^2}\right] dR\, dZ = \frac{j_p^{q-1} I}{q} \quad , \tag{5.11}$$

$$\iint R^2 j(\mathbf{R})^q\, dR\, dZ = \iint Z^2 j(\mathbf{R})^q\, dR\, dZ = \frac{j_p^{q-1} I \sigma_j^2}{q} \quad , \tag{5.12}$$

$$\iint RZ j(\mathbf{R})^q\, dR\, dZ = 0 \quad , \tag{5.13}$$

which simplify Eq. 5.10 up to 4th order corrections to

$$J_q(\mathbf{R}_0) \approx \frac{j_p^{q-1} I}{q} \left[f(\mathbf{R}_0) + \frac{\sigma_j^2}{2}(\partial_R^2 + \partial_Z^2) f\big|_{\mathbf{R}_0} \right] \tag{5.14}$$

From the case $q = 1$ we find $f(\mathbf{R}_0) \approx I^{-1} J(\mathbf{R}_0)$. Therefore, we lastly assume that $f(\mathbf{R})$ changes likewise on a typical scale similar to σ_J, i.e. we approximate

$$\left|\partial_R^2 f(\mathbf{R})\big|_{\mathbf{R}_0}\right| \sim \left|\partial_Z^2 f(\mathbf{R})\big|_{\mathbf{R}_0}\right| \sim \sigma_J^{-2} f(\mathbf{R}_0) \quad . \tag{5.15}$$

Dropping the subscript, this finally yields

$$J_q(\mathbf{R}) \approx \frac{j_p^{q-1}}{q} J(\mathbf{R}) \left[1 + \mathcal{O}\left(\frac{\sigma_j^2}{2\sigma_J^2}\right)\right] = \frac{j_p^{q-1}}{q} J(\mathbf{R}) \left[1 + \mathcal{O}\left(\frac{\rho^2}{2}\right)\right] \approx \frac{j_p^{q-1}}{q} J(\mathbf{R}) \quad . \tag{5.16}$$

Imposing $\rho^2 \ll 1$ in the last step seems well-justified from the numerical results concerning $j(\mathbf{R})$ in Fig. 4.7 and Fig. 4.8, as well as the observed peaks in the time-series e.g. in Fig. 3.1(a,c). From Eq. 5.3 we find for the second and third *central* moments

$$J_{C,2} = \frac{1}{2} j_p J(\mathbf{R}) - J(\mathbf{R})^2 \quad , \tag{5.17}$$

$$J_{C,3} = \frac{1}{3} j_p^2 J(\mathbf{R}) - \frac{3}{2} j_p J(\mathbf{R})^2 + 2J(\mathbf{R})^3 \quad . \tag{5.18}$$

We can likewise predict the on-phase skewness again using Eq. 5.5 based on $J(\mathbf{R})$, while treating j_p as free fitting parameter. The results of the minimum-χ^2-fits are shown in Fig. 5.4.

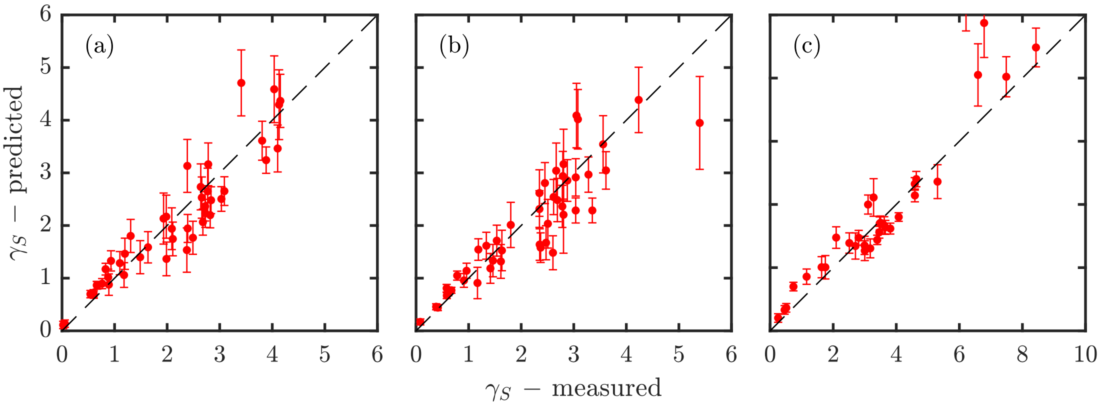

Figure 5.4 – Predicted vs. measured on-phase skewness γ_S for 30 eV ions at $D = \{126, 146, 171\}$ cm (a-c) as shown in the profiles in Fig. 3.2(d-f). The predictions are based on a minimum-χ^2-fit of the analytical model using a Taylor expansion of $f(\mathbf{R})$ about $\mathbf{R}_0$ as shown in Eq. 5.10 to express J_q.

With minimal *reduced* χ^2 of $\chi_r^2 = \{2.5, 2.8, 4.3\}$ for (a-c), the predictions are again in good overall agreement with measurements. The requisite errors have been calculated as described in the previous section. The peak current density inferred from the best fits is $j_p = \{9.7, 8.5, 15.3\}\,\mathrm{mA\,m^{-2}}$. Pending noise, the latter value appears similar to the time-series peaks in Fig. 3.1(a,c). When scaling again towards $I_{av} = 2.85\,\mu\mathrm{A}$ with the total currents of $I = \{2.35, 2.4, 3.3\}\,\mu\mathrm{A}$ one finds $j_p = \{11.7, 10.1, 13.0\}\,\mathrm{mA\,m^{-2}}$. This is in strong agreement with the central values of the j_p-histogram in Fig. 4.10(a), drawn from the synthetic diagnostic (magenta).

The comparison between the $J_{C,2}$ and $J_{C,3}$ calculated from measurements with those predicted from the above fit is shown in Fig. 5.5. The calculations of the experimental values and errors are carried out as in the preceding section, while the predictions and their 95% confidence bounds are now drawn from the confidence region of the single fitted parameter j_p (see App. A).

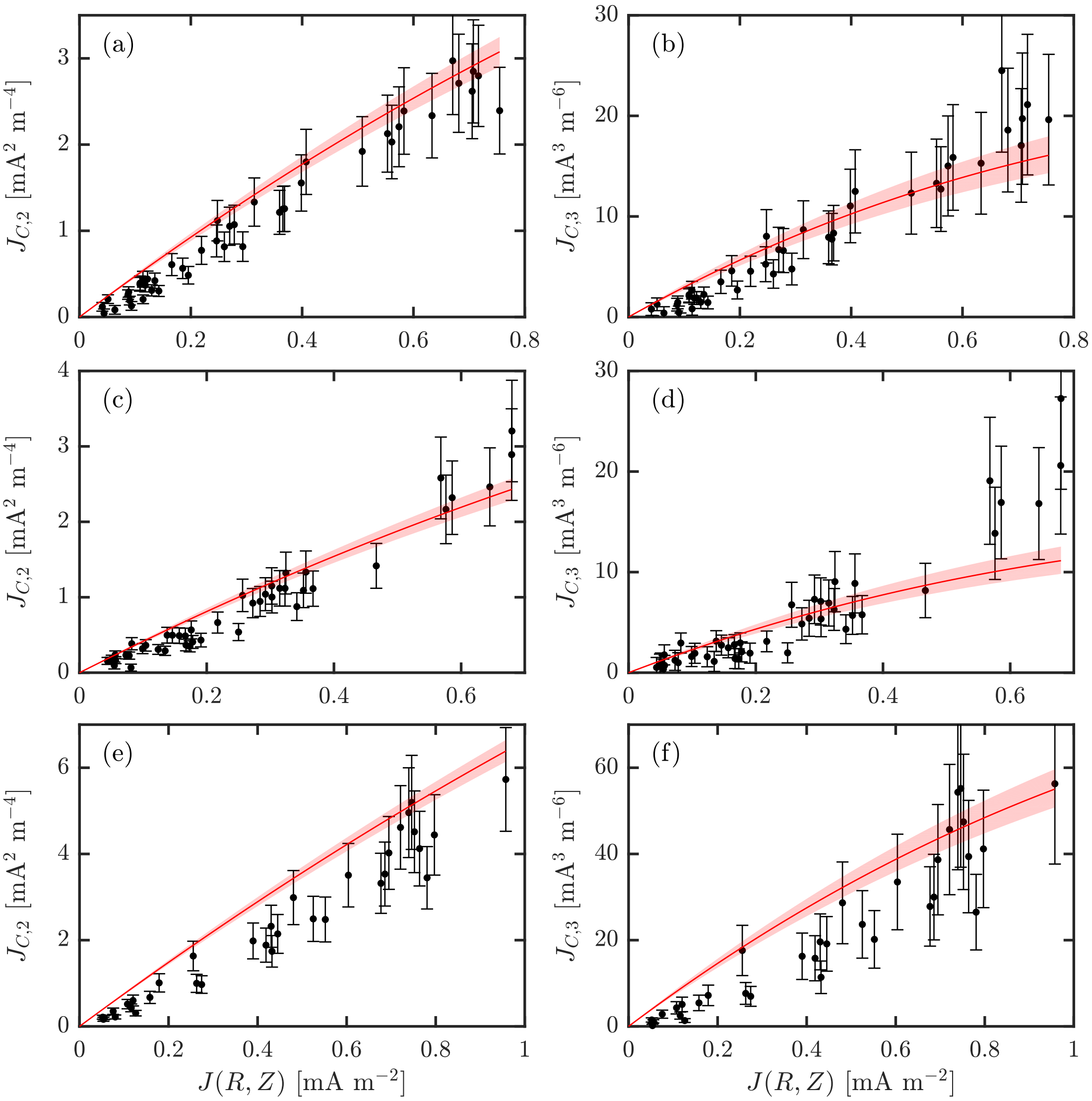

Figure 5.5 – The second and third central moment $J_{C,2}$ and $J_{C,3}$ of the fast ion signal shown for the super- to quasi-diffusive $E = 30$ eV case for the profiles at $D = \{126, 146, 171\}$ cm from top to bottom. The black dots show again experimental values, while the red lines are based on the results from Fig. 5.4.

Overall, we still find reasonable, but less strong agreement between predictions and measurements compared to the preceding section. Again, the error-bars in Fig. 5.4 indicate rather consistently that the suspected variations in the injected fast ion current are a major contributor to the observed deviations. In practice, especially the higher injected currents proved more difficult to maintain consistently, so that the larger deviations in Fig. 5.4(c) are not surprising. Moreover, the shapes of the numerically generated instantaneous profiles $j(\mathbf{R})$ in Fig. 4.8(b) clearly deviate from the assumed Gaussian shapes in many cases. The given degree of agreement between predictions and measurements is achieved most likely only because higher detected values of j_p dominate $J_{C,3}$ and the calculated values of skewness, and these values tend to belong to relatively concentrated and at least approximately Gaussian shaped $j(\mathbf{R})$. The impact e.g. of inclined and elliptical Gaussians and non-constant beam shapes have been discussed for the 1D case in Ref. [109], and the applied model is expected to similarly hold under these modifications.

5.4 Comparison to two-valued time-series

We now consider the limit of $\rho \ll 1$, which is even more stringent than $\rho^2 \ll 1$ in the preceding section. If we furthermore assume a finite detector size with a diameter $d \gg \sigma_j$ eventually in this limit, we reach a point where at most instances, $j(\mathbf{R})$ is either fully detected or not at all. This results in observed time-series becoming binary in this sense, i.e. ultimately with the two possible values $j_p = \frac{4I}{\pi d^2}$ and zero respectively. The mean $\mu_\mathcal{J}$ of such a two-values time-series with M entries and containing N peaks is given by $\mu_\mathcal{J} = \frac{N j_p}{M}$, and its skewness is hence found as

$$\begin{aligned}\gamma_{\mathcal{J},\mathcal{B}} &= \frac{\frac{1}{M}\sum_{i=1}^{M}(j_i-\mu_\mathcal{J})^3}{\left[\frac{1}{M}\sum_{i=1}^{M}(j_i-\mu_\mathcal{J})^2\right]^{\frac{3}{2}}} \\ &= \frac{\frac{N}{M}(j_p-\mu_\mathcal{J})^3}{\left[\frac{N}{M}(j_p-\mu_\mathcal{J})^2\right]^{\frac{3}{2}}} = \sqrt{\frac{M}{N}} = \sqrt{\frac{j_p}{\mu_\mathcal{J}}} \quad . \end{aligned} \tag{5.19}$$

Including contributions from noise, we find for the on-phase skewness

$$\gamma_{\mathcal{S},\mathcal{B}} = \frac{\mu_\mathcal{J} j_p^2(1-\frac{\mu_\mathcal{J}}{j_p})^3 + \sigma_\mathcal{N}^3\gamma_\mathcal{N}}{\left[\mu_\mathcal{J} j_p(1-\frac{\mu_\mathcal{J}}{j_p})^2 + \sigma_\mathcal{N}^2\right]^{\frac{3}{2}}} \quad . \tag{5.20}$$

In our experiments, the diameter of the detector $d = 8\,\mathrm{mm}$ is similar to the sizes of the typical fast ion Larmor-radii. A simultaneous detection of the full instantaneous fast ion beam is therefore unlikely, as can be seen from the lower $j_p < \frac{4I}{\pi d^2} = 57\,\mathrm{mA\,m^{-2}}$ (for $I = I_{av} = 2.85\,\mu\mathrm{A}$) usually seen in both the time-series and numerical results, especially in the subdiffusive case. However, if we wish to gain insight into the parameters of $j(\mathbf{R})$ based on single time-series, it is still worth comparing $\gamma_\mathcal{S}$ against $\gamma_{\mathcal{S},\mathcal{B}}$. Smaller discrepancies would indicate that the time-series is better approximated by the two-valued model, as a larger fraction of $j(\mathbf{R})$ is detected at many instances, indicating an on average smaller instantaneous beam-profile. Based on the different Larmor radii (see 2.2, Fig. 4.4), the numerical results in Fig. 4.7 and the fits in the preceding sections, on would suspect this to be the case for the super- to quasi-diffusive regime here. In Fig. 5.6, we show the relative error $\epsilon = \frac{\gamma_{\mathcal{S},\mathcal{B}}-\gamma_{\mathcal{S}}}{\gamma_{\mathcal{S},\mathcal{B}}}$ computed on the time-series from the treated profiles with $E = \{30, 70\}$ eV and $D = \{126, 146, 171\}$ cm, as a function of $\mu_{\mathcal{J}}$ and $\gamma_{\mathcal{S}}$.

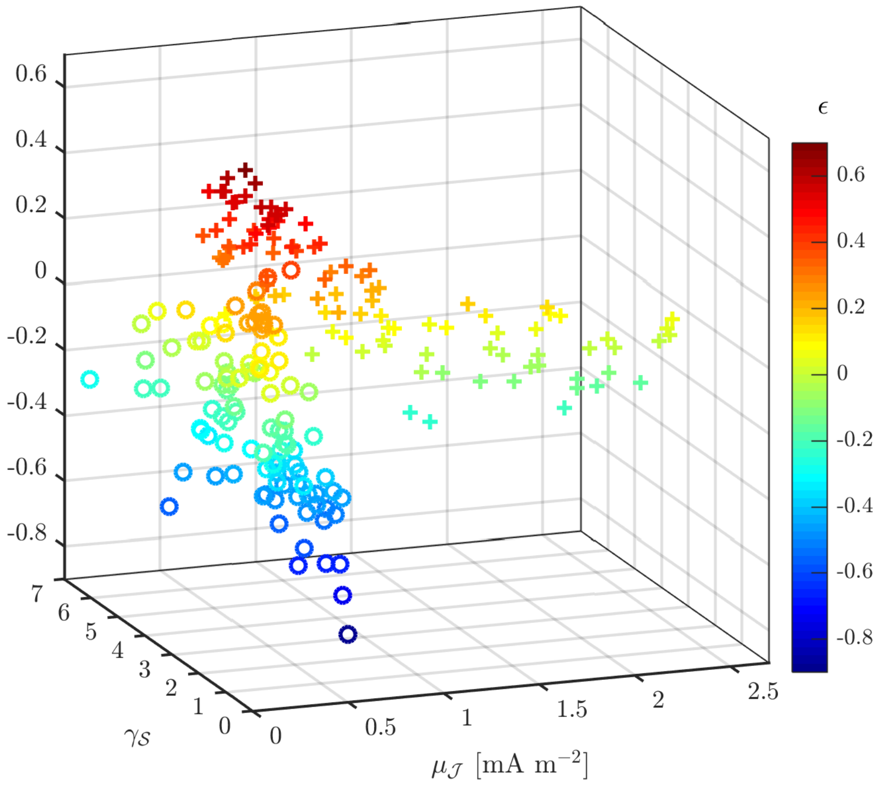

Figure 5.6 – Relative error ϵ between the on-phase skewness of a two-valued time-series (Eq. 5.20) and the experimentally measured values, as a function of $\gamma_{\mathcal{S}}$ and $\mu_{\mathcal{J}}$. Most time-series treated in the preceding 2 sections have been included. Circles correspond to the $E = 30$ eV set, crosses to $E = 70$ eV.

To only rely on local observations, j_p was not taken from the previous sections, but calculated as the average of the 10th upper percentile of the measured values for each time-series. We find that for most time-series with $E = 70$ eV, a distinctly higher value of ϵ is attained near a given $\gamma_{\mathcal{S}}$ and $\mu_{\mathcal{J}}$ than for those with $E = 30$ eV. Similar, albeit less distinct, results between both ion energies were obtained for other chosen percentiles down to 0.5%. In the far edges of the time-average fast ion beam, the full peak of $j(\mathbf{R})$ is detected too rarely (if at all), so that it is not feasible to define j_p through any given upper percentile. Thus, a few such cases with $\mu_{\mathcal{J}} < 0.1\,\mathrm{mA\,m^{-2}}$ and $\gamma_{\mathcal{S}} < 0.05$ have been excluded.

This concurs with the expectation that $j(\mathbf{R})$ is on average more concentrated in the super- to quasi-diffusive case, particularly when considering the highest observed values for j_p, that impact the value of the skewnesses most strongly. Therefore, combined with the local measurements of $\gamma_{\mathcal{S}}$ and $\mu_{\mathcal{J}}$ as shown in Fig. 5.6, we have a relative indication of whether a given time-series belongs to the subdiffusive or the super- to quasi-diffusive set of measurements, which does not require results or parameter estimates from simulations or fitting. The absolute values of ϵ of course still vary depending on the specific local definition of j_p, as well as the actual effective detector diameter. Furthermore, due to the stronger variations in σ_j, this observation can become less consistent at early propagation times, especially for higher E.

5.5 Conclusions

In this chapter we have leveraged the insights into the qualitative dynamics of the meandering fast ion beam from Ch. 4, to motivate and introduce an analytical model [109] that can predict the moments of time-series generated in such a system, based on their time-average values. Using concise analytical expressions for the prediction of the skewness of fast ion time-series, we find good agreement with measurements in both the subdiffusive as well as the super- to quasi-diffusive regimes. To arrive at these concise expressions, different assumptions had to be made between both cases, based on the differences in the dynamics of the meandering fast ion beam. The high consistency in the presented results illustrates conclusively how local time-intermittency can be generated across all non-diffusive transport regimes in our system, as shown in [110, 111]. Since no intrinsic assumptions are made on the physics underlying the meandering beam motion, this statistical model can potentially be applied to any conceptually similar systems. For the treatment of non-Gaussian beams, the assumption of a distinctly smaller instantaneous beam compared to its time-average profile is however essential. While not requiring a point-like source specifically, a relatively small source region is therefore needed in our settings. In general, if a larger, but still distinctly meandering particle beam was present, one could additionally adopt certain methods to infer certain features of the instantaneous beam profile shape [109]. The impact of different types of more dominantly mode-like or blob-like plasma structures on the presented results could also be investigated e.g. by using injection positions towards the HFS or LFS respectively or changing the position of the EC resonance layer. In closing, we considered how skewness is generated by a consistently point-like meandering beam, that produces two-valued time-series. Comparing this skewness measure to the actual skewness of a time-series can yield a relative indication on whether a time-series belongs to the subdiffusive or super- to quasi-diffusive data-set. While a specific transport regime cannot be inferred solely based on the present level of intermittency (skewness), this illustrates how one can leverage additional information or assumptions on the system to gain insights into different global behaviours of the fast ions based on local measurements.

6 Statistical modeling of non-diffusive transport

Having described the generation of local time-intermittency across all observed non-diffusive transport regimes through experimental, numerical and analytical studies, the following chapters present the second central subject of this thesis. The model of Truncated Asymmetric Fractional Lévy Motion (TAFLM) is derived through path-integral methods adapted from [183] for the first time to our knowledge [112], as a general statistical model for bounded non-diffusive transport. Subsequently, it is applied to cross-field transport of fast ions in SMT plasma turbulence. To provide a more detailed and generally accessible discussion of the subject, this chapter firstly reviews different random-walk based approaches to the description of diffusion. We then motivate the introduction of Lévy statistics for their generalizations to non-diffusive transport, as described by Fractional Diffusion Equations (FDEs), while focusing on relevant previous work [108]. Finally, tempered stable distributions are introduced in the context of Ref. [120], to discuss how they help address physically problematic properties of FDEs, such as certain diverging moments in the associated Green's functions. With these key properties in mind, we then construct the TAFLM model by building directly on the methods presented in Refs. [120] and [183] and previous work in Ref. [108, 136]. Most of the content related to the derivation in Sec. 6.4 and some of the analysis in Ch. 7 have been successfully published by the author in Ref. [112].

6.1 Review of diffusion models

The first comprehensive phenomenological and mathematical description of diffusion is often credited to Fick in 1855 [184]. Based on his experiments with salt solutions, he surmised that the local flux of a solute $J(x)$ at a given point x be driven opposite the local gradient of the concentration $n(x)$. Fick's 1st Law thus reads

$$J(x) = -D\, d_x n(x) \quad , \tag{6.1}$$

where D denotes a proportionality constant. Immediately, he drew the analogy to Fourier's treatment of heat transport [185] and identified the same resulting equation for the evolution of $n(x)$

$$\partial_t n(x,t) = -D\,\partial_x^2 n(x,t) \quad , \tag{6.2}$$

commonly known as the 'Diffusion Equation' (DE) in one dimension or 'Fick's 2nd Law', identifying D as the diffusion coefficient. Formally, the 2nd Law can be derived by substituting his 1st Law into the continuity equation

$$\partial_t n(x,t) = \partial_x J(x,t) \quad , \tag{6.3}$$

while assuming D to be independent of position. Fick's treatment thereby relies on the fundamental assumptions that the local transport of $n(x,t)$ is entirely determined by effects that can be described as both, local in space at x, and local in time at t ('markovian').

6.1.1 Einstein's random walk model

Although Fick made extensive use of the concepts of atoms and molecules, that were 'at least tolerated by most physicists as a useful tool' [184], he mostly argued about supposed differences in the forces of attraction and repulsion between different particle species and the implications on their average motion towards an equilibrium. It was only in 1905/06 that Einstein [186] consistently formulated the microscopic picture of Brownian particle motion in terms of a random walk (see e.g. Fig. 6.1) and thus re-derived the diffusion equation and its coefficient in terms of microscopic quantities [116].

In one dimension x, it is assumed that starting at $t = 0$ a particle undertakes random steps Δx at given time intervals Δt. The step-sizes are distributed independently and symmetrically according to a PDF $P(\Delta x) = P(-\Delta x)$, whereas the time-steps Δt are constant. For the evolution of a given distribution of walkers $n(x,t)$, we can thus write

$$n(x,t+\Delta t) = \int_{-\infty}^{\infty} n(x+\Delta x,t) P(\Delta x)\, d\Delta x \equiv \langle n(x+\Delta x,t)\rangle \quad , \tag{6.4}$$

where $\langle . \rangle$ thus denotes the average over the distribution $P(\Delta x)$. One can perform a Taylor expansion of $n(x,t)$ in space by assuming Δx as a small expansion parameter for a peaked distribution $P(\Delta x)$. For an expansion in time, it is assumed that the induced variations are thus also appropriately small over the expansion parameter Δt. These expansions thus yield

$$\begin{aligned} n(x,t) + \Delta t\,\partial_t n(x,t) &\approx \langle n(x,t)\rangle + \langle \Delta x\rangle\, \partial_x n(x,t) + \frac{1}{2}\langle \Delta x^2\rangle \partial_x^2 n(x,t) && (6.5)\\ \Delta t\,\partial_t n(x,t) &\approx \frac{1}{2}\langle \Delta x^2\rangle\, \partial_x^2 n(x,t) \quad . && (6.6) \end{aligned}$$

To clarify, we have thus implicitly assumed and that $P(\Delta x)$ is peaked and bounded such that it features finite (and decreasing) moments at all even orders. Odd orders in the expansion are neglected due to the symmetry of $P(\Delta x)$. The 0th order terms cancel as $\langle 1\rangle = 1$. In the limit of sufficiently small expansion parameters compared to sufficiently large scales of x and t, the so-called 'fluid-limit' [117] in the following, we therefore retrieve the diffusion equation

$$\partial_t n(x,t) = \underbrace{\frac{\langle \Delta x^2 \rangle}{2\Delta t}}_{D} \partial_x^2 n(x,t) \quad . \tag{6.7}$$

These assumptions are then effectively equivalent to those of space- and time-locality in Fick's description. However, the diffusion coefficient is now given by the variance of the step-sizes Δx and the waiting-time Δt between steps. Note that supposing exponentially distributed Δt and thus averaging the LHS of Eq. 6.5 represents an equivalent ansatz to the above for $t \gg \Delta t$. The solution $n(x,t)$ of this equation for a Dirac-δ initial condition $n(x,0) = \delta(x)$, i.e. its propagator, or Green's function $G(x,t)$, is given as the well-known Gaussian distribution

$$G(x,t) = \frac{1}{\sqrt{4\pi D t}} \exp\left(\frac{-x^2}{4Dt}\right) \tag{6.8}$$

and can be obtained straightforwardly e.g. by using a Fourier transforms.

6.1.2 Langevin's approach

Only a few years after Einstein and independently Smoluchowski [187] published their works on Brownian motion, Langevin formulated a different approach [188, 189]. The acceleration of a particle is expressed as the sum over a constant damping term with coefficient γ and a random contribution $\xi(t)$, e.g. by collisions,

$$d_t^2 x = -\gamma d_t x + \xi(t) \quad . \tag{6.9}$$

This equation of motion, the Langevin Equation (LE), is thus termed a stochastic differential equation, as $\xi(t)$ formally represents a stochastic process, that can take a variety of realizations. In the simplest case, $\xi(t)$ is assumed to be a markovian process, i.e. with vanishing correllations between different times. The resulting velocities $v(t)$ and the trajectory $x(t)$ can be written as a stochastic integral equations [190],

$$\begin{aligned} v(t) &= d_t x = v_0 e^{-\gamma t} + \int_0^t e^{-\gamma(t-t')} \xi(t')\, dt' \quad , & (6.10) \\ x(t) &= \frac{v_0}{\gamma}(1 - e^{-\gamma t}) + \frac{1}{\gamma}\int_0^t (1 - e^{-\gamma(t-t')}) \xi(t')\, dt' \quad , & (6.11) \end{aligned}$$

for arbitrary time-scales and assuming $v(t=0) = v_0$ and $x(t=0) = 0$. At short times, the damped exponential terms can model friction between collisions, a behaviour that is not treated by Einstein's approach. Solving these equations corresponds to determining the average behaviour of particles subject to this process, i.e. finding their propagator in velocity-space $G(v,t)$ and configuration-space $G(x,t)$ respectively. This was first accomplished by Ornstein and Uhlenbeck [190] by taking moments of $U = v - v_0 e^{-\gamma t}$ and $S = x - \frac{v_0}{\gamma}(1 - e^{-\gamma t})$ involving Eqs. 6.10,6.11, proving that the distributions of $G(U,t)$ and $G(S,t)$ take the Gaussian

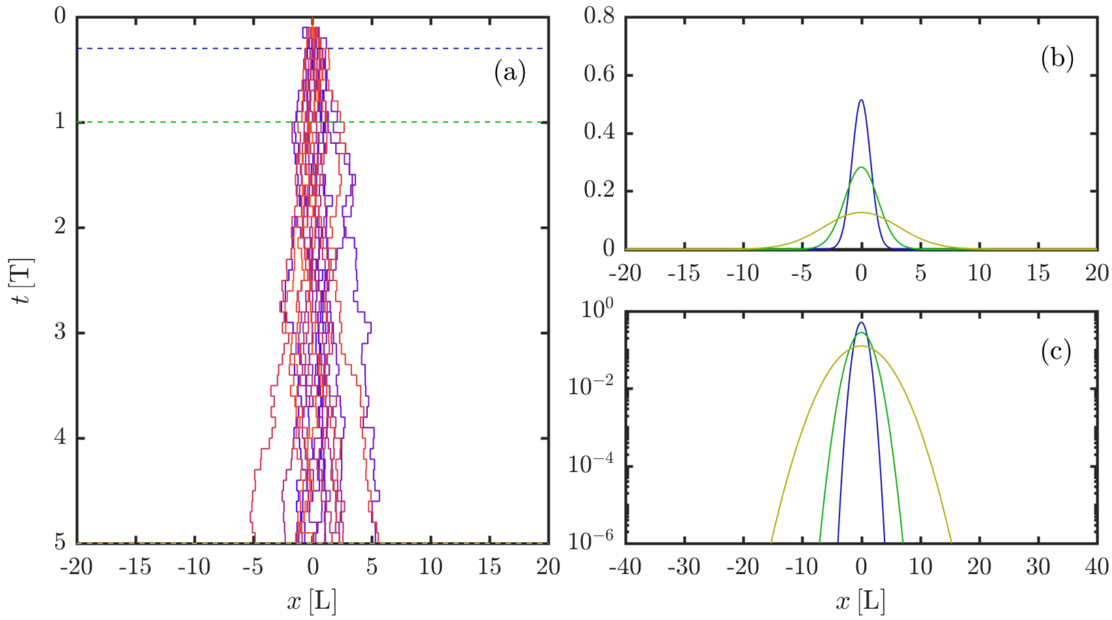

Figure 6.1 – In (a), 20 random walk paths generated from a standard normal distribution of step-sizes, taken at $N = 50$ regular time intervals $\Delta t = 0.1$ until $t = 5$ are shown. The propagator $G(x,t)$ is shown in (b) at the times $t = \{0.3, 1, 5\}$ in blue, green and dark yellow respectively, as indicated by the dashed lines in (a). To illustrate the shape of the 'light' tails of these distributions, $G(x,t)$ is again shown with a logarithmic ordinate in (c) as well as a doubled range in x. The dimensions in space and time are of arbitrary units of length L and time T, while the propagators are normalized and thus have arbitrary units of L^{-1}. These conventions and the ranges in x are kept for comparison with other distribution types below. As will be outlined in the presentation of the Central Limit Theorem (CLT) below, the step-sizes are scaled to the appropriate step-times by $\Delta t^{1/2}$. Alternatively, the time-argument of the propagator would need to be rendered adimensional (i.e. $N = \frac{t}{\Delta t}$), and straightforwardly represent and N-fold convolution of the independently drawn step-size distributions. With the more practical convention chosen here and in the following, the same could be illustrated by letting $\Delta t = 1$.

Normal form. For $\gamma t \gg 1$, Einstein's result for $G(x,t)$ is retrieved from the latter as expected. Correspondingly, the stochastic equation for Ordinary Brownian Motion (OBM) is obtained in the same limit directly from Eq. 6.11

$$x(t) = \frac{v_0}{\gamma} + \frac{1}{\gamma}\int_0^t \xi(t')\,dt' \quad , \tag{6.12}$$

for which step-wise generalizations are introduced in the following sections, up to the derivation of Truncated Asymmetrical Lévy Motion (TAFLM) in the next chapter.

For completeness, it should be noted that various classical Langevin Equations, e.g. also of harmonically bound particles, can be treated and solved in a number of ways [191, 192, 193].

Already in Ref. [190], techniques are applied to first retrieve the corresponding non-stochastic equations of motion of a propagator through the moments of the Langevin Equations. These are referred to as Fokker-Planck equations and describe, in the most general cases, the full evolution of the distribution $G(x,v,t)$ in phase-space, as e.g. for the free damped Brownian particle [192]

$$\partial_t G = -v\partial_x G + \gamma\left(\partial_v v + \frac{D}{\gamma}\partial_v^2\right)G \quad . \tag{6.13}$$

Formally, a possible ansatz is given by casting the Langevin Equations into an integral form

$$x(t+\Delta t) - x(t) = \int_t^{t+\Delta t} v dt' \quad , \tag{6.14}$$

$$v(t+\Delta t) - v(t) = \int_t^{t+\Delta t} -\gamma v + \xi dt' \tag{6.15}$$

and iteratively Taylor-expanding the non-stochastic parts of the integrands about $x(t)$ and $v(t)$ to 1st order. The Fokker-Planck equation is then found by identifying the different terms of its Kramers-Moyal-Expansion (the formal generalization of Eq. 6.5) from the moments of the expanded forms of Eqs.6.14, 6.15. Through these, the diffusion coefficient is introduced through the correlations of the noise terms $\langle\xi(t_1)\xi(t_2)\rangle = 2D\delta(t_1 - t_2)$, where $\langle.\rangle$ still denotes the distribution average over $\xi(t)$. The diffusion equation can be retrieved as a simplified case based on Eq. 6.12. It corresponds to the 'over-damped' scenario of Eq. 6.9 as the accelleration term is effectively dropped compared to the damping and stochastic terms, yielding the differential form of the OBM equation $d_t x = \frac{1}{\gamma}\xi(t)$. This is not counter-intuitive, as in Einstein's approach, the particle is treated as stationary in between distinct jumps. In this context, the continuous motion of a particle can still be treated e.g. using Persistent Random Walks with Poisson-distributed waiting times, as we have done in Ref. [194] to investigate transient non-diffusive transport regimes in the short-time regime. However, since we wish to treat fractional generalizations of Eq. 6.12 in the following, the availability of moment-based averages is subject to certain constraints. Hence a path-integral based approach for solving the resulting Langevin Equations has been adopted from Ref. [195] for the work in Ref. [108] as well as the following.

6.1.3 The Gaussian limit

From the perspective of a Brownian random walk as an uncorrelated random process, it is indeed inevitable that the solutions to the classical diffusion equation embodies the form of a Gaussian Normal distribution, no matter the method of description and solution. The stochastic integral equation 6.12 represents the limit of an infinite sum of random variables $\xi(t_n)$ that in case of statistical independence, for a finite variance, zero means and uniform 'smallness', must converge to a Normal distribution, according to the Central Limit Theorem as given by Feller [196]. Various forms of this theorem have been formulated since Laplace, who extended De Moivre's and Bernoulli's work that demonstrated the Normal distribution as an approximation for binomial distribution [197]. Many of the most pre-eminent mathematicians of the 19th and early 20th century contributed to its formalization and generalization including Poisson, Markov, Lindeberg and Lyapunov, until the most definitive proofs were given by Lévy and Feller [196, 197]. These treatments are thus very detailed, and we only recall a simplified proof valid for random variables with finite moments, featuring a common mean of zero and variance σ^2, as similarly shown e.g. in [191, 182]. This furthermore highlights the importance of characteristic functions, which will be used extensively in the following. The characteristic function of a probability distribution $P(\xi)$ of a (continuous) random variable ξ is defined as its Fourier transform

$$\hat{P}(k) = \int e^{ik\xi} P(\xi)\, d\xi = \langle e^{ik\xi} \rangle \quad . \tag{6.16}$$

The $\hat{:}$-notation will be used to denote both Fourier transforms in space, as well as Laplace transforms in time in the following. The nature of the transform can be deduced from the indicated transform variables k and s, respectively. If no transform variable is given for brevity, a pure Fourier transform is implied. The characteristic function is directly linked to the moments of $P(x)$ (assumed finite), and we can deduce by definition

$$\hat{P}(k) = \langle e^{ik\xi} \rangle = \langle \sum_n^{\infty} \frac{(ik)^n}{n!} \xi^n \rangle \quad \Rightarrow \quad \langle \xi^n \rangle = (-i)^n \partial_k^n \hat{P}(k) \Big|_{k=0} \quad . \tag{6.17}$$

If all moments converge indeed, we can likewise take the sum outside the integral and therefore expand

$$\hat{P}(k) = \sum_n^{\infty} \frac{(ik)^n}{n!} \langle \xi^n \rangle . \tag{6.18}$$

If we now consider the N-fold sum of (any) independent random variables $y = \sum_{n=1}^{N} \xi_n$, its characteristic is given by

$$\hat{P}_y(k) = \int e^{ik \sum_{n=1}^{N} \xi_n} \prod_{n=1}^{N} P(\xi_n)\, d\xi_n = \prod_{n=1}^{N} \int e^{ik\xi_n} P(\xi_n) d\xi_n \quad , \tag{6.19}$$

since the joint PDFs of independent random variables must be separable as a product. Note that this equivalently implies that the PDF of a sum of independent random variables be the convolution of their individual PDFs. To make the most use of a series-expansion as in Eq. 6.18, we re-scale to $z = yN^{-1/2}$, which yields up to second order

$$P_z(k) \simeq \left(1 - \frac{\sigma^2 k^2}{2N}\right)^N \Rightarrow \lim_{N \to \infty} P_z(k) = e^{\frac{-\sigma^2 k^2}{2}} \quad , \tag{6.20}$$

where we approach an exact limit for large enough N, since higher orders of the expansion become negligible. Fourier-inverting $P_z(k)$ therefore yields a normalized Gaussian with zero mean and variance σ^2. Alternatively, one can allow different finite means and variances for $P(\xi_n)$ and scale the sum by N^{-1} to find that $P(z)$ converges to a δ-function on the average of the means [182]. Conversely, when un-scaling towards y the distribution variance grows as $N\sigma^2$.

This limit has the far reaching implication that no matter the description, the limit of any population of random walkers with any such step-size distributions as described above, will ultimately converge to a Gaussian and, at an average constant rate of steps, the variance of this Gaussian will grow linearly in time $\sigma^2 \propto t^\nu$ with $\nu = 1$ being the 'transport exponent'. These are thus the defining features of all diffusive transport. Indeed for the variance of Einstein's result we immediately identify $\sigma^2 = \langle \Delta x^2 \rangle = 2Dt$. This was likewise recovered in Langevin's paper [188], who also identified $D = \frac{RT}{\gamma N} = \frac{k_B T}{\gamma}$ by considering the average 1D kinetic particle energy $\frac{m}{2}\langle \xi^2 \rangle = \frac{RT}{2N}$.

6.2 Non-diffusive transport

The fundamental assumptions for all descriptions of the random-walk based classical diffusion processes are therefore locality in space and markovianity in time, and are embodied by the given constraints on the probability distributions. Since these assumptions are hardly restrictive and often well-justified in practice, the paradigm that all observed transport be a combination of advection and diffusion has successfully underpinned a plethora of transport studies e.g. in physics and chemistry. In principle, even turbulent transport can be described as a combination of classical diffusion and turbulent advection [86, 21]. However, since the advection patterns are often inherently unpredictable, the construction of effective statistical models for the resulting global transport can be difficult. The introduction of *effective* diffusion coefficients based on global instead of local observations has thus become common practice for many plasma simulations seeking to include the effects of turbulence, e.g. on particle and heat transport in tokamaks [21]. Sophisticated transport codes such as UEDGE [198] and SOLPS-ITER [199], aimed at predicting conditions in the tokamak SOL, have indeed been successfully implemented based on these considerations. Nonetheless, this approach inherently neglects the fact that the fundamental assumptions underlying the diffusion model may no longer be satisfied, and non-Gaussian transport features may thus occur. In the case of fast ions specifically, both, the presence of medium-scale turbulent electric fields as well as the large Larmor radii of these ions represent a clear departure from the assumptions of locality and often result in highly non-Gaussian statistics, as already outlined in the previous chapters. Therefore, we will instead review and build upon the statistical methods that have been specifically devised to describe inherently non-diffusive transport, as outlined in many of the above examples.

In fact, more and more scenarios have emerged in modern research, where complex or non-linear systems appeared to behave in a non-local or non-markovian manner, resulting in non-diffusive transport [116, 200, 114]. In bio-chemistry for instance, it has become clear that the transport of proteins does not always follow Gaussian statistics [201, 202]. This general observation was made for transport in a variety of fields in the life-sciences, such as animal roaming [203, 204], human travel [205] and epidemiology [206]. Non-Gaussian statistics have become a wide field of interest in mathematics [118], and have found further applications in finance [207], criminology [208] and even quantum mechanics [209].

Other applications in physics [116, 114] are routed around the subject of turbulence. In particular, the intermittent observation of coherent structures can lead to non-diffusive behaviour, with examples in both atmospheric physics [210] and plasma physics [211]. Naturally, the description of non-diffusive fast ion transport has thus also been subject to a variety of investigations in this context, both in astrophysical [93, 212, 96] and laboratory settings [94, 95], including fusion plasmas [84] and previous work in our group [104, 107, 103].

6.2.1 Lévy stable distributions

In the context of random walk descriptions, many non-diffusive settings have in common, that either particle steps, the waiting time between them or both can favour disproportionately large values compared to the diffusive case. More specifically, if one wishes to describe transport with a long-time propagator other than a Gaussian with $\sigma^2 \propto t$, we require distributions for the particle step sizes $P(\xi)$ and waiting times $w(\tau)$ that abandon some of the assumptions underlying the classical Central Limit Theorem. The further generalization of this theorem was indeed successfully treated e.g. by Lévy and Khintchine [213], as well as Kolmogorov and Gnedenko [214]. Following the outlines in [116, 118] here, it states that if the distribution $P(Z)$ of an appropriately normalized sum of independent, identically distributed (iid) random variables

$$Z = A_N + \frac{\sum_{n=1}^{N} \xi_n}{B_N} \quad , \tag{6.21}$$

converges for $N \to \infty$ with some $\{A_N\} \in \mathbb{R}$ and $\{B_N\} \in \mathbb{R} > 0$, $P(Z)$ must converge to a distribution that is thus defined as 'stable'. No assertions on the moments of the individual distributions $P(\xi_n)$ are made, except that for a finite variance, the Gaussian case must be recovered. This is in fact equivalent [118, 116] to stipulating the iid random variables ξ_n and their normalized sum to follow the same form of distribution P and thus requiring

$$P\left(\sum_{n=1}^{N} \xi_n\right) = P\left(B_N \xi + A_N\right) \quad , \tag{6.22}$$

for some $A_N \in \mathbb{R}$ and $B_N \in \mathbb{R} > 0$ for any $N \geq 2$. Following Eq. 6.19 this reads in terms of the characteristic function

$$\hat{P}(k)^N = \hat{P}(B_N k)\, e^{ikA_N} \quad . \tag{6.23}$$

This equation is solved exactly by the characteristic function that consequently defines the family of α-stable Lévy distributions $L_\alpha(\xi)$ with and exponent of

$$\ln \hat{L}_\alpha(k) = i\mu k - \sigma^\alpha |k|^\alpha \begin{cases} \left[1 + i\theta \operatorname{sgn}(k) \tan(\frac{\pi\alpha}{2})\right] & \text{for} \quad \alpha \neq 1 \\ \left[1 + i\theta \operatorname{sgn}(k) \frac{2}{\pi} \ln|k|\right] & \text{for} \quad \alpha = 1 \end{cases} \quad , \tag{6.24}$$

where sgn(k) is the sign function. Inserting and equating the real and imaginary parts of Eq. 6.23 straightforwardly yields $B_N = N^{\frac{1}{\alpha}} > 0$ and $A_N = (N - N^{\frac{1}{\alpha}})\mu$. Note that this scaling generalizes the method applied for Eq. 6.20. The parameter $0 < \alpha \leq 2$ denotes the 'index of stability' of the distribution, and we recover the Gaussian for the special case of $\alpha = 2$, with a variance of $2\sigma^2$. The parameter $-1 \leq \theta \leq 1$ determines the asymmetry of the distribution, where e.g. $\theta < 0$ results in a distributions that are skewed to the right. The scale of the distribution is given by σ, and a shift can be induced by μ, but is set to zero in the following for simplicity. Examples of markovian random walks with such step size distributions are shown in Fig. 6.2. By definition of α-stable random variables, their propagator must remain an α-stable distribution, as it represents an increasing number of their convolutions.

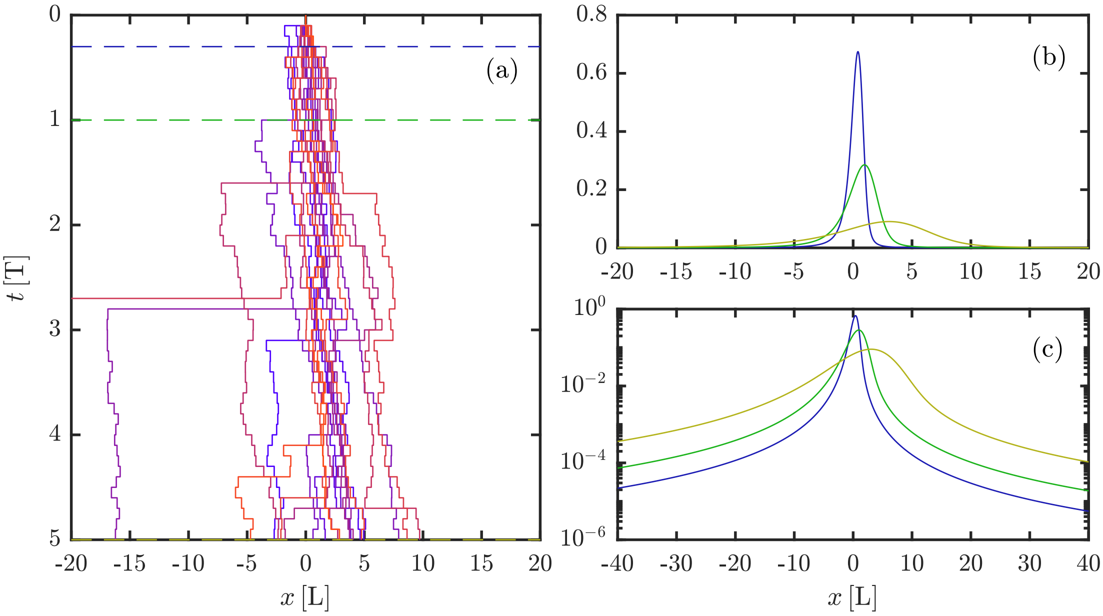

Figure 6.2 – We show 20 random walks based on a Lévy stable distribution $L_\alpha \xi$ of step-sizes, taken at regular time-intervals of $\Delta t = 0.1$ in (a). The parameters of $L_\alpha \xi$ are chosen according to Eq. 6.24 as $\alpha = 1.4$, $\sigma = 1$ and $\theta = 0.6$. Note the distinctly non-Gaussian properties of the propagators of the same form in (b), in particular the much heavier, algebraic tails compared to Fig. 6.1, each following $G(x,t) \sim |x|^{-(\alpha+1)}$. With a significant $\theta > 0$, their left tail in (c) for $x < 0$ is heavier still than the right, but converges to the same overall slope. Note that similar, markovian random walks and identical propagators would be found if the given step sizes Δt were not constant, but followed an exponential distribution type with an average of Δt, as described by Poisson-processes. With a transport exponent of e.g. $\nu = \frac{2}{\alpha} 1.43 > 1$ from Eq. 6.33, any markovian Lévy-stable processes with $\alpha < 2$ fall within the superdiffusive regime.

Many equivalent parameterizations exist [116, 136], and are usually adopted to simplify the algebra of a given problem. Note that the above parameters, except α, are often combined and redefined in this process and thus take different values. For instance, in [116] and previous work [108, 136] one finds for $\alpha \neq 1$

$$\ln \hat{L}_\alpha(k) = i\mu k - \sigma^\alpha |k|^\alpha \exp\left[i \,\mathrm{sgn}(k) \frac{\pi\theta}{2} \right], \tag{6.25}$$

where the new asymmetry parameter must follow the restrictions $|\theta| \leq \alpha$ for $\alpha < 1$ and $|\theta| \leq$

$2-\alpha$ for $1<\alpha<2$. Closed form expressions of the distributions $L_\alpha(\xi)$ are only available in a few special cases of α, so that most manipulations in the following are performed on the characteristic function. However, it can be shown e.g by Taylor-expanding $\hat{L}_\alpha(k)$ to 1st order in k before Fourier-inverting, that we have $L_\alpha(\xi)\sim|\xi|^{-(\alpha+1)}$ for $\xi\to\pm\infty$. These heavy, algebraic tails of $L_\alpha(\xi)$ thus accommodate e.g. the described occurrences of long jumps, while their variance becomes infinite for any $\alpha<2$.

6.2.2 Continuous Time Random Walks

To use Lévy distributions in the description of a non-markovian random walk, we firstly turn to the generalization of Einstein's approach in the form of Continuous Time Random Walks (CTRWs) as introduced by Montroll and Weiss in 1965 [117]. This model has since received extensive attention as outlined in [116, 200, 114] and generally defines the arrival probability $\eta(x,t)$ of a random walker at a given time and position as

$$\eta(x,t)=\iint dx'\,dt'\,\eta(x',t')w(t-t')P(x-x')+\delta(x)\delta(t)\,, \tag{6.26}$$

where $w(\tau)$ denotes the waiting time distribution. It has been assumed that step-sizes and waiting times are independent, and their distribution thus separable. The equation for the propagator of a CTRW is consequently defined by

$$G(x,t)\;=\;\int_0^t dt'\,\eta(x,t')\left(1-\int_0^{t-t'}d\tau\,w(\tau)\right)\,. \tag{6.27}$$

After solving Eq. 6.26 for $\hat{\eta}(k,s)$ using a Fourier-Laplace transform from (x,t)-space into (k,s)-space, the result can be inserted into the Fourier-Laplace transform of Eq. 6.27 to yield the well-known Montroll-Weiss equation

$$\hat{G}(k,s)\;=\;\frac{1}{1-\hat{P}(k)\hat{w}(s)}\left(\frac{1-\hat{w}(s)}{s}\right)\quad. \tag{6.28}$$

To approach the generalized form of the governing diffusion equation, we again employ the fluid limit, i.e. we let $k\ll 1$ and $s\ll 1$ in Fourier-Laplace space. This yields $\hat{P}(k)=\hat{L}_\alpha(k)\to 1-\sigma^\alpha|k|^\alpha\exp(i\,\mathrm{sgn}(k)\frac{\pi\theta}{2})$, for the parameterization in Eq. 6.25. Since only positive values of waiting times are allowed, a one-sided Lévy distribution must be used if we wish to generalize from the Markovian case. Again using the parameterization in Eq. 6.25, they are available for a stability index $\alpha\to\beta<1$, with a minimum value of $\theta=-\beta$, such that $w(\tau)$ is only defined for $\tau>0$ while still obeying $w(\tau)\sim\tau^{-(\beta+1)}$ for $\tau\to\infty$ and conversely $\hat{w}(s)\to 1-\sigma_w^\beta s^\beta$ for $s\ll 1$. Inserting into Eq. 6.28, this yields to 1st order

$$\hat{G}(k,s)\;=\;\frac{\sigma_w^\beta s^{\beta-1}}{\sigma_w^\beta s^\beta-\sigma^\alpha|k|^\alpha\exp(i\,\mathrm{sgn}(k)\frac{\pi\theta}{2})}\quad, \tag{6.29}$$

from which we can separate all explicit dependence on s and k to find

$$s^{\beta}\hat{G}(k,s) - s^{\beta-1} = \frac{\sigma^{\alpha}}{\sigma_w^{\beta}}|k|^{\alpha} e^{(i\,\mathrm{sgn}(k)\frac{\pi\theta}{2})}\hat{G}(k,s) \quad . \tag{6.30}$$

On the LHS one recognizes the Laplace transform of the Caputo derivative ${}_{C}\mathcal{D}_t^{\beta}$ of fractional order β and on the RHS the Fourier transform of the Riesz-Feller derivative ${}_{RF}\mathcal{D}_x^{\alpha,\theta}$ of fractional order α and asymmetry θ [215]. The forms of all fractional integro-differential operators relevant to these chapters are motivated and summarized in App. C. Inverting both transforms therefore yields the general space- and time-Fractional Diffusion Equation (FDE)

$${}_{C}\mathcal{D}_t^{\beta} G(x,t) = \underbrace{\frac{\sigma^{\alpha}}{\sigma_w^{\beta}}}_{D_{\alpha,\beta}} \;{}_{RF}\mathcal{D}_x^{\alpha,\theta} G(x,t) \tag{6.31}$$

The long-range dependence in x and t introduced by the heavy tailed Lévy distributions, are therefore embodied by the integrals involved in these fractional derivatives. Since they determine the weight and range of the respective integration kernels, the stability indices α and β are respectively referred to as the *space-fractional* exponent and the *time-fractional* exponent, while the scaling parameters determine the fractional diffusion coefficient $D_{\alpha,\beta}$. The initial conditions enter the equation by the finite lower limit of the Caputo derivative, as the differentiation occurs inside the integral in this case. Note that we recover Markovianity through a 1st order time-derivative for $\beta = 1$, but only recover a Gaussian propagator by simultaneously letting $\alpha = 2$ to retrieve the 2nd order spatial derivative, which results in the ordinary diffusion equation. The general propagator solutions $G(x,t)$ have been detailed by Mainardi, Luchko and Pagnini in Ref. [215], but again do not possess a general closed form. They can rather be written as Fox-H or Meijer-G functions in terms of Mellin-Barnes integrals or series representations [215, 216]. Examples for sub- and superdiffusive CTRWs are shown in Figs. 6.3 and 6.4 respectively.

Many key properties of the CTRW transport process can already be illustrated using $\hat{G}(k,s)$. Writing the Fourier-Laplace inversion of Eq. 6.29, the probability of finding a random walker between x and $x + dx$ at time t is given by

$$G(x,t)\,dx = \frac{1}{4\pi^2 i}\int_{-\infty}^{\infty} dk\, e^{-ikx} \oint_{\delta-i\infty}^{\delta+i\infty} ds\, e^{st}\, \frac{\sigma_w^{\beta} s^{\beta-1}}{\sigma_w^{\beta} s^{\beta} - \sigma^{\alpha}|k|^{\alpha}\exp(i\mathrm{sgn}(k)\frac{\pi\theta}{2})} \quad dx \quad , \tag{6.32}$$

where the usual conventions of convergence hold for the contour choice in the inverse Laplace transform. This probability is invariant under the similarity transformation $\{x,t\} \to \{c^H x, ct\}$ for $H = \frac{\beta}{\alpha}$, which can be shown through the changes of the integration variables $k \mapsto c^{-H}k$ and $s \mapsto c^{-1}s$, as expected from the scaling properties of Fourier and Laplace transforms. Therefore, $G(x,t)$ is classified as H-self-similar and its moments have to follow a fixed scaling in time, with H denoting the *Hurst-exponent*. Suppose some possibly fractional moments $\langle x^q\rangle$ of order $q \in \mathbb{R} > 0$ exist and follow $\langle x^q\rangle \propto t^{q\nu/2}$, where $\nu > 0$ denotes the transport exponent

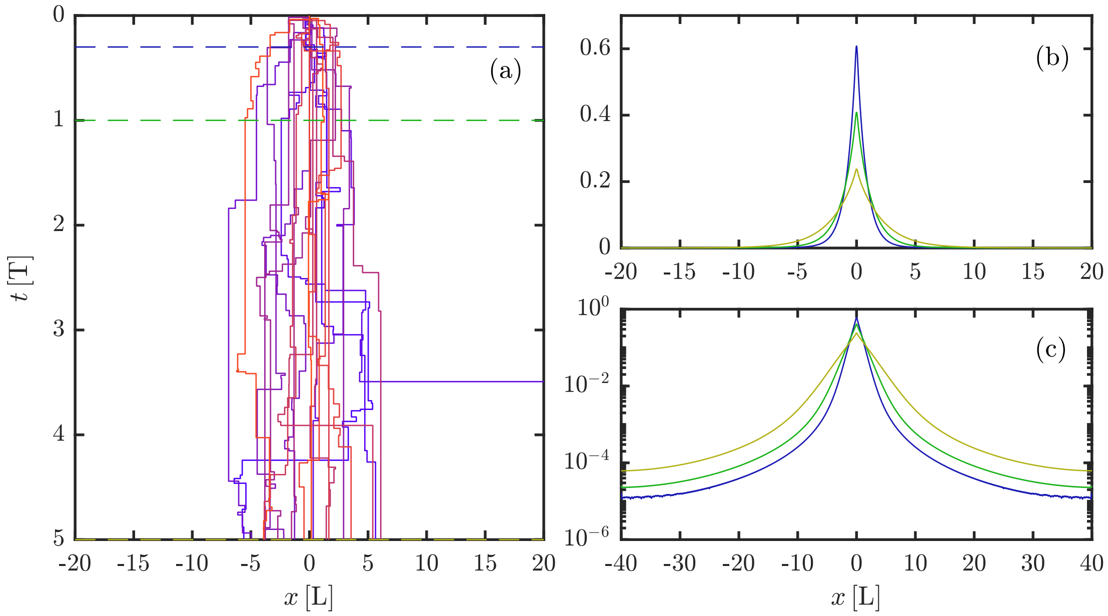

Figure 6.3 – Sub-diffusive ($\nu = 0.7$), symmetric CTRWs as in (a) are generated by using a one-sided Lévy-stable waiting time PDF, with time-fractional exponent $\beta = 0.6 < 1$ in this case. Consequently we chose $\alpha = \frac{2\beta}{\nu} = 1.71$, allowing for a still visible number of long jumps. However, the waiting times outweigh this effect and reduce transport to the subdiffusive level, and $G(x,t)$ stays peaked near the origin for longer (b). The tails of $G(x,t)$ in (c) remain nonetheless heavy especially compared to the Gaussian case.

as defined above from the case $q \to 2$. Based on the self-similarity property, one immediately finds

$$\langle (c^H x)^q \rangle = c^{qH} \langle x^q \rangle \propto (ct)^{\frac{q\nu}{2}} \Rightarrow \nu = 2H = \frac{2\beta}{\alpha} \quad . \tag{6.33}$$

This directly illustrates the non-diffusive nature of such a CTRW, and permits to identify the cases of subdiffusion for $2\beta < \alpha$, and super-diffusion for $2\beta > \alpha$. The case $2\beta = \alpha$ denotes quasi-diffusion, which is more general than the diffusive case due to the possible presence of non-Gaussian features. Note that the variance $\langle x^2 \rangle$ of $G(x,t)$ need not (and does not) always converge. To directly investigate diverging moments, one can either analytically truncate them above a given scale [116], or use Monte-Carlo sampling on an appropriate numerical implementation of the propagator up to a desired degree of convergence. Furthermore, it should be noted that, the functional form of the inverse Laplace transform in Eq. 6.32 is known to be the Mittag-Leffler function and one can therefore write [215]

$$\hat{G}(k,t) = E_\beta\left(\sigma^\alpha |k|^\alpha \exp(i \mathrm{sgn}(k) \frac{\pi\theta}{2}) t^\beta\right) \quad \text{with} \quad E_\beta(\tau) \equiv \sum_{n=0}^{\infty} \frac{\tau^n}{\Gamma(\beta n + 1)} \quad , \tag{6.34}$$

from which the above invariance becomes even more directly visible.

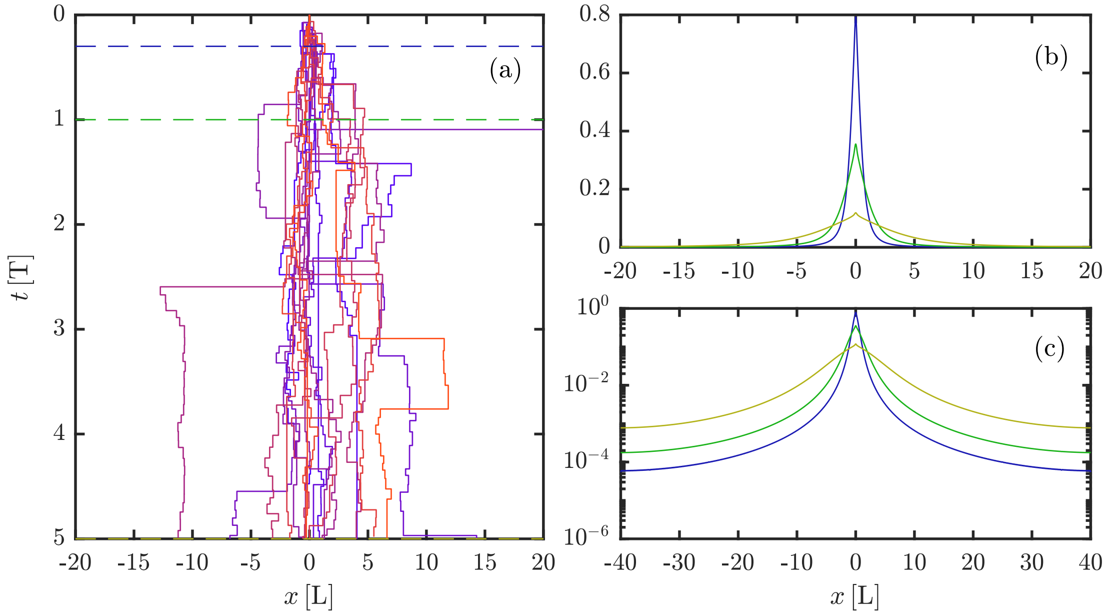

Figure 6.4 – In (a), we show non-markovian superdiffusive CTRWs with $\nu = 1.5$. While we still have $\beta = 0.9 < 1$ for the time-fractional exponent, long waiting times are clearly less prevalent compared to Fig. 6.3. To return to superdiffusion, the space fractional exponent was additionally lowered to $\alpha = 1.2$, to allow for an increase in longer jumps. Consequently, the bulk of the propagator in (b) clearly decays faster, and the tails in (c) are distinctly heavier than in Fig. 6.3.

6.2.3 Generalized Langevin Equations

Naturally, also Langevin's approach can be adapted to accommodate non-diffusive transport and has been discussed extensively in the literature [116, 119, 136, 118]. A particularly in-depth treatment is given by Samorodnitsky and Taqqu [118], where such definitions and properties as in the following are analyzed from first principles. Non-markovian behavior is implemented by introducing a non-constant friction coefficient $\gamma(t)$, and requiring a convolution instead of a simple multiplication in Eq. 6.9 to arrive at the Generalized Langevin Equation (GLE). Equivalently, one can directly generalize Eq. 6.12 (with $v_0 = 0$) by introducing a memory kernel $M(t)$ into the integral

$$x(t) = \int_0^t M(t-t')\xi(t')\,dt' = \frac{1}{\Gamma(H+1/2)}\int_0^t (t-t')^{H-\frac{1}{2}}\xi(t')\,dt' \quad . \tag{6.35}$$

This choice of kernel defines Fractional Brownian Motion (FBM) [217], if the random increments ξ are drawn from a Gaussian distribution $P(\xi)$. A second generalization is implemented by choosing α-stable Lévy distributions, to allow for non-local behaviour, resulting in a definition for Fractional Lévy Motion

$$x(t) = \frac{1}{\Gamma(H-1/\alpha+1)} \int_0^t (t-t')^{H-\frac{1}{\alpha}} \xi(t')\, dt' = {}_0\mathcal{I}_t^{H-1/\alpha+1} \xi(t) \quad . \tag{6.36}$$

For brevity, we can use the notation of the Riemann fractional integral ${}_0\mathcal{I}_t^q$ of order q that this equation represents [183, 209] (see App. C). The exponents of the kernels have been chosen such that the above equations yield H-self-similar solutions, as will become apparent later. With probability distributions for the random increments that are stationary in time, these radom processes are classified as H-self similar with stationary increments, short H-sssi. The invariance under the similarity transform $\{x, t\} \to \{c^H x, ct\}$ can already be intuited here. For the scaling of $\xi(t)$, consider the scaling of the discretized sums of random steps in the Generalized Central Limit Theorem of $N^{\frac{1}{\alpha}}$. With N being related to t by an arbitrarily small constant $\epsilon = \frac{t}{N}$, this suggests a step-size scaling of $c^{1/\alpha}$, before being weighed by the memory kernel. Indeed, it can be shown straightforwardly that Markovian Lévy processes are H-self similar with $H = \frac{1}{\alpha}$, since the $\beta = 1$ case of the CTRW must be equivalent by definition. Inspecting the OBM in Eq. 6.12 as the simplest case, it can however be seen that due to its position inside the integral, ξ acquires an additional scaling inversely to time (e.g. as a velocity would in Eq. 6.12), leading to a total of $\xi \to c^{1/\alpha-1}\xi$ under the similarity transform. From this, the invariance of the FLM equation and any special cases such as FBM are directly verified.

As detailed e.g. in previous work [136], the use of these memory kernels can lead to persistent or anti-persistent behaviour in the trajectories $x(t)$, as their auto-correlations between different times can either become positive or negative depending on the choice of $H > \frac{1}{\alpha}$ or $H < \frac{1}{\alpha}$. Keeping the definition of $\beta = \alpha H > 0$, this corresponds to $\beta > 1$ and $\beta < 1$ respectively. Furthermore, based on the scaling of the moments of such an H-sssi process, the values of β are bounded to $\beta \leq 1$ for $\alpha < 1$ and $\beta \leq \alpha$ for $1 \leq \alpha < 2$ [118, 183]. We emphasize that this implementation of non-Markovianity is not equivalent to the CTRW approach that utilizes heavy-tailed waiting-times. This is illustrated in Figs. 6.5 and 6.6 for a subdiffusive and a superdiffusive FLM process, with their transport exponents chosen such that they correspond to those shown for the CTRWs in Figs. 6.3,6.4.

The method employed to find the propagator of these processes that we will focus on in all that follows has been introduced by Calvo, Sánchez and Carreras in Refs. [195, 183]. This approach discretizes the integrals of the trajectories until $x(t = T)$ into $N \to \infty$ steps of duration $\epsilon = \frac{T}{N}$,

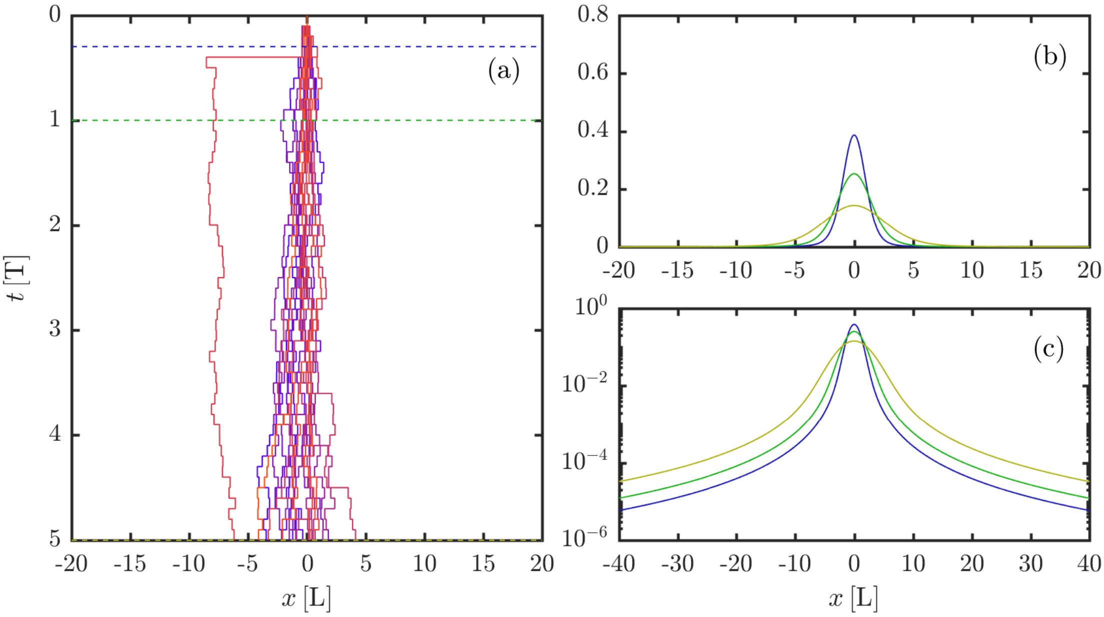

Figure 6.5 – Random walks as realizations of subdiffusive FLM processes with $\nu = 0.7$ are shown in (a), with both $\beta = 0.6$ and $\alpha = 1.71$ as for the CTRW case in Fig. 6.3. While waiting times are not needed to be drawn randomly in this approach, and long jumps are still possible, the average trajectories only diverge slowly due to anti-correlations introduced between consequent increments with $\beta < 1$. Note that due to the simpler Fourier transforms involved in the numerical calculations of the propagators in (b,c), that do not involve a Mittag-Leffler function on the characteristic exponent anymore, there is no discontinuity in slope at $x = 0$.

based on Feynman's path-integral approach to quantum field theory such that

$$\begin{aligned} x(T) &= \lim_{N\to\infty}\sum_{n=1}^{N}\delta x_n = \lim_{N\to\infty}\sum_{n=1}^{N}\frac{\epsilon^{1/\alpha-1}\,\xi_n}{\Gamma(\frac{\beta-1}{\alpha}+1)}\int\limits_{(n-1)\epsilon}^{n\epsilon}(T-t)^{\frac{\beta-1}{\alpha}}\,dt \\ &= \lim_{N\to\infty}\sum_{n=1}^{N}\frac{\epsilon^{H}\,\xi_n}{\Gamma(\frac{\beta-1}{\alpha}+2)}\underbrace{\left[(N-n+1)^{\frac{\beta-1}{\alpha}+1}-(N-n)^{\frac{\beta-1}{\alpha}+1}\right]}_{B_n} \\ &= \lim_{N\to\infty}\sum_{n=1}^{N}\frac{\epsilon^{H}\,\xi_n}{\Gamma(\frac{\beta-1}{\alpha}+2)}B_n\,\xi_n \quad . \end{aligned} \tag{6.37}$$

Analogous to the above scaling arguments, it is assumed that under discretization $\xi(t) \to \epsilon^{1/\alpha-1}\xi_n$ and that ξ_n be constant over the arbitrarily short step duration of each integral. Within this framework, the probability measure for each step is the distribution of the $L_\alpha(\xi_n)d\xi_n$, and the propagator is thus defined by an N-fold nested convolution of these step-size distributions

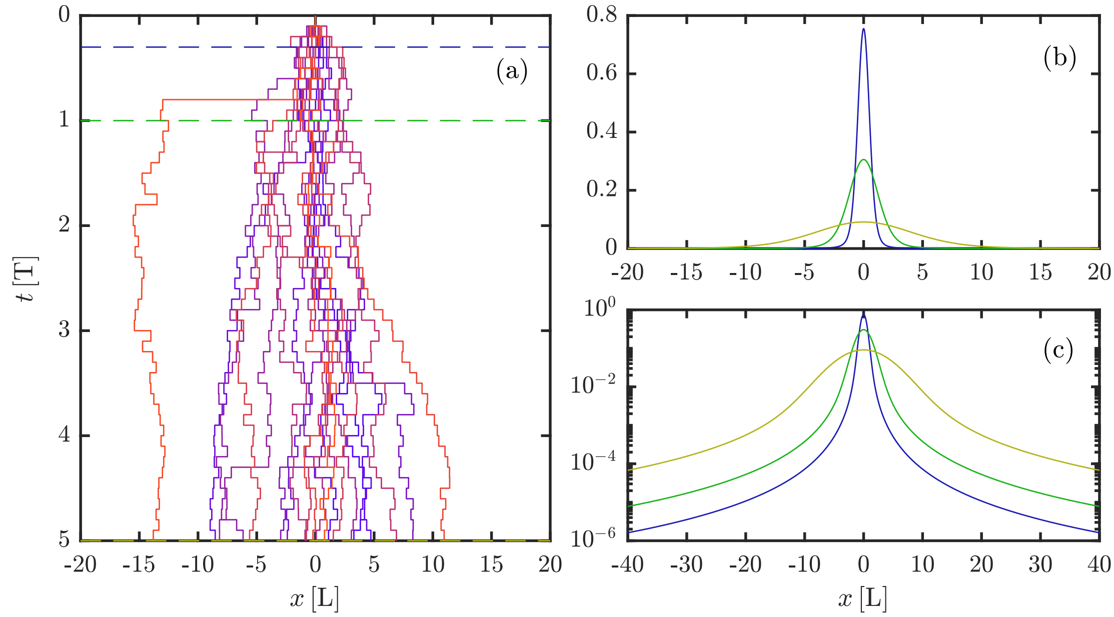

Figure 6.6 – In (a), we show realizations of non-Markovian superdiffusive Lévy processes, again with $\nu = 1.5$ as in the CTRW case in Fig. 6.4. To illustrate the introduction of positive correlations between consequent increments, we chose $\beta = 1.3 > 1$ here and note that the steps in many trajectories tend to follow consistent trends in the positive or negative direction, and therefore diverge faster than a diffusive case. The chosen value of $\alpha = 1.73$ is still very close to most other cases suggesting a similarly moderate occurrence of long jumps.

$$G(x(T),T) = \lim_{N\to\infty} f(N,T) \int \delta\big(\xi_N - \underbrace{\frac{\Gamma(\frac{\beta-1}{\alpha}+2)x(T)}{\epsilon^H}}_{A} + \sum_{n=1}^{N-1} B_n \xi_n\big) \prod_n = 1^N L_\alpha(\xi_n)\, d\xi_n \tag{6.38}$$

up to a normalization factor $f(N,T)$. The GLE of $x(T)$ represents the constraint on the path and thus enters within a δ-function. In its discretized form above, it has been rearranged for the last increment ξ_N (with $B_N = 1$), and can thus be used to solve the last convolution integral

$$G(x(T),T) = \lim_{N\to\infty} f(N,T) \int L_\alpha\left(A - \sum_{n=1}^{N-1} B_n \xi_n\right) \prod_n = 1^{N-1} L_\alpha(\xi_n)\, d\xi_n\, . \tag{6.39}$$

Retrieving the form of the propagator $G(x,t)$ therefore relies on the ability to evaluate the remaining $N-1$ nested convolutions analytically and before taking the limit $N \to \infty$ again. In Ref. [183] this is accomplished for symmetric Lévy distributions of ξ_n by iteratively using the identity

$$\int L_\alpha(\xi) L_\alpha(y - c\xi)\, d\xi = \frac{1}{g_\alpha(c)} L_\alpha\left(\frac{y}{g_\alpha(c)}\right) \quad \text{with} \quad g_\alpha(c) = (1 + c^\alpha)^{1/\alpha}, \tag{6.40}$$

which is proven there by using their scaling properties in Fourier-space. Since these apply to both symmetric and asymmetric distributions alike, Bovet likewise deduced the propagator for Asymmetrical Fractional Lévy Motion (AFLM) using the parameterization in Eq. 6.25 as detailed in Refs. [108, 136] as

$$G(x,T) = \frac{1}{Q(T)} L_\alpha\left(\frac{x}{Q(T)}\right) \quad \text{with} \quad Q(T) = \frac{T^H}{\beta^{1/\alpha}\Gamma(\frac{\beta-1}{\alpha}+1)} \quad . \tag{6.41}$$

The appropriate FDE is found by taking the time-derivative of the resulting $\hat{G}(k,t)$ before Fourier-inverting again, which yields

$$\partial_T G(x,T) = \underbrace{\frac{\sigma^\alpha t^{\beta-1}}{\Gamma(\frac{\beta-1}{\alpha}+1)^\alpha}}_{D_{\alpha,\beta}(t)} \; {}_{RF}\mathcal{D}_x^{\alpha,\theta} G(x,t)\,. \tag{6.42}$$

In the case of $\theta = 0$, ${}_{RF}\mathcal{D}_x^{\alpha,\theta}$ reduces to the symmetric Riesz-derivative ${}_{RZ}\mathcal{D}_x^{\alpha}$ as shown in Ref. [183] (see also App. C). In the case of $\alpha = 2$, $\sigma = 1$, the propagator for FBM is recovered as [195]

$$G(x,T) = \sqrt{\frac{\beta}{2\pi}}\frac{\Gamma(H+1/2)}{T^{\beta/2}} \exp\left(\frac{-\beta\Gamma(H+1/2)^2 x^2}{2T^\beta}\right) \tag{6.43}$$

and the spatial derivative smoothly recovers the ordinary 2nd order. Focusing on the time-dependence, a 'stretched time-derivative' [136, 218] of $\partial_{T^\beta} = \frac{1}{\beta T^{\beta-1}}\partial_T$ is recovered in all cases, so e.g. the FDE in the AFLM case can be written

$$\partial_{T^\beta} G(x,T) = \underbrace{\frac{\sigma^\alpha}{\beta\Gamma(\frac{\beta-1}{\alpha}+1)^\alpha}}_{D_{\alpha,\beta}} \; {}_{RF}\mathcal{D}_x^{\alpha,\theta} G(x,t) \quad . \tag{6.44}$$

In line with the concepts of positive or negative step-correlations, time is scaled to advance the decay of the δ-function initial conditions faster or slower than in the ordinary $\beta = 1$ case. This becomes particularly clear in the FBM case, where the time-dependence of the variance is changed to $\sigma^2 \propto t^\beta$. Note that if we keep an ordinary time-derivative as before, the fractional diffusion coefficient acquires time-dependence, which remains a fundamental difference to CTRW descriptions. The only direct equivalent is therefore the Markovian case of $\beta = 1$. Since the time-dependence in FLM therefore does not take the form of a Mittag-Leffler function, the propagator keeps the much more tractable (albeit not generally closed) form of the underlying step-size distributions.

The AFLM model was used successfully to model the asymmetric and superdiffusive nature of the (horizontal) cross-field transport of fast ions with $E \lesssim 30\,\text{eV}$ in the SMT geometry, based on simulations with GBS (see Sec. 2.5). Yet, certain practical and conceptual problems have remained. As described above, Lévy distributions are characterized by their heavy tails, implying the possibility of infinitely long jumps and indeed suggest non-finite spreading when considering the diverging variance of $G(x,t)$. Infinitely long jumps are natural impossibilities for physical particles, and indeed the tail region of the numerically simulated fast ion distributions is strongly over-estimated by any AFLM fits [108, 136]. In practice, some of the mathematical implications of diverging moments can be avoided as only finite numbers of tracers (walkers) are ever considered, and sample moments can be taken at any order. This results in an effective truncation of the distribution and its moments above some scale, related to the probability of finding at least one walker of a given sample number [219]. However, this scale thus appears somewhat arbitrarily defined. In practice, truncations can rather be due to attaining a certain, experimentally relevant scale that limits the effective domain size of a given transport process. In the following, we will therefore introduce models treating truncation effects at a fixed spatial scale explicitly, in order to derive Truncated Asymmetrical Lévy Motion (TAFLM) using the above path-integral methods.

The crux of the derivation will therefore lie in choosing and scaling our truncation parameter in such a way as to enforce a constant truncation effect, by compensating the memory kernel. This way, we will recover the ability to use an identity similar to Eq. 6.40.

6.3 Tempered stable distributions

In 1994, Mantegna and Stanley proposed the model of truncated Lévy flights, already with applications to turbulence in mind [220]. Koponen's approach from 1995 [221], in which he employs an exponential decay of $e^{-\lambda|x|}$, quickly became a widely used basis for investigations of tempered stable random processes, as e.g. those presented in depth in Refs. [222, 223]. A variety of distributions that temper the heavy tails of the α-stable Lévy case have been discussed and remain an active field of research in applied mathematics [224] as they indeed share the useful feature of finite moments at all orders [223, 224]. Applications of tempered stable dynamics range again across many fields, and are found particularly in finance [172, 223, 224], but also e.g. in criminology [225] and of course physics [120, 226, 114].

We will utilize a form and parameterization based on Refs. [120, 114], and thus write the characteristic exponent $\Lambda_{\alpha,\lambda}(k)$ of a tempered α-stable Lévy distribution $P_{\alpha,\lambda}(\xi)$ with $0 < \alpha \leq 2\,, \alpha \neq 1$ as

$$\ln \hat{P}_{\alpha,\lambda}(k) \equiv \Lambda_{\alpha,\lambda}(k) = -\underbrace{\frac{\sigma^{\alpha}}{2\cos(\frac{\alpha\pi}{2})}}_{\sigma^{\alpha}M}\left[(1+\theta)(\lambda+ik)^{\alpha}+(1-\theta)(\lambda-ik)^{\alpha}-2\lambda^{\alpha}-2i\theta k\alpha\lambda^{\alpha-1}\right].$$

The truncation parameter employed here is $\lambda > 0$, and represents an inverse truncation length-scale. While many authors utilize different parameters for the left- and right tail described by the first and second term respectively [223, 224], we will restrain ourselves to a symmetric truncation length at first. Clearly, $\sigma > 0$ still functions as a scale-parameter, and $-1 \leq \theta \leq 1$ quantifies the asymmetry of the distribution. As neither is essential for the distribution, unless it is single-sided, they will only appear in the explicitly written forms of $\Lambda_{\alpha,\lambda}(k)$. The third term preserves the normalization of the distribution, requiring $\hat{P}_{\alpha,\lambda}(k=0)=1$. The fourth term centers the distribution with its mean at zero, as can be shown by letting $\partial_k \hat{P}_{\alpha,\lambda}(k)|_0 = 0$. In contrast to [120], this term is kept for the full given range of α as we exclude the $\lambda = 0$ case, that would otherwise cause it to diverge for $\alpha < 1$. The centering of the distributions will facilitate their application to numerical fast ion distributions, as we wish to focus on their cross-field spreading without having to consider residual drifts. General closed form expressions of the distributions $P_{\alpha,\lambda}(\xi)$ are not available here either, but their tail behaviour of $P_{\alpha,\lambda}(\xi) \sim e^{-\lambda|\xi|}|\xi|^{-(\alpha+1)}$ can be verified again e.g. by the first order terms of a series expansion of the characteristic. Again, examples of markovian random walks using this type of distribution are shown in Fig. 6.7.

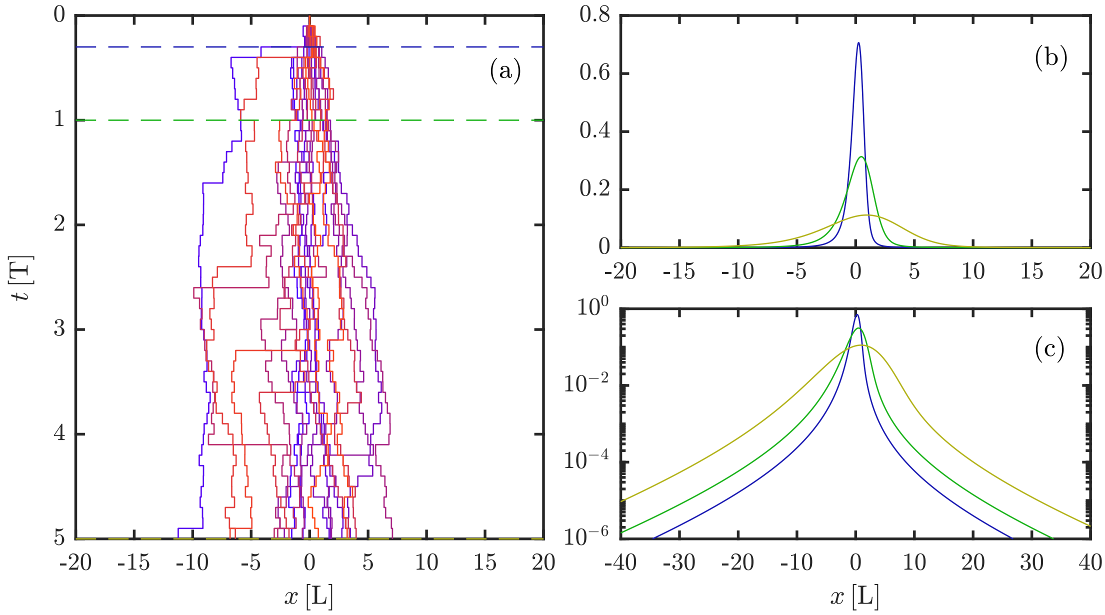

Figure 6.7 – Again, (a) shows 20 random walks with their step-sizes drawn from truncated Lévy stable distributions. Their parameters with $\alpha = 1.4$ and $\theta = 0.6$ are chosen equivalently to those in the Lévy stable case in Fig 6.2, but a truncation parameter of $\lambda = 0.1$ has been added. Therefore, jumps beyond the truncation scale $\lambda^{-1} = 10$ are being suppressed. Following the CLT, this implies that markovian tempered stable processes must be of a diffusive nature and recover FBM in the long run as discussed in [222, 223], although clearly non-Gaussian behaviour occurs within the truncation scale, which is reflected in initially likewise non-Gaussian propagators as shown in (b). The tails illustrated in (c) follow the exponentially tempered algebraic trend $G(x,t) \sim e^{-\lambda|x|}|x|^{-(\alpha+1)}$, and are therefore found between the algebraic tails from Lévy-type processes and the Gaussian case.

6.3.1 A truncated CTRW

Following the development in Ref. [120] further, one can use the characteristic $\Lambda_{\alpha,\lambda}(k)$ for the step-size distributions, which immediately yields for the fluid-limit of the Montroll-Weiss-

Equation 6.28

$$\hat{G}(k,s) = \frac{\sigma_w^\beta s^{\beta-1}}{\sigma_w^\beta s^\beta - \Lambda_{\alpha,\lambda}(k)} \quad . \tag{6.45}$$

This is therefore solved in Fourier-space analogously to Eq. 6.34 as $\hat{G}(k,t) = E_\beta\left(\Lambda_{\alpha,\lambda}(k)t^\beta\right)$, for which explicit series and further integral representations are given in [227], as well as finite double series expressions for all integer moments. However, some crucial properties of these propagators can again be made apparent just by writing the probabilities $G(x,t)\,dx$ explicitly using the inverse Fourier transform. For the Markovian case of $\beta = 1$ we have

$$\begin{aligned} G(x,t)\,dx \;=\; & \frac{1}{2\pi}\int_{-\infty}^{\infty} dk \exp\Big\{-ikx + t\sigma^\alpha M\big[(1+\theta)(\lambda+ik)^\alpha + (1-\theta)(\lambda-ik)^\alpha \\ & -2\lambda^\alpha - 2i\theta k\alpha\lambda^{\alpha-1}\big]\Big\} \quad dx \quad , \end{aligned} \tag{6.46}$$

for which the solution should be equivalent to the corresponding uncorrelated tempered stable process [222]. Clearly, due to the introduction of the truncation parameter $\lambda > 0$ into the characteristic, the invariance under the transformation $\{x,t\} \to \{c^H x, ct\}$ is lost, and therefore also the resulting scaling of the moments in Eq. 6.33. With their heavy tails truncated, these distributions are thus no longer H-self-similar. However, if we scale the truncation parameter inversely to x, we recover invariance under the transformation $\{x,t\} \to \{c^H x, ct, c^{-H}\lambda\}$, as would be expected from the scaling properties of $P_{\alpha,\lambda}(\xi)$ [219]. We will make use of this property in the following section, to adapt tempered stable distributions for the random increments $\xi(t)$ in a GLE.

The FDE associated with the truncated CTRW is again found by rearranging the Montroll-Weiss equation as in Eq. 6.30, and the performing an inverse Fourier-Laplace transform to yield [120]

$$\begin{aligned} \sigma_w^\beta\, {}_C\mathcal{D}_t^\beta G(x,t) \;=\; & \sigma^\alpha M\Big[(1-\theta)\, e^{-\lambda x}\, {}_{-\infty}\mathcal{D}_x^\alpha\big(e^{\lambda x}\, G(x,t)\big) + (1+\theta)\, e^{\lambda x}\, {}_x\mathcal{D}_\infty^\alpha\big(e^{-\lambda x}\, G(x,t)\big)\Big] \\ & -2\sigma^\alpha M\lambda^\alpha G(x,t) - 2\sigma^\alpha M\alpha\theta\lambda^{\alpha-1}\partial_x G(x,t) \\ \frac{\sigma_w^\beta}{\sigma^\alpha}\, {}_C\mathcal{D}_t^\beta \;=\; & {}_\lambda\mathcal{D}_x^{\alpha,\theta} G(x,t) - 2M\lambda^\alpha G(x,t) - 2M\alpha\theta\lambda^{\alpha-1}\partial_x G(x,t) \quad . \end{aligned} \tag{6.47}$$

The operators ${}_{-\infty}\mathcal{D}_x^\alpha$ and ${}_x\mathcal{D}_\infty^\alpha$ denote the left-handed and the right-handed Liouville derivatives of order α respectively [209]. Their explicit definitions, along with the truncated asymmetrical fractional derivative ${}_\lambda\mathcal{D}_x^{\alpha,\theta}$ are given again in App. C. The third term results from the normalization requirement, and the fourth term represents the centering drift in the $\theta \neq 0$ case. The coefficient $D_{\alpha,\beta}$ is found again as its inverse on the LHS, but will affect not just the diffusion terms, but also the normalization and drift, so that its interpretation as a pure diffusion coefficient is no longer exhaustive. Examples of tempered CTRWs as described here are shown along with their propagators in Fig. 6.8

As we proceed towards a model for a Langevin-based alternative to the truncated CTRW, it should be kept in mind that the Markovian case as illustrated in Fig. 6.7 of both approaches

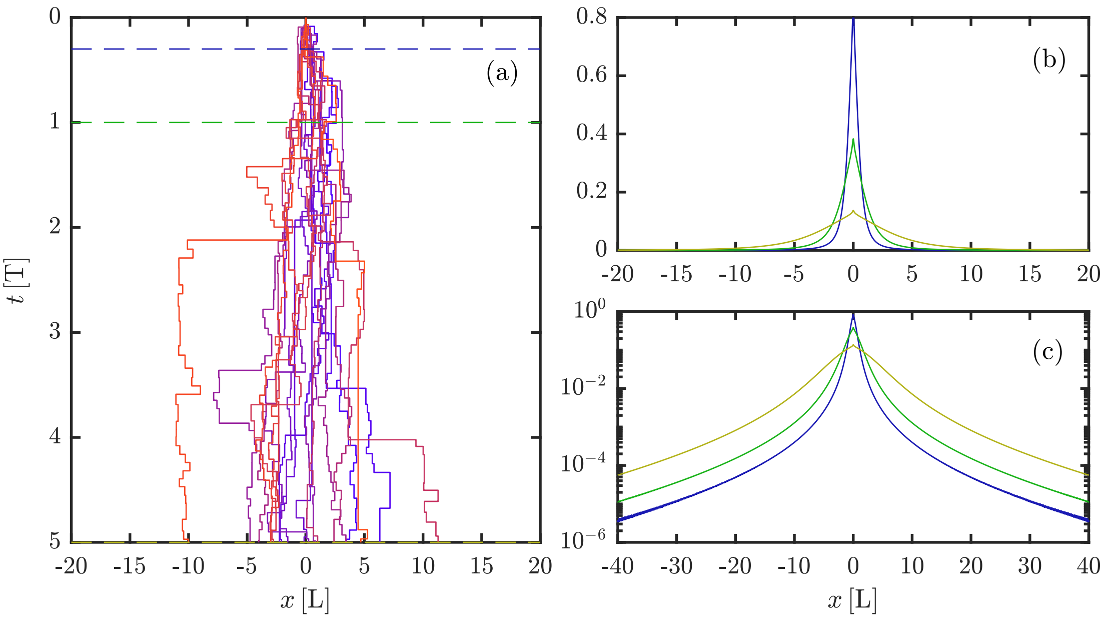

Figure 6.8 – Random walks based on the truncated CTRW model are shown in (a), with $\alpha = 1.2$ and $\beta = 0.9$ as in the superdiffusive CTRW case in Fig. 6.4. A small truncation of only $\lambda = 0.05$ has been introduced, effectively limiting Lévy-type jumps to the shown domain-size of $\lambda^{-1} = 20$ when comparing panel (a,b). Although the principal shapes of the propagators in (b) still appear very similar, their tails in (c) are clearly diminished due to the suppression of the longest jumps.

should recover the same FDE, with a first order time-derivative on the LHS.

6.4 Truncated Asymmetrical Fractional Lévy Motion

While much of the above introduction to truncated CTRWs has likewise been given in a more condensed form in Ref. [112], we will now present the core of this paper. Based on the path-integral methods for its solution from Ref. [195] we wish to develop a case where the path increments are drawn from a tempered stable distribution. Starting from the same GLE as in Eq. 6.36, we firstly need to apply a discretization again. For the increments we will still assume $\xi(t) \to \epsilon^{1/\alpha-1}\xi_n$, based on the scaling properties of uncorrelated tempered stable processes illustrated from the Markovian CTRW, if we simultaneously insist that the truncation parameter scales inversely to this. This of course implies that the truncation parameter for the increments ξ acquires time dependence. In a different context, some uses of time-dependent truncation parameters have been discussed in [228] and related works, but we will still need to determine their specific forms required for the TAFLM process in the following.

Since there is thus no difference to the rest of the integral in the GLE, the discretization from

Eqs.6.37 is still taken as valid under this condition, giving

$$x(T) = \lim_{N\to\infty} \sum_{n=1}^{N} \delta x_n = \lim_{N\to\infty} \sum_{n=1}^{N} \underbrace{\frac{\epsilon^H}{\Gamma(\frac{\beta-1}{\alpha}+2)} B_n}_{S_n} \xi_n \quad . \tag{6.48}$$

Since we wish to implement a constant truncation-scale in space, we must thus insist that this be a property of the distribution of δx_n, i.e. that we have

$$P(\delta x_n) = P_{\alpha,\lambda}(\delta x_n) = P_\alpha(\delta x_n|\lambda) \quad \forall n \quad . \tag{6.49}$$

Since we insist on the same truncation scale λ^{-1} and thus the same form of distribution at all steps δx_n, the process is rendered stationary in this sense. As in the last step, we will from now on write the truncation parameter as an argument of P, separated by the |-notation, as showing its manipulations is impractical for subscripts.

To progress the solution we require the form of the distribution of ξ_n. From the above, it is clear that ξ_n is related to δx_n by a local scaling induced by the memory kernel of $\delta x_n \to S_n^{-1}\delta x_n$. Again enforcing the requirement of the truncation parameter to always scale inversely to the argument of the distribution, we find

$$P(\xi_n) = P\left(\frac{\delta x_n}{S_n}\right) = P_\alpha(\xi_n|S_n\lambda) = P_\alpha(\xi_n|\gamma_n) , \tag{6.50}$$

where we have defined the discretized time-dependent truncation parameter $\gamma_n = S_n\lambda$. To obtain units of time in the scaling factor S_n, as one would while returning towards the continuous form of the GLE, we require indeed a factor of $\epsilon^{1/\alpha-1}$, so that the inverse scaling under discretization as described above appears valid for this choice of truncation. Furthermore, the product $\gamma_n\xi_n$ occurring in any exponential truncation factors, as in $P(\xi_n|\gamma_n) \sim e^{-\gamma_n|\xi_n|}|\xi_n|^{-(\alpha+1)}$ to first order, clearly remains dimensionless as required. The resulting random walks as incrementally described by Eq. 6.48 are illustrated in Fig. 6.9, along with their propagators as detailed in the following.

With the distribution $P_\alpha(\xi_n|\gamma_n)$ determined for each step n, we continue to adopt the same definition of the propagator as given in Eqs. 6.38,6.39 without further changes to the form of the constraint, provided ξ_n are drawn accordingly, i.e.

$$G(x(T),T) = \lim_{N\to\infty} f(T,N) \int P_\alpha\left(A - \sum_{n=1}^{N-1} B_n\xi_n \middle| \gamma_N\right) \prod_{n=1}^{N-1} P_\alpha(\xi_n|\gamma_n)\, d\xi_n \quad . \tag{6.51}$$

To solve the remaining $N-1$ convolutions, we need to verify if an identity such as Eq. 6.40 is still iteratively valid for this choice of distribution. For ease of notation during this, we write

$$\gamma_n = S_n\lambda = B_n\gamma \quad \text{with} \quad \gamma = \frac{\epsilon^H\,\lambda}{\Gamma(\frac{\beta-1}{\alpha}+2)} \quad , \tag{6.52}$$

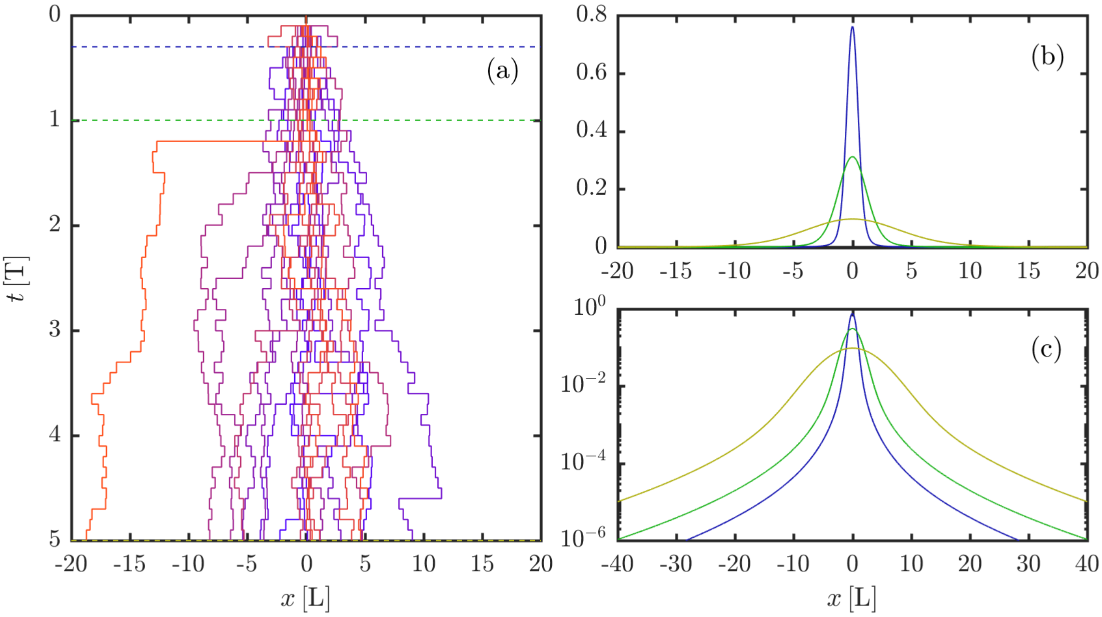

Figure 6.9 – Random walks according to as described by the discretized GLE in Eq. 6.48, using truncated α-stable random variables for step-increments for a symmetric case. The parameters $\alpha = 1.73$ and $\beta = 1.3$ have been chosen as for the untruncated, superdiffusive case in Fig. 6.6. However, due to the same slight truncation as for the CTRW case with $\lambda = 0.05$, the impact of the heavy jumps is curtailed, which reduces the transport exponent from $\nu = 1.5$ to $\nu = \beta = 1.3$, as will be demonstrated in the sections below.

to then verify if

$$\int P_\alpha(x|c\gamma)P_\alpha(y-cx|\gamma)dx = \frac{1}{g_\alpha(c)}P_\alpha\left(\frac{y}{g_\alpha(c)}\middle|\gamma g_\alpha(c)\right) \quad \text{with} \quad g_\alpha(c) = (1+c^\alpha)^{1/\alpha} \quad . \tag{6.53}$$

This can be illustrated most directly by treating the propagator for the simplest case of $N-1 = 2$, for which Eq. 6.51 becomes

$$\begin{aligned} G(x,t) &= \int P_\alpha(A-B_2\xi_2-B_1\xi_1|\gamma)P_\alpha(\xi_1|\gamma_1)P_\alpha(\xi_2|\gamma_2)d\xi_1 d\xi_2 \\ &= \int P_\alpha(A-B_2\xi_2-\xi_1|\gamma)P_\alpha(\frac{\xi_1}{B_1}|\gamma_1)P_\alpha(\xi_2|\gamma_2)\frac{d\xi_1}{B_1}d\xi_2 \\ &= \int I_1 P_\alpha(\xi_2|\gamma_2)d\xi_2\,, \end{aligned} \tag{6.54}$$

where we have used $\gamma_N = \gamma$ and changed the inner integration variable $\xi_1 \mapsto \xi_1/B_1$. We now evaluate the inner integral I_1, for which we have $c = B_1$, $x = \xi_1$, $y = A - B_2\xi_2$ when comparing to Eq. 6.53. Analogously to the probability distribution $P_\alpha\xi_n|\gamma_n$, we furthermore now denote

$\Lambda_{\alpha,\gamma_n}(k) = \Lambda_\alpha(k|\gamma_n)$ for clarity. Evaluating I_1 thus reads

$$\begin{aligned}
I_1 &= \frac{\mathcal{F}^{-1}}{B_1}\left\{\mathcal{F}\{P_\alpha(A - B_2\xi_2 - \xi_1|\gamma)\}\mathcal{F}\left\{P_\alpha\left(\frac{\xi_1}{B_1}\middle|\gamma_1\right)\right\}\right\} \\
&= \mathcal{F}^{-1}\left\{\hat{P}_\alpha(k|\gamma)\hat{P}_\alpha(B_1k|B_1\gamma)\right\}(A - B_2\xi_2) \\
&= \mathcal{F}^{-1}\Big\{\exp\left[\Lambda_\alpha(k|\gamma) + \Lambda_\alpha(B_1k|B_1\gamma)\right]\Big\}(A - B_2\xi_2) \\
&= \mathcal{F}^{-1}\Big\{\exp\left[(1 + B_1^\alpha)\Lambda_\alpha(k|\gamma)\right]\Big\}(A - B_2\xi_2) \\
&= \mathcal{F}^{-1}\Big\{\hat{P}_\alpha(g_\alpha(B_1)k\,|\,g_\alpha(B_1)\gamma)\Big\}(A - B_2\xi_2) \\
&= \frac{1}{g_\alpha(B_1)}P_\alpha\left(\frac{A - B_2\xi_2}{g_\alpha(B_1)}\middle|g_\alpha(B_1)\gamma\right) \quad . \qquad (6.55)
\end{aligned}$$

This demonstrates that Eq. 6.53 is valid for the first convolution. This is accomplished specifically by our choice of $\gamma_1 = B_1\gamma$ as truncation parameter, so that we can use $\Lambda_\alpha(B_1k|B_1\gamma) = B_1^\alpha\Lambda_\alpha(k|\gamma)$ in the 4th line. To show that this procedure remains valid iteratively, we continue to evaluate the 2nd integral in Eq. 6.54, for which we again change the integration variable $\xi_2 \mapsto \frac{g_\alpha(B_1)\xi_2}{B_2}$, yielding

$$\begin{aligned}
G &= \frac{1}{g_\alpha(B_1)}\int P_\alpha\left(\frac{A - B_2\xi_2}{g_\alpha(B_1)}\middle|g_\alpha(B_1)\gamma\right)P_\alpha(\xi_2|B_2\gamma)d\xi_2 \\
&= \frac{1}{B_2}\int P_\alpha\left(\frac{A}{g_\alpha(B_1)} - B_2\xi_2\middle|g_\alpha(B_1)\gamma\right)P_\alpha\left(\frac{g_\alpha(B_1)\xi_2}{B_2}\middle|\frac{B_2}{g_\alpha(B_1)}g_\alpha(B_1)\gamma\right)d\xi_2 \\
&= \frac{1}{g_\alpha(\frac{B_2}{g_\alpha(B_1)})g_\alpha(B_1)}P_\alpha\left(\frac{A}{g_\alpha(\frac{B_2}{g_\alpha(B_1)})g_\alpha(B_1)}\middle|g_\alpha\Big(\frac{B_2}{g_\alpha(B_1)}\Big)g_\alpha(B_1)\gamma\right) \\
&= \frac{1}{(1 + B_1^\alpha + B_2^\alpha)^{1/\alpha}}P_\alpha\left(\frac{A}{(1 + B_1^\alpha + B_2^\alpha)^{1/\alpha}}\middle|(1 + B_1^\alpha + B_2^\alpha)^{1/\alpha}\gamma\right) \quad .
\end{aligned}$$

Therefore we have shown that Eq. 6.53 can be used to iteratively evaluate the convolutions within the propagator in Eq. 6.51. Using the relation

$$\left(\sum_{n=1}^{N-1} B_n^\alpha\right)^{1/\alpha} \sim \frac{(\frac{\beta-1}{\alpha} + 1)}{\beta^{1/\alpha}}N^H \qquad (6.56)$$

in the limit of $N \to \infty$, as proven in [195], we therefore recover the TAFLM propagator as

$$\begin{aligned}
G(x,T) &= f(N,T)\,P_\alpha\left(\frac{\Gamma(\frac{\beta-1}{\alpha} + 2)\beta^{1/\alpha}x(T)}{(\frac{\beta-1}{\alpha} + 1)\epsilon^H N^H}\middle|\frac{(\frac{\beta-1}{\alpha} + 1)N^H\epsilon^H\lambda}{\Gamma(\frac{\beta-1}{\alpha} + 2)\beta^{1/\alpha}}\right) \\
G(x,T) &= \frac{1}{Q(T)}P_\alpha\left(\frac{x}{Q(T)}\middle|\lambda Q(T)\right) \quad \text{with} \quad Q(T) = \frac{T^H}{\beta^{1/\alpha}\Gamma(\frac{\beta-1}{\alpha} + 1)} \, . \qquad (6.57)
\end{aligned}$$

In second step, the normalization factor $f(N,T)$ was again verified straightforwardly in

Fourier-space by taking

$$1 = \hat{G}(k)|_{k=0} = Q(T) f \hat{P}_\alpha(kQ(T)|\lambda Q(T))|_{k=0} = Q(T) f \exp\left[Q(T)^\alpha \underbrace{\Lambda_\alpha(k|\lambda)\right]|_{k=0}}_{0} . \tag{6.58}$$

The above assumptions therefore lead us to a form of $G(x,t)$ that appears to be an intuitive, albeit not necessarily straightforward, generalization from the FLM case in Eq. 6.41, since we continually insisted on the inverse scaling of the truncation parameter compared to x. Again returning to Fourier-space, the associated FDE is found analogously to the one in Eq. 6.44 by taking

$$\begin{aligned} \partial_T \hat{G}(k,T) &= \partial_T \hat{P}_\alpha(kQ(T)|\lambda Q(T)) = \partial_T \exp\left[Q(T)^\alpha \Lambda_\alpha(k|\lambda)\right] \\ &= \exp\left[Q^\alpha \Lambda_\alpha(k|\lambda)\right] \Lambda_\alpha(k|\lambda)\, \partial_T Q(T)^\alpha \\ &= \frac{T^{\beta-1}}{\Gamma(\frac{\beta-1}{\alpha}+1)^\alpha} \Lambda_\alpha(k|\lambda) \hat{G} \quad . \end{aligned} \tag{6.59}$$

After an inverse Fourier transform and re-introducing the stretched-time derivative and the coefficient $D_{\alpha,\beta} = \frac{\sigma^\alpha}{\beta\Gamma(\frac{\beta-1}{\alpha}+1)^\alpha}$ this yields

$$D^{-1}_{\alpha,\beta} \partial_{T^\beta} G(x,T) = {}_\lambda\mathcal{D}^{\alpha,\theta}_x G(x,T) - 2M\left[\lambda^\alpha G(x,T) + \alpha\theta\lambda^{\alpha-1}\partial_x G(x,T)\right] \quad , \tag{6.60}$$

where we retrieved the RHS of the FDE of truncated CTRW in Eq. 6.47 as expected, so that the markovian case $\beta = 1$ indeed yields the same FDE in both cases. This concludes the path-integral based derivation of our TAFLM model, as detailed in Ref. [112] for the first time to our knowledge.

To further verify this propagator and its properties, a Monte-Carlo solution based on the discretized GLE in Eq. was implemented for comparison, similar to the procedure employed to illustrate the different types of random walks throughout. As shown in Fig. 6.10, there is generally excellent agreement with the analytical form of the propagator at in both the bulk and the tails of the distributions, pending the finite number (10^7) of random walkers. For a weak truncation of $\lambda = 0.1$ in (a-c), there are strongly non-Gaussian features present, as already expected form Fig. 6.9. The chosen $\alpha = 1.4$ results in heavy tails, that are tempered only beyond the truncation scale of $\lambda^{-1} = 10$. They clearly approach the expected trend $G(x,t) \sim e^{-\lambda|x|}|x|^{-(\alpha+1)}$ (dashed green), especially compared to the tails of an un-truncated distribution with $G(x,t) \sim |x|^{-(\alpha+1)}$ (dashed gray). Due to the chosen asymmetry of $\theta = 0.6$, the left tail [cyan and magenta in (c)] is heavier still than the right, even at longer ranges. The bulk of the distribution is still well contained within the chosen truncation scale, and therefore the Central Limit Theorem has not yet taken fully effect. The converse is the case for a strong truncation of $\lambda = 10$ as shown in (d-f), with the same remaining parameters. The bulk of the distribution follows almost indistinguishably a Gaussian shape (dashed green), and a residual asymmetry is only apparent in the slightly heavier left far tail in (f).

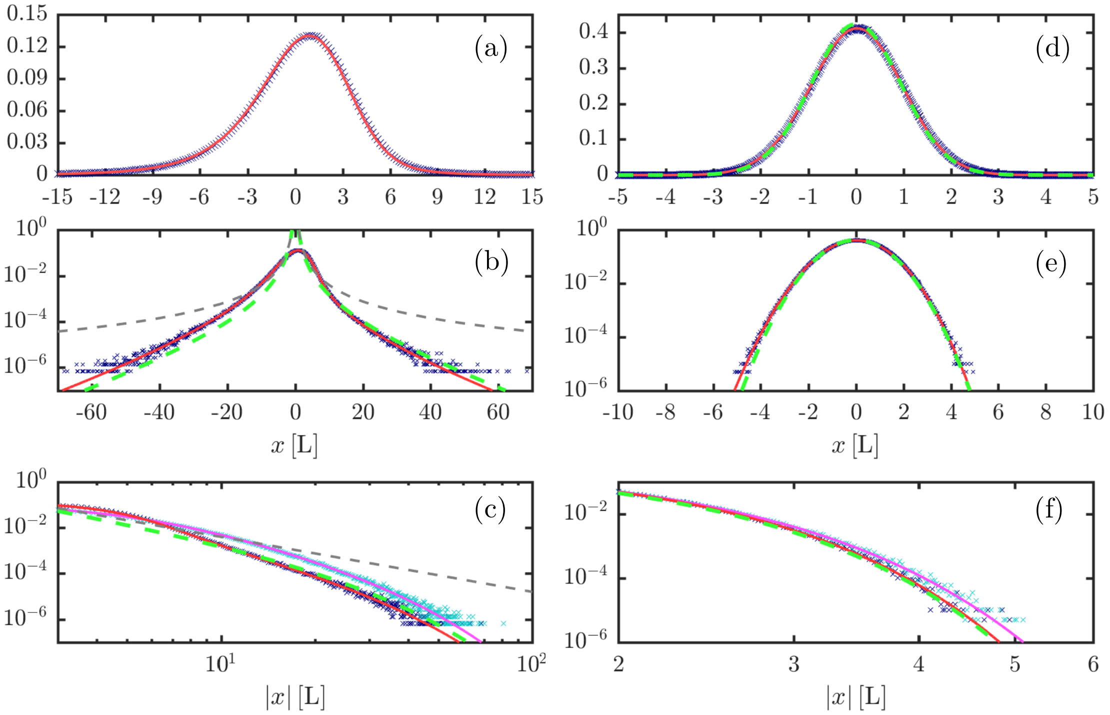

Figure 6.10 – Comparison between the analytical form of the propagator $G(x,t)$ (red) and binned Monte-Carlo solutions (blue crosses) based on 10^7 radom walks as illustrated in Fig. 6.9, where we are showing the time $T = 5$ here after likewise $N = 50$ random steps. For (d-f), the truncation parameter was augmented to $\lambda = 10$, resulting in a closely Gaussian transport, albeit both are strictly subdiffusive with $\nu = \beta = 0.8$.

These behaviours can be assessed more quantitatively using the moments of $G(x,t)$. Since all moments of truncated Levy distributions are however finite for a finite truncation $\lambda > 0$ [219], this property should extend to the propagator for $t > 0$ and $H > 0$. Therefore, they can be found using the appropriate integer derivatives in Fourier-space as shown in Eq. 6.17. For the CTRW case this has been done e.g. in [227], while the technique is applied to tempered stable processes in [223], where combinations of moments are even employed for direct parameter estimation. In our zero-centered stretched-time case, we thus find for the variance σ_G^2 of the propagator

$$\begin{aligned}\sigma_G^2 &= \mu_2 = -[\partial_k^2 \hat{G} - (\partial_k \hat{G})^2]|_{k=0} = -\partial_k^2 \Lambda_{\alpha,\lambda}(k)|_{k=0} Q^\alpha \\ &= \underbrace{\frac{\alpha(\alpha-1)}{-\cos\left(\frac{\pi\alpha}{2}\right)}}_{>0\,\forall\alpha} \sigma^\alpha \lambda^{\alpha-2} Q(T)^\alpha \quad . \end{aligned} \tag{6.61}$$

From this, the transport exponent is identified as $\nu = \beta$ at all time-scales, in contrast to $\nu = \frac{2\beta}{\alpha}$ in the un-truncated case. The same result is only obtained there in the case of FBM, by letting $\alpha = 2$. We likewise restrict our attention to values of $\beta \leq 2$, and thus transport regimes up to ballistic transport as detailed in Ch. 3. Considering the skewness S_G, we have

$$\begin{aligned} S_G &= \frac{\mu_3}{\mu_2^{3/2}} = \frac{\partial_k^3 \hat{G} - 3\partial_k^2 \hat{G} \partial_k \hat{G} + (\partial_k \hat{G})^3}{\left[\partial_k^2 \hat{G} - (\partial_k \hat{G})^2\right]^{\frac{3}{2}}}\Bigg|_{k=0} = \frac{\partial_k^3 \Lambda_{\alpha,\lambda}(k)\, Q^\alpha}{\left[\partial_k^2 \Lambda_{\alpha,\lambda}(k)\, Q^\alpha\right]^{\frac{3}{2}}}\Bigg|_{k=0} \\ &= \underbrace{\frac{\alpha(\alpha-1)(\alpha-2)}{-\cos\left(\frac{\pi\alpha}{2}\right)}}_{<0\,\forall\alpha} \Bigg(\underbrace{\frac{-\cos\left(\frac{\pi\alpha}{2}\right)}{\alpha(\alpha-1)}}_{>0\,\forall\alpha}\Bigg)^{\frac{3}{2}} \theta[\sigma\lambda Q(T)]^{\frac{-\alpha}{2}} \quad . \end{aligned} \tag{6.62}$$

As should be expected from a process converging to a Gaussian, the skewness is decaying over time, specifically with $S_G \propto T^{-\frac{\beta}{2}}$. The property $S_G \propto -\theta$ directly reflects how a positive asymmetry parameter results in a heavy left-hand tail, which could be reversed by redefining θ. To further quantify the tail behaviour in the symmetric case, one can similarly find the *excess* kurtosis

$$\begin{aligned} K_G &= \frac{\mu_4}{\mu_2^2} - 3 = \frac{\partial_k^4 \hat{G} - 4\partial_k^3 \hat{G} \partial_k \hat{G} + 6\partial_k^2 \hat{G} (\partial_k \hat{G})^2 - 3(\partial_k \hat{G})^4}{\left[\partial_k^2 \hat{G} - (\partial_k \hat{G})^2\right]^2}\Bigg|_{k=0} - 3 = \frac{\partial_k^4 \Lambda_{\alpha,\lambda}(k)\, Q^\alpha}{\left[\partial_k^2 \Lambda_{\alpha,\lambda}(k)\, Q^\alpha\right]^2}\Bigg|_{k=0} \\ &= \underbrace{\frac{(\alpha-2)(\alpha-3)\cos\left(\frac{\pi\alpha}{2}\right)}{-\alpha(\alpha-1)}}_{>0\,\forall\alpha} [\sigma\lambda Q(T)]^{-\alpha} \quad . \end{aligned} \tag{6.63}$$

With $K_G > 0$ for any finite t, this defines the TAFLM propagator as *leptokurtic*, while it converges towards the Gaussian *mesokurtic* case with $K_G \propto T^{-\beta}$. Furthermore both S_G and K_G appear invariant under the transformation $\{t, \lambda\} \to \{ct, c^{-\beta/\alpha}\lambda\}$, as would be expected from the invariance property of $G(x,t)$, and the product $\sigma\lambda$ must be dimensionless for a scale parameter σ with units of length. The variance being additionally scaled by λ^{-2} is thus also intuitive from its units.

The behaviour of these moments is not dissimilar to those in the CTRW case as given by [227], particularly compared to the obtained dependences on λ and t in the first terms of his summations. Furthermore, their scaling with time is generally very indicative towards the convergence to a Gaussian for large λ or t. Since the convergence to Brownian Motion was documented in detail in [222, 223], it seems intuitive that we should converge towards Fractional Brownian Motion in the same way, just with a re-scaled time-axis T^β. This brings the possible restrictions between the parameter values of α and β as detailed in Sec. 6.2.3 to our attention [118]. Knowing that all moments of our distributions are finite and seemingly converge to FBM could lead one to view the FBM restriction of $H < 1$ as generally applicable. However, it must be emphasized, that α in our case is more akin to a shape parameter, only affects tail behaviour up to the truncation scale and is not responsible for the bounding of any moments. More concisely, the underlying assumption of an H-sssi process is no longer generally valid in our case. However, the assumptions of a non-degenerate, stationary process with finite moments still do appear valid, and could be used to construct similar inequalities as those used to bound FLM parameter-space in Ref. [118]. The use of their self-similar scaling property can be emulated by using the scaling property of tempered stable processes.

However, this would lead to a bound that depends on the ratio of fractional moments strictly of order $q < 1$ with differently scaled truncation parameters. Including the approximation of such moments and comparisons with non-Gaussian FBM models [118], we have not yet been able to further pursue these investigations in detail. However, since tempered Lévy processes mediate between Lévy-stable dynamics in the short term and Gaussian dynamics in the long term, it seems reasonable that this should continue to be the case. Since we will be dealing with strongly non-Gaussian distributions in the following, we have therefore not restricted our parameter space to $H < 1$ when attempting parameter fits in the region of $\alpha < 1$. Interestingly, the parameter region of the best fits of TAFLM distributions does seem to approximately follow the FLM bound of $H < \frac{1}{\alpha}$ naturally in this case.

The only restriction between α and β that we require regardless is

$$\frac{\beta - 1}{\alpha} + 1 > 0 \Rightarrow \alpha > 1 - \beta \qquad , \tag{6.64}$$

such that the order of the fractional integral that defines the GLE ${}_0\mathcal{I}_t^{\frac{\beta-1}{\alpha}+1}$ remains positive. In the converse case, its Γ-function would attain a negative argument, leading to invalid propagators. Furthermore, divergent cases would be encountered when the argument draws near negative integers. While one could replace the fractional integral by an appropriately defined fractional derivative instead, this case has not been studied here as it does not appear relevant to the study of the fast ion distributions in the following.

7 Truncated Lévy motion in fast ion transport

Having introduced various statistical models for non-diffusive transport up to the derivation of Truncated Asymmetrical Fractional Lévy Motion (TAFLM) via path-integrals, we now seek to apply this model to distributions of fast ion tracers obtained using the Global Braginskii Solver (GBS) code. Many of the below results have similarly been published in Ref. [112], and as therein, we credit A. Bovet with the production of the raw fast ion tracer data during his previous investigations leading to Refs. [108, 103, 136]. Before attempting to fit distributions as predicted from TAFLM to the extracted tracer distributions directly, we consider their variance, skewness and kurtosis separately and compare their time evolution to expectations from the analytical results at the end of the preceding chapter. This analysis proves highly useful in assessing the applicability of TAFLM model in different transport regimes and supports the most consistent results in the asymmetric, quasi-diffusive case. The details of the employed fitting methods and estimate of statistical errors are described in App. A for brevity.

7.1 Treating numerical fast ion distributions

As detailed in Sec. 2.5, experimental measurements of the time-average fast ion profiles in the TORPEX SMT plasma [169, 103] were complemented by fluid-tracer simulations with GBS [128, 106] to enable the identification of different non-diffusive regimes [104, 103, 136] during previous studies. As the cross-field transport was to be assessed, the transport exponents were extracted from the horizontal variance (along R) of numerically sampled distributions of fast ions as a function of their propagation time [103], as also shown in Sec. 4.3. To proceed to a more general comparison between higher order moments as predicted by the TAFLM model and those of GBS-based fast ion distributions, some details of the fitting process will be clarified.

Any analysis is done on the distributions of the radial *displacements* of the fast ion tracers, denoted here $F(R,t)$, not their absolute *positions*. This is done to emulate a δ-distributed initial condition as assumed by definition for a Green's function $G(R,t)$. For the sake of experimental comparison, Gaussian initial conditions were used to describe the numerical injection region within the ≈ 8 mm aperture of the fast ion source casing. Since the fast ion transport process is then to be decomposed into multiple consecutive phases with different transport exponents, each phase must be treated separately and an initial condition $F_0(R) = F(R, t_0)$ be defined at their beginning t_0. The TAFLM model is not able to recover time-varying or transient transport exponents either, as can be seen directly from Eq. 6.61, so we will continue this practice. Formally, the predicted distributions $N(R,T)$ at a time $T = t - t_0$ are thus defined by the convolution

$$N(R,T) = \int G(R-R',T)F_0(R')dR' \quad , \tag{7.1}$$

where we recall the full form of $G(R,T)$ from Eqs. 6.57,6.58,6.45 as

$$\begin{aligned} G(R,T) &= \frac{1}{Q(T)} P_\alpha\left(\frac{R}{Q(T)}\middle|\lambda Q(T)\right) \quad \text{with} \quad Q(T) = \frac{T^H}{\beta^{1/\alpha}\Gamma(\frac{\beta-1}{\alpha}+1)} \\ &= \frac{1}{2\pi}\int \exp\left\{-ikR - \frac{Q(T)^\alpha\,\sigma^\alpha}{2\cos(\frac{\alpha\pi}{2})}\left[(1+\theta)(\lambda+ik)^\alpha\right.\right. \\ &\qquad \left.\left. +(1-\theta)(\lambda-ik)^\alpha - 2\lambda^\alpha - 2i\theta k\alpha\lambda^{\alpha-1}\right]\right\} . \end{aligned}$$

Each transport phase can feature a propagator $G(R,T)$ with a different set of parameters $\vec{\Theta} = (\alpha, H, \sigma, \theta, \lambda)$ and thus also differences in transport exponents $\nu = \beta = \alpha H$ and asymmetry θ. In the last section of this chapter, these predictions will be fitted directly against the corresponding $F(R,T)$. We will therefore assume the corresponding units of length for the dimensional parameters $[\sigma]$ = cm and $[\lambda]$ = cm^{-1}, without always stating them explicitly. Moreover, $H = \frac{\beta}{\alpha}$ was chosen as the second parameter to better visualize parameter bounds of the un-truncated AFLM model, whose adaptation is still under investigation for TAFLM as outlined at the end of Sec. 6.4. However beforehand we separately fit the variance, skewness and kurtosis of the evolving $F(R,T)$ to the time-dependences on the transport exponent $\nu = \beta$, as predicted by Eqs. 6.61-6.63. All statistical quantities related to these different distributions will carry one of the corresponding subscripts F, N, G and 0.

For consistency, the fast ion tracer distributions $F(R,T)$ have been extracted from two sets of GBS-based simulations performed by our former group member A. Bovet, as acknowledged already in Ref. [112]. Similarly described in Secs. 2.5,4.3, bunches of 40 tracer trajectories each were integrated at 4000 sufficiently spaced time-intervals such as to sample different realizations of the quasi-steady turbulent plasma conditions simulated with GBS. The resulting distributions $F(R,T)$ are binned from $N_p = 1.6 \times 10^5$ trajectories recorded at 968 steps in propagation time of ≈ 0.26 μs length and their statistics were found well converged e.g. compared to results from runs with 6000 bunches of 100 particles. While we use two sets of previously recorded trajectories in the following, the methods and conventions for retrieving, interpolating and ultimately fitting the requisite data have been adapted or replaced as outlined in the following and App. A.

7.2 TAFLM analysis of the moments of fast ion distributions

The main goal of analyzing the different moments of the fast ion propagator is to establish how consistently the evolution of their bulk, tails and asymmetry can be described by the TAFLM approach before attempting a direct fit of their parameters. With five dimensions and few restrictions in parameter space, the shape of the distributions is quite flexible and may even reveal itself as over-parameterized in certain cases, e.g. if trade-offs between parameters occur due to some residual trends or noise in the data. Further constraints and indications on the applicability of the TAFLM model are therefore highly advantageous from any practical standpoint.

In Fig. 7.1(a), we show the evolution of the radial variance σ_F^2 of the numerically obtained distributions of the radial fast ion displacement F(R,T). Results for an injection energy of $E = 30\,\mathrm{eV}$ are shown in thin-lined red, while those for $E = 75\,\mathrm{eV}$ are shown in blue. As shown in previous studies (see Sec. 2.5), and reiterated in Ch. 4, the variance and all other quantities show oscillations due to the Larmor-motion of the particles narrowing and widening the beam periodically until their spreading due to the turbulent electric fields eventually dominates. To assess the changing statistics of the fast ion distribution due to the latter effect, we again focus on the data-points at times when σ_F^2 has a local maximum, as indicated by the circles. Points expected to belong to the previously established super-diffusive regime are given in orange, the later asymmetric and quasi-diffusive regime in red and the subdiffusive regime in purple. The distributions taken at their first respective maximum t_0 (see crosses) serve as their respective initial conditions $F_0(R)$. To perform the fit of the transport exponent, we need the variance of the propagator $\sigma_G^2(T)$. Adopting the definition of Eq. 7.1 with an expected distribution $F(R,T)$, this is found as

$$\sigma_G^2 = \sigma_F^2 - \sigma_0^2 \propto T^\beta \quad , \tag{7.2}$$

analogous to the method used in previous work [103, 136]. In Fig. 7.1(b), we thus show the σ_G^2, obtained at the times chosen for each transport phase (still circles), while the time base T has been shifted accordingly to their respective t_0, and scaled to the angular fast ion gyro-frequency $\Omega \approx 1.2\,\mathrm{MHz}$ as given in Tab. 2.2. The slope of the straight line fits on these logarithmic axes thus leads to the shown transport exponents $\nu = \beta$, which are indeed similar to those given e.g. in Sec. 2.5 (from [103]) for the super- to quasi-diffusive regimes. Based on standard methods using the covariance matrix of the employed R^2-measure for the quality of fit [229], we estimate an error of $\lesssim 5\%$ on the values of most fitted slopes. The larger value for the still subdiffusive regime is probably due to a selection of later time-indices here, as similarly seen in Sec. 4.3. It should thus again be noted that the specific choice of the maxima for all transport phases distinctly affects the values of the inferred transport exponents and other parameters. However, their overall behaviour and the given regime of transport appear relatively consistent for similar choices. Returning to Fig. 7.1(a), the bold lines indicate predictions based on the fits in (b), found after inverting Eq. 7.2.

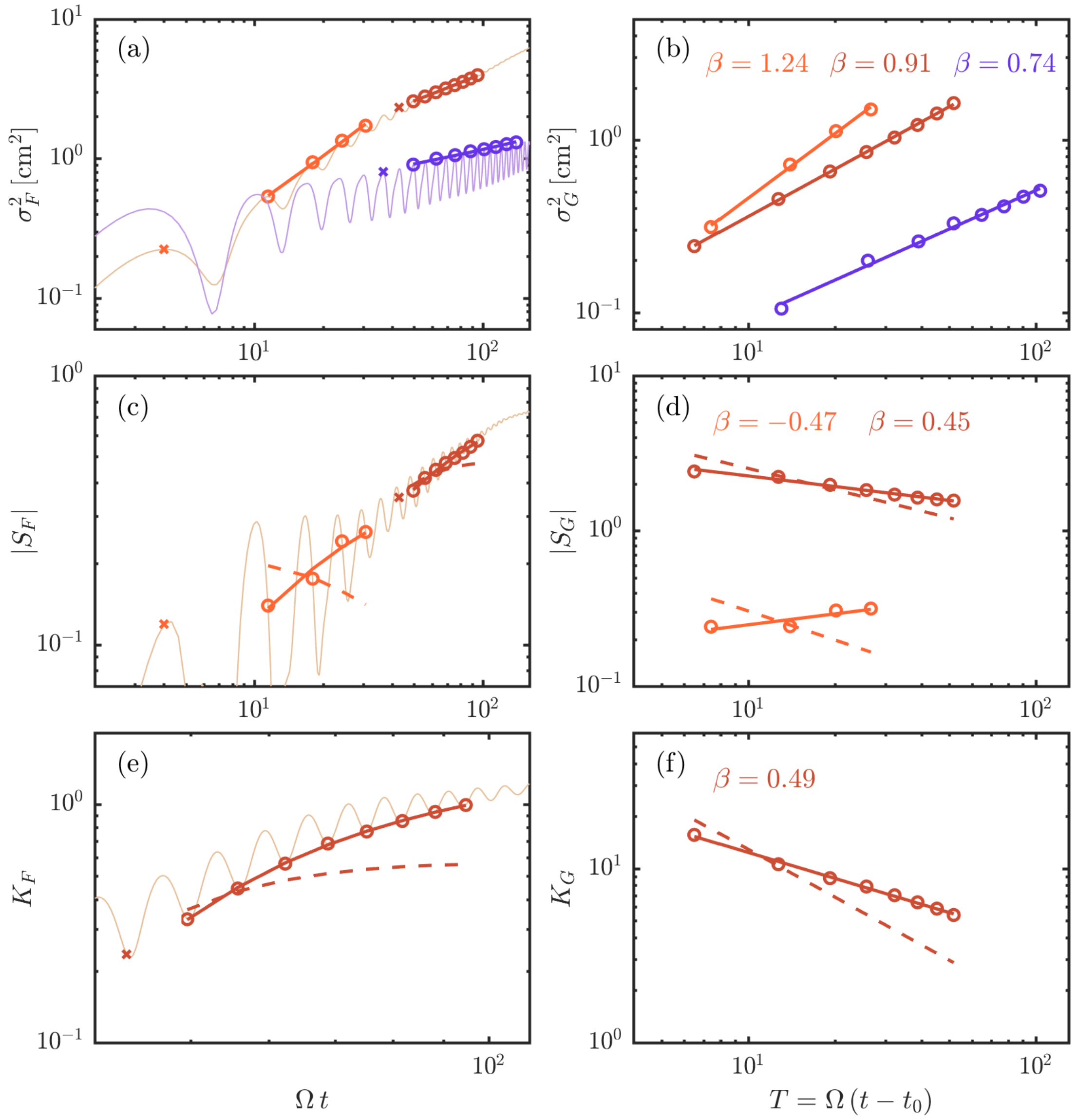

Figure 7.1 – The variance (a,b), skewness (c,d) and excess kurtosis (e,f) are shown for the distributions of fast ion tracer displacements $F(R,T)$ (a,c,e) and as inferred for the propagator $G(R,T)$ (b,d,f) by taking the initial conditions $F_0(R)$ into account for each transport phase using Eqs. 7.2-7.4. The propagation times on the abscissa have been scaled by the Larmor frequency Ω and are shifted to the beginning of each transport phase in (b,d,f). As described in the text, bold lines show fits on the selected data-points (circles) of each quantity to the time-dependences expected for TAFLM propagators given in Eq. 6.61-6.63 in (b,d,f), while dashed lines indicate expectations purely based on the fits of the variance. The transport exponents $\nu = \beta$ inferred from each fit is shown in the corresponding pannels. Bold and dashed lines in (a,c,e) are found based on these fits after inverting Eqs. 7.2-7.4.

In (c) the modulus of the skewness $|S_F|$ is shown, as the tracer distributions with $E = 30\,\mathrm{eV}$ are negatively skewed due to stronger fluctuations in the plasma potential towards the HFS of TORPEX driving stronger turbulent transport. Such observations already motivated the deployment of the un-truncated AFLM model in this case. In the 70 eV case, distributions appear approximately symmetric with $|S_F| < 0.1$, and the sign of S_F changes between different selected times. Therefore this case is excluded here, and only the 30 eV case of the modulus of the propagator skewness $|S_G|$ with

$$S_G = \frac{\sigma_F^3 S_F - \sigma_0^3 S_0}{\left(\sigma_F^2 - \sigma_0^2\right)^{\frac{3}{2}}} \propto T^{-\beta/2} \tag{7.3}$$

is fitted in the super- and the quasi-diffusive regimes as shown in (d). Note that the first part of Eq. 7.3 has the same structure as Eq. 3.7, since also the sum of two random variables that are assumed independent has a distribution given by the convolution of their individual distributions, as also outlined in Sec. 6.1.3. Clearly, the superdiffusive case is problematic as $|S_G|$ grows, leading to an unphysical, negative estimate of the transport exponents. While $|S_F|$ also grows in the asymmetric regime, we find that $|S_G|$ indeed decays after taking the initial conditions into account, albeit more slowly than would be expected from the fits of σ_G^2. For comparison, the dashed lines indicate the slopes that would be attained by using the transport exponents found from the fits of σ_G^2 in (b).

In (e), we show the excess kurtosis K_F for the asymmetric regime only, as we find *mesokurtic* ($K_F \approx 0$) distributions with during superdiffusion with $K_F < 0.07$, so that any further decay as expected from Eq. 6.63 cannot be feasibly fitted. In the subdiffusive regime, we even find $K_F < 0$, i.e. *platykurtic* forms of the distributions $F(R,T)$. Even after accounting for initial conditions and using

$$K_G = \frac{\sigma_F^4 K_F - \sigma_0^4 K_0}{\left(\sigma_F^2 - \sigma_0^2\right)^2} \propto T^{-\beta} \quad , \tag{7.4}$$

we still find $K_G < 0$ in the subdiffusive case, which is incompatible with Eq. 6.63, as it defines TAFLM propagators as lepto- to mesokurtic. The remaining asymmetric case shown in (f) features a decaying K_G, with a slope that is consistent with the decay in $|S_G|$, as shown by the similar inferred transport exponents. As again illustrated by the dashed line, both remain distinctively lower than the parameter found for the growth of σ_G^2 though. Since contributions from the tails of the distributions affect the higher moments more strongly, this indicates that there may be some discrepancies between the evolution of the bulk and the tail when modeling them using TAFLM propagators in the following.

7.3 Fitting the TAFLM propagator

We will now attempt to fit the predicted distributions $N(R,T)$ calculated through Eq. 7.1 to the corresponding fast ion tracer distributions $F(R,T)$. For each transport phase, we select the same initial times and propagation times as during the fitting of the moments above. However, the fit now simultaneously involves the full 5-dimensional parameter space $\vec{\Theta}$. We use again a least-χ^2-method to quantify the quality of a fit for each set of parameters $\vec{\Theta}$ on the

TAFLM propagator $G(R,T)$ that is used to predict the distributions $N(R,T)$ for all considered propagation times T simultaneously. The details of the method are given in App. A. The main motivations for deviating from standard approaches are in fact the resulting high number of $N > 200$ fitted data-points across each transport phase, as well as the presence of irregularities such as valleys and flat minima of χ^2 in many regions of parameter-space, particularly in the superdiffusive and subdiffusive regimes. Hence no local minimum finder has been used, but full scans of χ^2 across the relevant ranges of $\vec{\Theta}$ are performed. A given set of parameters is deemed part of the region of acceptable fits (see Figs. 7.2,7.4,7.6), if its χ^2 is below a threshold, that is set based on the expected level of statistical fluctuations from sampling $F(R,T)$, as quantified by bootstrapping (see also App. A). The best-fitting distributions $N(R,T)$ with the parameters that minimize χ^2 are shown against $F(R,T)$ for selected T in Figs. 7.3,7.5,7.7. As can be seen from the given *reduced* χ^2 of these fits with n_d degrees of freedom, denoted again $\chi_r^2 = \frac{\chi^2}{n_d}$, the distinctly best agreement is found in the quasi-diffusive, asymmetric transport regime. Nonetheless, the results for the sub- and superdiffusive regimes are shown to begin with, as they serve to illustrate how naive applications of the TAFLM model can be misleading, which in turn highlights the value of the pre-analysis performed in the previous section.

7.3.1 Subdiffusive regime

In Fig. 7.2, we show four projections of parameter-space and indicate through the color-scale how many acceptable fits are found at each pair of shown parameters, given the indicated discrete steps in parameter resolution. As visible in many of the projections in the following, note that the parameter regions of acceptable fits are often not continuous. Furthermore, the total number of acceptable fits changes with the parameter resolution and their χ^2-threshold values used for each transport phase. Regardless, the structure of this region can reflect problems for the fitting of the TAFLM model as well as how much certainty (if any) one should attach to the best-fitting set of parameters with χ^2_{min}, shown by red crosses. In (a), we can see that most acceptable fits lie naturally within the parameter bounds of the un-truncated AFLM model, i.e. to the left and below the dashed gray line. Furthermore, the shape of the region follows the line defined by the expected $\beta = \frac{\alpha}{H} = 0.74$. From (b) one suspects a high degree of uncertainty in the asymmetry parameter θ, as expected from the inconsistent trends of the skewness S_G. In (c), we find a clear parameter trade-off between α and λ, both competing in the assignment of a limited degree of heaviness towards the poorly defined, flat tails of $N(R,T)$. Since the best possible fit to these platykurtic distributions using a TAFLM propagator is achieved with a mesokurtic Gaussian, with subdiffusively growing width, the trade-offs are even more dire in (d). Since any large choice in λ is bound to produce approximately Gaussian propagators, the whole range of $\lambda \gtrsim 5$ can potentially produce a similar level of fit-quality, if the scale parameter σ compensates the truncation accordingly in the bulk. Since there are no sufficiently populated tails, this trade-off cannot result in any discrepancies there. Otherwise this would be expected e.g. given that the relation between σ and λ differs between the variance in Eq. 6.61, which grows with $\sigma^\alpha \lambda^{\alpha-2}$ and the skewness and kurtosis in Eqs. 6.62,6.63, where only the product $\sigma\lambda$ enters.

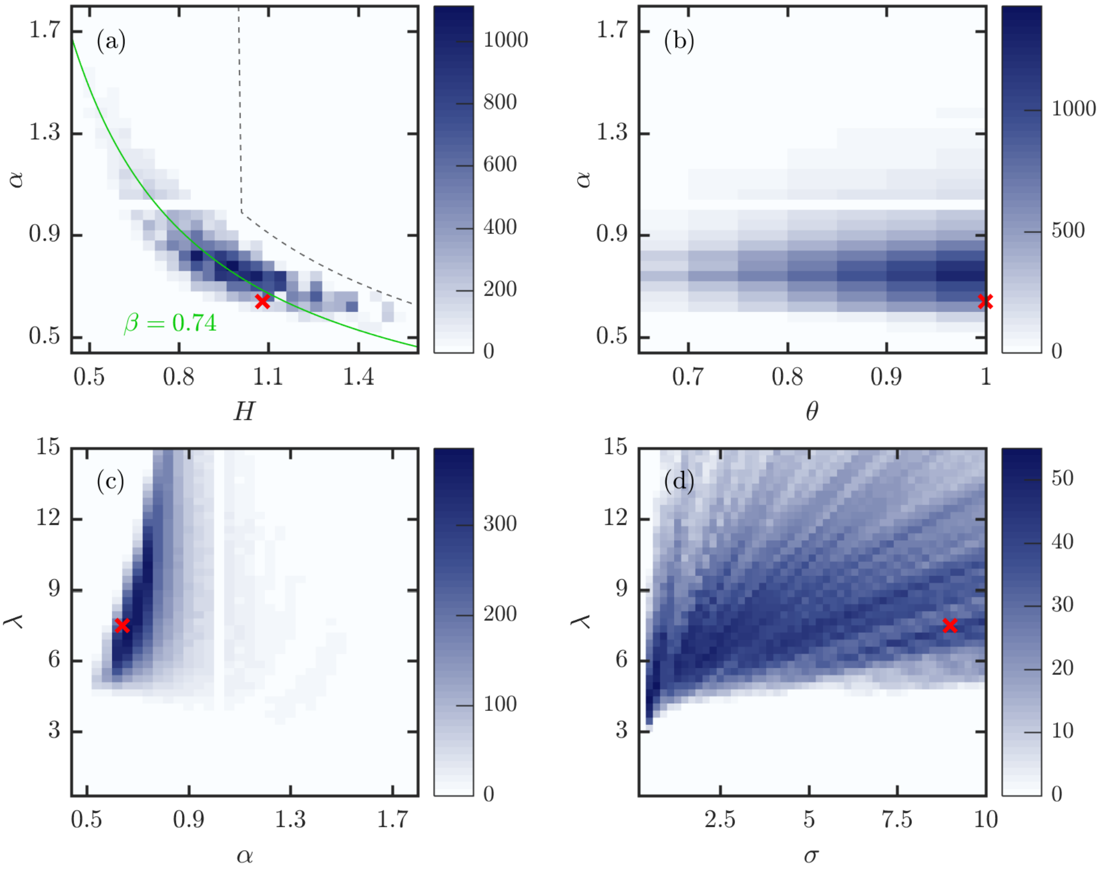

Figure 7.2 – Illustration of the parameter-space relevant for fitting the TAFLM model in the subdiffusive regime. The region of acceptable fits (see App. A) is shaded blue, with the color-scale indicating how many acceptable fits are found at each pair of parameters from (a) to (d), given the shown parameter resolutions. Red crosses indicate the set of parameters corresponding to χ^2_{min}, for which the fit result is shown in Fig. 7.3. In (a), we show the location of β fitted using σ_G^2 [see Fig. 7.1(b)] in green. Furthermore, we delineate the parameter bounds of the un-truncated AFLM model with $H \leq 1$ for $\alpha \geq 1$ and $H \leq \frac{1}{\alpha}$ for $\alpha < 1$ in dashed gray.

Given the stringent choice of statistical errors in the χ^2 calculation, it is finally not surprising that even the best fits result in a reduced χ^2 of more than 50. Therefore, as expected from the previous section, this transport regime appears unsuitable for modeling with TAFLM, and the only useful parameter-estimate of β is more straightforwardly achieved by fitting σ_G^2. Note however that, pending the obvious discrepancies near the peak of the distributions, the fitted $N(R,T)$ still appear to conform relatively well to the rest of the data $F(R,T)$ as seen in Fig. 7.3, due to the flexible shape of the TAFLM propagator, that is thus not just unsuitable but also over-parameterized for this problem. If a less stringent error estimate was chosen in the χ^2 calculation, e.g. a fixed 10% based on some systematic uncertainties, this would effectively more than triple the errors near the peaks and diminish the reduced χ^2 potentially below 5, and thus mislead conclusions that do not consider the full region of similar fits or analyze the

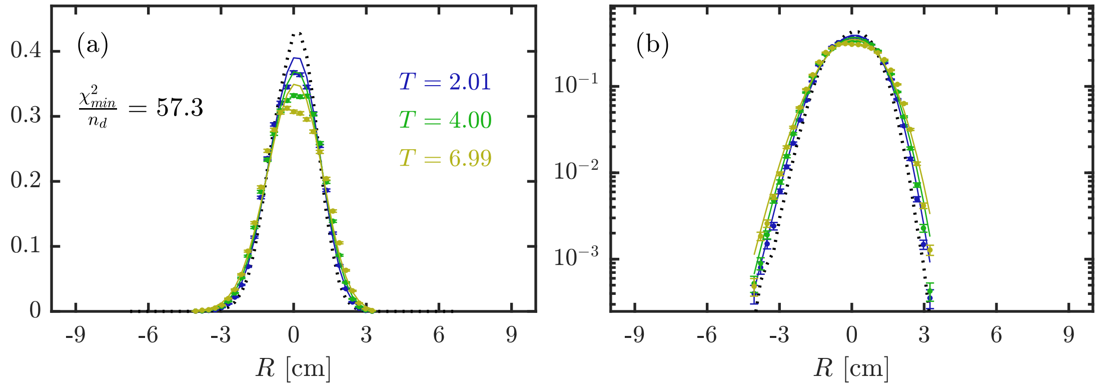

Figure 7.3 – Best fits when using the TAFLM model to describe the fast ion distributions in the subdiffusive regime, on both a linear scale in (a) and a logarithmic scale in (b). The indicated times T elapsed since attaining the initial condition (dotted black). The data $F(R,T)$ is dotted, with its error-bars based on statistical uncertainties from bootstrapping (see App. A). The lines indicate the respectively predicted $N(R,T)$ as defined in Eq. 7.1, with the parameters of $G(R,T)$ shown by red crosses in Fig. 7.2. The units on the ordinate are of inverse length and correspond to normalized distributions in all cases, as in the previous chapter. The reduced minimal χ^2, with $n_d = 209$ degrees of freedom in this fit, reflects clear discrepancies near the peak of the distributions.

moments of $F(R,T)$.

7.3.2 Superdiffusive regime

In Fig. 7.4, we illustrate the parameter region of acceptable fits for the superdiffusive regime. In (a), we find very strong agreement with the value $\beta = 1.24$ inferred from fitting σ_G^2. However, almost all fits that appear acceptable are outside the region of permissible parameters of the un-truncated AFLM model. While a strong (and growing) asymmetry is quite clearly indicated in (b), we find some residual trade-offs between λ and α in (c) and very clearly problematic trade-offs between again between λ and σ in (d), albeit not quite as spread as in the subdiffusive case. The source of these trade-offs remains at least partially the fact that the far tails of the fitted distributions are still very poorly populated, so that the latter two parameters can compete for the scale of the bulk of the distribution. However, as can be seen in Fig. 7.5, there are very clear non-Gaussian features present, so that the TAFLM model is not as over-parameterized as in the previous case. However, the fact that the skewness $|S_G|$ grows in this regime still seems to imply that early left tails [(b), blue] are over-estimated, and later under-estimated (yellow) by the TAFLM model, limiting accuracy and allowing other trade-offs. For instance, a relatively strong truncation by the large $\lambda > 1$ still leads to a visible second trade-off with α towards lower values, to find the seemingly same, imprecisely fitted degree of heaviness in the near-tails of the distribution compared e.g. to the scale of its peak-region. Given that β appears quite effectively determined by the growth of σ_G^2 over time, any decrease in α thus pushes H into the region of non-permissible values for AFLM.

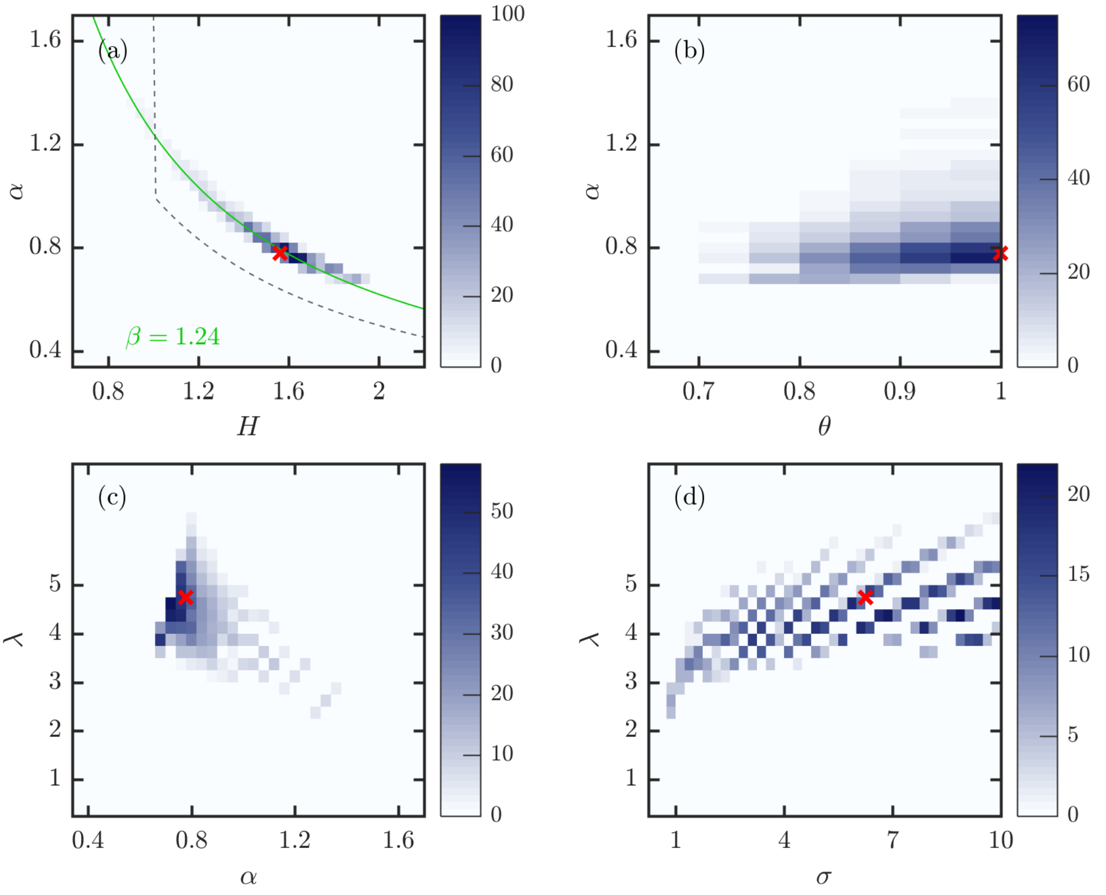

Figure 7.4 – Illustration of the parameter region of acceptable fits in the superdiffusive regime, as projected and described for the subdiffusive case in Fig. 7.2. Note the reduced, but nonetheless problematic valleys in (c) and (d). While the region conforms strongly to the expected β (green) from the growth of σ_G^2, most of it lies outside the permissible parameter region of the AFLM case. Further analysis of these features is given in the text. The red crosses show again the parameter set for χ^2_{min}, used to fit the distributions in Fig. 7.5.

Interpreting the parameters of the obtained best fits is therefore problematic. Especially the truncation parameter still appears arbitrary, and we do not immediately find any physically resolvable effects on a fixed scale of $\lambda^{-1} \sim 0.3\,\text{cm}$ that would hinder transport. Especially taking into account the findings in the later, asymmetric regime, a more consistent conclusion can instead be drawn assuming we have not yet reached a scale where truncation effects play a well quantifiable role. Therefore assuming the lowest indicated $\lambda \lesssim 1$ to be most pertinent, these would indicate that a higher value of $\alpha \approx 1.3$ is more applicable and indeed, this results in a few acceptable fits that lie near this value with $H \lesssim 1$ in the region of permissible fits for AFLM. Therefore, assuming a small impact of fixed-scale truncation effects in this regime appears more consistent.

The importance of such considerations, aided by the analysis of the moments and parameter-scans, can be regarded as more crucial in this regime, than in the subdiffusive one, since even the highly stringent error-estimates employed in the χ^2 measure here lead to fits in Fig. 7.5 with a minimal reduced χ^2 of less than 10. Since any increase in error uncertainties would quickly result in values near unity, this case provides a clear example of how misleading fits could be found, and how additional analysis as in the proceeding section is needed for a reasonable assessment of the applicability of the TAFLM model.

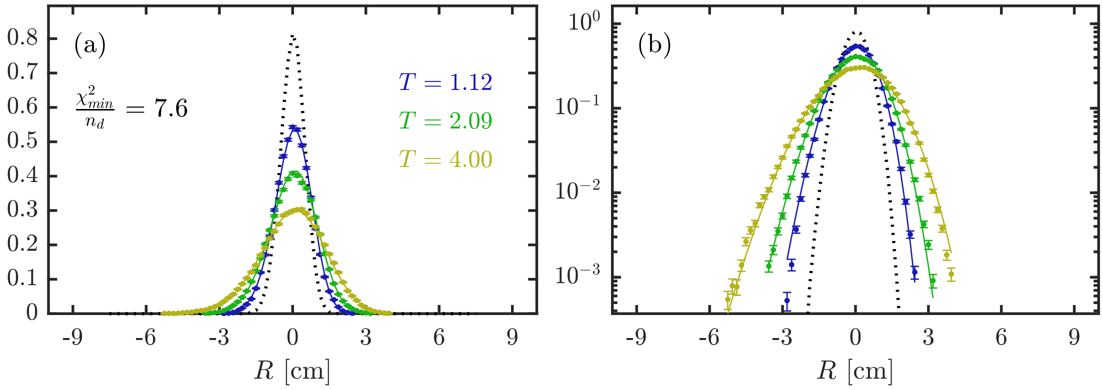

Figure 7.5 – Best fits of the TAFLM model for the superdiffusive regime, on a linear (a) and logarithmic scale (b), with all distributions again normalized. For the indicated times T since attaining the initial condition (black, dotted), predictions $N(R,T)$ are shown with lines compared to the dotted data points from $F(R,T)$, again indicating their respective statistical uncertainties. The minimal reduced χ^2, with $n_d = 152$ degrees of freedom here, reflects an overall decent agreement of the model with the data, despite it not being strictly applicable.

7.3.3 Quasi-diffusive regime

Finally, we turn to the fitting of the TAFLM model in the asymmetric, quasi-diffusive transport phase, for which the region of acceptable fits is illustrated in Fig. 7.6. It becomes immediately apparent that this region is now much better bounded in parameter-space, and only limited trade-offs are seen. In (a), α and H of most acceptable fits still lie near the line of $\beta = 0.91$ as found from fitting σ^2_G, and occupies the fully permissible region of values of AFLM. The asymmetry parameter for all acceptable fits is still significant, but no longer near its maximum value as seen in (b). A limited trade-off between λ and α remains in (c), but is strictly limited to values $\lambda < 1$. In complete contrast to the two previos examples, the parameter region between λ and σ in (d) appears the most localized, suggesting a likely value of $\lambda \approx 0.25$. This localization in parameter-space most likely results from the fact that the sampled $F(R,T)$ are now increasingly populated also in their far-tails. Since the shape of both bulk and tails must now be modeled simultaneously, the potential for parameter trade-offs is drastically reduced. Furthermore, there is now drastically problematic trend such as a growth of $|S_G|$ during superdiffusion, that would likewise lead to a substantial trade-off between fit quality during early and late times T for different sets of parameters. Some of the residual uncertainty is nonetheless due to the fact that the left-tails of the distributions as seen in Fig. 7.7(b) at

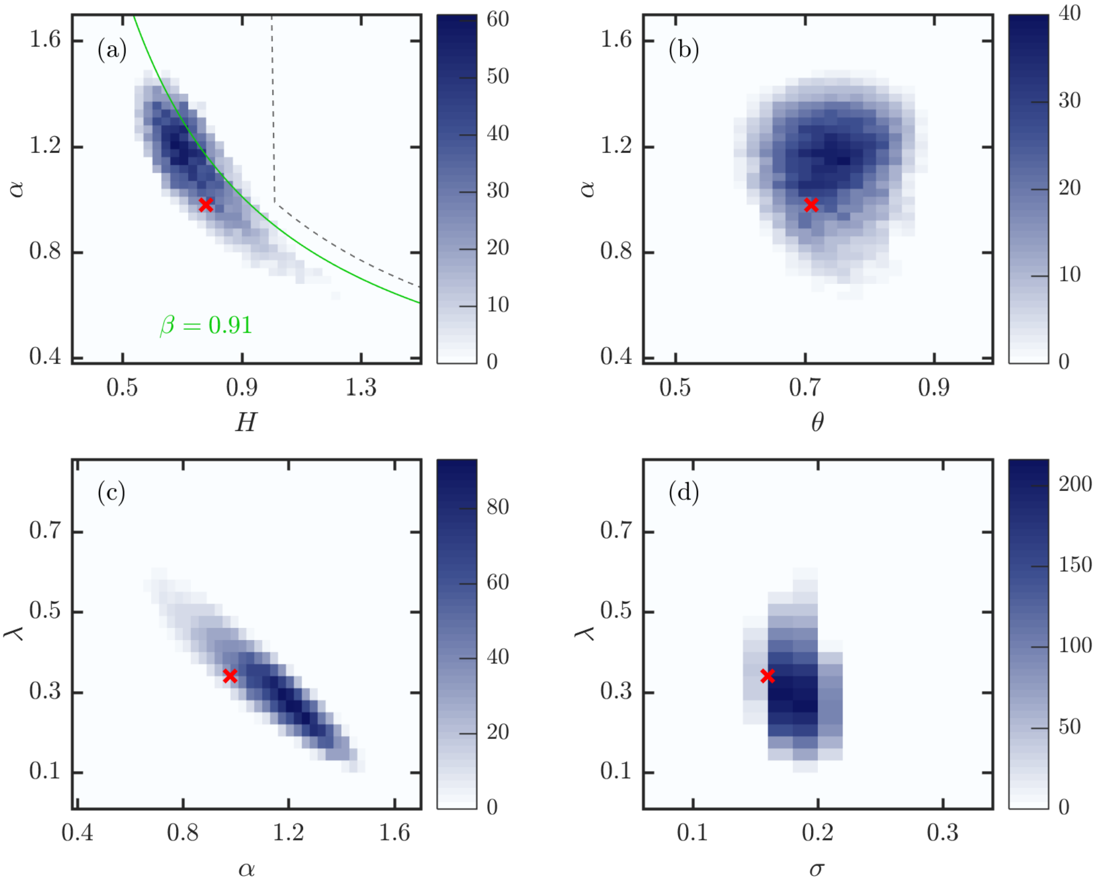

Figure 7.6 – Parameter regions of acceptable fits in the asymmetric, quasi-diffusive regime, as similarly shown for the sub- and superdiffusive case in Figs. 7.2 and 7.4 respectively. Note the absence of any significant valleys and trade-offs in parameter-space here, particularly in (d), since both the bulk and tails of the distributions $F(R,T)$ are populated during this transport phase. Further analysis is given in the text, particularly regarding the inferred truncation parameter $\lambda \approx 0.25$. In (a), we find again reasonable agreement with the line of β expected from analyzing σ_G^2, and most acceptable fits have returned within the (dashed) bounds associated with the AFLM case. The parameters corresponding to χ^2_{min} are again marked by red crosses and were used to produce the fits shown in Fig. 7.7.

late times appear slightly over-estimated, as the skewness of the distributions decays more slowly than would be expected from the growth of σ_G^2, as discussed in the previous section. Nonetheless, a very high quality of agreement is reflected by the minimum reduced χ^2 of 3.6, both in the bulk and tails of the distribution.

In this case, one may reasonably attempt to give a physical interpretation to the truncation parameter, as the tails of the distributions appear distinctly and consistently affected beyond the scale of $\lambda^{-1} \approx 4\,\text{cm}$. Recalling Ch. 2 and Tab. 2.1, this is indeed very close to the pressure-gradient scale in TORPEX. The size of the domain over which significant plasma density fluctuations tend to propagate also has an extent of $2\lambda \approx 8 - 10\,\text{cm}$, often centered near the investigated fast ion profiles. Since it is these plasma structures whose potential fluctuations result in the turbulent electric fields responsible for the cross-field transport of fast ions as illustrated in Sec. 3.3, it does appear reasonable that any apparent truncation scale be determined by the domain of their average dynamics. Since the fast ions are now beginning to propagate across the extent of this domain, the TAFLM model appears applicable in this regime, and recovers an intuitive parameter-value for the employed λ.

Finally, it should also be noted, that the somewhat larger extent of the region of acceptable fits compared to the bounded cases in the other transport regimes is also due to a systematically higher threshold in χ^2 compared to its minimum. As discussed in the concluding remarks of App. A, a more restrictive threshold and smaller regions of acceptable fits could be discussed in this case from a purely statistical stand-point, without affecting the error-estimates in the χ^2-measure itself.

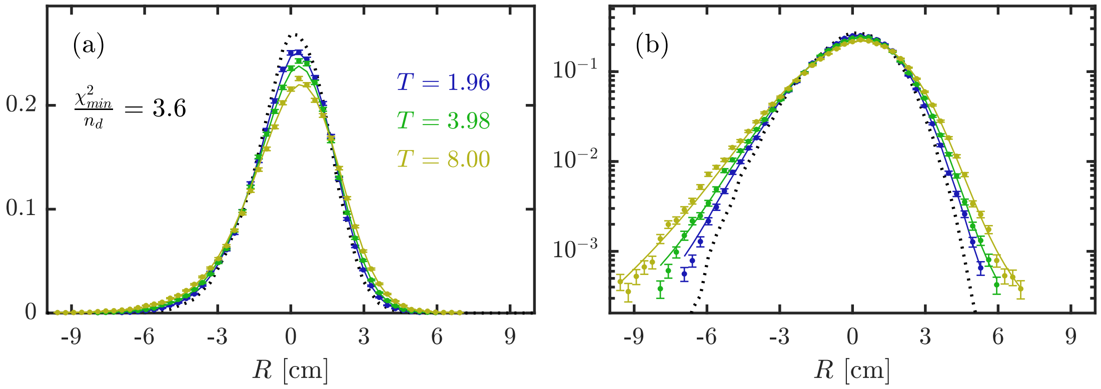

Figure 7.7 – Best fits of the TAFLM model in the quasi-diffusive regime, again shon on linear and logarithic scales in (a) and (b) respectively, with normalized distributions. The fitted predictions $N(R,T)$ (lines) at the indicated times T since the initial condition (black) are in very strong agreement with the data in both bulk and tails of $F(R,T)$ (dotted), often close to or within the associated statistical uncertainties. This is also reflected by the shown minimal reduced χ^2, here with $n_d = 339$ degrees of freedom in the fit.

7.4 Conclusions

Based on the fast ion tracer distributions obtained using GBS, we have illustrated both the limitations and the potential of applying the TAFLM model as a statistical description of non-diffusive transport. Given the significant freedom in shaping the TAFLM propagator within the parameter-space $\vec{\Theta} = (\alpha, H, \sigma, \theta, \lambda)$, fits of apparently good quality can often be obtained especially if uncertainties beyond the minimal statistical errors were to be assigned to the data. However, physically instructive direct fits are only obtained in the quasi-diffusive, asymmetric regime, where the bounds of the transport domain indeed begin to affect the further propagation of the tracers, as similarly seen in other studies on tempered stable distributions [219]. When this is not the case, parameter trade-offs can produce misleading fits, especially if the tails of the distributions are not well populated with data-points. Additional considerations are needed to distinguish such scenarios. The analysis of the evolution of variance, skewness and kurtosis compared to expectations from their analytical forms prescribed in TAFLM has proven highly effective in this regard. We therefore recommend it as a general first step when investigating the use of TAFLM in any other scenarios, to avoid precipitate conclusions from brute-force fitting attempts.

Succinctly put: *One does not simply* fit truncated fractional diffusion models.

As confirmed by the presented results, TAFLM seems generally of most use in systems where non-diffusive transport, experiences a physical bound at a consistent length-scale of steps. In any such settings, one can potentially obtain reasonable predictions on the dispersal of a given initial particle distribution, if appropriate, constant model parameters can be set e.g. based on a smaller subset of data. The existence of a maximal particle velocity is not an equivalent criterion to the above, unless one treats the mid- to long-term behaviour of the markovian case, which is intrinsically consistent with jumps over constant, uncorrelated time-intervals. For a more general treatment of particles undergoing jumps in velocity space at arbitrary time-scales, we refer the reader to the formalism akin to Persistent Random Walks detailed in Ref. [194], which is beyond the scope of this thesis.

8 Outlook and conclusions

In this thesis, a number of other investigations have been put forth, which have only been touched upon in passing, or when presenting the TORPEX experiment in Ch. 2. Here, we wish to give a brief account of the current state of some, that will most likely be pursued further in the future and open new avenues of investigations. Thereafter, we summarize the conclusions and perspectives gained from the presented findings on intermittency and truncated fractional diffusion models.

8.1 Other avenues of investigation

8.1.1 Multiple time-series

Much of the analysis presented in Sec. 3.3 and Ch. 5, as well as the vast majority of the numerical efforts in Ch. 4, were motivated by the fact that our investigations have been limited to single-point measurements, not unlike other settings where fast ions are investigated, as e.g. satellites in the Van-Allen belts [97]. The multi-GEA presented in Sec. 2.4.3 featuring five adjacent collectors is dedicated to overcoming this limitation in TORPEX. Besides significantly increasing the efficiency of time-resolved and time-average measurements, the path would be opened towards new analysis techniques such as correlation studies, or an adapted CS-method just to begin with. Further investigations could thus focus around a more detailed characterization of the instantaneous fast ion beam motion in different transport regimes. To some degree, the detector could in principle even assess the shape of a wider instantaneous beam, e.g. from a larger source region. Such results, as well as correlation studies could then potentially be linked to further analysis methods based on the meandering beam model detailed in [109]. The design and commissioning of the developed hardware was largely successful as outlined in the first two project reports by L. Kadi [230, 113]. During a preliminary experimental campaign, strong reductions in capacitive and inductive pick-up noise were achieved through the careful and well-insulated wiring used inside and outside the TORPEX vacuum vessel[231]. Nonetheless, a number of issues prevented the investigation from progressing further, mainly related to the employed electronic equipment.

The existing amplification circuitry only permits two collector channels that are subtracted in a single amplifier during the last stage. To utilize at least two of the provided collectors simultaneously, a second amplifier was introduced to separately amplify both collector signals. Due to the reduced noise on both channels, a subtraction akin to that of the back-side GEA signal in the current set-up did not appear necessary at first. However, setting a consistent reference to ground between all elements of the equipment proved increasingly challenging. Likely related to this, the on-phase signal would receive an inconsistent negative offset compared to the weaker off-phase signals, so that even the obtained mean-profiles would appear negative, despite fast ion peaks still appearing as positive in the calibrated time-series as expected. These shifts in the signal mean also inevitably affect the measured values in skewness, that nonetheless appeared most significant in the tail regions of the suspected fast ion profiles as expected e.g. from Ch. 3.

Furthermore, the introduction of noise from the plasma, even at low densities, hindered correlation analysis. Since many plasma structures (few cm) are larger than adjacent collectors (8 mm), the signal noise is highly correlated between them. In fact, with an often smaller or deformed instantaneous fast ion beam as expected from Ch. 4, correlations often appeared weaker during ion source on-phases. While attempts were made to account for such noise-induced correlations, also while adapting CS-techniques, results remained largely inconclusive and a more in-depth analysis is needed. The outlined preliminary results are given in the third report by L. Kadi [231].

Above all, it has become abundantly clear that a customized implementation of a five-fold amplification circuit, with a single common ground and noise-insulated power-supplies, is required to make data from the multi-GEA amenable to analysis. The introduction of a 6th 'blind' channel can also aid in the identification of noise within the system. While this circuitry has now mostly been conceptualized by M. Baquero and P. Lavanchy [232], its implementation into a new fast ion electronics crate and slave are not foreseen before autumn 2020.

8.1.2 Onset of transport

Since the time-average measurement campaigns by A. Bovet [169, 103] and the related analysis by K. Gustafson [104], the transition of early ballistic behavior of the fast ion trajectories, or their gyro-center, to other non-diffusive transport regimes has attracted interest. As the measured transport exponents during this transition are bound to be transient as well, a clearer experimental quantification of the onset of measurable turbulent transport based on fast ion time-series measurements, e.g. through transfer entropy analysis [233], has been under preparation. A better understanding on how the ballistic transport exponent gradually transitions to sub- or superdiffusive values could be obtained by combining such early measurements with analysis based on the formalism presented in [194], treating random walks in velocity space and transient transport exponents between early and late propagation times.

Based on existing measurements, such an investigation would have to be performed at source-detector distances of at most $D < 15\,\text{cm}$. Given the current limitations on available ports on TORPEX with two HEXTIP arrays, a new arm has been implemented for the ion source, to advance its position in the toroidal direction and allow arbitrarily close distances D to the closest possible location of the GEA. As shown in Fig. 2.11(a), a counter-weight has been added on the back of this source arm to reduce any torques on the movable system in the direction of the rail. Nonetheless, the total added weight of this piece appears to be too challenging a load for the fast ion movable system. Even during recent campaigns with the standard Z-shaped source arm [see Fig. 2.7(b)], the piezo-electric motor often appears blocked due to uneven strains in the springs that clench the ceramic ball-bearings of the chassis onto the rail. This, combined with an uneven radius of curvature of the toroidal rail, is known to lead to misalignments of the revolving gear that is engaged by the motor, causing it to block. The additional torque about the toroidal axis introduced by the heavier version of the source arm thus renders a reliable use of the movable system impossible in its current state. Due to the described general problems with the assembly, a new implementation of the system has been discussed, focusing on a more robust dynamic alignment between the chassis and the rail, as well as the symmetric distribution and compensation of added load. This overhaul is not foreseen to be completed before the end of 2020, and will most likely require extensive testing and adjustments as work progresses, similar to the original commissioning of the movable system in 2012.

8.1.3 Complex field-line configurations

The possibility of producing complex magnetic field-line geometries has been extended through the thesis work of F. Avino [135], opening new research avenues on the TORPEX device. Measurements of fast ion transport in partially closed field-lines or near an X-point would potentially be of more direct interest to research related to fusion devices with similar magnetic topologies. However, the required operation of the internal toroidal conductor introduces further technical difficulties. Even when water-cooled, shot durations must be kept within a few seconds to not over-heat the device. This is more than sufficient for time-resolved measurements, but can preclude the effective use of lock-in amplification. Since many explored scenarios show local plasma densities distinctly higher than in the SMT configuration, lock-in measurements may however become essential there. An alternative X-point configuration has been introduced for an ongoing Enabling Research project headed by C. Theiler, with the aim of again providing a reproducible test-bench for the validation of multiple turbulence codes, including GRILLIX, STORM, TOKAM3X, FELTOR and of course GBS [234]. The projections of the magnetic field-lines into the poloidal plane are outlined in gray in Figs.8.1,8.2. Since this set-up does not require the internal toroidal conductor, but uses two oppositely directed currents in the vertical magnetic field coils, the option of using lock-in amplification is kept open. Furthermore, the absence of the toroidal conductor from the centre of the device allows more freedom for choosing the fast ion injection position and considerably facilitates the movement of the GEA detection system across the poloidal cross-section.

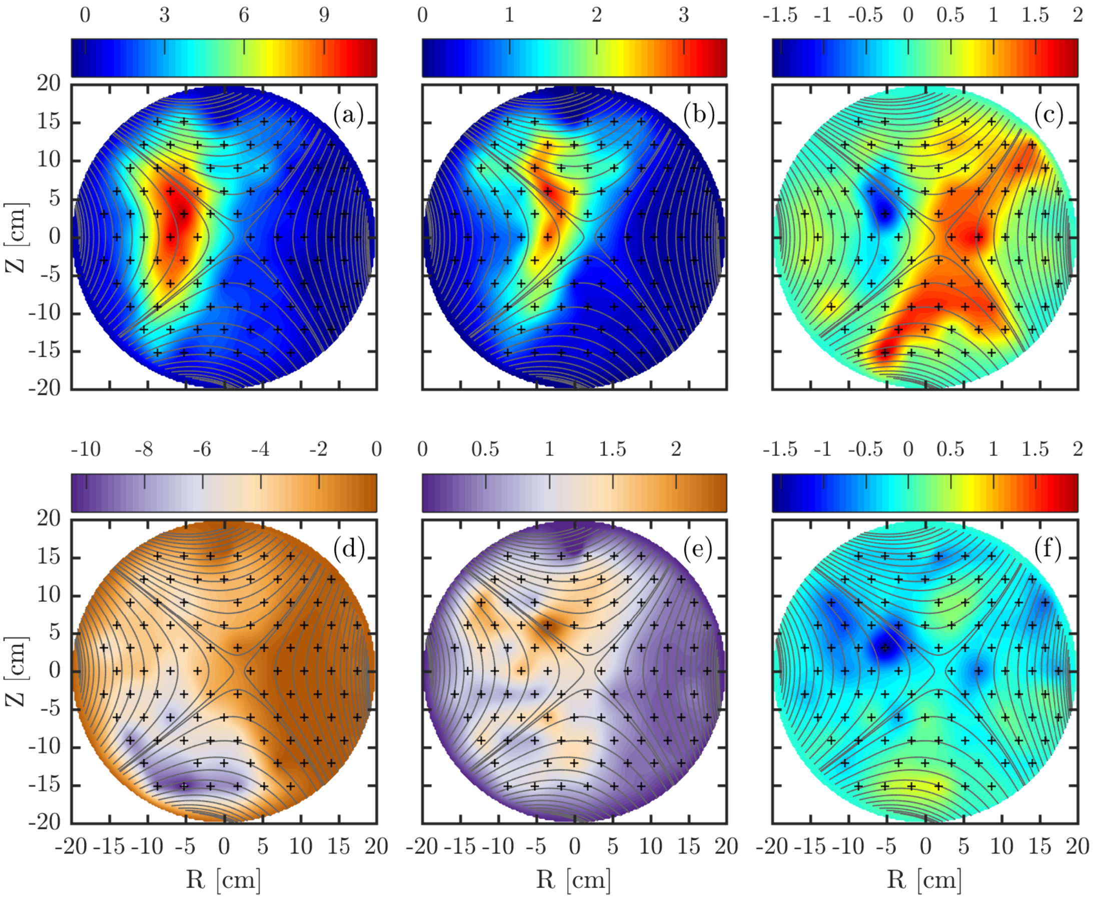

Figure 8.1 – Results from X-point configuration experiments with HEXTIP-U. Profiles interpolated from the time-average and standard deviation of plasma-density time-series from HEXTIP-1 are given in (a) and (b) respectively, with units of $\times 10^{15}\mathrm{m}^{-3}$, while (c) shows the profile of their skewness. Densities are again converted from ion-saturation currents by approximating a constant $T_e = 5\,\mathrm{eV}$. The crosses show the positions of functioning Langmuir-probe tips, while poloidal projections of magnetic field-lines outline the X-point and its four 'legs' in gray. In (d) and (e), we show interpolated profiles of the time-average and standard deviation of floating potential time-series as measured by HEXTIP-2 in units of V. The corresponding skewness profile is given in (f).

The principal characteristics of the plasmas produced in this X-point configuration as measured with HEXTIP-U are given in Fig. 8.1. The time-average plasma density profile in (a) shows lower maximum densities compared to the SMT plasmas in Fig. 2.4, but are positioned closer to the centre of the cross-section. Moving the EC-resonance further to the HFS than shown here tends to impede a reliable plasma breakdown, especially if we wish to maintain a relatively low injection power of 150 W. In (b), the strongest fluctuations occur near the observed density gradients, and like the time-average profile, extend more distinctly into the region above the X-point than below. In recent measurements, this asymmetry has been reversed by inverting the direction of the toroidal field [235]. The positive skewness of the

HEXTIP density time-series shown in (c) still indicates the intermittent propagation of different plasma structures. These are detected more frequently near the ’legs’ leading from the X-point, making them quite visible in this profile. Plasma structures are not observed to propagate far across the legs of the X-point, which is likely due to faster parallel transport along the field-lines. Respectively shown in (d) and (e) the time-average floating potential and its fluctuations therefore also remain close to zero in the LFS region, analogous to the density. Since most plasma structures may still carry positive and negative fluctuations in floating potential, the skewness profile in (f) appears much less distinct than its counterpart for density.

This naturally leads to the expectation that turbulent fast ion propagation, due to the electric fields associated with such potential fluctuations, should be affected by the legs in a similar manner. This is supported by first results from the tracer algorithm presented in Ch. 4 in the X-point configuration. As illustrated in Fig. 8.2, the fraction of tracers that ultimately cross into the lower region is strongly dependent on how far above the X-point they were injected. In (a-c) we see results for an injection position at $x_1 = 100\,\mathrm{cm}$ and $y_1 = +2\,\mathrm{cm}$, while results in (d-f) are obtained by injecting at $y_1 = 0\,\mathrm{cm}$. In both cases, we take $E = 30\,\mathrm{eV}$ to firstly focus on the case least affected by gyro- and drift-averaging. The adjustment factor for the strength of the electric fields $E_f = 2.2$ is chosen as for the SMT, but should be verified as soon as full experimental measurements of the time-average fast ion profile are available.

Going forward, quantifying the fraction of fast ions crossing the X-point experimentally as a function of injection position and energy thus seems to be a promising first step in characterizing the effect of X-points on their turbulent transport. Many of the newly introduced parts of the fast ion set-up have to work in tandem to pursue this investigation. The position of the X-point inside the TORPEX vessel has been verified to $\approx 3\,\mathrm{mm}$ accuracy, so that with the newly developed periscopic probe-arm (see Sec. 2.4.3), injection at different positions should be consistently possible. Since a wide spread of the fast ions can be expected as seen in Fig. 8.2(c,f), lock-in detection may indeed be needed at the corresponding longer source-detector distances of $D \approx 171\,\mathrm{cm}$. This holds especially in the region close to and above the X-point, where significant plasma density fluctuations introduce noise.

An additional problem has been found in the form of a certain population of suprathermal electrons apparently propagating counter-clockwise there, and introducing significant, asymmetrical noise through the back-side GEA of the older detection set-up. Since even biases near the maximum of the available range have not sufficiently mitigated the effect, measurements with the single-sided multi-GEA prove more promising at this point. Additionally, some portions of larger time-average fast ion profiles could lie outside the range of angles at which the movable system of the GEAs reliably functions, if estimates from Fig. 8.2 apply. An estimate of the total current, and thus the fraction of ions in any given region, is therefore only possible if a workable measurement of the injected fast ion current using the dedicated acquisition circuit in Fig. 2.12 is supplied. A detailed quantification of the expected losses from grids, apertures and other factors should be carried out, e.g. in the frame of the investigation of early

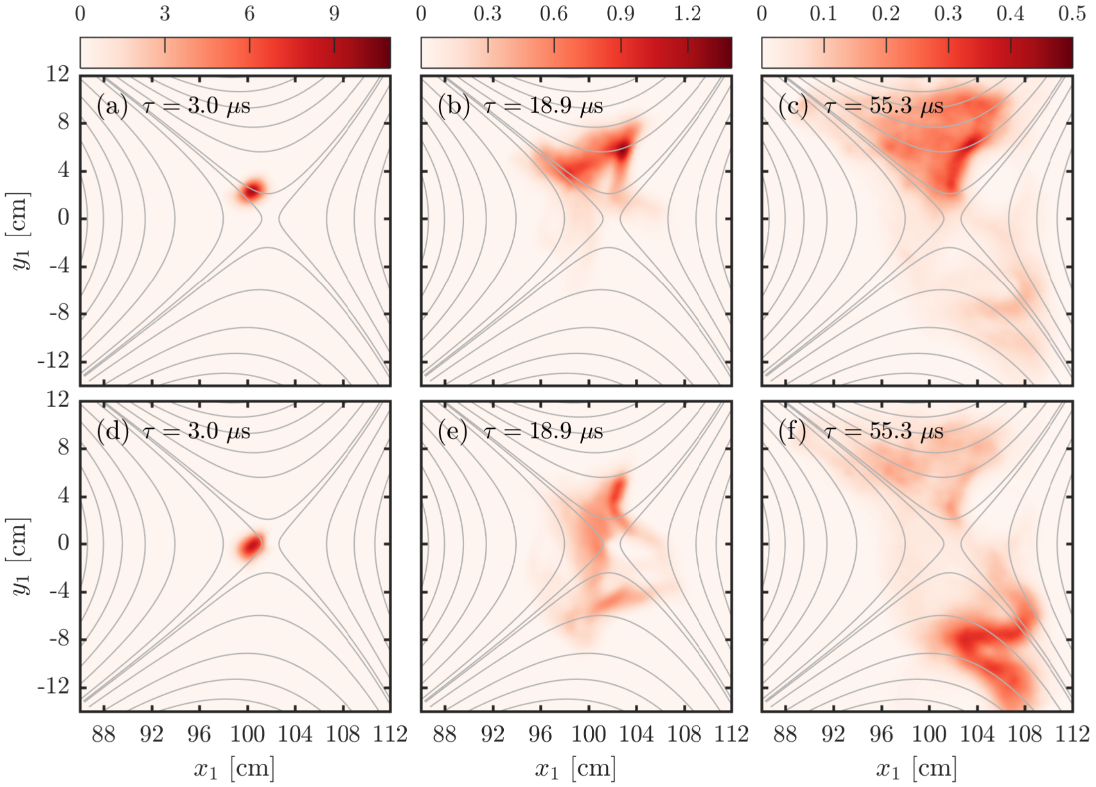

Figure 8.2 – Poloidal fast ion tracer profiles $J(x_1, y_1, \tau)$ in units of $\mathrm{mA\,m^{-2}}$, averaged over all ≈ 4000 injected bunches of 400 tracers each, at the indicated propagation times τ. A total injected current of $2.85\,\mu$A has again been assumed. Pending effects due to time-of-flight dispersion as described in Ch. 4, Fig. 4.6 for the SMT, these profiles provide first estimates of time-average fast ion profiles (see Sec. 3.2) in the X-point configuration. Profiles (a-c) are based on an injection position of $x_1 = 100$ cm and $y_1 = +2$ cm, while $y_1 = 0$ cm was chosen in (d-f). The magnetic field geometry is again outlined in gray. An artifact is visible on the upper outer leg in (c,f), due to a Langmuir probe on HEXTIP-1 beginning to malfunction, leading to a local deformation of the profile. This issue has meanwhile been addressed for current studies.

transport, so that the currents measured on the external grid of the source assembly can be more reliably converted to total measurable currents with the multi-GEA. A refurbishment of the movable systems with slower, more powerful motors is planned in the upcoming months. Furthermore, the ion source assembly requires more detailed attention as no discernible ion current could be injected from the last two installed sources. Thorough maintenance of the wiring, grids and insulating parts, as performed before the longer experimental campaign on time-resolved measurements, is currently underway.

Nonetheless, any eventual conclusions on the potential non-diffusive nature of fast ion transport in devices with similar magnetic topology, such as a tokamak divertors, must be taken with severe scrutiny. While the generally established results on the increased effects of orbit-averaging of lower energy ions can give first indications, the particular turbulent structures in each environment and their statistics need to be analyzed in detail. Benchmarking efforts on various turbulence codes and especially GBS for the simulation of such plasma structures are ongoing, and should be concluded before investigating fast ion trajectories e.g. by using similar tracing-methods as in the SMT [104, 103]. Such simulations should be able to help bridge the remaining gap between preliminary results from the presented fast ion tracer and upcoming experimental measurements, and could hopefully lead to some more general applications.

8.2 Intermittency studies

Moving on towards the conclusions of the work presented within this thesis, we firstly return to the studies of local time-intermittency across the different non-diffusive regimes of fast ion turbulent transport. Quantified by the skewness of local fast ion time-series from the GEA, earlier investigations only found distinct intermittency above the local noise level during superdiffusion [107, 136]. A comprehensive set of time-average and skewness profiles based on time-resolved fast ion measurements have been presented in Ch. 3 as in Refs. [110, 111], and includes both the sub-diffusive regime for injection energies of $E = 70\,\text{eV}$, as well as the super- to quasi-diffusive regime for $E = 30\,\text{eV}$. Distinct instances of time-intermittency are found across all investigated transport regimes, in particular in the outer regions of the time-average fast ion beam. Both the time-average and skewness profiles are now normalized to a common total fast ion current. This gives the fast ion signal a consistent weight relative to statistical contributions from the background noise. The consequently found maximum values of skewness appear still higher in the super- to quasi-diffusive regimes, and grow with increasing source-detector distance, i.e. with fast ion propagation time. Investigations using conditional sampling analysis consistently indicates the average response of the fast ions to the dipole-like potential fluctuations associated with larger plasma structures from the ideal interchange-mode. Fast ions with $E = 30\,\text{eV}$ move almost twice as strongly in response to the turbulent E×B-flows compared to the $E = 70\,\text{eV}$ case. As already reasoned in [104, 103], ions with higher injection energies remain subject to stronger gyro- and drift averaging, as well as proportionately smaller propagation times in the plasma.

Throughout the analysis, we were led to suspect that the intermittent peaks in the fast ion time-series indicate instances of a much smaller and more concentrated instantaneous fast ion beam, compared to the time-average and CS-profiles. Lacking as of yet the capacity of reliably acquiring multiple simultaneous fast ion measurements, we have introduced a numerical tracing algorithm in Ch. 4, to investigate the statistical properties of the simulated instantaneous fast ion beam. The tracer uses an arbitrary static magnetic geometry as input (here the SMT), as well as time-resolved floating potential measurements from HEXTIP-U to approximate the turbulent electric fields of TORPEX plasmas. Tracers are injected with similar initial conditions compared to earlier investigations based on GBS [104, 103] and their trajectories integrated using the explicit Boris-method. The time-average behaviour of the tracers was studied to adjust the impact of electric fields to match the GBS studies, and thus the experiment. The statistics of individual bunches of simultaneously injected tracers coupled with a synthetic diagnostic indicate indeed that the instantaneous fast ion beam often features a distinctly smaller width than the time-average, particularly for $E = 30\,\text{eV}$. With peak current densities similar to those expected form experimental measurements, synthetic time-series were generated for the 30 eV case [109]. Given a reasonable contribution from noise, their skewness profile shows strong qualitative and often even quantitative agreement with experimental data. These insights helped to establish the principal physical picture of a concentrated, meandering fast ion beam, which over time builds a distinctly larger time-average profile.

In Ch. 5, we have introduced the principal elements of an analytical model that is based on the physical picture described above, as detailed in [109]. Firstly assuming approximately Gaussian instantaneous and time-average profiles with constant shape for simplicity, this model closely recovers many instances of the skewness of time-series in the subdiffusive data-set, given their time-average value. The model parameters fitted in this process are the instantaneous peak fast ion current density, and the ratio between the widths of the instantaneous and time-average fast ion profile. Generally good agreement with expectations from time-series measurements and the fast ion tracer are found, pending expected deviations due to fluctuations in the injected fast ion current and from the limited resolution of the tracer respectively. However, the presence of non-Gaussian features in the fast ion profiles is a limiting factor in the applicability of the model here, so that a different approach based on the assumption of a very small instantaneous beam width was adopted for the 30 eV case. Results for the predicted values of skewness are again in good overall agreement with measurements, as are the fitted peak instantaneous current densities. In closing, some additional considerations on point-like meandering beams and the expected skewness of the resulting two-valued time-series often yield distinct relative differences between the 30 eV and the 70 eV data-set, when comparing the expected skewness to measurements.

We have therefore established a consistent model for the generation of intermittency across all investigated non-diffusive transport regimes in our system. It is our hope that the developed analytical methods, as applied here and in [110, 111], will prove a useful tool in general settings where meandering particle beams are investigated, since no intrinsic assumptions on the underlying physics are made. It furthermore provides an illustrative example for the importance of considering the specific statistical dynamics of a given system when analyzing intermittency in the wider context of non-diffusive transport.

8.3 Truncation effects

In the second part of this thesis, we develop a truncated fractional diffusion model for the statistical description of fast ion cross-field transport in SMT plasmas as simulated using GBS. Therefore, much of Ch. 6 was dedicated to reviewing the necessary mathematical concepts, starting with Einstein's and Langevins descriptions of diffusion as the result of the local and markovian random walk process of Ordinary Brownian Motion. Starting from a review of Central Limit Theorems, we systematically recapitulated generalizations of both approaches towards non-Gaussian and non-diffusive Continuos Time Random Walks (CTRWs) and Generalized Langevin Equations (GLEs) respectively, leading to different forms of Fractional Diffusion Equations. While both acquire non-local features due to the use of heavy-tailed Lévy stable distributions for the step-sizes of the underlying random walks, their implementation of non-Markovian behaviour differs. While CTRWs rely on heavy-tailed distributions for the waiting times between steps, GLEs feature a memory-kernel, that gives different weights to consecutive random steps. These weights introduce positive or negative correlations between these steps, by effectively stretching the time-variable in the FDE. One solution method for such a GLE has been established in [183] based on path-integrals, and was already adopted successfully to deduce the FDE and Green's function ('propagator') of the Asymmetrical Fractional Lévy Motion (AFLM) process in previous work [108]. This model successfully recovered the non-diffusive and asymmetrical features of superdiffusive fast ion cross-field transport in GBS simulations. However, like many similar descriptions, AFLM features a heavy tailed propagator due to random steps with infinite variance. Since quasi-infinite jumps cannot be executed by any physical particles, this leads to severe over-estimates in the tails of the propagator, compared to simulated or measured fast ion distributions.

One method to address this criticism in fractional diffusion models, is the use of tempered stable distributions for the step-sizes in the underlying random walk. As proposed in [221], an exponential truncation beyond a certain, fixed scale is used. This truncation still allows for the presence of non-Gaussian features at short scales in space and time. However, we ultimately recover Gaussian features due to the Central Limit Theorem taking effect at large scales and long times. This concept has been applied successfully in a variety of settings such as the description of tempered stable processes e.g. in [222, 223] and tempered CTRWs e.g. in [120]. Based on the conventions and parameterization in the latter, we again formulate a GLE and generalized the solution methods from [183] to derive the propagator and FDE for Truncated Asymmetrical Fractional Lévy Motion through path-integrals as detailed in [112]. Since all moments of the generally non-Gaussian propagator of this non-diffusive process are finite, concise expressions for its variance, skewness and kurtosis as a function of time were obtained directly from the corresponding derivatives in Fourier-space.

Finally, we applied the TAFLM model to the fast ion tracer distributions from GBS simulations in Ch. 7. With five parameters to determine the shapes of the propagator in terms of scale, asymmetry, and the relative weights and shape of its tails and bulk over time, the TAFLM model can yield highly flexible fits. Especially in scenarios where the tails of the tracer distributions are not well populated, this leads to over-fitting and can result in misleading estimates for the fitted parameters, in particular the applied truncation scale. Transport in the subdiffusive and early superdiffusive regimes are not appropriately modeled, although fitting results may appear promising on first glance, especially during superdiffusion. To discern such problematic cases more distinctly, the separate fitting of the time evolution of the variance, skewness and kurtosis, by using the available analytical results for TAFLM, has proven highly effective. While some residual uncertainties remain, the most promising results for the application of TAFLM have thus been found in the later asymmetric and quasi-diffusive transport regime. The inferred truncation scale of ≈ 4 cm on each side of the propagator is strongly reminiscent of the radial pressure gradient scales in the TORPEX SMT plasma. Since the fast ions have spread out significantly in this transport phase, the truncation scale naturally reflects the domain over which the dominantly responsible plasma structures propagate, as e.g. illustrated using CS-analysis in Ch. 3.

The possible applications for the TAFLM description range across many fields, in which bounded fractional dynamics are being investigated. We hope that it can continue to serve as a useful statistical tool, as well as the methods outlined for the assessment of its suitability. Further generalizations of TAFLM are possible, e.g. by the currently investigated introduction of two separate truncation scales for the left- and right-hand tails as in [223]. It remains to be seen whether the introduction of even more fit parameters would be useful for the application to fast ion transport. In this context, we welcome any further discussions with groups outside plasma physics, that are currently investigating similar approaches, and possibly even different versions of TAFLM outside our knowledge. Within plasma physics, there are many instances, where purely empirically justified models for transport descriptions are employed, e.g. in the simulation of plasma profiles in the bounded, turbulent edge region of tokamaks. It may prove instructive to assess the utility of a bounded, non-diffusive description such as TAFLM in comparison to the currently employed effective diffusion models. The relatively concise analytical results may in turn even limit the complexity of numerical implementations.

As stated from the outset in Ch. 1, we have therefore attempted to judiciously adopt, develop and apply different statistical models to better describe the intermittent and non-diffusive aspects of fast ion transport in a bounded turbulent environment as found in the TORPEX device. We therefore hope that the continued improvement of these methods, along with the results they provide, will prove a small aid in the analysis of statistical problems in science, and in particular plasma physics aimed at the pursuit of fusion energy.

A Fitting methods

A.1 Chi-squared fitting

At multiple points in this thesis, we need to assess the quality of agreement between different numerically obtained data-sets (Ch. 4) or the goodness of fits between experimental or numerical data and analytical predictions (Chs. 5,7). The generally preferred method is χ^2-minimization, usually through a combination of parameter-scans and local minimum finders supplied in MATLAB R2016b. This goodness-of-fit measure has been extensively documented in statistics standard texts such as [229] and is defined as

$$\chi^2 = \sum_{i=1}^{N} \left(\frac{D_i(x_i) - Y_i(x_i)}{\epsilon_i} \right)^2 \tag{A.1}$$

for a fit of N data-points $D_i(x_i)$ to the predicted or fitted values $Y_i(x_i)$, both defined at the same arguments x_i. When Y_i represents a set of points generated from a fitting function $Y_i = Y(x_i|\vec{\Theta})$ with parameters $\vec{\Theta}$, the formal definition becomes

$$\chi^2 \left(\vec{\Theta} | \{D_i\} \right) = \sum_{i=1}^{N} \left(\frac{D_i - Y(x_i|\vec{\Theta})}{\epsilon_i} \right)^2 \tag{A.2}$$

In any case, the assumed errors $\{\epsilon_i\}$ in the data points are key to the application of this method. Since through these, the fit of each point in the data-set is weighed by the relative degree of certainty in the attained values, we usually employ methods to bound $\{\epsilon_i\}$ from below, so as to not over-weigh points in the lower tails of the set, that often feature stronger impacts of statistical noise (see below). Beyond this, χ^2 fitting allows by definition the treatment of fits across a wide range of values. Conversely, a least-R^2-fit, defined by letting $\epsilon_i = 1 \forall i$, naturally places higher weights on larger values in the set, which may not be desirable in all circumstances.

To scale the attained value of χ^2 with the given number of data-points N, the *reduced* χ^2 is defined as $\chi_r^2 = \frac{1}{n_d}\chi^2$, with n_d being the number of degrees of freedom in the fit. This number is defined as $n_d = N - n_\theta - n_c$, where n_θ is the number of fitted parameters and n_c the number of present constraints on the fit, such as normalizations. By design, finding $\chi_r^2 \sim 1$ defines a good fit as, on average, all fitted or predicted points lie approximately within their specified errors.

A variety of methods employs the χ^2-probability distribution in the analysis of the goodness of a least-χ^2-fit, or the calculation of confidence intervals on the fitted parameters. At their core lies the assumption that all given errors ϵ_i represent the standard deviations of statistically independent Gaussian distribution centered on the fit, from which the associated measurements D_i be drawn upon repeating the experiment. The probability of obtaining a given value of χ^2 from a set of measurement points with n_d degrees of freedom is then given by the χ^2-probability distribution

$$P(\chi^2|n_d) = \frac{(\chi^2)^{n_d/2-1}}{2^{n_d/2}\Gamma(\frac{n_d}{2})}\exp\left(-\frac{\chi^2}{2}\right) \quad . \tag{A.3}$$

For instance, a p-test could thus be performed using the cumulative χ^2-distribution up to the obtained value of χ^2. However, the precise result is heavily dependent on the particular error values chosen, and can thus be misleading unless the above assumptions are satisfied in the same detail. Any unresolved trends in the data can quickly lead to diminished values of probability, especially for higher n_d. Alternatively, one can find confidence bounds by performing a parameter scan in the vicinity of minimum $\chi^2 = \chi^2_{min}$, and find the parameter-region containing e.g. 95% of the probability content, irrespective of the particular assigned probability values. This has been done to visualize the variability of the predicted vs. the measured values of the central moments of the fast ion time-series in Ch. 5, Figs. 5.5,5.3. Specifically, their bands indicate the minimum and maximum attainable predicted values using the parameters within the confidence region defined by fitting the predicted on-phase skewness to measurements. If the χ^2 values around χ^2_{min} appear approximately parabolic in parameter-space, the region with $\chi_r^2 \leq \chi^2_{min,r} + 1$ is often similarly identified as confidence region, as it includes by definition all fits that, on average, pass within the 2σ region of the Gaussians that the measurements are assumed to be drawn from.

A.2 Bootstrap error estimates

In Ch. 5, the error estimates on the skewness are based on fluctuations in the injected fast ion current as a known dominant source of shot-to-shot deviations in the measurements. However, such a direct estimate is not always available. Especially when treating fast ion tracer distributions $F(R,T)$ in Sec. 7.3, which are numerically obtained based on GBS results, the assignment of measurement errors for the purpose of χ^2-minimization is not as straightforward. One possibility is using the bootstrap method, as described with numerous applications in [236]. Through it, we can quantify the statistical uncertainties in the distribution, due to the finite number of available samples, i.e. the $N_p = 1.6 \times 10^5$ tracer displacements, that are assigned into the set of bins centered at $R = \{R_i\}$. To do so, each data-set at one given

$T = T_j$ is re-sampled *with replacement* a total of likewise N_p times, to generate a synthetic, *bootstrapped* data-set, from which the distribution $F_{bs}(R,T_j)$ is obtained using the same bin centres $R = \{R_i\}$. This can naturally lead to slightly different numbers of tracers in each bin $F_{bs}(R_i,T_j)$, compared to the original $F(R_i,T_j)$. After repeating this process a statistically significant number of $N_{bs} = 1000$ times, the obtained numbers of tracers in each bin R_i form an approximately Gaussian distribution, and the corresponding statistical error ϵ_i is taken as its standard deviation. For all of the distributions $F(R,T_j)$ under consideration, it should be noted that almost all obtained $\epsilon_i(j)$ fall within ≈ 10% of $\sqrt{F(R_i,T_j)}$. These errors ϵ_i should be regarded indeed as the smallest reasonable estimate of uncertainty in the distributions $F(R,T)$, as they do not take any other sources of random or systematic error into account that may affect the data-set of tracer displacements itself.

A.3 Acceptable fits of the TAFLM propagator

Having motivated our error-estimates for the different $F(R,T)$ in Sec. 7.3, it remains to define χ^2-measure for the quality of the fits. To begin with, the total number of regularly spaced bins was chosen as $< \frac{\sqrt{N_p}}{3}$, to find distributions with a smooth, single peak. However, to avoid the largest statistical errors in the far tails, we firstly exclude any bins with less than 15 tracers within them. Since the (normalized) distributions $F(R,T_j)$ spread for later times T_j, the number of bins considered in the fit $n_b(j)$ can thus change between them. As the full time evolution of the distributions $F(R,T)$ in a given transport phase is to be fitted, we furthermore consider all N_T times in the set $\{T_j\}$ simultaneously in the fit, and likewise write $\epsilon_i = \epsilon_i(j)$ for clarity. This yields for the quality of fit measure

$$\chi^2\left(\vec{\Theta}\middle|F(R,T)\right) = \sum_{j=1}^{N_T}\sum_{i=1}^{n_b(j)}\left(\frac{F(R_i,T_j) - N(R_i,T_j|\vec{\Theta})}{\epsilon_i(j)}\right)^2 \quad , \tag{A.4}$$

where $N(R,T|\vec{\Theta})$ are the tracer distributions predicted by convolving the TAFLM propagator $G(R,T)$ with parameters $\vec{\Theta} = (\alpha,H,\sigma,\theta,\lambda)$ with the initial condition $F_0(R)$ as shown in Eq. 7.1. Again, the minimum of χ^2 is to indicate the best fit between prediction and data.

However, for some cases in Sec. 7.3, the relevant regions in parameter-space feature multiple adjacent local minima in χ^2, or even valleys and flat regions along different dimensions, so that detailed parameter-scans appear in order. Furthermore, it is problematic to judge the relative importance of different minima by assigning probabilities using the χ^2 distribution in Eq. A.3. All fits feature $n_d > 200$, and thus values of $\chi^2_{min} \gtrsim 1000$. Even if the χ^2 value of a given parameter set was only 1% higher than χ^2_{min}, it would be assigned an $\approx \times e^{-5}$ lower probability. While mathematically inevitable, this seems misleading from a practical standpoint, since even a minuscule level of statistical fluctuations in $F(R,T)$ can introduce similar or larger changes to χ^2_{min} (see Fig. A.1) itself. Consequently, any confidence bounds based on such relative probabilities would be highly restrictive and loose any information on the structure of χ^2 in the parameters space that χ^2_{min} is embedded in.

We therefore choose a less reductive approach for indicating parameter regions of acceptable fits, and hence visualize the uncertainties attached to the parameters of the best fits. The degree of statistical uncertainties in the distributions $F(R,T)$ is by definition reflected in the bootstrapped distributions $F_{bs}(R,T)$ as described above. Using the same, best fitting parameter-set $\vec{\Theta}_b$ identified by χ^2_{min} of the original data-set $F(R,T)$, we re-calculate the corresponding $\chi^2_{bs} = \chi^2(\vec{\Theta}_b|F_{bs})$ on all $N_{bs} = 1000$ bootstrapped distributions $F_{bs}(R,T)$. The closely Gaussian distributions of χ^2_{bs} are shown for the subdiffusive, superdiffusive and quasi-diffusive transport phase in Fig. A.1(a), (b) and (c) respectively. Only those sets of parameters $\vec{\Theta}$ are deemed acceptable, whose χ^2-fit with the original data $F(R,T)$, i.e.$\chi^2(\vec{\Theta}|F)$, falls below the upper 2σ-value of the shown distributions. These definitions of the regions of acceptable fits are thus intrinsically based on the expected level of statistical uncertainty in each data-set, instead of an arbitrary or conventional threshold in χ^2. Their locations in parameter-space illustrated in the projections in Figs. 7.2,7.4 and 7.6 thus effectively indicate potential trade-offs between different parameters, that produce fits of practically similar, albeit not identical quality.

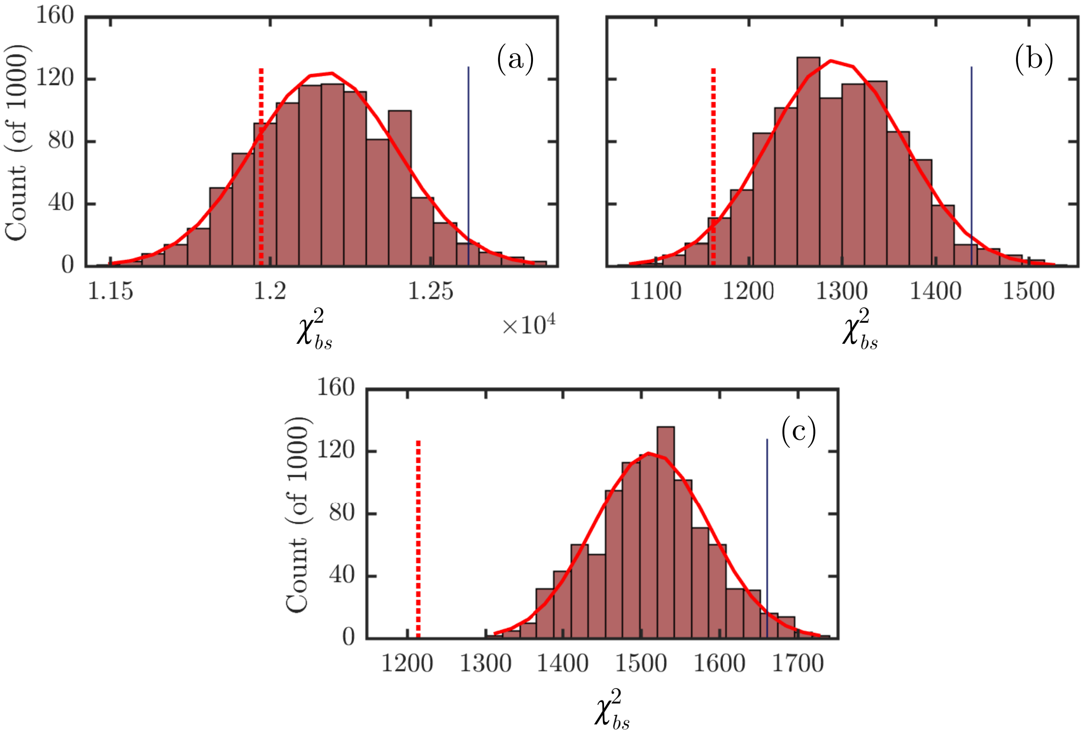

Figure A.1 – Distributions of the χ^2 calculated on the $N_{bs} = 1000$ bootstrapped data-sets $F_{bs}(R,T)$, using the best fitting parameters $\vec{\Theta}_b$ of the original data, i.e. $\chi^2_{bs} = \chi^2(\vec{\Theta}_b|F_{bs})$. Results are shown for the sub-, super- and quasi-diffusive data-set in (a), (b) and (c) respectively. The red curves show a Gaussian with its mean and variance taken from the un-binned values of χ^2_{bs}. The red dashed line shows the χ^2_{min} of the original data $F(R,T)$ for comparison. The maximum threshold of χ^2 for $\chi^2(\vec{\Theta}|F)$ to qualify a parameter set $\vec{\Theta}$ as an acceptable fit of $F(R,T)$, is defined as the upper 2σ value (blue line) of the χ^2_{bs} distribution.

A few concluding remarks should be made regarding the calculations of χ^2_{bs}. As outlined in Ref. [112], we have pursued a modified approach in which the distributions of χ^2_{bs} are found by actually locating the χ^2_{min} for each $F_{bs}(R,T)$ separately. However, in most cases the identified parameter-set still corresponds to $\vec{\Theta}$ from the χ^2_{min} of the original $F(R,T)$. Therefore, distributions as in Fig. A.1 are expected to generally only differ negligibly from these, while obtainable at a fraction of the computational effort.

The position of the χ^2_{min} of the original data $F(R,T)$ (red, dashed line) is significantly shifted relative to the mean of the χ^2_{bs} distributions when comparing (c) to (a) and (b). The likely dominant underlying reason is that the tails of $F(R,T)$ and $F_{bs}(R,T)$ reach further in the quasi-diffusive regime, as illustrated in Fig. 7.7. Therefore, they contain a higher number of bins that have collected a relatively small number of tracers compared to the bulk. Under bootstrapping, it is the bins with relatively small numbers of tracers, that will be subject to the largest relative uncertainties, which renders the bootstrapped distributions $F_{bs}(R,T)$ subtly less smooth compared to $F(R,T)$. One could argue, that the resulting shift in values is somewhat artificial, and should be removed, i.e. that we only consider the actual spread of the Gaussian distributions of χ^2_{bs} when defining the χ^2 threshold. While this makes little difference to the parameter regions and trade-offs shown in the sub- and superdiffusive regimes, the bounded region of acceptable fits in the quasi-diffusive regime would appear indeed more concentrated near $\vec{\Theta}$ at χ^2_{min}. However, even in this less restrictive form, the presented data is found quite informative, as e.g. the inferred truncation scale is found very similar to radial density gradient scales in the SMT plasmas.

B The Boris algorithm

As stated in Sec. 4.1, the method chosen to advance the fast ion tracer position and velocity is the Boris-algorithm. Originally proposed in Ref. [175], it has become a standard choice in a variety of applications and detailed documentation can be found in many textbooks on numerical methods such as Ref. [237]. The equations of motion for the position $\vec{r}$ and velocity $\vec{v}$ with

$$\begin{aligned} d_t\vec{r} &= \vec{v} && \text{(B.1)}\\ d_t\vec{v} &= \frac{q}{m}\left[\vec{E}+\left(\vec{v}\times\vec{B}\right)\right] && \text{(B.2)}\end{aligned}$$

are discretized into propagation times $t = \{\tau_i\}$ separated by a time interval $\Delta\tau$, and can be integrated explicitly. While defining $\vec{t} = \frac{q}{2m}\Delta\tau\vec{B}_0$, the integration scheme for the step from τ_0 to τ_1 reads

$$\begin{aligned} \vec{v}_- &= \vec{v}_0 + \frac{q}{2m}\Delta\tau\vec{E}_0 && \text{(B.3)}\\ \vec{v}' &= \vec{v}_- + \vec{v}_- \times \vec{t} && \text{(B.4)}\\ \vec{v}_+ &= \vec{v}_- + \vec{s} = \vec{v}_- + \frac{2}{1+\left|\vec{t}\right|^2}\left(\vec{v}'\times\vec{t}\right) && \text{(B.5)}\\ \vec{v}_1 &= \vec{v}_+ + \frac{q}{2m}\Delta\tau\vec{E}_0 && \text{(B.6)}\\ \vec{r}_1 &= \vec{r}_0 + \vec{v}_1\Delta\tau \quad . && \text{(B.7)}\end{aligned}$$

To advance the velocities, half of the contribution from the electric field is added before, the other half after treating the rotation due to the magnetic field in Eqs. B.4-B.5. The angle of this rotation can be approximated using the small angle formula

$$\frac{\theta}{2} \approx \tan\left(\frac{\theta}{2}\right) = \frac{q}{2m}\Delta\tau\left|\vec{B}_0\right| = \left|\vec{t}\right| \quad . \qquad \text{(B.8)}$$

The approximate rotation process is geometrically visualized in Fig. B.1.

First, the vector $\vec{v}'$ bisecting the angle θ is found in Eq. B.4. Then, its orthogonal $\vec{s}$ is used in Eq.

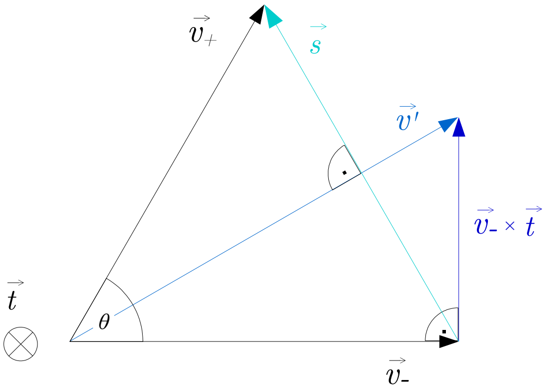

Figure B.1 – Illustration of the $\vec{v} \times \vec{B}$-rotation of $\vec{v}_-$ into $\vec{v}_+$ through the vector operations given in Eqs. B.4-B.5.

B.5 to rotate $\vec{v}_-$ into $\vec{v}_+$, while $|\vec{s}|$ is fixed by the requirement of $|\vec{v}_-| = |\vec{v}_+|$ leading to the factor $\frac{2}{1+t^2}$. While the approximation of θ introduces a small phase error [176], the computational cost of the tan(.) function is avoided. Note further that the energy and the magnitude of the momentum of the tracers are exactly conserved in this step. Relativistic corrections are straightforwardly possible, but clearly unnecessary in our settings.

C Fractional derivatives

The concept of differentiation to non-integer orders was studied already in the 18th century by Leibniz and Euler and the arising field of fractional calculus has received renewed attention in applied mathematics over the past decades [238, 114, 209]. The related definitions and properties of 'fractional' derivatives and integrals are documented with varying conventions in number of textbooks, such as [238, 209], along with their historical development. We mostly follow [209] here and in the text, unless specified otherwise.

In the 19th century, different types of fractional derivatives were defined in terms of series representations, based on their expected action on a given type of basis function, i.e. separately for polynomials (by Riemann), exponentials (by Liouville) and trigonometric functions (by Fourier). Their later representation in terms of integrals were based on Cauchy's repeated integral theorem that states for well-behaved functions that

$$ {}_a\mathcal{I}_x^n f(x) \equiv \int_a^x \int_a^{x_{n-1}} \dots \int_a^{x_1} f(x_0)\, dx_0 \dots dx_{n-1} = \frac{1}{(n-1)!} \int_a^x (x-x')^{n-1} f(x')\, dx' \quad , \tag{C.1} $$

which is proven by induction. Krug extended this theorem to fractional order $\alpha \in \mathbb{R} > 0$ in 1890, so that e.g. the 'left-handed' Riemann fractional integral (see e.g. Eq. 6.36) can be defined as

$$ {}_0\mathcal{I}_x^\alpha f(x) = \frac{1}{\Gamma(\alpha)} \int_0^x (x-x')^{\alpha-1} f(x')\, dx' \tag{C.2} $$

where we find that polynomials $x^k \to 0$ in the lower limit. The 'right-handed' version of the integral is defined analogously by swapping the integral limits and keeping the argument of the kernel positive i.e.

$$ {}_x\mathcal{I}_0^\alpha f(x) = \frac{1}{\Gamma(\alpha)} \int_x^0 (x'-x)^{\alpha-1} f(x')\, dx' \tag{C.3} $$

Fractional differentiation is accomplished by combining fractional integrals with integer differentiation, so that the left- and right-handed Riemann derivatives of order α read

$$
\begin{aligned}
{}_0\mathcal{D}_x^{\alpha} f(x) &= \frac{d}{dx}\frac{1}{\Gamma(1-\alpha)}\int_0^x (x-x')^{-\alpha} f(x')\,dx' \quad , && \text{(C.4)}\\
{}_x\mathcal{D}_0^{\alpha} f(x) &= \frac{d}{dx}\frac{1}{\Gamma(1-\alpha)}\int_x^0 (x'-x)^{-\alpha} f(x')\,dx' \quad . && \text{(C.5)}
\end{aligned}
$$

Using the limits $\pm\infty$ instead, where we have $e^{\mp kx} \to 0$ (for $k > 0$), yields the definition of the Liouville fractional derivatives

$$
\begin{aligned}
{}_{-\infty}\mathcal{D}_x^{\alpha} f(x) &= \frac{d}{dx}\frac{1}{\Gamma(1-\alpha)}\int_{-\infty}^x (x-x')^{-\alpha} f(x')\,dx' \quad , && \text{(C.6)}\\
{}_x\mathcal{D}_{\infty}^{\alpha} f(x) &= \frac{d}{dx}\frac{1}{\Gamma(1-\alpha)}\int_x^{\infty} (x'-x)^{-\alpha} f(x')\,dx' \quad . && \text{(C.7)}
\end{aligned}
$$

One particularly useful feature is by design the properties of the Fourier-transform $\mathcal{F}\{.\}(k)$ of the latter, i.e. we have

$$
\mathcal{F}\left\{{}_{-\infty}\mathcal{D}_x^{\alpha} f(x)\right\}(k) = (-ik)^{\alpha}\hat{f}(k) \quad , \quad \mathcal{F}\left\{{}_x\mathcal{D}_{\infty}^{\alpha} f(x)\right\}(k) = (ik)^{\alpha}\hat{f}(k) \quad . \tag{C.8}
$$

The definition of a symmetrized version thus follows naturally in the form of the Riesz derivative with

$$
{}_{RZ}\mathcal{D}_x^{\alpha} f(x) = \frac{-\left({}_{-\infty}\mathcal{D}_x^{\alpha} + {}_x\mathcal{D}_{\infty}^{\alpha}\right)}{2\cos\left(\frac{\pi}{2}\alpha\right)} f(x) \quad \Longleftrightarrow \quad \mathcal{F}\left\{{}_{RZ}\mathcal{D}_x^{\alpha} f(x)\right\}(k) = -|k|^{\alpha}\hat{f}(k) \quad , \tag{C.9}
$$

where $\alpha \to 2$ smoothly retrieves the second order ordinary derivative. The particular usefulness of this derivative in fractional diffusion is linked to the fact that its Fourier-transform corresponds to the first order term of the characteristic of a symmetric α-stable Lévy distribution (with $\sigma = 1$), so that it appears naturally as the space-fractional derivative in FDEs with symmetric propagators. Its generalization to the asymmetric case is given by the Riesz-Feller derivative as in [215] with

$$
\begin{aligned}
{}_{RF}\mathcal{D}_x^{\alpha,\theta} f(x) &= \frac{-\left[\sin\left(\frac{\pi}{2}(\alpha+\theta)\right)\, {}_{-\infty}\mathcal{D}_x^{\alpha} + \sin\left(\frac{\pi}{2}(\alpha-\theta)\right)\, {}_x\mathcal{D}_{\infty}^{\alpha}\right]}{\sin(\pi\alpha)} f(x) && \text{(C.10)}\\
\Longleftrightarrow \quad & \mathcal{F}\left\{{}_{RF}\mathcal{D}_x^{\alpha,\theta} f(x)\right\}(k) = -|k|^{\alpha}\exp\left(i\,\mathrm{sgn}(k)\frac{\pi\theta}{2}\right)\hat{f}(k) \quad , && \text{(C.11)}
\end{aligned}
$$

where with an asymmetry parameter $\theta \to 0$ one retrieves the Riesz derivative. Again, we find exact correspondence when comparing the Fourier transform to the characteristic exponent of asymmetric Lévy distributions as parameterized in Eq. 6.25, so that the Riesz-Feller derivative naturally appears in asymmetric space-fractional FDEs (see [215]).

Following the same pattern, a different generalization is undertaken when introducing the truncated asymmetrical fractional derivative ${}_{\lambda}\mathcal{D}_x^{\alpha,\theta}$, as e.g. used in the CTRW equation Eq.

6.47 in [120] with

$$
\begin{aligned}
{}_{\lambda}\mathcal{D}_x^{\alpha,\theta} f(x) &= \frac{-1}{2\cos\left(\frac{\pi}{2}\alpha\right)} \Big[(1-\theta)\, e^{-\lambda x}\, {}_{-\infty}\mathcal{D}_x^{\alpha}\big(e^{\lambda x} f(x)\big) \\
&\qquad + (1+\theta)\, e^{\lambda x}\, {}_{x}\mathcal{D}_{\infty}^{\alpha}\big(e^{-\lambda x} f(x)\big)\Big] \qquad \text{(C.12)} \\
\iff \quad \mathcal{F}\big\{{}_{\lambda}\mathcal{D}_x^{\alpha,\theta} f(x)\big\}(k) &= \frac{-\big[(1+\theta)(\lambda+ik)^{\alpha} + (1-\theta)(\lambda-ik)^{\alpha}\big]}{2\cos\left(\frac{\pi}{2}\alpha\right)} \hat{f}(k)\,. \qquad \text{(C.13)}
\end{aligned}
$$

The exponential truncation clearly tempers the arguments of the corresponding Liouville derivative in the limits ±∞ as part of the convolution kernel. For the symmetric, untruncated case with $\lambda \to 0$ and $\theta \to 0$ we recover the Riesz derivative.

Lastly, it should be remarked, that the order of differentiation and fractional integration is no longer interchangeable as for the integer orders. This leads to the distinct definition of the Caputo derivative with

$$
{}_{C}\mathcal{D}_t^{\alpha} f(t) = \frac{1}{\Gamma(1-\alpha)} \int_0^t (t-t')^{-\alpha} \frac{df(t')}{dt'}\, dt' \quad . \qquad \text{(C.14)}
$$

This derivative is found most useful when applied on a time-like domain as it allows for the implementation of initial conditions through the finite lower limit of the integral, that is not lost due to differentiation. As seen e.g. also in [215], this is most directly shown in its Laplace-transform $\mathcal{L}\{.\}(s)$ with

$$
\mathcal{L}\big\{{}_{C}\mathcal{D}_t^{\alpha} f(t)\big\}(s) = s^{\alpha}\hat{f}(s) - s^{\alpha-1} f(t\to 0^{+}) \quad \text{for} \quad 0 < \alpha \le 1 \quad , \qquad \text{(C.15)}
$$

which can be found in all Fourier-Laplace forms of CTRW equations as in Eq. 6.30, if the waiting-times between steps are drawn from one-sided stable distributions.

Acronyms

2DSSLP	2-Dimensional Single Sided Langmuir Probe
AFLM	Asymmetrical Fractional Lévy Motion
C(A)S	Conditional (Average) Sampling
CTRW	Continuous Time Random Walk
EC	Electron Cyclotron
FBM	Fractional Brownian Motion
FDE	Fractional Diffusion Equation
FLM	Fractional Lévy Motion
GBS	Global Braginskii Solver
GEA	Gridded Energy Analyzer
GLE	Generalized Langevin Equation
FRIPLE	Five tip tRIPLE probe
HEXTIP-U	HEXagonal Turbulence Imaging Probe - Upgrade
HFS	High Field Side
LFS	Low Field Side
LP	Langmuir Probe
OBM	Ordinary Brownian Motion
SLP	Slow Langmuir Probe
SMT	Simple Magnetized Torus
TAFLM	Truncated Asymmetrical Fractional Lévy Motion
TCV	Tokamak à Configuration Variable
TORPEX	TORoidal Plasma EXperiment

Repeatedly used symbols

c	Normalization factor for variations in fast ion injection current
D	Toroidal distance between fast ion source and detector
E	Fast ion injection energy
$f, f(\mathbf{R})$	PDF of displacements of instantaneous fast ion profile
F, $F(R,T)$	Fast ion tracer distributions based on GBS simulations
G, $G(R,T)$	Propagators of different types of random walks
H	Hurst exponent / self similarity exponent
j, $j(\mathbf{R})$	Instantaneous fast ion profile
J, $J(\mathbf{R})$	Time-average fast ion profile
$N(R,T)$	Predicted fast ion tracer distributions obtained via propagator
$P(.), P(\xi)$	PDFs in various contexts, e.g. of random noise increments ξ
$\mathbf{R} = [R, Z]$	Coordinates in poloidal plane - horizontal, vertical
t	Time in local fast ion time-series (up to Ch. 5)
t	Propagation time of random walkers and fast ion tracers (after Ch. 5)
T	Propagation time of fast ions in given transport regime
x	Generic spatial coordinate in random walks
α	Space fractional exponent
β	Time fractional exponent
γ_x	Skewness in fast ion time series, various subscripts
ϵ	Arbitrarily small time increment
θ	Asymmetry parameters
$\vec{\Theta}$	Vector of TAFLM parameters used in fitting
λ	Truncation parameter
μ_x	Time-average (mean) in fast ion time-series, various subscripts
ν	Fast ion transport exponent
ξ	Fluctuating force / noise increments in random walks
σ	Standard deviation in various contexts, Chs.6,7: scale parameter
τ	Propagation time of fast ions since injection (up to Ch. 5)
Ω	Fast ion Larmor frequency
$\mathcal{S}$	Subscript for time-series statistics during ion source on-phase
$\mathcal{N}$	Subscript for time-series statistics during ion source off-phase
$\mathcal{J}$	Subscript for noise-reduced time-series statistics

Figure attributions

Figure 1.1 While the figure was produced by the author, the displayed data was retrieved from Table 1 and Fig. 1 in Ref. [29]: Ghahramany, N. and Gharaati, S. and Ghanaatian, M: *New approach to nuclear binding energy in integrated nuclear model*, Journal of Theoretical and Applied Physics, vol. 6, pp.3, Springer, 2012, https://link.springer.com/article/10.1186/2251-7235-6-3, available as Open Access publication via Springer Link under Creative Commons Coyright license 2.0 . Compared to the original table and figure, only a smaller subset of data is shown here, on a logarithmic abscissa. Changed axes labels and annotations have been added.

Figure 1.3(a) Cropped from: *NIF Hohlraum* as *nif-1209-18059.jpg*, Credits to Lawrence Livermore National Laboratory (LLNL), permitted uses under Creative Commons copyright license *CC BY-NC-SA 4.0*, as stated under *Copyright and Reuse* at https://www.llnl.gov/copyright-and-reuse, retrieved from: https://lasers.llnl.gov/media/photo-gallery?id=nif-1209-18059, date: 31.10.19

Figure 1.3(b) Reprinted from Ref. [41], with permission from AIP. License number: 4743751427715, 07.01.2020, Furthermore, the author appears as 3rd author on Ref. [41].

Figure 1.4 Adapted from: *Schematic of a tokamak chamber and magnetic profile.*, by S. Li, H. Jiang, Z. Ren, C. Xu: *'Optimal Tracking for a Divergent-Type Parabolic PDE System in Current Profile Control'*, for *Abstract and Applied Analysis*, 2014, 940965, Hindawi, doi:10.1155/2014/940965, available under Creative Commons copyright license 4.0. The annotations have been simplified by the author, and their font adjusted.

Figure 1.5(a) Cropped from: *TCV 3D views by Matthieu Toussaint* as *TCV_1*, permission to use obtained from original author, retrieved from: https://crpplocal.epfl.ch/gallery/v/scientific/crpptcv/assembly/TCV_1.jpg.html date: 10.11.2019

Figure 1.5(b-d) Cropped from: *Omnium gatherum of TCV plasma shapes. Figure 2.3.2 of Ch. Schlatter PhD thesis* as *TCV_shapes*, permission to use and modify obtained from original author, retrieved from: https://crpplocal.epfl.ch/gallery/v/scientific/crpptcv/assembly/TCV_shapes.pdf.html date: 09.11.2019

Figure 1.6 Cropped from: *Schematic view of the Wendelstein 7-X superconducting magnets system with non-planar coils (blue) and planar coils (brown).* as *800px-Wendelstein_7-*

X_schematic_view_of_magnets_system.jpg, by *M. Nagel, C.P. Dhard, H. Bau, H.-S. Bosch, U. Meyer, S. Raatz, K. Risse and T. Rummel* : *'Cryogenic commissioning, cool down and first magnet operation of Wendelstein 7-X'*, IOP Conference Series: Materials Science and Engineering, vol. 171,1, 012050, IOP, 2017, https://doi.org/10.1088/1757-899X/171/1/012050, Available from IOP Publishing under Creative Commons copyright license 3.0, see https://creativecommons.org/licenses/by/3.0/

Figure 1.7(a) Re-used from: *The largest tokamak in the world, 15 January 2013*, as *in-cryostat overview 20130116.jpg*, ITER Image Gallery, Credit ©ITER Organization, http://www.iter.org/, Permitted for educational and informational use, furthermore cleared with ITER Communications office, retrieved from: https://www.iter.org/doc/all/content/com/gallery/media/7-technical/, date: 12.11.2019

Figure 1.7(b) Re-used from: *The precision of a clockmaker, 04.09.2019*, as *pit_from_above.jpg*, ITER Image Gallery, Credit ©ITER Organization, http://www.iter.org/, Permitted for educational and informational use, furthermore cleared with ITER Communications office, retrieved from: https://www.iter.org/doc/all/content/com/gallery/construction/tkmcomplex/pit_from_above.jpg, date: 12.11.2019

Figure 1.8(a) Cropped from: *Accelerating Jet*, as *xrbs_nustar.jpg*, HEASARC picture of the week, credit: NASA/JPL-Caltech, Published: November 6, 2017, A service of the Astrophysics Science Division at NASA/GSFC, Generally non-copyrighted, permitted for non-commercial use, as outlined in *Media Usage Guidelines* under *https://www.nasa.gov/multimedia/guidelines/index.html* retrieved from: https://heasarc.gsfc.nasa.gov/docs/objects/heapow/archive/compact_objects/xrbs_nustar.html date: 22.06.2019

Figure 1.8(b) Cropped from: *Sun's Busy Week*, as *COR2_busyweek.jpg*, Courtesy of STEREO/COR2 consortium (NASA), Generally non-copyrighted, permitted and encouraged for educational and non-commercial use, as outlined in *STEREO Copyright Notice* under https://stereo.gsfc.nasa.gov/gallery/copyright.shtml retrieved from: https://stereo.gsfc.nasa.gov/gallery/item.php?id=stereoimages&iid=229 date: 15.01.2020

Figure 2.12(a,b) Technical drawings credited to Swiss Plasma Center Technical Drawing and Design Office, Robert Bertizzolo, permission to use and adapt obtained.

Figure 2.13 Reprinted figure from Ref. [103], with permission from APS. License number: RNP/20/JAN/021876, 13.01.2020, Permission for adaptations obtained from original author. Fonts changed, labels adapted and grid lines added by author.

Figure 2.14 Reprinted figure from Ref. [103], with permission from APS. License number: RNP/20/JAN/021876, 13.01.2020, Permission for adaptations obtained from original author. Fonts changed, annotations adapted and grid lines added by author.

All further photography in Figs. 2.3, 2.6(a,b), 2.7(a), 2.9(a,b), 2.10(a,b), 2.11(a), 2.12(c) has been carried out by the author.

The 3D illustrations of TORPEX and the fast ion systems in Figs. 2.1, 2.5, 2.6(c), 2.7(b), 2.8, 4.2 have been assembled, textured and rendered by the author in Blender 2.78, and incorporate parts and older files supplied by A. Bovet. Most 3D model files were supplied from the archives of the Swiss Plasma Center Technical Drawing and Design Office and sometimes adapted by the author.

All remaining figures consist of graphs produced in MATLAB 2016b-2018b, by The MathWorks Inc., Natick MA, USA. The routines for creating Fig. 4.1 are credited to Fabio Avino. If similar figures to those presented in this work have been published by the author, references to the respective journal papers are given usually at the beginning of the sections where the published content is adapted.

For the illustrations of different types of random walks, the following MATLAB resources are acknowledged: Mark Veillette (2020). STBL: Alpha stable distributions for MATLAB (https://www.github.com/markveillette/stbl), GitHub. Retrieved December 08, 2018.

Igor Podlubny (2020). Mittag-Leffler function (https://www.mathworks.com/matlabcentral/fileexchange/8738-mittag-leffler-function), MATLAB Central File Exchange. Retrieved January 01, 2020.

Bibliography

[1] U.S. Energy Information Administration. International energy outlook 2019 - with projections to 2050. 2019. URL https://www.eia.gov/outlooks/ieo.

[2] F. Wagner. The complex story of energy transition, an introduction. In *EPJ Web of Conferences*, volume 189, page 00002. EDP Sciences, 2018.

[3] S.H. Mohr, J. Wang, G. Ellem, J. Ward, and D. Giurco. Projection of world fossil fuels by country. *Fuel*, 141:120–135, 2015.

[4] S. Solomon, G.-K. Plattner, R. Knutti, and P. Friedlingstein. Irreversible climate change due to carbon dioxide emissions. *P. Natl. Acad. Sci.*, 106(6):1704–1709, 2009.

[5] M. Höök and X. Tang. Depletion of fossil fuels and anthropogenic climate change, a review. *Energ. Policy*, 52:797–809, 2013.

[6] H. Shue. Climate dreaming: negative emissions, risk transfer, and irreversibility. *Forthcoming in Special Issue of Journal of Human Rights and Environment*, 2017.

[7] J. Rogelj, M. Den Elzen, N. Höhne, T. Fransen, H. Fekete, H. Winkler, R. Schaeffer, F. Sha, K. Riahi, and M. Meinshausen. Paris agreement climate proposals need a boost to keep warming well below 2 c. *Nature*, 534(7609):631–639, 2016.

[8] J. Hansen, M. Sato, P. Kharecha, K. Von Schuckmann, D.J. Beerling, J. Cao, S. Marcott, V. Masson-Delmotte, M.J. Prather, E.J. Rohling, et al. Young people's burden: requirement of negative CO2 emissions. *arXiv preprint arXiv:1609.05878*, 2017.

[9] D.G. Victor, K. Akimoto, Y. Kaya, M. Yamaguchi, D. Cullenward, and C. Hepburn. Prove paris was more than paper promises. *Nature News*, 548(7665):25, 2017.

[10] F. Wagner. Considerations for an eu-wide use of renewable energies for electricity generation. *Eur. Phys. J. Plus*, 129(10):219, 2014.

[11] M. Hock. Aufstieg und fall der photovoltaik. *Frankfurter Allgemeine Zeitung, FAZ.NET*, 11.05.2017. URL https://www.faz.net/aktuell/finanzen/aktien/wie-solarworld-co-abstiegen-15010799.html.

[12] K. Muraoka, F. Wagner, Y. Yamagata, and A.J.H. Donné. Short-and long-range energy strategies for japan and the world after the fukushima nuclear accident. *J. Instrum.*, 11 (01):C01082, 2016.

[13] M. Hoogwijk and W. Graus. Global potential of renewable energy sources: a literature assessment. *Background report for REN21 - Renewable Energy Policy Network for the 21st Century, PECSNL072975*, 2008.

[14] D. Grand, C. Le Brun, R. Vidil, and F. Wagner. Electricity production by intermittent renewable sources: a synthesis of french and german studies. *Europ. Phys. J. Plus*, 131 (9):329, 2016.

[15] Friedrich Wagner. Surplus from and storage of electricity generated by intermittent sources. *Eur. Phys. J. Plus*, 131(12):445, 2016.

[16] G. Nicoletti, N. Arcuri, G. Nicoletti, and R. Bruno. A technical and environmental comparison between hydrogen and some fossil fuels. *Energ. Convers. Manage.*, 89: 205–213, 2015.

[17] D. Egré and J.C. Milewski. The diversity of hydropower projects. *Energ. Policy*, 30(14): 1225–1230, 2002.

[18] G. Locatelli, M. Mancini, and N. Todeschini. Generation iv nuclear reactors: Current status and future prospects. *Energ. Policy*, 61:1503–1520, 2013.

[19] I. Pioro. *Handbook of generation IV nuclear reactors*. Woodhead Publishing / Elsevier, 2016.

[20] J. Canton, M. Tomasi, P. Arnoldus, J. Pienkowski, N. Darnaut, E. Maincent, A. Rezessy, M. Spooner, A. Sripathy, et al. Member states energy dependence: an indicator-based assessment. *European Economy, Occasional Papers*, 145, 2013.

[21] Jeffrey P Freidberg. *Plasma physics and fusion energy*. Cambridge University Press, 2008.

[22] U. Stroth. *Plasmaphysik*. Springer, 2011.

[23] D.D. Clayton. *Principles of stellar evolution and nucleosynthesis*. University of Chicago Press, 1983.

[24] M.L.E. Oliphant, Harteck P., and E. Rutherford. Transmutation effects observed with heavy hydrogen. *Proc. R. Soc. Lond. A*, 144, 1934.

[25] L. Meitner and O. Frisch. Disintegration of uranium by neutrons: a new type of nuclear reaction. *Nature*, 143:239–240, 1939.

[26] J.D. Huba. NRL plasma formulary. Technical report, Naval Research Laboratory - Beam Physics Branch - Plasma Physics Division - Washington DC, 2013.

[27] S. Atzeni and J. Meyer-ter Vehn. *The physics of inertial fusion: beam plasma interaction, hydrodynamics, hot dense matter.* Oxford University Press, 2004.

[28] J. Cirincione. *Bomb scare: the history and future of nuclear weapons.* Columbia University Press, New York/Chichester, 2007.

[29] N. Ghahramany, S. Gharaati, and M. Ghanaatian. New approach to nuclear binding energy in integrated nuclear model. *J. Theor. Appl. Phys.*, 6(1):3, 2012.

[30] S.O. Dean. *Search for the ultimate energy source: a history of the US fusion energy program.* Springer Science & Business Media, 2013.

[31] J.D. Lawson. Some criteria for a power producing thermonuclear reactor. *Proc. Phys. Soc. B*, 70(1):6, 1957.

[32] J.T. Hunt, K.R. Manes, J.R. Murray, P.A. Renard, R. Sawicki, J.B. Trenholme, and W. Williams. Laser design basis for the national ignition facility. *Fusion Technol.*, 26 (3P2):767–771, 1994.

[33] E.I. Moses and C.R. Wuest. The national ignition facility: laser performance and first experiments. *Fusion Sci. Technol.*, 47(3):314–322, 2005.

[34] OA Hurricane, DA Callahan, DT Casey, PM Celliers, Charles Cerjan, EL Dewald, TR Dittrich, T Döppner, DE Hinkel, LF Berzak Hopkins, et al. Fuel gain exceeding unity in an inertially confined fusion implosion. *Nature*, 506(7488):343, 2014.

[35] O.A. Hurricane, P.T. Springer, P.K. Patel, D.A. Callahan, K. Baker, D.T. Casey, L. Divol, T. Döppner, D.E. Hinkel, M. Hohenberger, et al. Approaching a burning plasma on the NIF. *Phys. Plasmas*, 26(5):052704, 2019.

[36] R. Kishony and D. Shvarts. Ignition condition and gain prediction for perturbed inertial confinement fusion targets. *Phys. Plasmas*, 8(11):4925–4936, 2001.

[37] S. Taylor and J.P. Chittenden. Effects of perturbations and radial profiles on ignition of inertial confinement fusion hotspots. *Phys. Plasmas*, 21(6):062701, 2014.

[38] O.A. Hurricane, D.A. Callahan, D.T. Casey, E.L. Dewald, T.R. Dittrich, T. Döppner, M.A. Barrios Garcia, D.E. Hinkel, L.F. Berzak Hopkins, P. Kervin, et al. The high-foot implosion campaign on the national ignition facility. *Physics of Plasmas*, 21(5):056314, 2014.

[39] A.J. MacKinnon, N.B. Meezan, J.S. Ross, S. Le Pape, L. Berzak Hopkins, L. Divol, D. Ho, J. Milovich, A. Pak, J. Ralph, et al. High-density carbon ablator experiments on the national ignition facility. *Phys. Plasmas*, 21(5):056318, 2014.

[40] T. Döppner, D.A. Callahan, O.A. Hurricane, D.E. Hinkel, T. Ma, H.-S. Park, L.F. Berzak Hopkins, D.T. Casey, P. Celliers, E.L. Dewald, et al. Demonstration of high performance in layered deuterium-tritium capsule implosions in uranium hohlraums at the national ignition facility. *Phys. Rev. Lett.*, 115(5):055001, 2015.

[41] J.P. Chittenden, B.D. Appelbe, F. Manke, K. McGlinchey, and N.P.L. Niasse. Signatures of asymmetry in neutron spectra and images predicted by three-dimensional radiation hydrodynamics simulations of indirect drive implosions. *Phys. Plasmas*, 23(5):052708, 2016.

[42] A.J. Crilly, B.D. Appelbe, K. McGlinchey, C.A. Walsh, J.K. Tong, A.B. Boxall, and J.P. Chittenden. Synthetic nuclear diagnostics for inferring plasma properties of inertial confinement fusion implosions. *Phys. Plasmas*, 25(12):122703, 2018.

[43] L.J. Perkins, D.D.-M. Ho, B.G. Logan, G.B. Zimmerman, M.A. Rhodes, D.J. Strozzi, D.T. Blackfield, and S.A. Hawkins. The potential of imposed magnetic fields for enhancing ignition probability and fusion energy yield in indirect-drive inertial confinement fusion. *Phys. Plasmas*, 24(6):062708, 2017.

[44] C.A. Walsh, K. McGlinchey, J.K. Tong, B.D. Appelbe, A. Crilly, M.F. Zhang, and J.P. Chittenden. Perturbation modifications by pre-magnetisation of inertial confinement fusion implosions. *Phys. Plasmas*, 26(2):022701, 2019.

[45] M.L. Spaeth, K.R. Manes, M. Bowers, P. Celliers, J.-M. Di Nicola, P. Di Nicola, S. Dixit, G. Erbert, J. Heebner, D. Kalantar, et al. National ignition facility laser system performance. *Fusion Sci. Technol.*, 69(1):366–394, 2016.

[46] Haro Fritsche, Fabio Ferrario, Ralf Koch, Bastian Kruschke, Ulrich Pahl, Silke Pflueger, Andreas Grohe, Wolfgang Gries, Florian Eibl, Stefanie Kohl, et al. Direct diode lasers and their advantages for materials processing and other applications. In *High-Power Laser Materials Processing: Lasers, Beam Delivery, Diagnostics, and Applications IV*, volume 9356, page 93560I. International Society for Optics and Photonics, 2015.

[47] E.A. Azizov. Tokamaks: from a. d. sakharov to the present (the 60-year history of tokamaks). *Physics-Uspekhi*, 55(2):190, 2012.

[48] T.H. Stix. *Waves in plasmas.* AIP Press, New York, 1992.

[49] J. Wesson and D.J. Campbell. *Tokamaks.* Oxford university press, 2011.

[50] F. Hofmann, J.B. Lister, W. Anton, S. Barry, R. Behn, S. Bernel, G. Besson, F. Buhlmann, R. Chavan, M. Corboz, et al. Creation and control of variably shaped plasmas in TCV. *Plasma Phys. Control. Fusion*, 36(12B):B277, 1994.

[51] R.S. Cohen, L. Spitzer Jr, and P.M.C.R. Routly. The electrical conductivity of an ionized gas. *Phys. Rev.*, 80(2):230, 1950.

[52] M. Kong, T.C. Blanken, F. Felici, C. Galperti, B. Maljaars, O. Sauter, T. Vu, F. Carpanese, A. Merle, J.-M. Moret, et al. Control of NTMs and integrated multi-actuator plasma control on TCV. *Nucl. Fusion*, 59(7):076035, 2019.

[53] S. Coda, M. Agostini, R. Albanese, S. Alberti, E. Alessi, S. Allan, J.S. Allcock, R. Ambrosino, H. Anand, Y. Andrebe, et al. Physics research on the TCV tokamak facility: From conventional to alternative scenarios and beyond. *Nucl. Fusion*, 59(11):112023, 2019.

[54] V.A. Soukhanovskii. A review of radiative detachment studies in tokamak advanced magnetic divertor configurations. *Plasma Phys. Control. Fusion*, 59(6):064005, 2017.

[55] K. Verhaegh, B. Lipschultz, B.P. Duval, O. Février, C. Theiler, M. Wensing, C. Bowman, D.S. Gahle, J.R. Harrison, B. Labit, et al. An improved understanding of the roles of atomic processes and power balance in divertor target ion current loss during detachment. *Nucl. Fusion*, 59(12):126038, 2019.

[56] M. Wensing, B.P. Duval, O. Février, A. Fil, D. Galassi, E. Havlickova, A. Perek, H. Reimerdes, C. Theiler, K. Verhaegh, et al. SOLPS-ITER simulations of the TCV divertor upgrade. *Plasma Phys. Control. Fusion*, 61(8):085029, 2019.

[57] JET Team et al. Physics of high performance JET plasmas in DT. *Nucl. Fusion*, 39(9Y): 1227, 1999.

[58] M. Keilhacker, A. Gibson, C. Gormezano, and P.H. Rebut. The scientific success of JET. *Nucl. Fusion*, 41(12):1925, 2001.

[59] L. Spitzer Jr. A proposed stellarator. Technical report, Princeton University, NJ Forrestal Research Center, 1951.

[60] I. Milch. Wendelstein 7-X im betrieb: Fusionsforschung mit stellaratoren. *Physik in unserer Zeit*, 50(1):16–23, 2019.

[61] J. Ongena and Y. Ogawa. Nuclear fusion: Status report and future prospects. *Energ. Policy*, 96:770–778, 2016.

[62] K. Tomabechi, ITER Team, et al. ITER: design overview. *J. Nucl. Mater.*, 179:1173–1178, 1991.

[63] O. Motojima. The ITER project construction status. *Nucl. Fusion*, 55(10):104023, 2015.

[64] T. Donne, W. Morris, et al. European research roadmap to the realisation of fusion energy. 2018. URL https://www.euro-fusion.org/eurofusion/roadmap/.

[65] G. Federici, C. Bachmann, W. Biel, L. Boccaccini, F. Cismondi, S. Ciattaglia, M. Coleman, C. Day, E. Diegele, T. Franke, et al. Overview of the design approach and prioritization of R&D activities towards an eu demo. *Fusion Eng. Des.*, 109:1464–1474, 2016.

[66] C. Bachmann, S. Ciattaglia, F. Cismondi, T. Eade, G. Federici, U. Fischer, T. Franke, C. Gliss, F. Hernandez, J. Keep, et al. Overview over DEMO design integration challenges and their impact on component design concepts. *Fusion Eng. Des.*, 136:87–95, 2018.

[67] M.E. Sawan and M.A. Abdou. Physics and technology conditions for attaining tritium self-sufficiency for the DT fuel cycle. *Fusion Eng. Des.*, 81(8-14):1131–1144, 2006.

[68] M. Kovari, M. Coleman, I. Cristescu, and R. Smith. Tritium resources available for fusion reactors. *Nucl. Fusion*, 58(2):026010, 2017.

[69] D. Fasel and M.Q. Tran. Availability of lithium in the context of future D-T fusion reactors. *Fusion Eng. Des.*, 75:1163–1168, 2005.

[70] F.L. Hinton and R.D. Hazeltine. Theory of plasma transport in toroidal confinement systems. *Rev. Mod. Phys.*, 48(2):239, 1976.

[71] E.J. Doyle, W.A. Houlberg, Y. Kamada, V. Mukhovatov, T.H. Osborne, A. Polevoi, G. Bateman, J.W. Connor, J.G. Cordey, T. Fujita, et al. Plasma confinement and transport. *Nucl. Fusion*, 47(6):S18, 2007.

[72] G.D. Conway. Turbulence measurements in fusion plasmas. *Plasma Phys. Control. Fusion*, 50(12):124026, 2008.

[73] D.A. D'ippolito, J.R. Myra, and S.J. Zweben. Convective transport by intermittent blob-filaments: Comparison of theory and experiment. *Phys. Plasmas*, 18(6):060501, 2011.

[74] O.E. Garcia, J. Horacek, R.A. Pitts, A.H. Nielsen, W. Fundamenski, J.P. Graves, V. Naulin, and J.J. Rasmussen. Interchange turbulence in the TCV scrape-off layer. *Plasma Phys. Control. Fusion*, 48(1):L1, 2005.

[75] F. Riva, C. Colin, J. Denis, L. Easy, I. Furno, J. Madsen, F. Militello, V. Naulin, A.H. Nielsen, J.M.B. Olsen, et al. Blob dynamics in the TORPEX experiment: a multi-code validation. *Plasma Phys. Control. Fusion*, 58(4):044005, 2016.

[76] F. Wagner, G. Becker, K. Behringer, D. Campbell, A. Eberhagen, W. Engelhardt, G. Fussmann, O. Gehre, J. Gernhardt, G.v. Gierke, et al. Regime of improved confinement and high beta in neutral-beam-heated divertor discharges of the asdex tokamak. *Phys. Rev. Lett.*, 49(19):1408, 1982.

[77] C.P. Ritz, H. Lin, T.L. Rhodes, and A.J. Wootton. Evidence for confinement improvement by velocity-shear suppression of edge turbulence. *Phys. Rev. Lett.*, 65(20):2543, 1990.

[78] P.H. Diamond, Y.-M. Liang, B.A. Carreras, and P.W. Terry. Self-regulating shear flow turbulence: A paradigm for the L to H transition. *Phys. Rev. Lett.*, 72(16):2565, 1994.

[79] G.R. Tynan, I. Cziegler, P.H. Diamond, M. Malkov, A. Hubbard, J.W. Hughes, J.L. Terry, and J.H. Irby. Recent progress towards a physics-based understanding of the H-mode transition. *Plasma Phys. Control. Fusion*, 58(4):044003, 2016.

[80] A. Fasoli, C.B.H.L. Gormenzano, H.L. Berk, B. Breizman, S. Briguglio, D.S. Darrow, N. Gorelenkov, W.W. Heidbrink, A. Jaun, S.V. Konovalov, et al. Physics of energetic ions. *Nucl. Fusion*, 47(6):S264, 2007.

[81] L. Chen and F. Zonca. Physics of alfvén waves and energetic particles in burning plasmas. *Rev. Mod. Phys.*, 88(1):015008, 2016.

[82] D. Moseev, M. Salewski, M. Garcia-Muñoz, B. Geiger, and M. Nocente. Recent progress in fast-ion diagnostics for magnetically confined plasmas. *Rev. Mod. Plasma Phys.*, 2(1): 7, 2018.

[83] WW Heidbrink and GJ Sadler. The behaviour of fast ions in tokamak experiments. *Nucl. Fusion*, 34(4):535, 1994.

[84] T. Hauff and F. Jenko. Mechanisms and scalings of energetic ion transport via tokamak microturbulence. *Phys. Plasmas*, 15(11):112307, 2008.

[85] W.W. Heidbrink, J.M. Park, M. Murakami, C.C. Petty, C. Holcomb, and M.A. Van Zeeland. Evidence for fast-ion transport by microturbulence. *Phys. Rev. Lett.*, 103(17):175001, 2009.

[86] P. Davidson. *Turbulence: An Introduction for scientists and engineers.* Oxford University Press, 2015.

[87] S. Sridhar and P. Goldreich. Toward a theory of interstellar turbulence. i: Weak alfvénic turbulence. *Astrophys. J.*, 432(2):612–621, 1994.

[88] P. Goldreich and S. Sridhar. Toward a theory of interstellar turbulence. 2: Strong alfvenic turbulence. *Astrophys. J.*, 438:763–775, 1995.

[89] R. Bruno and V. Carbone. The solar wind as a turbulence laboratory. *Living Rev. Sol. Phys.*, 2(1):4, 2005.

[90] K. Fang and K. Murase. Linking high-energy cosmic particles by black-hole jets embedded in large-scale structures. *Nature Physics*, 14(4):396, 2018.

[91] E. Amato and P. Blasi. Cosmic ray transport in the galaxy: A review. *Adv. Space Res.*, 62 (10):2731–2749, 2018.

[92] L. Vlahos, A. Anastasiadis, A. Papaioannou, A. Kouloumvakos, and H. Isliker. Sources of solar energetic particles. *Philos. T. Roy. Soc. A*, 377(2148):20180095, 2019.

[93] G. Zimbardo, P. Pommois, and P. Veltri. Superdiffusive and subdiffusive transport of energetic particles in solar wind anisotropic magnetic turbulence. *Astrophys. J. Lett.*, 639(2):L91, 2006.

[94] D. Perrone, R. O. Dendy, I. Furno, R. Sanchez, G. Zimbardo, A. Bovet, A. Fasoli, K. Gustafson, S. Perri, P. Ricci, and F. Valentini. Nonclassical transport and particle-field coupling: from laboratory plasmas to the solar wind. *Space Sci. Rev.*, 178(2):233–270, 2013.

[95] G. Zimbardo, E. Amato, A. Bovet, F. Effenberger, A. Fasoli, H. Fichtner, I. Furno, K. Gustafson, P. Ricci, and S. Perri. Superdiffusive transport in laboratory and astrophysical plasmas. *J. Plasma Phys.*, 81(6):495810601, 2015.

[96] T. Laitinen, A. Kopp, F. Effenberger, S. Dalla, and M.S. Marsh. Solar energetic particle access to distant longitudes through turbulent field-line meandering. *Astron. Astrophys.*, 591:A18, 2016.

[97] C.C. Chaston, J.W. Bonnell, J.R. Wygant, G.D. Reeves, D.N. Baker, and D.B. Melrose. Radiation belt 'dropouts' and drift-bounce resonances in broadband electromagnetic waves. *Geophys. Res. Lett.*, 45(5):2128–2137, 2018.

[98] A. Fasoli, B. Labit, M. McGrath, S.H. Müller, M. Podestà, and F.M. Poli. The TORoidal Plasma EXperiment TORPEX for basic turbulence and transport studies. In *Bull. Am. Phys. Soc.*, volume 48. APS, 2003.

[99] A. Fasoli, A. Burckel, L. Federspiel, I. Furno, K. Gustafson, D. Iraji, B. Labit, J. Loizu, G. Plyushchev, P. Ricci, C. Theiler, A. Diallo, S. Müller, M. Podestà, and F. Poli. Electrostatic instabilities, turbulence and fast ion interactions in the TORPEX device. *Plasma Phys. Control. Fusion*, 52(12):124020, 2010.

[100] I. Furno, F. Avino, A. Bovet, A. Diallo, A. Fasoli, K. Gustafson, D. Iraji, B. Labit, J. Loizu, S. Müller, et al. Plasma turbulence, suprathermal ion dynamics and code validation on the basic plasma physics device TORPEX. *J. Plasma Phys.*, 81(3):345810301, 2015.

[101] S.H. Müller, A. Fasoli, B. Labit, M. McGrath, M. Podestà, and F.M. Poli. Effects of a vertical magnetic field on particle confinement in a magnetized plasma torus. *Phys. Rev. Lett.*, 93(16):165003, 2004.

[102] G. Plyushchev, A. Diallo, A. Fasoli, I. Furno, B. Labit, S. H. Müller, M. Podestà, F. M. Poli, H. Boehmer, W. W. Heidbrink, and Y. Zhang. Fast ion source and detector for investigating the interaction of turbulence with suprathermal ions in a low temperature toroidal plasma. *Rev. Sci. Instrum.*, 77(10):10F503, 2006.

[103] A. Bovet, A. Fasoli, P. Ricci, I. Furno, and K. Gustafson. Nondiffusive transport regimes for suprathermal ions in turbulent plasmas. *Phys. Rev. E*, 91(4):041101, 2015.

[104] K Gustafson, P Ricci, A Bovet, I Furno, and A Fasoli. Suprathermal ion transport in simple magnetized torus configurations. *Phys. Plasmas*, 19(6):062306, 2012.

[105] K Gustafson, P Ricci, I Furno, and A Fasoli. Nondiffusive suprathermal ion transport in simple magnetized toroidal plasmas. *Phys. Rev. Lett.*, 108(3):035006, 2012.

[106] P. Ricci, F. D. Halpern, S. Jolliet, J. Loizu, A. Mosetto, A. Fasoli, I. Furno, and C. Theiler. Simulation of plasma turbulence in scrape-off layer conditions: the GBS code, simulation results and code validation. *Plasma Phys. Control. Fusion*, 54(12):124047, 2012.

[107] A. Bovet, A. Fasoli, and I. Furno. Time-resolved measurements of suprathermal ion transport induced by intermittent plasma blob filaments. *Phys. Rev. Lett.*, 113(22): 225001, 2014.

[108] A. Bovet, M. Gamarino, I. Furno, P. Ricci, A. Fasoli, K. Gustafson, D.E. Newman, and R. Sanchez. Transport equation describing fractional lévy motion of suprathermal ions in TORPEX. *Nucl. Fusion*, 54(10):104009, 2014.

[109] M. Baquero-Ruiz, F. Manke, I. Furno, A. Fasoli, and P. Ricci. Meandering particle bunches and a link between averages of time series of particle counts and higher-order moments. *Phys. Rev. E*, 98(3):032111, 2018.

[110] F. Manke, M. Baquero-Ruiz, I. Furno, O. Chellaï, A. Fasoli, and P. Ricci. Time intermittency in non-diffusive transport regimes of suprathermal ions in turbulent plasmas. *Phys. Rev. E*, 99(5):053208, 2019.

[111] F. Manke, M. Baquero-Ruiz, I. Furno, O. Chellaï, A. Fasoli, and P. Ricci. Characterizing time intermittency in nondiffusive fast ion transport through plasma turbulence. *Plasma Phys. Control. Fusion*, 2019. doi: 10.1088/1361-6587/ab433b.

[112] F. Manke, M. Baquero-Ruiz, I. Furno, O. Chellaï, A. Fasoli, and P. Ricci. Truncated Lévy motion through path integrals and applications to nondiffusive suprathermal ion transport. *Phys. Rev. E*, 100:052122, 2019.

[113] L. Kadi. Installation of the quintuple GEA on TORPEX and first measurements. Technical report, Ecole Polytechnique Fédérale de Lausanne - Swiss Plasma Center, 2018.

[114] R. Klages, G. Radons, and I.M. Sokolov. *Anomalous Transport: Foundations and Applications.* Wiley-VCH, Weinheim, 2008.

[115] M.M. Meerschaert and A. Sikorskii. *Stochastic Models for Fractional Calculus.* De Gruyter Studies in Mathematics. De Gruyter, Berlin/Boston, 2012.

[116] R. Metzler and J. Klafter. The random walk's guide to anomalous diffusion: a fractional dynamics approach. *Phys. Rep.*, 339(1):1–77, 2000.

[117] E.W. Montroll and G.H. Weiss. Random walks on lattices. II. *J. Math. Phys.*, 6(2):167–181, 1965.

[118] G. Samorodnitsky and M.S. Taqqu. *Stable Non-Gaussian Random Processes: Stochastic Models with Infinite Variance.* Chapman and Hall / CRC, 1994.

[119] R. Metzler and J. Klafter. Subdiffusive transport close to thermal equilibrium: from the langevin equation to fractional diffusion. *Phys. Rev. E*, 61(6):6308, 2000.

[120] D. del Castillo-Negrete. Truncation effects in superdiffusive front propagation with Lévy flights. *Phys. Rev. E*, 79(3):031120, 2009.

[121] A. Fasoli, B. Labit, M. McGrath, S.H. Müller, G. Plyushchev, M. Podestà, and F.M. Poli. Electrostatic turbulence and transport in a simple magnetized plasma. *Phys. Plasmas*, 13(5):055902, 2006.

[122] S. H. Müller, A. Fasoli, B. Labit, M. McGrath, O. Pisaturo, G. Plyushchev, M. Podestà, and F. M. Poli. Basic turbulence studies on TORPEX and challenges in the theory-experiment comparison. *Phys. Plasmas*, 12(9):090906, 2005.

[123] O. Chellaï, S. Alberti, M. Baquero-Ruiz, I. Furno, T. Goodman, F. Manke, G. Plyushchev, L. Guidi, A. Koehn, O. Maj, et al. Millimeter-wave beam scattering by field-aligned blobs in simple magnetized toroidal plasmas. *Phys. Rev. Lett.*, 120(10):105001, 2018.

[124] M. Podestà, A. Fasoli, B. Labit, M. McGrath, S.H. Müller, and F.M. Poli. Plasma production by low-field side injection of electron cyclotron waves in a simple magnetized torus. *Plasma Phys. Control. Fusion*, 47(11):1989, 2005.

[125] M. Podestà, A. Fasoli, B. Labit, M. McGrath, S.H. Müller, and F.M. Poli. Experimental characterization and modelling of the particle source in an electron-cyclotron wave driven toroidal plasma. *Plasma Phys. Control. Fusion*, 48(8):1053–1062, 2006.

[126] S. H. Müller, A. Diallo, A. Fasoli, I. Furno, B. Labit, G. Plyushchev, M. Podestà, and F. M. Poli. Probabilistic analysis of turbulent structures from two-dimensional plasma imaging. *Phys. Plasmas*, 13(10):100701, 2006.

[127] F.M. Poli, P. Ricci, A. Fasoli, and M. Podestà. Transition from drift to interchange instabilities in an open magnetic field line configuration. *Phys. Plasmas*, 15(3):032104, 2008.

[128] P. Ricci and B. N. Rogers. Turbulence phase space in simple magnetized toroidal plasmas. *Phys. Rev. Lett.*, 104:145001, 2010.

[129] S. H. Müller, C. Theiler, A. Fasoli, I. Furno, B. Labit, G. R. Tynan, M. Xu, Z. Yan, and J.H. Yu. Studies of blob formation, propagation and transport mechanisms in basic experimental plasmas (TORPEX and CSDX). *Plasma Phys. Control. Fusion*, 51(5):055020, 2009.

[130] F. M. Poli, S. Brunner, A. Diallo, A. Fasoli, I. Furno, B. Labit, S. H. Müller, G. Plyushchev, and M. Podestà. Experimental characterization of drift-interchange instabilities in a simple toroidal plasma. *Phys. Plasmas*, 13(10):102104, 2006.

[131] I. Furno, B. Labit, M. Podestà, A. Fasoli, S.H. Müller, F.M. Poli, P. Ricci, C. Theiler, S. Brunner, A. Diallo, et al. Experimental observation of the blob-generation mechanism from interchange waves in a plasma. *Phys. Rev. Lett.*, 100(5):055004, 2008.

[132] C. Theiler, A. Diallo, A. Fasoli, I. Furno, B. Labit, M. Podestà, F.M. Poli, and P. Ricci. The role of the density gradient on intermittent cross-field transport events in a simple magnetized toroidal plasma. *Phys. Plasmas*, 15(4):042303, 2008.

[133] I. Furno, B. Labit, A. Fasoli, F.M. Poli, P. Ricci, C. Theiler, S. Brunner, A. Diallo, J.P. Graves, M. Podestà, et al. Mechanism for blob generation in the TORPEX toroidal plasma. *Physics of Plasmas*, 15(5):055903, 2008.

[134] C. Theiler, I. Furno, P. Ricci, A. Fasoli, B. Labit, S.H. Müller, and G. Plyushchev. Cross-field motion of plasma blobs in an open magnetic field line configuration. *Phys. Rev. Lett.*, 103(6):065001, 2009.

[135] F. Avino. *Turbulence at the boundary of toroidal plasmas with open and closed magnetic flux surfaces.* PhD thesis, École Polytechnique Fédérale de Lausanne, 2015.

[136] A. Bovet. *Suprathermal ion transport in turbulent magnetized plasmas.* PhD thesis, École Polytechnique Fédérale de Lausanne, 2015.

[137] P. Ricci, C. Theiler, A. Fasoli, I. Furno, B. Labit, S. Müller, M. Podestà, and F. M. Poli. Langmuir probe-based observables for plasma-turbulence code validation and application to the TORPEX basic plasma physics experiment. *Phys. Plasmas*, 16(5):055703, 2009.

[138] P. Ricci, C. Theiler, A. Fasoli, I. Furno, K. Gustafson, D. Iraji, and J. Loizu. Methodology for turbulence code validation: Quantification of simulation-experiment agreement and application to the TORPEX experiment. *Phys. Plasmas*, 18(3):032109, 2011.

[139] F. Avino, A. Fasoli, and I. Furno. The new TORPEX in-vessel toroidal conductor for the generation of a poloidal magnetic field. *Rev. Sci. Instrum.*, 85(3):033506, 2014.

[140] F. Avino, A. Fasoli, I. Furno, S. Jolliet, and P. Ricci. Basic characterization of TORPEX electrostatic modes in closed field line configurations. *Phys. Plasmas*, 21(12):122115, 2014.

[141] F. Avino, A. Fasoli, I. Furno, P. Ricci, and C. Theiler. X-point effect on plasma blob dynamics. *Phys. Rev. Lett.*, 116(10):105001, 2016.

[142] H.M. Mott-Smith and I. Langmuir. The theory of collectors in gaseous discharges. *Phys. Rev.*, 28(4):727, 1926.

[143] F.F. Chen. Electric probes. In R.H. Huddlestone and S.L. Leonard, editors, *Plasma Diagnostic Techniques*, chapter 4, pages 113–200. New York Academic Press, 1965.

[144] P.C. Stangeby. *The plasma boundary of magnetic fusion devices.* Chapman & Hall / CRC Press, 2000.

[145] I.H. Hutchinson. *Principles of plasma diagnostics, 2nd ed.* Cambridge University Press, 2002.

[146] C.K. Tsui, J.A. Boedo, P.C. Stangeby, and TCV Team. Accounting for debye sheath expansion for proud langmuir probes in magnetic confinement fusion plasmas. *Rev. Sci. Instrum.*, 89(1):013505, 2018.

[147] C. Theiler, I. Furno, A. Fasoli, P. Ricci, B. Labit, and D. Iraji. Blob motion and control in simple magnetized plasmas. *Phys. Plasmas*, 18:055901, 2011.

[148] S. Müller. *Turbulence in basic toroidal plasmas.* PhD thesis, École Polytechnique Fédérale de Lausanne, 2007.

[149] M. Baquero-Ruiz, F. Avino, O. Chellaï, A. Fasoli, I. Furno, R. Jacquier, F. Manke, and S. Patrick. Dual langmuir-probe array for 3d plasma studies in TORPEX. *Rev. Sci. Instrum.*, 87(11):113504, 2016.

[150] B. Labit, I. Furno, A. Fasoli, A. Diallo, S. H. Müller, G. Plyushchev, M. Podestà, and F. M. Poli. Universal statistical properties of drift-interchange turbulence in TORPEX plasmas. *Phys. Rev. Lett.*, 98(25):255002, 2007.

[151] B. Labit, A. Diallo, A. Fasoli, I. Furno, D. Iraji, S. Müller, G. Plyushchev, M. Podestà, F.M. Poli, P. Ricci, C. Theiler, and J. Horacek. Statistical properties of electrostatic turbulence in toroidal magnetized plasmas. *Plasma Phys. Control. Fusion*, 49(12B):B281, 2007.

[152] Ramalingam Shanmugam and Rajan Chattamvelli. *Statistics for scientists and engineers.* Wiley Online, 2015.

[153] H. Johnsen, H.L. Pécseli, and J. Trulsen. Conditional eddies, or clumps, in ion-beam-generated turbulence. *Phys. Rev. Lett.*, 55(21):2297, 1985.

[154] H. Johnsen, H.L. Pécseli, and J. Trulsen. Conditional eddies in plasma turbulence. *Phys. Fluids*, 30(7):2239–2254, 1987.

[155] F.J. Øynes, H.L. Pécseli, and K. Rypdal. Fluctuations in a magnetized toroidal plasma without rotational transform. *Phys. Rev. Lett.*, 75(1):81, 1995.

[156] F.J. Øynes, O.-M. Olsen, H.L. Pécseli, Å. Fredriksen, and K. Rypdal. Experimental study of low-frequency electrostatic fluctuations in a magnetized toroidal plasma. *Phys. Rev. E*, 57(2):2242, 1998.

[157] C. Theiler, I. Furno, A. Kuenlin, Ph Marmillod, and A. Fasoli. Practical solutions for reliable triple probe measurements in magnetized plasmas. *Rev. Sci. Instrum.*, 82(1):013504, 2011.

[158] D. Iraji, A. Diallo, A. Fasoli, I. Furno, and S. Shibaev. Fast visible imaging of turbulent plasma in TORPEX. *Rev. Sci. Instrum.*, 79(10):10F508, 2008.

[159] D. Iraji, I. Furno, A. Fasoli, and C. Theiler. Imaging of turbulent structures and tomographic reconstruction of torpex plasma emissivity. *Phys. Plasmas*, 17(12):122304, 2010.

[160] P. Micheletti, M. Baquero-Ruiz, F. Manke, I. Furno, P. Ricci, A. Fasoli, P. Bowen, C. Morais, and W. Zhao. Cathodoluminescent screen imaging system for seeded blob detection in TORPEX. *submitted to Rev. Sci. Instrum.*, 2019.

[161] M. Baquero-Ruiz, S. Alberti, O. Chellaï, I. Furno, T. Goodman, F. Manke, P. Micheletti, G. Plyushchev, and A.K. Skrivervik. Optically isolated millimeter-wave detector for the toroidal plasma experiment. *Rev. Sci. Instrum.*, 89(12):124702, 2018.

[162] O. Chellaï, S. Alberti, M. Baquero-Ruiz, I. Furno, T. Goodman, B. Labit, O. Maj, P. Ricci, F. Riva, L. Guidi, et al. Millimeter-wave beam scattering by edge-plasma density fluctuations in TCV. *Plasma Phys. Control. Fusion*, 61(1):014001, 2018.

[163] O. Chellaï. *Millimeter-wave beam scattering by edge turbulence in magnetically-confined plasmas.* PhD thesis, École Polytechnique Fédérale de Lausanne, 2019.

[164] G. Plyushchev. *Interaction of supra-thermal ions with turbulence in a magnetized toroidal plasma.* PhD thesis, École Polytechnique Fédérale de Lausanne, 2009.

[165] CF Barnett, JA Ray, and JC Thompson. Atomic and molecular cross sections of interest in controlled thermonuclear research. In *Report ORNL-3113, Revised.* Oak Ridge National Laboratory, 1964.

[166] A. Bovet, I. Furno, A. Fasoli, K. Gustafson, and P. Ricci. Three-dimensional measurements of non-diffusive fast ion transport in TORPEX. *Plasma Phys. Control. Fusion*, 55(12): 124021, 2013.

[167] P. Ricci, B. N. Rogers, and S. Brunner. High- and low-confinement modes in simple magnetized toroidal plasmas. *Phys. Rev. Lett.*, 100:225002, 2008.

[168] P. Paruta. *Simulation of plasma turbulence in the periphery of diverted tokamaks.* PhD thesis, École Polytechnique Fédérale de Lausanne, 2018.

[169] A. Bovet, I. Furno, A. Fasoli, K. Gustafson, and P. Ricci. Investigation of fast ion transport in TORPEX. *Nucl. Fusion*, 52(9):094017, 2012.

[170] K. Gustafson and P. Ricci. Lévy walk description of suprathermal ion transport. *Phys. Plasmas*, 19(3):032304, 2012.

[171] H. Kantz and T. Schreiber. *Nonlinear time series analysis*, volume 7. Cambridge university press, 2004.

[172] J.-P. Bouchaud and M. Potters. *Theory of financial risk and derivative pricing: from statistical physics to risk management.* Cambridge University Press, 2003.

[173] D. Guszejnov, N. Lazányi, A. Bencze, and S. Zoletnik. On the effect of intermittency of turbulence on the parabolic relation between skewness and kurtosis in magnetized plasmas. *Phys. Plasmas*, 20(11):112305, 2013.

[174] Z.S. She, E. Jackson, and S.A. Orszag. Intermittent vortex structures in homogeneous isotropic turbulence. *Nature*, 344(6263):226, 1990.

[175] J.P. Boris. Relativistic plasma simulation optimization of a hybrid code. In *Proceedings of the Fourth Conference on Numerical Simulation of Plasmas, November 2, 3, 1970*. Washington : Naval Research Laboratory, 1972.

[176] S. Zenitani and T. Umeda. On the boris solver in particle-in-cell simulation. *Phys. Plasmas*, 25(11):112110, 2018.

[177] Antti Snicker, Taina Kurki-Suonio, and Seppo K Sipila. Realistic simulations of fast-ion wall distribution including effects due to finite larmor radius. *IEEE T. Plasma Sci.*, 38(9): 2177–2184, 2010.

[178] R.J. Akers, E. Verwichte, T.J. Martin, S.D. Pinches, and R. Lake. Gpgpu monte carlo calculation of gyro-phase resolved fast ion and n-state resolved neutral deuterium distributions. In *Proc. 39th EPS Conference on Plasma Physics*, page P5, 2012.

[179] H. Qin, S. Zhang, J. Xiao, J. Liu, Y. Sun, and W. M. Tang. Why is boris algorithm so good? *Phys. Plasmas*, 20(8):084503, 2013.

[180] C.F. Beadle and P. Ricci. Understanding the turbulent mechanisms setting the density decay length in the tokamak scrape-off layer. *to be submitted to J. Plasma Phys.*, 2020.

[181] D. Shepard. A two-dimensional interpolation function for irregularly-spaced data. In *Proceedings of the 1968 23rd ACM national conference*, pages 517–524. ACM, 1968.

[182] K.F. Riley, M.P. Hobson, and S.J. Bence. *Mathematical methods for physics and engineering: a comprehensive guide*. Cambridge University Press, 2006.

[183] I. Calvo, R. Sanchez, and B.A. Carreras. Fractional Lévy motion through path integrals. *J. Phys. A- Math. Theor.*, 42(5):055003, 2009.

[184] A. Fick. Ueber diffusion. *Annalen der Physik*, 170(1):59–86, 1855.

[185] J. B. J. baron Fourier. *Théorie analytique de la chaleur*. F. Didot, 1822.

[186] A. Einstein. Zur theorie der brownschen bewegung. *Annalen der physik*, 324(2):371–381, 1906.

[187] M. Von Smoluchowski. Zur kinetischen theorie der brownschen molekularbewegung und der suspensionen. *Annalen der Physik*, 326(14):756–780, 1906.

[188] P. Langevin. Sur la théorie du mouvement brownien. *C. R. Acad. Sci. (Paris)*, 146:530–533, 1908.

[189] D.S. Lemons and A. Gythiel. Translation of Paul Langevin's 1908 paper "On the theory of Brownian motion". *Am. J. Phys.*, 65(11):1079–1081, 1997.

[190] G.E. Uhlenbeck and L.S. Ornstein. On the theory of the brownian motion. *Phys. Rev.*, 36 (5):823, 1930.

[191] J.L. Garcia-Palacios. Introduction to the theory of stochastic processes and brownian motion problems. *arXiv preprint cond-mat/0701242*, 2007.

[192] N.G. Van Kampen. *Stochastic processes in physics and chemistry*, volume 1. Elsevier, Amsterdam/Oxford, 1992.

[193] H. Risken. *The Fokker-Planck equation.* Springer, 1996.

[194] M. Baquero-Ruiz, F. Manke, I. Furno, A. Fasoli, and P. Ricci. Particle transport at arbitrary timescales with poisson-distributed collisions. *Phys. Rev. E*, 100(5):052134, 2019.

[195] I. Calvo and R. Sanchez. The path integral formulation of fractional brownian motion for the general Hurst exponent. *J. Phys. A- Math. Theor.*, 41(28):282002, 2008.

[196] W. Feller. Über den zentralen grenzwertsatz der wahrscheinlichkeitsrechnung. In *Selected Papers I*, pages 167–205. Springer, 2015.

[197] L. Le Cam. The central limit theorem around 1935. *Stat. Sci.*, pages 78–91, 1986.

[198] TD Rognlien, ME Rensink, and GR Smith. Users manual for the uedge edge-plasma transport code. Technical report, Lawrence Livermore National Lab., Livermore, CA (US), 2000.

[199] S. Wiesen, D. Reiter, V. Kotov, M. Baelmans, W. Dekeyser, A.S. Kukushkin, S.W. Lisgo, R.A. Pitts, V. Rozhansky, G. Saibene, et al. The new SOLPS-ITER code package. *J. nucl. mater.*, 463:480–484, 2015.

[200] R. Metzler and J. Klafter. The restaurant at the end of the random walk: recent developments in the description of anomalous transport by fractional dynamics. *J. Phys. A - Math. Gen.*, 37(31):R161, 2004.

[201] W.G. Glöckle and T.F. Nonnenmacher. A fractional calculus approach to self-similar protein dynamics. *Biophys. J.*, 68(1):46–53, 1995.

[202] D.S. Banks and C. Fradin. Anomalous diffusion of proteins due to molecular crowding. *Biophys. J.*, 89(5):2960–2971, 2005.

[203] P.E. Smouse, S. Focardi, P.R. Moorcroft, J.G. Kie, J.D. Forester, and J.M. Morales. Stochastic modelling of animal movement. *Philos. T. Roy. Soc. B*, 365(1550):2201–2211, 2010.

[204] D.W. Sims, E.J. Southall, N.E. Humphries, G.C. Hays, C.J.A. Bradshaw, J.W. Pitchford, A. James, M.Z. Ahmed, A.S. Brierley, M.A. Hindell, et al. Scaling laws of marine predator search behaviour. *Nature*, 451(7182):1098, 2008.

[205] D. Brockmann, L. Hufnagel, and T. Geisel. The scaling laws of human travel. *Nature*, 439(7075):462, 2006.

[206] K.B. Gustafson, B.S. Bayati, and P.A. Eckhoff. Fractional diffusion emulates a human mobility network during a simulated disease outbreak. *Front. Ecol. Evol.*, 5:35, 2017.

[207] B.B. Mandelbrot. *Fractals and scaling in finance: Discontinuity, concentration, risk. Selecta volume E.* Springer Science & Business Media, New York, 2013.

[208] S. Chaturapruek, J. Breslau, D. Yazdi, T. Kolokolnikov, and S.G. McCalla. Crime modeling with Lévy flights. *SIAM J. Appl. Math.*, 73(4):1703–1720, 2013.

[209] Richard Herrmann. *Fractional calculus: an introduction for physicists.* World Scientific, 2014.

[210] P. Paradisi, R. Cesari, A. Donateo, D. Contini, and P. Allegrini. Scaling laws of diffusion and time intermittency generated by coherent structures in atmospheric turbulence. *Nonlinear Proc. Geoph.*, 19(1):113–126, 2012.

[211] V.P. Budaev, S. Takamura, N. Ohno, and S. Masuzaki. Superdiffusion and multifractal statistics of edge plasma turbulence in fusion devices. *Nucl. Fusion*, 46(4):S181, 2006.

[212] F. Alouani-Bibi and J.A. Le Roux. Transport of cosmic-ray protons in intermittent heliospheric turbulence: model and simulations. *Astrophys. J.*, 781(2):93, 2014.

[213] P. Lévy. *Théorie de l'addition des variables Aléatoires.* Gauthier-Villars, Paris, 1954.

[214] A.N. Kolmogorov and B.V. Gnedenko. *Limit distributions for sums of independent random variables.* Addison-Wesley, 1968.

[215] F. Mainardi, Y. Luchko, and G. Pagnini. The fundamental solution of the space-time fractional diffusion equation. *arXiv preprint cond-mat/0702419*, 2007.

[216] R. Beals and J. Szmigielski. Meijer G-functions: a gentle introduction. *Notices of the AMS*, 60(7):866–872, 2013.

[217] B.B. Mandelbrot and J.W. Van Ness. Fractional Brownian motions, fractional noises and applications. *SIAM Review*, 10(4):422–437, 1968.

[218] F. Mainardi, A. Mura, and G. Pagnini. The M-Wright function in time-fractional diffusion processes: A tutorial survey. *Int. J. Differ. Equ.*, 2010:104505, 2010.

[219] H. Nakao. Multi-scaling properties of truncated lévy flights. *Phys. Lett. A*, 266(4-6):282–289, 2000.

[220] R.N. Mantegna and H.E. Stanley. Stochastic process with ultraslow convergence to a gaussian: the truncated Lévy flight. *Phys. Rev. Lett.*, 73(22):2946, 1994.

[221] I. Koponen. Analytic approach to the problem of convergence of truncated Lévy flights towards the gaussian stochastic process. *Phys. Rev. E*, 52:1197–1199, 1995.

[222] J. Rosiński. Tempering stable processes. *Stoch. Proc. Appl.*, 117(6):677–707, 2007.

[223] U. Küchler and S. Tappe. Tempered stable distributions and processes. *Stoch. Proc. Appl.*, 123(12):4256–4293, 2013.

[224] H. Fallahgoul and G. Loeper. Modelling tail risk with tempered stable distributions: an overview. *Ann. Oper. Res.*, pages 1–28, 2019.

[225] C. Pan, B. Li, C. Wang, Y. Zhang, N. Geldner, L. Wang, and A.L. Bertozzi. Crime modeling with truncated Lévy flights for residential burglary models. *Math. Mod. Meth. Appl. S.*, 28(09):1857–1880, 2018.

[226] M.C. Mariani, I. Florescu, I. Sengupta, M.P.B. Varela, P. Bezdek, and L. Serpa. Lévy models and scale invariance properties applied to geophysics. *Physica A*, 392(4):824–839, 2013.

[227] A. Liemert and A. Kienle. Fundamental solution of the tempered fractional diffusion equation. *J. Math. Phys.*, 56(11):113504, 2015.

[228] B. Podobnik, P.Ch. Ivanov, Y. Lee, and H.E. Stanley. Scale-invariant truncated Lévy process. *EPL (Europhysics Letters)*, 52(5):491, 2000.

[229] P.R. Bevington and D.K. Robinson. *Data reduction and error analysis for the physical sciences - 3rd ed.* McGraw-Hill, New York, 2003.

[230] L. Kadi. Designing a suprathermal ion detector in TORPEX. Technical report, Ecole Polytechnique Fédérale de Lausanne - Swiss Plasma Center, 2017.

[231] L. Kadi. Investigation of suprathermal ions in TORPEX with a quintuple GEA. Technical report, Ecole Polytechnique Fédérale de Lausanne - Swiss Plasma Center, 2018.

[232] M. Baquero-Ruiz and P. Lavanchy. On the proposed multi-gea electronics system. private communication.

[233] T. Schreiber. Measuring information transfer. *Phys. Rev. Lett.*, 85(2):461, 2000.

[234] D. et. al. Galassi. Global simulations of the interaction between edge turbulence and magnetic X-point in magnetized toroidal plasmas. Poster contribution, 7th International Workshop on Plasma Edge Theory in Fusion Devices, UCSD, La Jolla, California, USA, .

[235] D. Galassi. On plasma measurements in the central X-point geometry in torpex. private communication, .

[236] B. Efron and R. J. Tibshirani. An introduction to the bootstrap. *MG Stat. Pro.*, 57:17, 1993.

[237] C.K. Birdsall and A.B. Langdon. *Plasma physics via computer simulation.* CRC press, Boca Raton, 2018.

[238] I. Podlubny. *Fractional Differential Equations*, volume 198 of *Mathematics in Science and Engineering*. Academic Press, San Diego / Boston, 1998.

Acknowledgements

None of this work, however useful it may prove or not, would have been possible without the continued professional support of my colleagues at the Swiss Plasma Center. My thanks go to all those who helped to get TORPEX running on occasion - from the mechanical, electronic and electrical engineers to the other members of my research group, especially Oulfa, Paolo, Marcelo and Ivo. My peers in the office - Lorenzo, Pedro, Mengdi, Francesco and Mirko - deserve my deep thanks for their good humour, helpful advice and so many a good chuckle. Furthermore, I am very grateful to Ambrogio Fasoli and Paolo Ricci, whose advice on my papers was always highly appreciated. To them, Ivo, and Jean-Phillipe Hogge go my thanks for their inspiring roles in teaching, that were a pleasure to assist in.

As the person with whom I have been working most closely, Marcelo Baquero deserves my thanks for patiently introducing me to the practical realities experimental physics, his substantial analytical work on intermittency, hundreds of invaluable discussions over the years, and for always treating me as a true colleague. As my thesis advisor, I am deeply grateful to Ivo Furno - for offering me this opportunity 5 years ago, for his intensely contagious curiosity, for the freedoms in pursuing my ideas, for his ability to bring things into focus, for his encouragement in failure and success and for his humanity and understanding, whenever a delay occurred. Rest both assured that your continued positivity has been thoroughly appreciated on a professional and personal level.

On the latter, I also wish to thank all my friends close and far, who have supported me with so many a kind word and pat on the back. Many thanks to the Cuerel family for welcoming me to Switzerland and inspiring me through the lives you chose. To Anna, Ronny, their daughter Maria and her little sibling - thank you for always reminding me that there is so much more meaning and joy to wrest from life. So many thanks and "biiiiiiig hugs" go to my friend Margaret-Anne, who always had an open ear when some venting was needed, encouraging words despite her own struggles, and who made me keep and loose my bit of sanity in equal measures.

Above all, I wish to thank my parents, without whom any of this would not have been possible. My everlasting, deepest thanks for your calm support and far-sighted advice, for your patience when I was busy as ever, for all the peaceful times we shared as well as the arguments, for keeping me tethered and feeling at home and for pushing me to reach just a bit further.

Lausanne, April 10, 2020 Fabian Manke

Fabian Manke

Sur Villard 7, 1026 Denges, Switzerland
✉ fabian.manke@epfl.ch
☎ +41 2169 36588 📱 +41 7677 89233
in www.linkedin.com/in/fabian-manke-sci

Personal data

Date/place of birth:	04/07/1991, *Zittau, Germany*

Most recent position

01/09/2015 - 29/02/2020	**PhD Plasma Physics** (defended) - EPFL, Swiss Plasma Center, Lausanne, Switzerland - Fundamental plasma physics on the TORPEX device, both experimental and numerical - Description of non-diffusive fast ion transport through analysis of intermittent time-series and development of truncated fractional diffusion equations

Education and work experience

10/2011-08/2015	**MSci Physics with Theoretical Physics**, Imperial College London, UK *First Class Honours* Master project: Modeling neutron diagnostics for inertial fusion experiments
08/2014-09/2014	**Internship** Geometrical description of stellarator coils in C++, Max Planck Institute for Plasma Physics, Greifswald, Germany
06/2014-08/2014	**UROP** Undergraduate Research OPportunity on inertial fusion neutron spectra, Imperial College London, UK
07/2013-09/2013	**UROP** Undergraduate Research OPportunity on charge transport in dye molecules for photovoltaics, Imperial College London, UK
09/2010-08/2011	**Social service** Volunteer with Action Reconciliation Service for Peace (ARSP / ASF): Full-time on-site assistant in a L'Arche living community for people with mental handicap, Wambrechies, France

Transferable skills

IT general	Office Suite, LaTeX (incl. Beamerposter), Linux, git version control, GIMP, blender
Programming	Matlab (professional), Fortran90, C++ (advanced), Python (basic)
Experimental	Handling high-vacuum equipment, D-TACQ acquisition systems, basic electronics
Mathematics	Data-driven statistics and fitting, non-gaussian random processes, fractional calculus

Achievements

07/2019	Invited talk at the European Physical Society's 46th Conference on Plasma Physics
06/2016	Faculty commendation for quality in a teaching assistantship
10/2015	Tessella prize for software, awarded for the best computational master projects
03/2013	Division 2 finalist medal for waltz at UK Inter-Varsity Dance Competition

Languages

German (native), English (C2), French (C1), Italian (basic)

Interests

Reading, fitness sports, ballroom dancing, finance

Publications

First author

F. Manke, M. Baquero-Ruiz, I. Furno, O. Chellaï, A. Fasoli, and P. Ricci: *"Truncated Lévy motion through path-integrals and applications to nondiffusive suprathermal ion transport"*, Phys. Rev. E **100**, 052122, APS, 2019

F. Manke, M. Baquero-Ruiz, I. Furno, O. Chellaï, A. Fasoli, and P. Ricci: *"Characterizing time intermittency in nondiffusive fast ion transport through plasma turbulence"*, invited talk and contribution to 46th EPS Conference on Plasma Physics (Milan 07/2019), Plasma Phys. Control. Fusion **62**, 014004, IOP, 2019

F. Manke, M. Baquero-Ruiz, I. Furno, O. Chellaï, A. Fasoli, and P. Ricci: *"Time intermittency in nondiffusive transport regimes of suprathermal ions in turbulent plasmas"*, Phys. Rev. E **99**, 053208, APS, 2019

F. Manke, J.M. Frost , V. Vaissier , J. Nelson and P. R. F. Barnes: *"Influence of a nearby substrate on the reorganization energy of hole exchange between dye molecules"*, Phys. Chem. Chem. Phys. **17**, 7345-7354, RSC, 2015

Co-author

M. Baquero-Ruiz, **F. Manke**, I. Furno, A. Fasoli, P. Ricci: *"Particle transport at arbitrary timescales with Poisson-distributed collisions"*, Phys. Rev. E **100**, 052134, APS, 2019

M. Baquero-Ruiz, S. Alberti, O. Chellaï, I. Furno, T. Goodman, **F. Manke**, P. Micheletti, G. Plyushchev, and A. K. Skrivervik: *"Optically isolated millimeter-wave detector for the Toroidal Plasma Experiment"*, Rev. Sci. Instrum. **89**, 124702, AIP, 2018

O. Chellaï, S. Alberti, M. Baquero-Ruiz, I. Furno, T. Goodman, **F. Manke**, G. Plyushchev, L. Guidi, A. Koehn, O. Maj, E. Poli, K. Hizanidis, L. Figini, and D. Ricci: *"Millimeter-Wave Beam Scattering by Field-Aligned Blobs in Simple Magnetized Toroidal Plasmas"*, Phys. Rev. Lett. **120**, 105001, APS, 2018

M. Baquero-Ruiz, **F. Manke**, I. Furno, A. Fasoli, P. Ricci: *"Meandering particle bunches and a link between averages of time series of particle counts and higher-order moments"*, Phys. Rev. E **98**, 032111, APS, 2018

M. Baquero-Ruiz, F. Avino, O. Chellai, A. Fasoli, I. Furno, R. Jacquier, **F. Manke**, and S. Patrick: *"Dual Langmuir-probe array for 3D plasma studies in TORPEX"*, Rev. Sci. Instrum. **87**, 113504, AIP, 2016

J.P. Chittenden, B.D. Appelbe, **F. Manke**, K. McGlinchey, and N.P.L. Niasse: *"Signatures of asymmetry in neutron spectra and images predicted by three-dimensional radiation hydrodynamics simulations of indirect drive implosions"*, Rev. Sci. Instrum. **87**, 113504, APS, 2016